Salinité de surface dans le gyre subtropical de l'Atlantique Nord (SPURS/SMOS/Mercator)

Anna Sommer

Laboratoire d'Océanographie et du Climat
Expérimentations et Approches Numériques

CENTRE NATIONAL D'ÉTUDES SPATIALES

SORBONNE UNIVERSITÉS

THESE DE DOCTORANT DE L'UNIVERSITE PARIS VI

PIERRE ET MARIE CURIE

Ecole doctorale des Sciences de l'Environnement d'Ile de France (ED129)

Spécialité: Océanographie Physique

Présentée par Anna SOMMER

Salinité de surface dans le gyre subtropical de l'Atlantique Nord (SPURS/SMOS/Mercator)

Pour obtenir le grade de

DOCTEUR de l'UNIVERSITE PIERRE ET MARIE CURIE

Soutenue 21 Novembre 2016

devant le jury composé de :

Thierry Delcroix	Rapporteur	LEGOS
Anne-Marie Treguier	Rapporteur	IUEM
Pascale Bouruet-Aubertot	Examinateur	LOCEAN
Yann Drillet	Examinateur	MERCATOR OCEAN
Thierry Penduff	Examinateur	LGGE
Philippe Escudier	Examinateur	CNES
Gilles Reverdin	Directeur de thèse	LOCEAN
Jacqueline Boutin	Co-directeur de thèse	LOCEAN

Remerciements

Ma thèse est terminée! L'un des chapitres de ma vie est presque clos! Il ne me reste qu'à me rappeler et qu'à remercier tous ceux qui étaient avec moi...

Tout d'abord, sans aucune doute, je voudrais remercier mes deux directeurs de thèse, Gilles et Jacqueline. Je remercie Gilles pour son attitude positive, son ouverture à la discussion, sa disponibilité, pour tous ses commentaires et ses suggestions. Un grand merci aussi à Jacqueline qui m'a appris beaucoup de choses. J'ai eu la chance de travailler pendant trois ans avec ces deux chercheurs. Tous les deux, ils ont partagé avec moi leur expérience dans le domaine de la salinité de surface de la mer. Je sens que «j'ai grandi» dans ma vie professionnelle avec vous! Merci aussi pour la possibilité que vous m'avez donné de participer à des conférences et réunions internationales. Cela m'a donné une grande expérience de la communication avec d'autres chercheurs et cela a élargi ma culture. Merci à vous deux!

Merci à mes deux rapporteurs, Thierry et Anne-Marie. Je vous remercie pour votre travail approfondi sur ma thèse, pour vos commentaires, ceux qui ont contribué à améliorer la présentation de mon travail. Merci aux autres membres de mon jury: Pascale, Thierry, Philippe et Yann. Je suis honorée que vous avez accepté mon invitation à participer à ma soutenance. Merci aussi à Thierry et Guy pour leur participation à mon comité de thèse pendant ces trois années.

Je tiens également à remercier le CNES qui a co-financé ce travail et m'a permis de contribuer à un sujet important, comme l'étude de la salinité de la mer depuis l'espace.

Merci à Nicolas K., qui m'a aidé au début de la thèse à m'intégrer rapidement dans un sujet nouveau pour moi. Et merci pour la "conversation à propos de l'avenir".

Merci au laboratoire où j'ai passé ces années et où j'ai acquis des grands amis. Merci Adele, Nicolas, Paul et Julien d'avoir été présent, je vous remercie de votre amitié, de votre soutien, des moments drôles. Il est formidable que nous étions tous ensemble dans notre bureau, le plus chaud et le plus ensoleillé, et un peu "étrange" (vous savez ce que je veux dire). Ça va me manquer nos sorties de mölkky, nos déjeuners ensemble et les soirées de "blablabla".

Merci à mes amis Laura et Julian. Nous ne nous sommes pas vu souvent, mais il était toujours agréable de savoir que mes amis étaient à proximité.

Merci à mes chers parents, Tatiana et Fedor. Malgré le fait que vous étiez loin, vous m'avez soutenu toujours, et tous ces trois ans, chaque jour, vous étiez avec moi. Merci à ma soeur Janna, mon meilleur ami "pour toujours". Merci à ma grand-mère pour son aide précieuse dans ma vie en France. Je vous remercie, mes chers!

Merci à la petite Iris de me distraire de «la dure vie quotidienne de la science" et de me faire revenir un peu à l'enfance.

Et enfin, merci à mon cher Sébastien pour tant de choses .. cette thèse sera mémorable pour moi encore plus par le fait que nous nous sommes rencontrés presque à son début... et il y a encore beaucoup de choses à venir!

Résumé

Ce travail a porté sur la variabilité de la salinité de surface (SSS) de l'océan dans le gyre subtropical nord Atlantique. J'ai étudié la variabilité saisonnière de la SSS en lien avec les flux d'eau douce échangés avec l'atmosphère et la circulation océanique à méso échelle, au cours de plus de deux ans, d'août 2012 à décembre 2014. Les produits issus de la mission satellitaire Soil Moisture and Ocean Salinity (SMOS) corrigés de biais systématiques aux grandes échelles ont été testés et utilisés pour restituer la variabilité méso-échelle de SSS. Nous avons de surcroit utilisé l'analyse numérique à haute résolution PSY2V4R2-R4 de Mercator. Les champs issus de SMOS et des analyses ont été comparés aux données in situ de bouées dérivantes et de thermosalinographes recueillies pendant l'expérience SPURS, avec des résultats satisfaisants, en particulier en hiver, et des écarts-type de différences typiques de l'ordre de 0.15 pss.

Le flux d'eau douce échangé avec l'atmosphère est le terme dominant dans le bilan saisonnier de la SSS. Ce sont des termes associés à la dynamique océanique qui le compensent partiellement. En particulier, l'entrainement des eaux sous-jacentes contribue fortement en début d'hiver, lorsque la couche mélangée (ML) s'approfondit. Il agit d'ordinaire à réduire la SSS, à l'exception de la région au sud du maximum de SSS, où c'est au contraire une augmentation qu'il induit, du fait de la remontée d'eaux salées issues de la subduction plus au nord associée à la cellule de circulation thermohaline superficielle des régions subtropicales. Ainsi, les gradients horizontaux de la ML jouent un rôle important dans le bilan de SSS.

L'advection est une seconde contribution importante à la variabilité de la SSS. Elle transfère ainsi plus au nord les eaux 'salinisées' plus au sud dans la région du maximum de perte d'eau douce vers l'atmosphère (excès d'évaporation). Quoique les bilans faits sur les champs PSY2V4 et ceux de SMOS (en combinaison avec les produits de l'altimétrie) soient en accord qualitatif, ils présentent des différences importantes en ce qui concerne l'amplitude de l'advection horizontale. Dans le cas de PSY2V4, le terme d'advection horizontale est une contribution dominante au bilan saisonnier de SSS qui contre-équilibre les flux de surface, avec des contributions associées aux courants moyens et à la variabilité méso-échelle du même ordre de grandeur. Par contre, le bilan s'appuyant sur les produits SMOS présente une plus faible advection avec une contribution très faible de l'activité tourbillonnaire. Une analyse détaillée montre que le produit SMOS lisse trop certaines petites échelles qui doivent contribuer fortement au terme d'advection. Par ailleurs, les données de courant des produits altimétriques pourraient aussi avoir une résolution insuffisante, par comparaison à ce que l'on observe dans l'analyse PSY2V4. Il n'en reste pas moins que les plus grandes incertitudes pourraient provenir de la façon dont les courants d'Ekman induits par les

tensions de vent à la surface sont calculés.

Mots-clés: salinité de l'océan, la variabilité océanique, SMOS, l'Atlantique Nord, flux d'eau douce, advection océanique

Abstract

The focus of this work is on sea surface salinity (SSS) variability in the North Atlantic subtropical gyre. We study seasonal SSS variability and its link to the atmospheric freshwater flux at the ocean surface and to ocean dynamics at meso-scales for the period August 2012 – December 2014. The products from the Soil Moisture and Ocean Salinity (SMOS) satellite mission corrected from large scale systematic errors are tested and used to retrieve meso-scale salinity features. Furthermore, the PSY2V4R2-R4 analysis produced by Mercator with a high spatial resolution is also used. The comparison of corrected SMOS SSS data and Mercator analysis with drifter's in situ and TSG measurements from the SPURS experiment shows a reasonable agreement with RMS differences on the order of 0.15 pss.

The freshwater seasonal flux is the leading term in the SSS seasonal budget. To balance its effect the ocean dynamics strongly contribute. The entrainment of deeper water is strong during the winter time when the mixed layer (ML) is deepening. It usually acts to lower SSS, except in the South of the SSS–max region where it contributes to increase salinity due to the subducted salty water that originates further north and is advected at subsurface by the shallow overturning circulation. Thus, the horizontal gradient of ML depth plays an important role in the SSS budget.

Advection is the second important component responsible for the SSS variability. It transfers further north the salty water from the evaporation maximum region. Although the budgets done with Mercator and SMOS (in combination with AVISO altimetry) fields agree qualitatively, they present a huge difference in the magnitude of the horizontal salinity advection. In the case of Mercator, horizontal advection is a dominant component of SSS budget that counteracts the effect of surface forcing, and the contribution of mean and turbulent advection have the same magnitude. On the other hand, the SMOS-based budget shows a smaller effect of advection with an almost negligible contribution of the turbulent advection. A detailed analysis shows that the SMOS satellite product smooths out small-scale salinity features that might be important in the eddy advection. Furthermore, the data used for ocean currents do not have sufficient resolution based on what is simulated in Mercator. However, it is shown that the largest uncertainties originate from the method used to estimate the Ekman current from observations.

Keywords: ocean salinity, ocean variability, SMOS, North Atlantic, freshwater flux, ocean advection

Contents

Acronyms

AQUARIUS	satellite mission (NASA US and CONAE Argentina)
AF-FOV	Alias-Free Field Of View
ASIMET	Air-Sea Interaction Meteorology
AVISO	Archiving, Validation and Interpretation of Satellite Oceanographic data
BL	Barrier Layer
CATDS	Centre Aval de Traitement des Données SMOS
CEC	CATDS Salinity Expertise center
CMIP	Coupled Model Intercomparison Project
CNES	Centre national d'études spatiales
CTD	Conductivity, Temperature, Depth
DUACS	Data Unification and Altimeter Combination System
E	Evaporation
ECMWF	European Centre for Medium-range Weather Forecasting
ENSO	El Niño Southern Oscillation
ERA-Interim	ECMWF Re-Analysis Interim
ESA	European Space Agency
FOV	Field Of View
GPCP	Global Precipitation Climatology Project
ISAS	In Situ Analysis System
ITCZ	InterTropical Convergence Zone
LICEF	Lightweight Cost Effective Front-end
LOCEAN	Laboratoire d'océanographie et du climat: expérimentations et approches numériques
MDT	Mean Dynamic Topography
MIDAS cruise	Marine Information and Data Acquisition System cruise
MIRAS	Microwave Imaging Radiometer by Aperture Synthesis
ML	Mixed Layer
MLD	Mixed Layer Depth

MLS	Mixed Layer Salinity
MLT	Mixed Layer Temperature
MOC	Meridional Overturning Circulation
NADW	North Atlantic Deep Waters
NASA	National Aeronautics and Space Administration
NRT	Near-Real Time
NSTG	North Atlantic SubTropical Gyre
OAFlux	Objectively Analyzed air-sea Fluxes
OI	Optimal Interpolation
OSCAR	Ocean Surface Current Analyses Real-time
OSTIA	Opertional SST and Sea Ice Analysis
P	Precipitation
RFI	Radio-Frequency Interference
RMS	Root Mean Square
S	Salinity
SIO	Scripps Institution of Oceanography
SLA	Sea Level Anomaly
SM	Soil Moisture
SMOS	Soil Moisture and Ocean Salinity
SPURS	Salinity Processes in the Upper-ocean Regional Study
SSALTO	Ssalto multimission ground segment
SSH	Sea Surface Height
SSM/I	Special Sensor Microwave/Imager
SSS	Sea Surface Salinity
SST	Sea Surface Temperature
STRASSE	SubTRopical Atlantic Surface Salinity Experiment
SVP-S	Surface Velocity Program – Salinity
T	Temperature
$\boldsymbol{T_B}$	Brightness temperature
TKE	Total Kinetic Energy
TMI	TRMM Microwave Imager
TRMM	Tropical Rainfall Measuring Mission
TSG	ThermoSalinoGraphs
XCTD	eX-pendable CTD
WHOI	Woods Hole Oceanographic Institution

Chapter 1

Introduction

1.1 What is Seawater Salinity?

Seawater contains 96.5% of water. The remaining mass (3.5%) is mostly dissolved material with the largest constituent corresponding to chloride sodium dissolved in ions. Among major ions (or hydrated ions), magnesium, sulfur or potassium are also found but in smaller quantity. All those components together constitute the seawater ***salinity*** defined as the dissolved salts in grams in 1kg of sea water.

At the beginning of the 19^{th} century the salinity was measured as the weight left after evaporation. However, this method was inaccurate as some elements were lost during this procedure (Millero et al., 2008).

Based on the Principle of Constant Proportions stating that the relative proportions of the principle constituents of sea water (based on samples mostly from Challenger expedition 1872–1876) are virtually constant in time and space (except in runoffs from continents), salinity can be estimated by measuring one of the dissolved materials. For this, the element chloride, one of the dominant components, was initially chosen. Thereby an empirical formula was used to estimate salinity based on chlorinity (Cl) (Knudsen, 1903): $S = 0.03 + 1.805 * Cl$. Here, chlorinity is the amount of chlorine, bromine and iodine in grams in 1kg of sea water assuming that the bromine and iodine are replaced by chlorine during the silver nitrate titration (Millero et al., 2008). To help in using this method, standards were distributed (standard sea water, initially from Copenhagen). But this method was not always very accurate and it was not easy to calibrate this empirical law. Moreover, in regions where the composition of sea water is not "standard"[1] this method in not applicable.

The chemical method was progressively replaced by an electrical method. Since the 1960s the salinity has been measured through the relation between the electrical conductivity of the sea water sample and the conductivity of the standard Potassium-

[1]The "Standard Seawater" or "Normal Water" is based on North Atlantic surface waters where certain samples were taken in specific regions (Knudsen, 1903). The chemical composition of these samples is practically identical. This water contains no nutrients.

Chloride solution (KCl) (Cox et al., 1967; Unesco, 1981; Millero et al., 2008):

$$S = 0.008 - 0.1692 * K_{15}^{1/2} + 25.3851 * K_{15} + 14.0941 * K_{15}^{3/2} \\ -7.0261 * K_{15}^{2} + 2.7081 * K_{15}^{5/2},$$

and

$$K_{15} = \frac{C(s, 15, 0)}{C(KCl, 15, 0)},$$

where $C(s, 15, 0)$ is the conductivity of the seawater sample at the temperature of 15^0C and the pressure of one standard atmosphere and $C(KCl, 15, 0)$ is the conductivity of KCl solution in which the mass fraction of KCl is 32. 4356 gr at the same temperature and pressure.

This salinity-conductivity relationship resulted in the introduction in 1978 of the Practical Salinity Scale, PSS-78, that is used today as the salinity value in all salinity data bases and in the present PhD work. Thus, salinity is dimensionless and does not have a unit but a scale corresponding to g/kg.

In 2009 the new standard TEOS-10 (Thermodynamic Equation of Seawater, 2010) was proposed during the International Oceanography Commission at its 25^{th} assembly (http://www.teos-10.org). This new standard, called "Absolute Salinity" (S_A), represents the mass fraction of dissolved material and now have units of g/kg that allows to use it in thermodynamic relationships. In the standard seawater the S_A equals to 35.1650 g/kg which is different from "Practical Salinity" (S_p), 35 pss. To estimate S_A the "Reference Salinity" has to be estimated:

$$S_R(g/kg) = \frac{35.16504}{35} \times S_p.$$

But the composition of seawater is not constant (changes in carbon, nutrients, calcium etc.) and, thus, S_R has to be corrected:

$$S_A = S_R + \delta S_A.$$

This correction δS_A is usually positive and varies between 0.02 g/kg in the open ocean and 0.09 g/kg in some coastal zones.

To measure Sea Surface Salinity (SSS) today a large variety of *in situ* instrumented platforms are used, such as surface drifters, moorings, TSG (ThermoSalinoGraph) which measure salinity near the surface or at a fixed depth, as well as CTD (Conductivity, Temperature, Depth) or XCTD (eXpendable CTD) instruments deployed from ships, or autonomous vehicles (gliders) and platforms (ARGO profilers) that measure the vertical profile of salinity from the surface to at least ∼200 m. But due to their diversity and spatial–temporal coverage the *in situ* salinity measurements remain under-sampled and unequally distributed. Recently, two projects were developed to measure SSS from space: SMOS (Soil Moisture and Ocean Salinity) from ESA (European Spatial Agency) and AQUARIUS from NASA. The advantages of satellite measurements is that they can provide global mapping of salinity at the surface. Later, in section 1.4, I will provide further information on *in situ* measurements and methods to measure salinity from instrumented satellites.

The average salinity concentration in the ocean is about 34.7 g of salt in 1kg of seawater. This concentration varies depending on the place and time and is directly influenced by precipitation and evaporation at the surface as well as by ocean circulation, diffusion, and mixing of water masses. The deep water is more homogeneous and its salinity is between 34 and 35 pss. At the surface the salinity variability is more important: away from river plumes, ocean surface salinity varies between 30 and 38 pss. The highest concentration of salinity is found at mid-latitudes between 20^0N and 30^0N, where evaporation plays an important role. The less salty water is located in areas of strong river runoff (such as the Amazon River runoff), in regions of strong precipitation (Intertropical Convergence Zone (ITCZ) during the boreal summer) or close to sea ice regions (high latitudes). In the next section I will present the importance of SSS in oceanography and for air-sea interaction studies.

1.2 Salinity in Oceanography and for Air-Sea Exchange studies

During the last century the importance of salinity in oceanography and its role in monitoring the climate of our planet were recognized and continue to gain interest. Salinity is a water mass tracer that can track the water masses movement and mixing. It also contributes to sea water density, thus has an important dynamical role. Moreover, salinity is one of the important components of water cycle on the planet, as it is an indicator of changes in freshwater flux. Through the water cycle, salinity can be used to understand and observe the climate of our planet. Further, I will focus a bit more on these important properties of salinity.

Salinity as a water mass tracer. A water mass is a body of water with a common formation history, having its origin in a particular region of the ocean (Tomczak, 1999). They (water masses) are usually formed at the surface or in the mixed layer where they acquire homogeneous properties defined by atmosphere–ocean interaction. Water masses have "conservative" and "non-conservative" properties. Non-conservative properties are, for example nutrients and oxygen. They are modified during the life of water mass by biochemical processes. Salinity and temperature are conservative properties that do not have (major) sources or sinks and can be changed only by mixing with the contiguous water.

T–S diagrams (temperature as a function of salinity) are used to define water masses, mixing between them and their travel path.

Salinity in the ocean dynamics. Salinity (S) as well as temperature (T) participates in ocean physics through the density (ρ). The relation between density and temperature is defined by the coefficient of thermal expansion α :

$$\alpha = -\frac{1}{\rho}\frac{\partial \rho}{\partial T}.$$

The influence of salinity on density can be expressed by the coefficient of haline expansion β :

$$\beta = \frac{1}{\rho}\frac{\partial \rho}{\partial S}.$$

At the surface and at a salinity of 35 pss α varies from 0.25 10^{-4} K^{-1} at -2^{0}C to 3.4 10^{-1} K^{-1} at 31^{0}C (Gill, 1982; Talley et al., 2011). Coefficient β in the same conditions is on the order of 0.75 10^{-4} pss^{-1}. α is smaller in cold water and, thus, in these waters the variability in salinity can influence more the density. As presented in Talley et al. (2011; Table 3.2), the change in salinity by 0.5 pss at a salinity 35 pss provides the change in density $\Delta\rho$ = 0.37 kg/m^3 at temperature 30^{0}C and $\Delta\rho$ = 0.40 kg/m^3 at 0^{0}C, while the change in temperature by 1^{0}C at a salinity 35 pss provides the change in density $\Delta\rho$ = -0.34 kg/m^3 at temperature 30^{0}C and $\Delta\rho$ = -0.06 kg/m^3 at 0^{0}C.

Through the density, salinity influences the ocean dynamics: mixing, subduction, dynamic height anomaly. The density is included in geostrophic equations. Thus, variations of salinity and inaccuracy in its measurement can bring errors in estimation of dynamic height gradient and, thus, geostrophic currents (Ueki et al., 2002). It poses a problem at high latitudes where salinity brings larger error in density at low temperature, as mentioned before.

Salinity as a control variable in barrier and mixed layers. The first several meters of the ocean surface present a turbulent and homogeneous layer. This layer is called mixed layer (ML). ML is characterized by well mixed and uniform properties. This layer is the boundary between the deep ocean and atmosphere. This layer is under the influence of the ocean circulation, wind waves, surface freshwater and heat fluxes and other processes that all together result in changing salinity and temperature at the ocean surface. The ML can be also affected by subsurface processes as vertical advection and mixing, entrainment and diffusion. The transfers with the atmosphere of mass, momentum and energy occur in mixed layer and generate the ocean motions. Thus, it plays a critical role in the ocean dynamics. The depth of this layer (MLD) depends on the temperature and salinity profiles. In some regions, the MLD can be controlled mostly by salinity.

In the case when the MLD is limited by the halocline[2] the vertical structure of the upper ocean presents three layers. The layer between the MLD defined by halocline and MLD defined by thermocline is called barrier layer (BL) (de Boyer Montégut et al., 2004, 2007; Sprintall and Tomczak, 1992). BLs are mostly found in the equatorial and tropical regions (de Boyer Montégut et al., 2007). The BL has a strong impact on the climate. Salinity shallows the MLD (as defined by BL), thus, the energy transferred across the MLD is limited by the halocline, and, as consequence, is more efficient as the momentum fluxes will be redistributed over this shallower depth (de Boyer Montégut et al., 2007; Vialard and Delecluse, 1998). Moreover, the BL can prevent the surface cooling and, thus, induces positive surface temperature anomaly than can influence the onset of El Niño-Southern Oscillation (ENSO).

Role of salinity in the global circulation and the formation of deep waters. Figure 1.1 presents the global thermohaline circulation. It is also referred to as the meridional overturning circulation (MOC). The MOC is responsible for a large part of the heat redistribution over the world. MOC is mostly caused by temperature and salinity gradients but also by the wind. In the North Atlantic the warm water moves from low to high latitudes through wind-driven western boundary currents. The water is cooling on its way and deepens as it becomes denser at high latitudes to form

[2]Halocline is vertical zone in the oceanic water column in which salinity changes rapidly with depth, located below the ML where salinity is uniformly distributed.

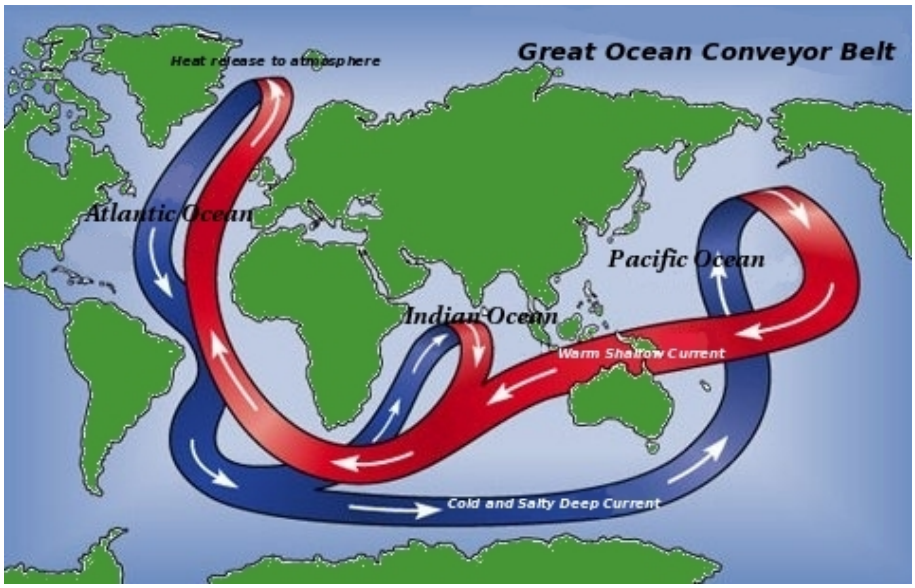

Figure 1.1: Global thermohaline circulation or "conveyor belt" circulation. Source: modified after Broecker (1991)

the North Atlantic Deep Waters (NADW). NADW moves in opposite direction to the surface flow (southward) and afterwards up-wells south of the Antarctic Circumpolar Current in the Southern Ocean.

Figure 1.1 is a schematic that gives the impression of a closed system, however, there is also mixing with the water from outside of this system (river runoff etc.).

Salinity and freshwater cycle. The water cycle is a predominant element of the Earth's climate which has a specific impact on human society through agriculture, energy and water supply. In the global water cycle, the ocean plays a key role, with approximately 86% of global evaporation and 78% of global precipitation taking place over the ocean (Schmitt, 1995). Figure 1.2 shows the schematic global water cycle for a solid box 10^3 km^3. Despite growing observing capability, in particular from satellites, our knowledge of precipitation (P) and evaporation (E) over the oceans is still rudimentary (Trenberth et al., 2007; Skliris et al., 2014; Durack, 2015). It is due to coarse available *in situ* measurements and insufficient sampling or systematic errors in satellite retrievals.

The climatological mean of sea surface salinity (SSS) is closely related to the surface $E - P$ flux (Fig. 1.3) (Schmitt, 1995; Durack, 2015). This relation has long been noted; Würst in 1936 has proposed the relationship between SSS and $E - P$: $S = 34.6 + 0.0175 * (E - P)$ based on individual observations. Thus, as the ocean salinity is better observed than P or E, its monitoring could also contribute to better understand the pattern and variability of the $E - P$ field. Large salinity trends or multi-decadal variability have been observed in large parts of the world ocean in the last 30 to 50 years (Cravatte et al., 2009; Durack and Wijffels, 2010; Terray et al., 2012; Skliris et al., 2014). They provide sharper information about a changing global water cycle than terrestrial data (river flows, evaporation or precipitation) which show less trends or are

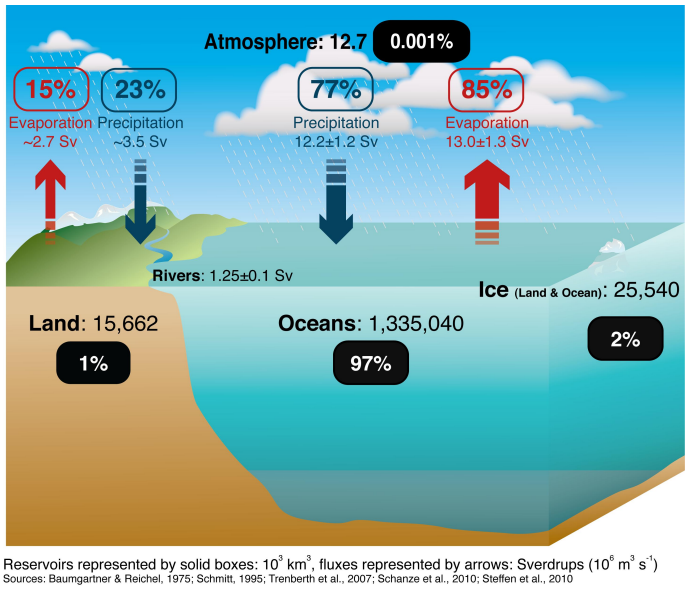

Figure 1.2: The global water cycle. Reservoirs represented by solid boxes: 10^3 km^3, fluxes represented by arrows: Sverdrups (10^6 m^{3}s -1). Sources: Durack (2015) (cover figure) after Baumgartner and Reichel (1975), Schmitt (1995), Trenberth et al. (2007), Schanze et al. (2010), Steffen et al. (2010)

more difficult to interpret (Dai et al., 2009; Lagerloef et al., 2010). Based on a model simulation from the Coupled Model Intercomparison Project (CMIP3) Durack and Wijffels (2010) have shown that the surface salinity responds to the surface warming in a way comparable with recent observations. The global water cycle is intensifying that results in the formula "fresh getting fresher and salty getting saltier" (Durack, 2015). The warmer atmosphere will carry more water vapor, as the water vapor is exponentially increasing with temperature, and, thus, it will intensify the evaporation in "dry" regions and precipitation in "wet" regions.

However, changes in salinity concentration originate not only from precipitation, evaporation, runoff, ice freezing and melting, but also from changes in ocean circulation and mixing (Talley, 2011). Thus, the ocean dynamics needs to be accurately assessed to link $E-P$ field's variability with change in SSS (Yu, 2011). At meso-scales, recent work in the North Atlantic subtropical gyre (Qu et al., 2011; Büsecke et al., 2014; Gordon and Giulivi, 2014; Farrar et al., 2015) shows a significant contribution of horizontal advection in governing surface salinity, with roughly half of the salinity variation being explained by ocean meso-scale dynamics. In the South Pacific, the compensation of fresh water loss is also made by vertical turbulent mixing and horizontal salinity advection (Hasson et al., 2013; Kolodziejczyk and Gaillard, 2013).

1.3 Sea surface salinity in the North Atlantic Ocean

In this thesis work the analysis of salinity is concentrated in the saltiest region of the world open ocean, the sub-tropical gyre of the North Atlantic Ocean (Fig. 1.3*a*).

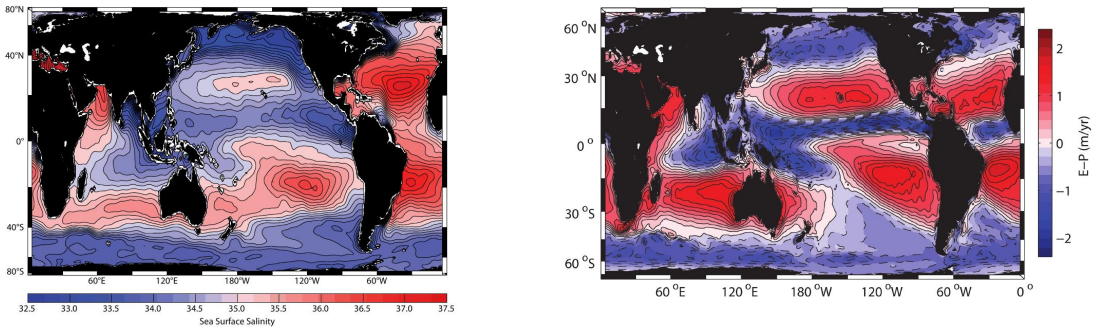

a *b*

Figure 1.3: *a* – Global surface salinity from the World Ocean Atlas, source: Lagerloef et al. (2010) (Fig. 2); *b* – Global annual average of $E - P$ field, source: Schanze et al. (2010) (Fig. 4)

In this region, evaporation is a dominant component of the salinity budget, as shown in the $E - P$ climatological map (Fig. 1.3*b*).

The eastern subtropical North Atlantic surface area is affected by dry continental air from North Africa. To balance this water loss due to an excess of the evaporation over the precipitation fluxes, fresh water transport is contributed by eddies, mixing processes, Ekman transport and the time mean circulation (Gordon and Giulivi, 2014). The Ekman transport from the tropics is large in this region and brings fresh and warm surface water from the tropics, while further north a weaker southward Ekman

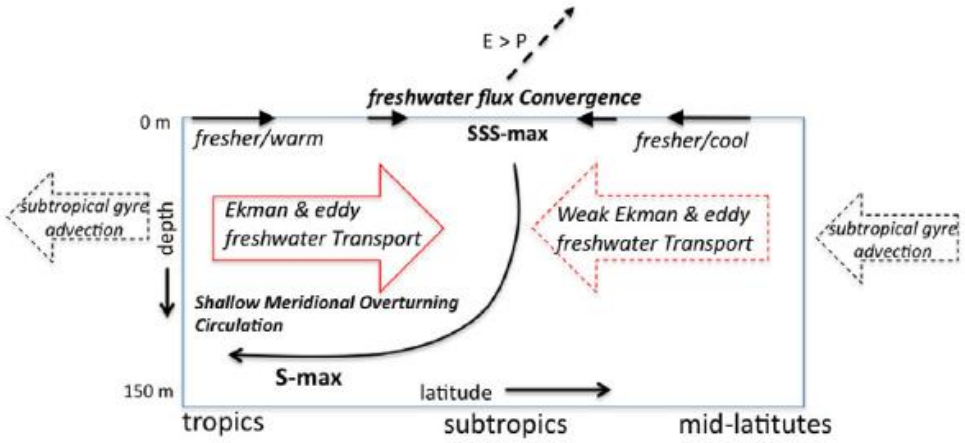

Figure 1.4: Schematic of the meridional freshwater balance within the ocean subtropical regime. The figure presents the SSS-max region generated by the strong evaporation that dominantes over precipitation. The water loss is compensated by ocean dynamics: Ekman and eddy freshwater transport from the South and North. Part of salty water is subducted and transfered to the equator by SMOC. Source: Gordon and Giulivi (2014) (Fig. 2)

transport brings fresh and cold water. As mentioned in the previous section the warm salty water from the SSS–max region participates in the deep water formation and is important for the global ocean circulation. After reaching the western boundary, as part of the wind-driven circulation (both at the surface and subsurface), it is carried further north by the Gulf Stream where it cools and then deepens.

In the eastern subtropical North Atlantic, the vertical entrainment of deeper water is expected to be a major contributor to the salinity variability, especially during the winter when ML is deepening (Dong et al., 2015). In the south of the region entrainment results in salting the surface water (Dong et al., 2015), which is due to the water from the Shallow Meridional Overturning Circulation[3] that brings salty water from the SSS–max region as subducted water that enters in ML when the latter is deepening in winter months in the southern region. Figure 1.4 presents the schematic of effects of different components on the salinity variability in the North Atlantic subtropical gyre.

The effect of ocean processes will strongly depend on the scale considered. Dohan et al. (2015) and Dong et al. (2015) estimated the MLS budget at large scales based on observation data. In Dohan et al. (2015) the estimation was made on the monthly $1/3^0 \times 1/3^0$ grid during the period September 2012 – August 2013, but the data used (Aquarius with spatial resolution 100–150 km and OSCAR analysis on $1/3^0$ grid) smooth the meso-scale effect. Dong et al. (2015) used the gridded T/S monthly field from Argo floats on $1^0 \times 1^0$ grids with spatial resolution $3^0 \times 3^0$ and initially averaged over 10 days for the period 2004–2013. However, due to the parameterization (interpolation of Argo profilers, monthly $E - P$ fields, constant eddy diffusion coefficient), as in previous case, meso-scale processes are weakly represented. These works showed that at large-scale, the change of SSS at monthly scale in salinity maximum region is small compared with the amplitude of the sea surface forcing and "residual terms" (subduction, vertical shear, vertical motions, internal waves and all small-scale and fast dynamics (Dohan et al., 2015)) that close the budget. Furthermore, Dong et al. (2015) found that for the SSS (or fresh water) budget the Ekman component dominates the total horizontal advection in this North Atlantic region. On the other hand, at the scale of turbulent advection (meso-scale), it is worth to note that the Ekman transport does not play a significant role. The turbulent advection is indeed mainly responsible for the freshening and warming/cooling by eddies (Treguier et al., 2012; Büsecke et al., 2014; Gordon and Giulivi, 2014). The three last works were concentrated on the contribution of eddy advection to balance the effect of freshwater flux. They present the analysis based on different types of data and periods: model (North Atlantic Model) (Treguier et al., 2012) with the resolution $1/12^0 \times 1/12^0$ and $1/4^0 \times 1/4^0$ and 5-days averaged data for 1993-2004, *in situ* data and model (ROMS) (Büsecke et al., 2014) at monthly and shorter time scale along the ship track for the short period March–April 2013, and reanalysis (SODA) (Gordon and Giulivi, 2014)

[3]The shallow meridional overturning circulation (SMOC) transfers a mass, heat, and salt between the subtropics and the equator and, thus, plays an important role in the redistribution of water properties in the ocean and in oceanic climate variability. In the North Atlantic, it consists of subtropical water subducted in eastern salty areas of the ocean, flowing to the west and equator. SMOC is closed by upwelling at the equator, with return flow to the subtropics in the surface Ekman layer. (Zilberman et al., 2013)

Table 1.1: Summary of recent works dedicated to the salinity variability in the North Atlantic

Work	Data	Terms estimated	Temporal scale	Sampling/ resolution
Treguier et al. (2012)	model: North Atlantic model	eddies adv. vs. freshwater, flux time-mean advection	5-days averaged data; 1993-2004 climatology	meso-scale ($1/12^0$, $1/4^0$)
Büsecke et al. (2014)	*in situ* (CTD, TSG), model ROMS	eddies adv. vs. freshwater flux	monthly and less; March/April 2013	meso-scale (ship track)
Gordon and Giulivi (2014)	Reanalysis SODA	eddies adv. vs. freshwater flux	monthly data, 1970-2010 - interan. var., 2004 - season. var.	meso-scale $0.4^0 \times 0.25^0$ (latitude band turb transp.)
Dohan et al. (2015)	Observation: Aquarius, OSCAR, Argo	total MLS budget	monthly data, Sept 2012 - Aug 2013, season. var.	large-scale (smooth data) $1/3^0 \times 1/3^0$/ 100-150km, 3^0
Dong et al. (2015)	Observation: Argo, GPCP, OAFlux, AVISO	total MLS budget	monthly data, 2004-2013, season. and interan. var.	large-scale (parameterization) $1^0 \times 1^0$/ 3^0
Farrar et al. (2015)	*in situ*: mooring, gliders	total MLS and MLT budgets	20 days period, Oct 2012 - Feb 2013	meso-scale (50km radius)
PhD thesis (2016)	Observation: SMOS, AVISO, *in situ*, model: Mercator	total MLS and MLT budgets	weekly data, Aug 2012 - Dec 2014, season. var.	meso-scale ($1/4^0$, $1/12^0$)/ (50km, $1/12^0$)

on the $0.4^0 \times 0.25^0$ monthly grid for 1970-2010. A summary of recent works dedicated to the analysis of SSS variability in the subtropical gyre on the North Atlantic can be found in Table 1.1.

1.4 Sea Surface Salinity measured *in situ* and from space

In situ salinity measurements are based on the measure of the sea water conductivity (see 1.1). In this thesis work, I am interested in the salinity close to the surface (between 0 and 10 m) and MLS that can be found from different type of *in situ* instruments that provide information at the surface as well as on the vertical stratification of salinity in the ML and even below. These measurements can be classified based on their spatial and temporal resolutions.

CTD (Conductivity, Temperature, Depth) and disposable sondes **XCTD** (eXpendable CTD) measure the conductivity, temperature and depth. They provide vertical profiles from typically 3–meters from the surface. The instruments are attached to a conducting wire cable that is connected to a computer on the ship board and allows to visualize the collected data on the computer screen. Moreover, rosette equipped with CTD allow to collect water samples.

Gliders collect data along a prescribed trajectory. Gliders float between the surface and some depth thanks to an external bladder. It is the autonomous underwater vehicle (AUV) that use its vertical motion (due to the change in buoyancy) to move forward. This is a significant advantage with respect to an electric motor that extends the mission to months and to thousands of kilometers. As the glider reaches the surface its trajectory can be modified. Gliders usually carry measurements of temperature, conductivity, currents, chlorophyll, bottom depth (typically, "good" measurements can be retrieved starting 1–m from the surface).

Surface drifters provide the data along their trajectories dictated by ocean currents during times often exceeding months to more than one year. The drifters measure salinity and temperature at a distance from the surface that depends on the size of the instrument (∼50 cm for Pacificgyre, Metocean and ICM drifters used in this work). They are also used to study ocean currents, as they are typically tethered to track currents at 15–m depth.

ARGO **profilers** provide the profiles of temperature and salinity of the upper 2000 m of the ocean. Argo profilers are battery-powered autonomous floats. These floats measure salinity and temperature from the depth deeper than 2000 m to the surface. The floats rise to the surface in about 6 hours. At the surface satellites or GPS determine the position of the floats and the floats transmit their data to the satellites, before the next cycle starts. Floats can make more than 150 such cycles.

TSG (ThermoSalinoGraphs) are installed on water inlets on ships-of-opportunity and research vessels. They continuously measure T and S in this water flow during the ship transits. The water intake is often installed inside or near to the hull of a ship in order to make measurements on uncontaminated seawater. Thus it measures the salinity (from the conductivity measurements), temperature, and can calculate sound velocity etc. at a nearly fixed depth (between 3 and 5 m, for research vessels; often deeper for merchant vessels and shallower for sailing vessels).

Moorings can provide T and S data close to the surface at one fixed point for a long period from months to several years with a time resolution on the order of an hour (or at high frequency).

As mentioned before, these data do not offer homogeneous and complete spatial or temporal sampling of the ocean. Figure 1.5 (taken from jcommops.org) shows the

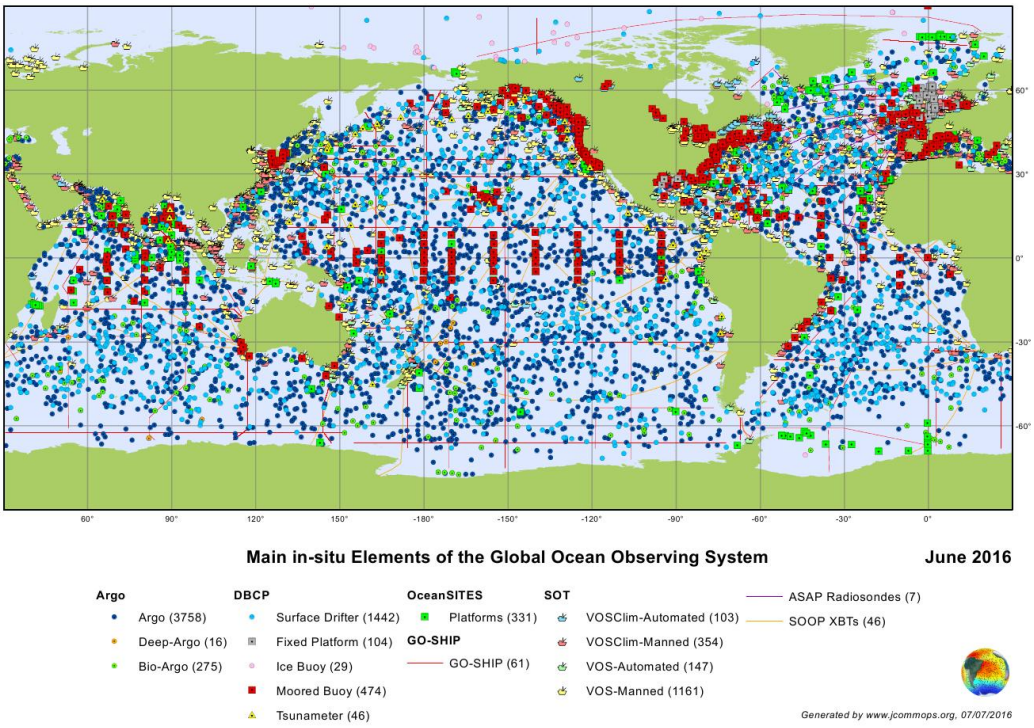

Figure 1.5: The spatial distribution of *in situ* instruments of Global Ocean Observing System, June 2016. Source: jcommops.org

combination of instruments that were observing the surface ocean in June 2016. The number of instruments as well as their types vary from one region to another. More instruments are concentrated in coastal areas, in particular in the northern hemisphere. Data collected from ships as well as moorings are also more common in the tropics and in the northern hemisphere.

Great expectations are thus laid on measurements from space that can provide homogeneous data at high spatial and time resolution. Measurement of salinity from space by microwave radiometry at L-band[4] was proposed for the first time by Swift and McIntosh (1983). In 1995, at the "Soil Moisture and Ocean Salinity" workshop organized by the European Space Research and Technology Centre, microwave radiometry at L-band was considered as the most promising and adequate technique to remotely measure Soil Moisture and Ocean Salinity, using synthesis radiometry (Font et al., 2010). SMOS satellite was launched on 2 November 2009 on a sun-synchronous circular orbit[5] (Fig. 1.6). It is the first interferometric radiometer that is used for earth observations and the first radiometer that works at L-band (1.413 GHz).

The low frequency L-band was the optimal choice between the sensitivity of the radiometer measurements to changes of moisture in the soil (SM) and salinity in the ocean

[4]The protected L-band used for earth observation is centered at 1.413 GHz.

[5]A Sun-synchronous orbit is a geocentric orbit that combines altitude and inclination in such a way that the satellite passes over any given point of the planet's surface at the same local solar time.

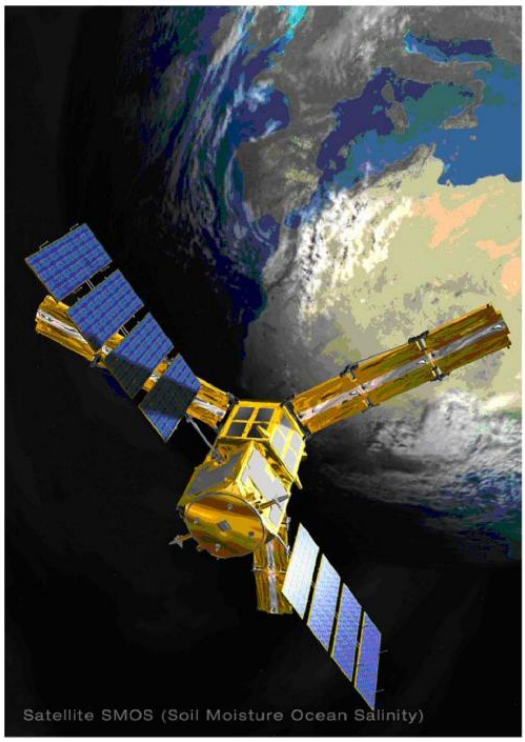

Figure 1.6: Artist view of SMOS. Source: Kerr et al. (2010) (Fig. 1) ©2010 IEEE

(SSS) versus antenna size and Faraday rotation effect: the sensitivity of the radiometric signal to the SM and SSS increases when the frequency decreases while the effect of Faraday rotation in the ionosphere increases and the spatial resolution degrades with decreasing frequency (Kerr et al., 2010). Observations at L-band are less sensitive to the effect of atmosphere that tends to reduce the signal than observations at higher frequencies (Mecklenburg et al., 2012). Moreover, L-band has a protected bandwith (1.4–1.427 GHz) reducing the radio-frequency interference (RFI) risk (Kerr et al., 2010).

The SMOS objectives are "to provide global soil moisture estimates with an accuracy of 0.04 m^3m^{-3} at a spatial resolution of 35–50 km and a temporal sampling of 1–3 days and to provide global ocean salinity estimates with an accuracy of 0.1 pss for a 10–30 day average for an open ocean area of 200 × 200 km^2" (Mecklenburg et al., 2012). More details on the SMOS satellite mission are presented in Appendix A.1.

Today there are many works dedicated to the calibration and validation of the SMOS salinity measurements as well as their use for studying air-sea flux of freshwater and heat, and ocean processes. SMOS detects well large-scale SSS anomalies such as the ones in the Indian Ocean, linked to the Indian Ocean Dipole (Durand et al., 2013), and in the western tropical Pacific, linked to the 2010-2011 La Niña (Hasson et al., 2014) and to the 2015 El Niño (Delcroix and Boutin, SMOS/Blog at CESBIO). These anomalies are explained by the freshwater flux and anomalies in the ocean advection. The comparison of SMOS with *in situ* data shows good agreement with the RMS differences of 0.2-0.3 pss in the Tropical Pacific Ocean. The seasonal longitudinal displacement of

the salinity maximum core (S>36) in the South Pacific was well captured by SMOS and confirmed by ship SSS and an ocean model (Hasson et al., 2013). In the North Atlantic it was shown that SMOS suffers from seasonal varying systematic errors, especially strong during boreal winter when the difference with *in situ* data can reach 0.4 pss (Hernandez et al., 2014). The comparison of corrected SMOS SSS and ship SSS at large-scale shows an accuracy of about 0.15 pss. Hernandez et al. (2014) also demonstrated by comparison with TSG data the capacity of SMOS data to well represent meso-scales (scale around 100 km). Reul et al. (2014) showed that the eddies (radius ∼100 km) resulting from the meandering Gulf Stream can be depicted by the SMOS SSS during the warming period when the SST signal is difficult to identify due to the intensive thermal stratification. The meso-scale horizontal thermohaline features on the order of 100 km and monthly time scales were studied in the SSS–max region in the North Atlantic in Kolodziejczyk et al. (2015b). The comparison with TSG and Argo products showed an advantage of the use of the satellite product.

It is worth to note that the SMOS satellite measures the salinity in the first few centimeters while a large proportion of *in situ* data gives the information further down, and often bellow a few meters depth. Thus, the radiometry results can make an important contribution in understanding the variability in the upper ocean.

All together *in situ* and satellite data provide complementary information on salinity at different depth, spatial and temporal scales: satellite, drifters and moorings provide salinity measurements at first meter (∼0.01-1 m) in the upper ocean and the use of profilers (floats) and gliders allow to extend these measurements into the subsurface ocean. *In situ* measurements are influenced by meso-scale signals (10-200 km, 1-30 days) that they do not resolve well, and can be used for validation and improvement of satellite data. Combining them with the satellite data can improve information on large-scale signals (>200 km, 30 days) and even on meso-scale signals.

1.5 Thesis objectives

The main objective of the thesis work is the investigation of the processes causing salinity variability in the North Atlantic subtropical gyre. Despite a number of recent studies dedicated to the same questions (Treguier et al., 2012; Büsecke et al, 2014; Gordon and Giulivi, 2014; Amores et al., 2015; Dohan et al., 2015; Dong et al, 2015; Farrar et al., 2015) the quantitative estimation of processes contributing to salinity change in the mixed layer remains an important issue. These works, as summarized in Table 1.1, present a wide range of data used, covering various temporal and spatial scales, periods and methods. In this PhD thesis work, I will try to cover this broad analysis. For the first time, I will present the analysis of domain-averaged seasonal SSS and SST budgets at meso-scales based on the weekly-averaged data from high-resolution SMOS satellite (75 km) and Mercator PSY2V4R2-R4 analysis (∼10 km). Also the *in situ* data from the SPURS experiment will be used to validate the mapped products. The analysis will be done for the period August 2012 – December 2014, period with an enough concentration of surface drifters in the region. The use of more than two year time series will allow to investigate the possible changes from one year to another.

The investigation of salinity variability at the meso-scale was motivated by results of few resent works that showed importance of small-scale processes in the MLS dynamics (Büsecke et al, 2014; Gordon and Giulivi, 2014; Amores et al., 2015; Farrar et al., 2015). The contribution of turbulent/eddy advection at meso-scale can explain a significant part of the freshwater flux.

Thus, the first part of this thesis is devoted to the comparison, analysis and validation of data used. SMOS salinity data is used as the sea surface salinity field. We also use the numerical analysis PSY2V4R2-R4 from Mercator Ocean with a high spatial resolution. The Mercator analysis allows us for example to examine processes at the base of mixed layer, such as entrainment.

Chapter 3 is devoted to the analysis method. I will present equations for MLS and MLT budgets as well as how a specific region for the analysis is retained. The seasonal MLT budget is easier to close, which contributes to better understand the accuracy of data used. Also in this chapter the estimation of ocean currents is discussed as the horizontal advection term is a major source of the debate in the literature.

Chapter 4 presents results for SSS and SST budgets from observations and numerical analysis. Chapter 5 focuses on the impact of ocean currents and the advection term in the SSS budget.

Part of the results in Chapters 2 and 4 was published in Frontiers in Marin Science in December 2015, and is presented in Appendix B (Sommer et al., 2015). The other results in Chapter 4 and 5 are being prepared for publication.

Chapter 2

Data evaluation and validation

2.1 Introduction

In this chapter I present the data that were used for this PhD thesis work and their validation. The data were used to estimate the sea surface salinity and temperature budgets and sea surface current variability in the SPURS region of the subtropical gyre of the North Atlantic (see Chapter 4 and 5). The SSS and SST variability results from ocean processes in the mixed layer and the air-sea fluxes (details in Chapter 3), in this chapter I will discuss the data required to estimate these processes. First I will present the drifters and mooring (as well as TSG and Argo profilers) data that we used to validate the satellite or model products presented later in this section. Gliders and TSG data, and Argo profilers were also collected in this region. General information on *in situ* data have already been presented in Chapter 1. Here I would like to emphasize that to a large extent, these data of SSS and SST are independent data from the mapped products of satellite observations and numerical analysis. In particular, the drifter data, thanks to SPURS experiment (see below), provide a good sampling of the central part of the North Atlantic subtropical gyre enabling to test mapped products for different seasons during more than two years. Fig. 2.1 shows the drifter spatial distribution over the first year August 2012 – August 2013. Data were weekly averaged for each drifter for comparison with other products.

The analysis of data accuracy is important for estimating which data errors propagate in MLS and MLT budgets. First, an analysis was made for the period August 2012 - August 2013 and then, when more data were available, the analysis was expanded to August 2012 - December 2014.

Part of this chapter corresponds to material briefly discussed in the paper published in December 2015 (Sommer et al., 2015; Appendix B).

2.2 SPURS Drifters

The SPURS international experiment and STRASSE (SubTRopical Atlantic Surface Salinity Experiment), its French component, took place over one seasonal cycle during 2012–2013 (Fig. 2.2, black box) (SPURS Workshop Report Committee, 2010). Around 150 drifters were deployed in the central NSTG (North Atlantic SubTropical

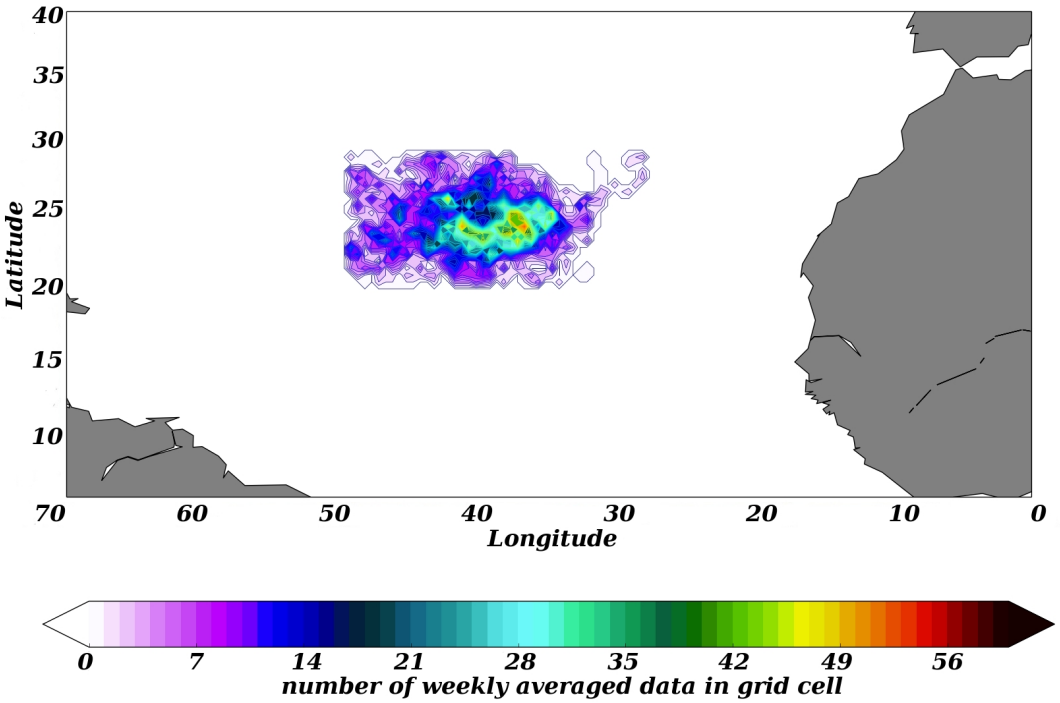

Figure 2.1: Weekly averaged drifter data distribution for the period August 2012 – August 2013

Gyre) mostly in August–October 2012 and March–April 2013 (Centurioni et al., 2015). Most of the drifters that we have used in our studies were SVP-S drifters (Surface Velocity Program – Salinity): mostly US–prepared SVP–S PacificGyre drifters ($\sim$ 90 drifters), but also 12 drogued ICM drifters (Spain), and 3 drogued SVP–S drifters and 1 METOCEAN drifter (LOCEAN). Data were partially processed at SIO (Scripps Institution of Oceanography), with additional data processing done at LOCEAN (S. Morisset, S. Marchand, G. Reverdin). SVP–S drifters (Lumpkin and Pazos, 2007; Reverdin et al., 2007; Centurioni et al., 2015) have a battery pack, a satellite transmitter, a conductivity sensor below the surface float at $\sim$50 cm depth as well as a sea surface temperature sensor located either next to the conductivity cell or at the base of the float to avoid direct radiative heating. The drifters initially have a drogue centered at 15m to follow the currents at this depth. The drogue can be lost which affects the buoy drift. Drogue loss detection is now routinely done based on different algorithms (Rio and Hernandez, 2003; Lumpkin and Johnson, 2013), so that drogued drifter data can be safely identified. For such drogued drifters it was found that a wind of 10 m/s induces a 0.7 cm/s downwind slip of the drifter (Lumpkin and Pazos, 2007). Most of the drifters had a sensor to identify the presence of the drogue. In this work I used data of drogued SVP–S drifters to investigate sea surface currents and data from all available drifters to estimate the SSS and SST. Most drifters relied on Argos (an American-French satellite-based system) for collecting data. Also, drifters are equipped by GPS system. The GPS positions are not significantly different from the positions located through Argos. The time step of the data records is usually 30

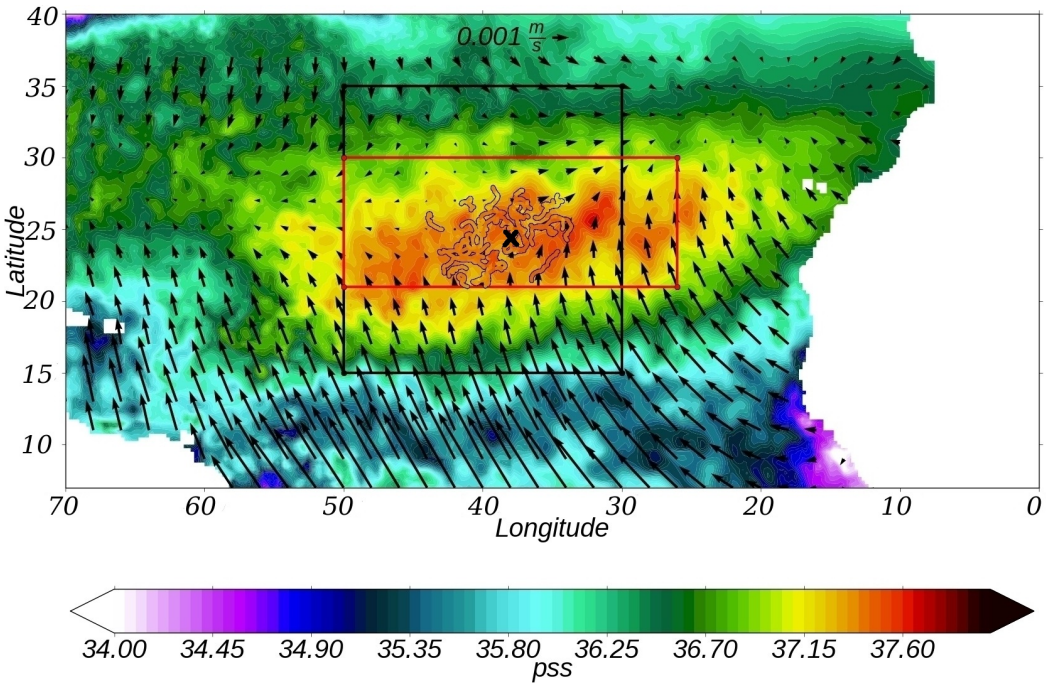

Figure 2.2: North Atlantic subtropical region, January 2013. Monthly mean SSS from SMOS and Ekman velocity field using ERA-Interim. The black box indicates SPURS region. The red box is the region that was chosen for estimation of salinity budget. Black cross is the mooring position at 24.5^0N 38^0W. The figure also presents drifter trajectories. Sommer et al. (2015) (Fig. 1)

minutes for PacificGyre drifters. For ICM drifters, a data is collected every 15 minutes, but is only available if there is a transmission in that time slot.

2.3 Mooring Data

The surface mooring was deployed as part of the SPURS project by the Upper Ocean Processes Group at WHOI (Woods Hole Oceanographic Institution) at approximately 24.5^0N, 38^0W (Fig. 2.2, black cross, PODAAC, WHOI mooring CTD). Data were collected from September 2012 until September 2013 by the ASIMET (Air-Sea Interaction Meteorology) system. The ASIMET system provides measurements of specific humidity (at 2.95 m height), sea surface temperature and conductivity (0.865 m depth), wind speed and direction (at 3.295 m height), barometric pressure (at 2.935 m height), shortwave and longwave radiations (at 3.44 m height), and precipitation (at 2.965 m height). These variables are used to compute air-sea fluxes of heat, moisture and momentum using bulk flux algorithm (Fairall et al., 1996). This algorithm follows the standard Monin–Obukhov similarity approach for near-surface meteorological measurements. It is an outgrowth of the Liu–Katsaros–Businger method with some modifications that help to improve the accuracy especially in case of the low wind (details can be found in Appendix A.3). The accuracy of the mooring data is 8 Wm^{-2} for

the heat fluxes, 6 $cm\ yr^{-1}$ for the evaporation and 10% for precipitation (Colbo and Weller, 2009; Farrar et al., 2015). We use these mooring data to validate the gridded data sets of heat fluxes, evaporation and precipitation.

2.4 SMOS

The SMOS satellite mission was launched in November 2009 on a sun-synchronous circular orbit with a local equator crossing time at 6 a.m. on ascending node and at 6 p.m. on descending node. The SMOS mission carries an L-band (1.4 GHz) interferometric radiometer that allows the reconstruction of a bi-dimensional multi-angular image of the L-band brightness temperatures (Tb) that is used to retrieve the SSS (Kerr et al., 2010) (see Chapter 1).

In the subtropical North Atlantic, SMOS SSS retrievals suffer from seasonally varying systematic errors (Hernandez et al., 2014), especially strong during boreal winter (RMS close to 0.5, Fig. 2.3*a*) due to sun contamination on descending orbits. Systematic errors in SMOS SSS originate mainly from inaccuracies in instrument calibration, in image reconstruction (in particular the one that depends on the distance to the coast (Kolodziejczyk et al., 2015a)), from anthropogenic RFI (Radio Frequency Interferences), as well as from the galactic and sun signals (Appendix A.1). The systematic errors were identified as the dominant errors in the SMOS mission (Mecklenburg et al., 2012). In particular, these errors are large in the vicinity of the coast due to the shadowing by land. The systematic errors affect mostly mean values and the comparison of SSS and SSS anomalies from different products can be one of the approach to demonstrate the importance of correcting for these errors as it was done in Boutin et al., 2016. The comparison of SSS anomalies derived from SMOS and an Argo product ISAS (*In Situ* Analysis System) (Gaillard et al., 2009) show std differences of ∼0.2 pss, smaller by more than 40% (with 30% in the open ocean) compared to the one between SMOS and ISAS SSS (Boutin et al., 2016).

Therefore reducing the systematic errors can significantly improve the SMOS SSS retrievals. There are several studies proposing different methods of corrections: optimal interpolation method using *in situ* data (Melnichenko et al., 2014), improvements of SMOS calibration and image reconstruction techniques based on the SMOS data themselves and further adjustment to *in situ* measurements (Kolodziejczyk et al., 2016).

In this thesis work I used a new corrected and optimal interpolated (OI) SMOS level 4 SSS fields described in Kolodziejczyk et al. (2015a) and Kolodziejczyk et al. (2016), providing SSS to 75 km and 10 days resolution. The new OI SMOS SSS was derived from SMOS ESA level 2 SSS v550 (10 days, 50 km), using the same flagging as Boutin et al. (2013): for example, this requires that there is no expected nearby sea ice and not many outliers, a good fit between measured and modelled Tbs, and only measurements with low sun glint and low galactic noise. The correction for systematic errors follows a two-step procedure: 1) removal of systematic errors in the vicinity to the coast; 2) removal of seasonal systematic errors. First, data are corrected for 4-year mean (07/2010-07/2014) near coastal discrepancies with respect to the ISAS Argo climatology taking into account that systematic errors depend on the location of the pixel across the track and on the orbit orientation. Then, ascending and descending

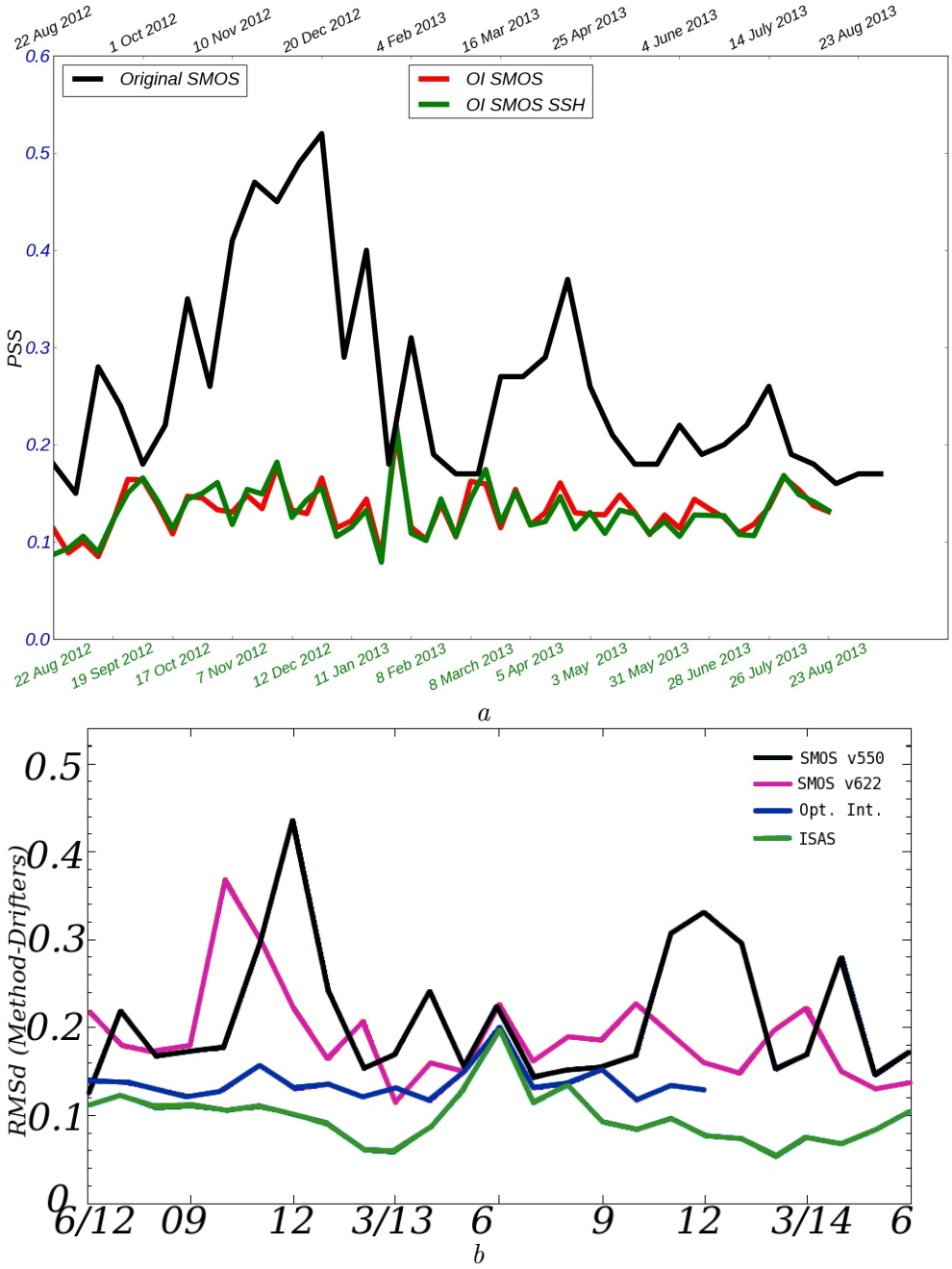

Figure 2.3: *a* – RMS differences at drifter positions (in pss) over the SPURS domain between drifters SSS and 10-day CEC-CATDS SMOS SSS field (black), OI SMOS SSS with (green) or without (red) SSH constrain, Sommer et al. (2015) (Fig. 2), *b* – monthly RMS differences between drifter data averaged on $0.125^0 \times 0.125^0$ over 9 h and SMOS v550 (black), SMOS v622 (purple), ISAS (green), OI SMOS (blue) that were taken in radius 50 km around drifter positions

orbit data are mapped separately with an optimal interpolation scheme at large scale (500 km) with a Gaussian shaped correlation function. The seasonal large scale biases are then derived from the comparison with monthly ISAS SSS fields and are removed from the individual data separately from the descending and ascending orbits. The last step is a noise reduction and mapping of bias corrected SMOS SSS every 7 days on the regular grid of 0.25^0 using optimal interpolation with a Gaussian correlation function scaled to 75 km over a window of 10 days centered on the day of mapping, using the corresponding monthly ISAS SSS fields as first guess.

Another field of SMOS OI SSS was also used. It was based on the introduction of a small constraint on along-stream-line (from AVISO SSH) orientation of the structures by including it in the Gaussian correlation function (Kolodziejczyk et al., 2015a) in order to improve the horizontal SSS gradient at meso-scale. This method allows to recover spatial scales slightly smaller than 75 km (OI SMOS SSH).

The SMOS OI (Fig. 2.3*a*, red curve, for the region $18^0 - 34^0$N and $50^0 - 10^0$W) shows significant improvement with respect to earlier products (Fig. 2.3*a*, black curve, original SMOS product). The RMS difference between SMOS SSS at 10 days 75 km resolution and *in situ* data (drogued drifters) is lower than 0.15 for most of the period. The introduction of the supplementary correction (OI SMOS SSH) marginally, but not significantly, improves the results (Fig. 2.3*a*, green curve). In this work we retained this last version of the weekly SMOS products with the spatial resolution of 0.25^0.

It is worth to note that the SMOS version 550 used in the present work was recently replaced by version 622 and is not used anymore. The principal improvements in version 622 affected the calibration method and filtering of bad measurements. Figure 2.3*b* (collaboration with S. Marchand) shows monthly-averaged RMS differences between drifters and two versions of SMOS, ISAS and OI SMOS used in this PhD work for a longer period than on the Figure 2.3*a*. The comparison with OI SMOS (blue curve) always presents stable RMS differences around 0.15 pss. The differences with ISAS product (green curve) are also small and around ∼0.1 pss. The comparison with the two SMOS version, old v550 (black) and new v662 (purple), shows obvious improvements in SMOS v662, especially in winter time, despite the continuing presence of systematic and seasonal errors. The peak in June 2013 is explained by the small filaments that were sampled by drifters but not SMOS or Mercator (Fig. 2.4; filament with the low salinity around 23^0N 40^0W).

We also estimated the RMS differences between OI SMOS SSH SSS and *in situ* SSS using all drifter data (from drogued and undrogued drifters) (Fig. 2.5*a*, blue curve, for the region $20.75^0 - 30^0$N and $49.25^0 - 26^0$W, this region was limited by Mercator available data, see further) and TSG data from OI SSS (Fig. 2.5*b*, blue curve) for a longer period including the year 2014. These two comparisons show similar results as on Fig. 2.3: RMS differences vary around 0.15. The big peaks at the beginning (August–September 2012) and at the end (from September 2014) can be explained by the small number of data in the region (and preferential drifter sampling along filaments for the initial period) (Fig. 2.5*d*). The comparison with monthly ISAS gridded product and monthly averaged SMOS (Fig. 2.5*c*, blue curve) shows RMS differences even smaller than 0.1 which is expected as the ISAS product was used in the large scale correction step of this SMOS SSS field.

As expected from the error statistics, the mapped (OI SSH) SMOS SSS field with

the drifters' trajectories and data overlaid for the week 8-14 January 2013 (Fig. 2.11) suggests that remaining systematic errors are small, and that the product captured part of the meso-scale variability.

From Fig. 2.3 and Fig. 2.5*a* we just note that the error budget seems to remain relatively stationary in time. The somewhat smaller RMS error during August 2012 (Fig. 2.3) results from a too small number of data for this period. There is a small peak of larger RMS difference in the week between January and February 2013 which could be due to a rain/wind front across this area inducing larger spatial variability and/or

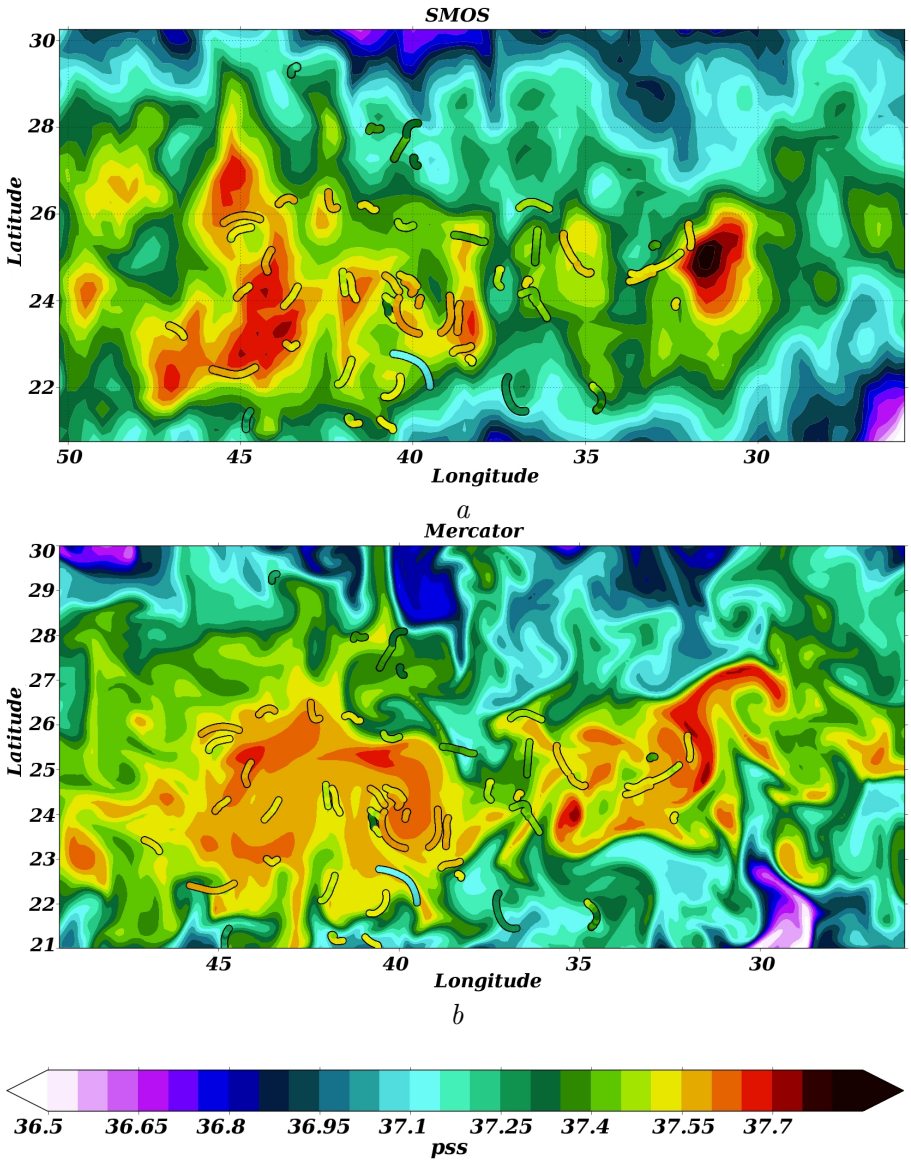

Figure 2.4: Mapped SSS fields vs. drifters, 18-24 June 2013: *a* – SMOS vs. drifters (∼55 drifters), *b* – Mercator analysis (section 2.6) vs. drifters (∼55 drifters)

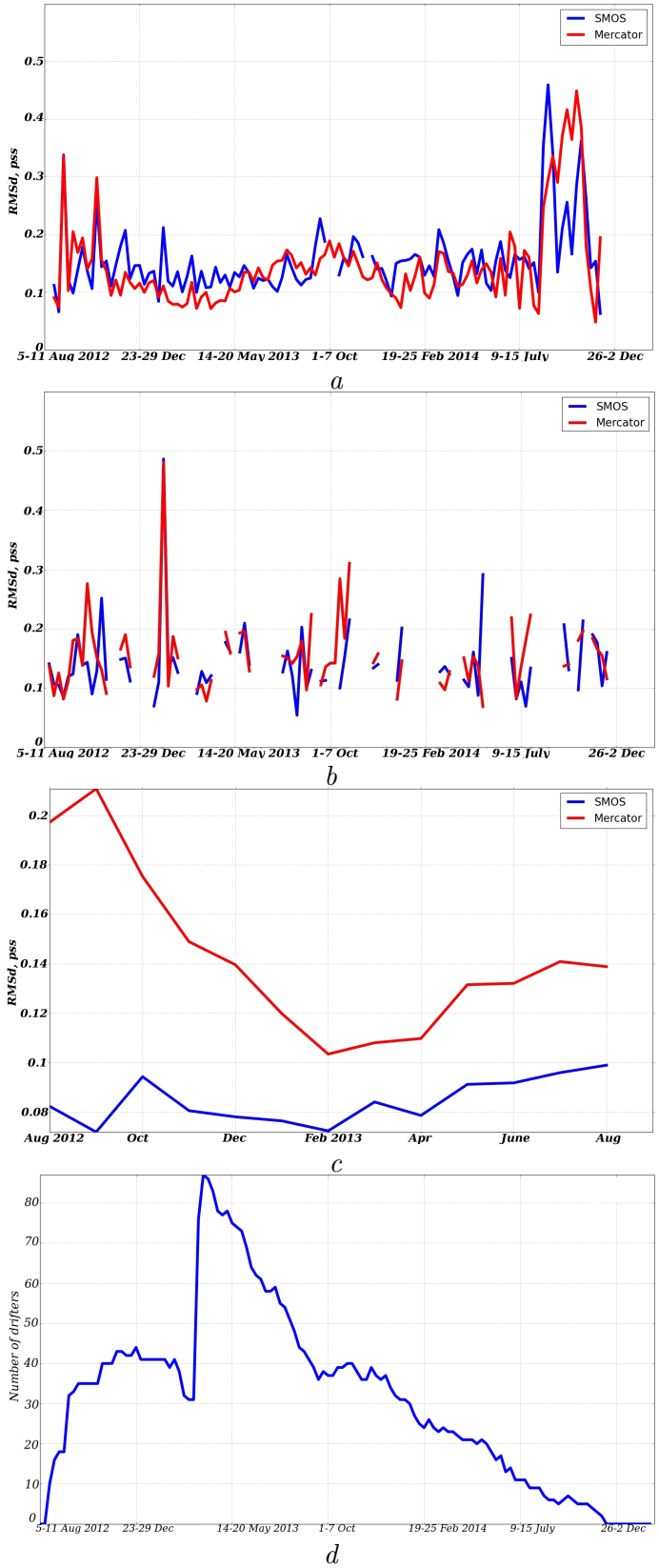

Figure 2.5: RMS differences of OI SMOS SSH SSS (blue curve) and Mercator SSS (red curve) with: *a* – drifters' SSS (at drifter positions), *b* – TSG's SSS (at TSG's positions), *c* – ISAS grided product (on the SMOS and Mercator grids, respectively) with monthly average of SMOS and Mercator, *d* – numbers of drifters used

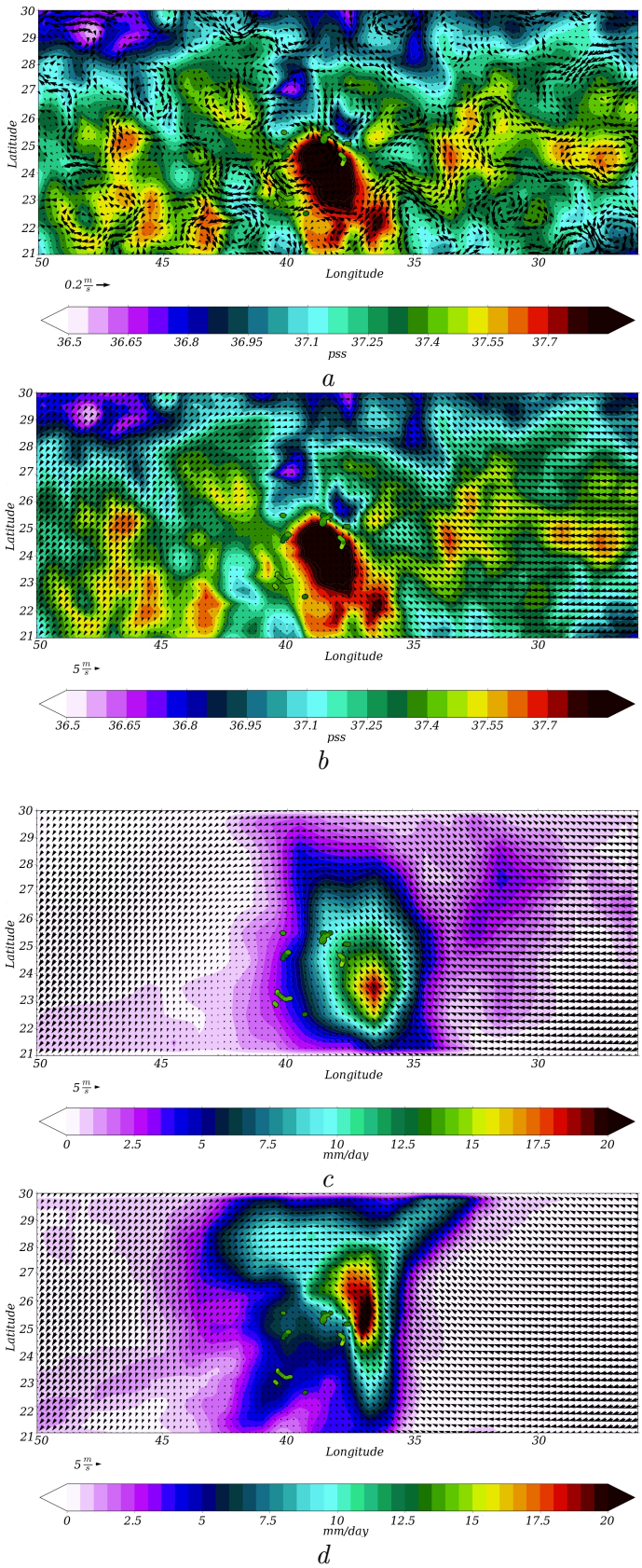

Figure 2.6: The week of high RMS difference between OI SMOS SSH SSS and drifters' SSS 29 January – 4 February 2013; *a* – OI SMOS SSH SSS vs. AVISO 2014 and drifters' SSS, *b* – OI SMOS SSH SSS vs. ERA-Interim wind and drifters' SSS, *c* – GPCP precipitation vs. ERA-Interil wind and drifters' SSS, *d* – ERA-interim precipitation vs. ERA-Interim wind and drifters' SSS

errors. It is possible that the rain front has generated rapid and small scale wind changes not well captured by ECMWF (European Center for Medium-Range Weather Forecasts) wind forecasts that are used in the SSS retrieval scheme. Indeed, during this week drifters were located in the salinity maximum zone (Fig. 2.6*a*) which coexisted with the wind (Fig. 2.6*b*) and rain fronts (Fig. 2.6*c*; GPCP satellite precipitation that will be presented further). Here we used ERA-Interim wind velocity field which is not strongly different from the ECMWF NRT winds used in SMOS retrievals. We found during this period that the wind in the region of high salinity (more than 37.8 pss) varied widely from 0.5 m/s to 5.5 m/s. It was noticed (Boutin et al., 2013; Reul et al., 2012) that SMOS retrieval algorithms have difficulties for winds lower than 3 m/s or higher than 12 m/s. The example on Fig. 2.6 corresponds to this low "boundary" conditions for a wind. Furthermore, Portabella et al. (2012) showed that in condition of high wind variability (the case of precipitation appearance) ECMWF shows RMS difference with drifter data equals to 3.54 m/s (in case of low wind variability it is 2.29 m/s). This can induce uncertainties in SMOS SSS: to give an idea, an uncertainty of 1 m/s wind speed (for example, due to mis-positioning of the fronts) leads to an uncertainty of about 0.2 K brightness temperature, thus roughly 0.4 pss in SSS (Yueh et al., 2001).

We also checked the ERA-Interim precipitation field (Fig. 2.6*d*) to understand the wind rotation found on Fig. 2.6*b* and *c*. Its position is coherent with expected frontal bands and associated deep convective processes. However, it is not coherent with the GPCP precipitation pattern (daily product) with more than 200 km displacement between the respective areas of large precipitation. The ERA-Interim wind pattern fits with the ERA-Interim precipitation fields. The displacement relative to GPCP and the

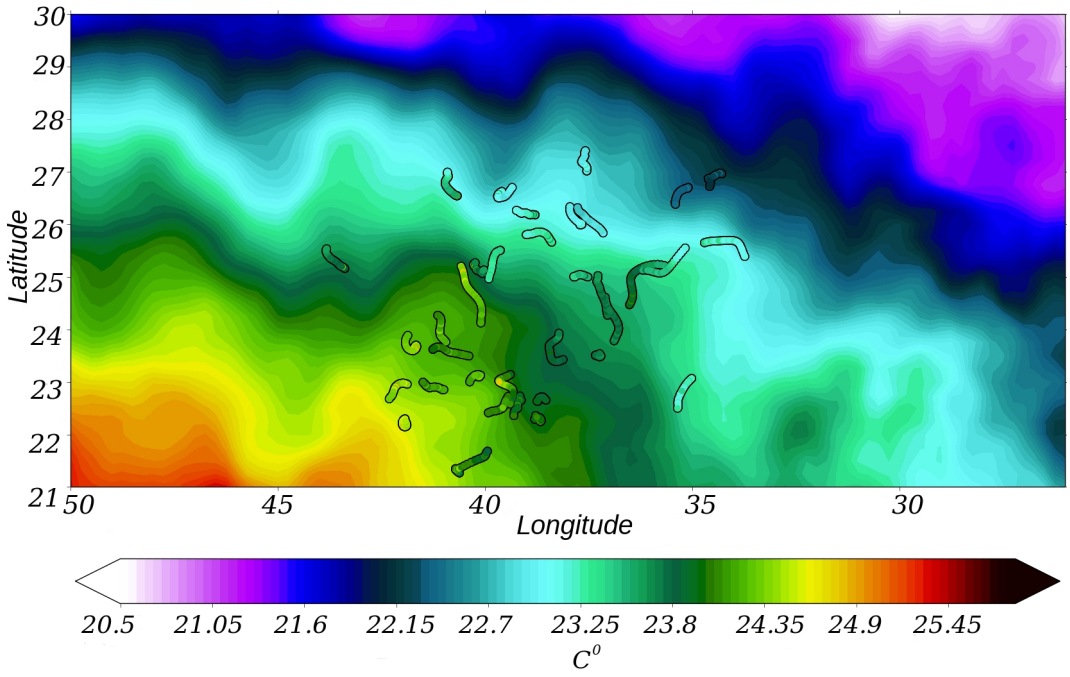

Figure 2.7: OSTIA SST vs. SPURS drifters, 8–14 January 2013

differences in rainfall suggest uncertainties in the winds, as well as in the precipitation data required to diagnose salinity variability. This will be further discussed in details in section 2.9.1.

Further on, for simplicity, we will refer to OI SMOS SSH product as SMOS.

2.5 Sea Surface Temperature OSTIA

To estimate the sea surface temperature (SST) we use daily Operational SST and Sea Ice Analysis (OSTIA) with horizontal resolution 0.05^0 ($\sim$6 km) (Reynolds and Chelton, 2010; Donlon et. al., 2012). The SST field from OSTIA has zero mean bias and an accuracy of $\sim$0.57 K compared to the *in situ* measurements as noted in Donlon et. al. (2012).

OSTIA products combine *in situ*, Advanced Very High Resolution Radiometer (AVHRR), Advanced Microwave Scanning Radiometer for EoS (AMSR), Tropical Rainfall Mapping Mission (TRMM) Microwave Imager (TMI), Advanced Along-Track Scanning Radiometer (AATSR), and geostationary Spinning Enhanced Visible and Infrared Radiometer (SEVIRI) data. All input satellite data are corrected from systematic errors by using the *in situ* and AATSR data (Reynolds and Chelton, 2010; Donlon et. al., 2012).

OSTIA analyzed SST fields are among the small number of analyses with high spatial resolution ($1/12^0$). Of course, the high resolution does not necessarily imply a good reproduction of small features. For example, the filtering of the diurnal variability and adjustment to SST to produce a foundation temperature can make the product from OSTIA analysis smoother than from other high-resolution SST analyses (Reynolds and Chelton, 2010; Donlon et. al., 2012; Martin et al., 2012). Nevertheless, inter-comparisons made by Reynolds and Chelton (2010) and Martin et al. (2012) show that the OSTIA provides reasonable estimates (this analysis is neither the best one nor the worse one to reproduce mesoscale features). Furthermore, in this region, OSTIA is in a good agreement with the drifter data (RMS differences $\sim$ 0.18 in North Atlantic, Reynolds and Chelton, 2010).

Figure 2.7 for the week 8–14 January 2013 illustrates this usual fine agreement between SPURS drifter SST and OSTIA SST. Drifters and OSTIA product show the same large scale horizontal temperature gradient oriented from the Southwest (warm water) to Northeast (cold water). RMS differences between OSTIA and drifter data (OSTIA temperature was taken at the positions of drifters) (Fig. 2.8*a*, blue curve) vary between 0.15 and 0.5^0C. The maxima were found predominantly in spring and summer seasons, the periods when the daily restratification induces large variations between day and night. We find the same tendency in RMS differences with monthly ISAS product (Fig. 2.8*b*, blue curve) but with a smaller range of variance, 0.2–0.3^0C. The difference in comparison of drifters and OSTIA product can be explained by the diurnal cycle that is strongly present in drifter data. The RMS differences with drifter SST is smaller for the night time (5–11am). It is near 0.2^0C for most of the period (Fig. 2.8*c*, blue curve) with no indication of a seasonal cycle in the differences. The peaks at the end of the period can be explained by a too small number of drifter data.

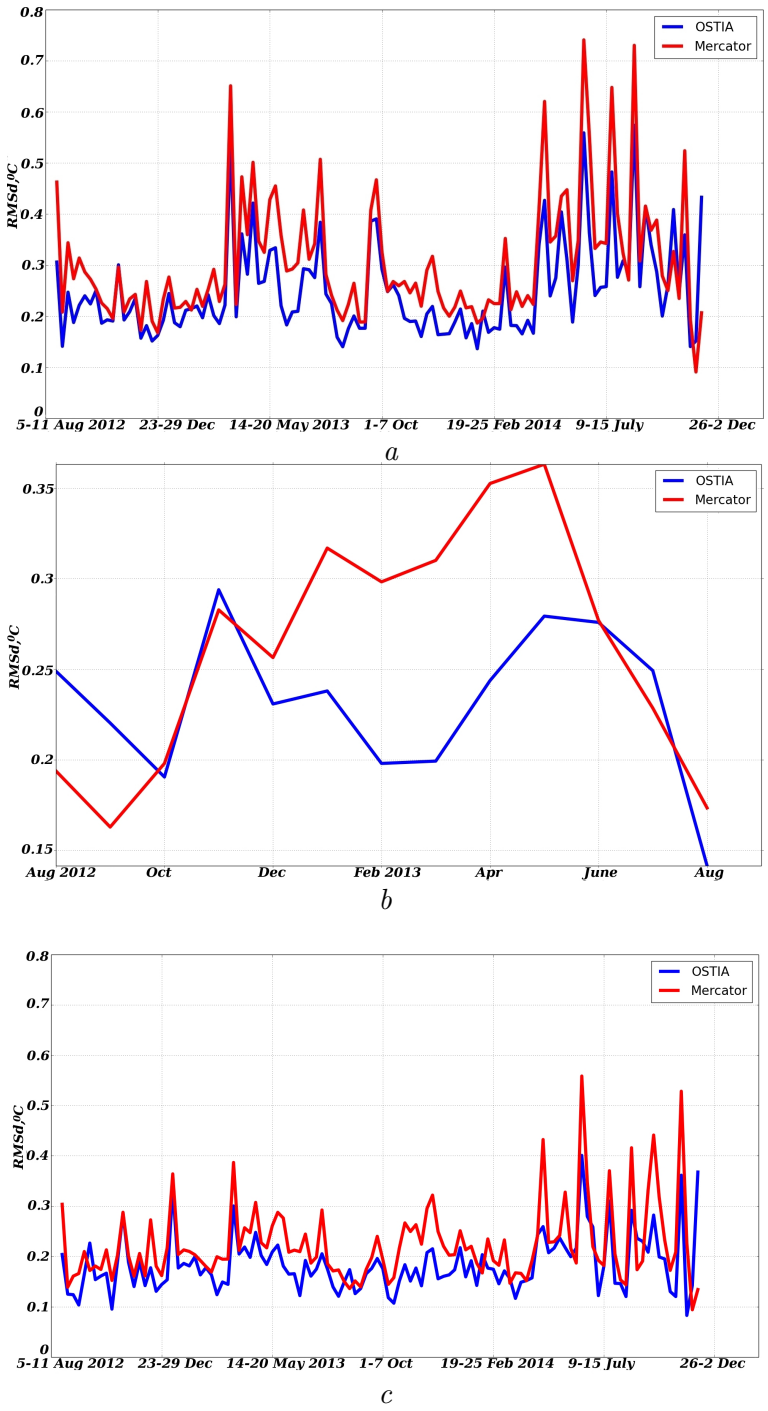

Figure 2.8: RMS differences of OSTIA SST (blue curve) and Mercator SST (red curve) with: *a* – drifters' SST (at drifter positions), *b* – ISAS grided product (on the OSTIA and Mercator grids, respectively), *c* – drifters' SST (at drifter positions) at night time 5–11 am GMT

2.6 Mercator analysis

Mercator proposes a series of French ocean analysis and forecasting systems operated by Mercator Ocean. In this PhD work I used files from the Mercator PSY2V4R2-R4 analysis in the North Atlantic with a $1/12^0$ horizontal resolution. The system was updated in April 2013 from version R2 to R4. The new version includes a new parameterization of vertical mixing and takes 50% of surface current for the computation of wind stress with bulk COARE (Appendix A.3). Also it includes a new procedure to avoid the damping of SST increments via the bulk forcing function in the assimilation (Drévillon et al., 2013). Data assimilation in PSY2 is done by a state-of-the-art data assimilation method[1] (e.g. optimal interpolation, variational assimilation, etc.). The model assimilates sea surface temperature data (SST AVHRR Pathfinder by NOAA/NCEP + SST AMSRE from NASA's AQUA satellite), sea level (Ssalto/Duacs) and *in situ* TS profiles (Coriolis, in situ TAC CMEMS). The atmospheric fields were estimated from ECMWF Integrated Forecast System with the sample pf 3-h. Details can be found in Lellouche et al. (2013).

RMS differences between Mercator and drifter SSS (Fig. 2.5*a*, red curve) as well as RMS differences between Mercator and TSG SSS (Fig. 2.5*b*, red curve) show results close to the ones from SMOS, with RMS difference around or slightly smaller than 0.15 pss. Sometimes the RMS difference is a little smaller compared to what is found with SMOS. It means that, as was found for the SMOS product, the Mercator analysis reproduces some of meso-scale salinity features. On the other hand, the RMS differences between monthly averaged Mercator and ISAS monthly products (Fig. 2.5*c*, red curve) present larger values than the comparisons between ISAS and SMOS, in the range 0.1-0.2 pss.

Attributing the differences with *in situ* data is difficult, as it can result both from relatively small scale features but also large scale differences. We can illustrate these points. For example, in January 2013 (Fig. 2.9), large positive local extrema in Mercator are suspicious. Indeed, Mercator (Fig. 2.9*b*) presents a maximum ∼37.7 pss in the eastern part of the region (near 24^0N/30^0W) that is surprising for the month of January, when Mercator mixed layers were relatively deep, thus expected to have entrained deeper fresher waters. Furthermore, in this location, SMOS (Fig. 2.9*a*) presents a minimum (close to 37.3 pss) and ISAS (Fig. 2.9*c*) a slowly decreasing large scale field. The high Mercator SSS can be associated with issues in ECMWF wind forcing Mercator analysis. (ECMWF wind stress was assimilated in Mercator.) Other possible source of uncertainties can be the mixing model used in Mercator or assimilation of outlying profile data. Such local maxima in the Mercator SSS field are found mostly out of the region of high drifter concentration which explains the good results on Fig. 2.5*a* (and from other SPURS *in situ* data). For example, for January, drifters were in $21^0 - 28^0$N $45^0 - 37^0$W thus further west from the maximum in Mercator salinity distribution.

[1] The principle idea of data assimilation is the combination of the available information (for example, observations) about atmosphere and/or ocean state with model predictions to provide an update of the model state. This updated model state is used after as the initial condition for the next forecast step. In the case of analysis (like Mercator analysis) data assimilation procedure corrects the output of the model for the resent ocean (or atmospheric) states. Then present ocean states are estimated by the model based on these corrected results.

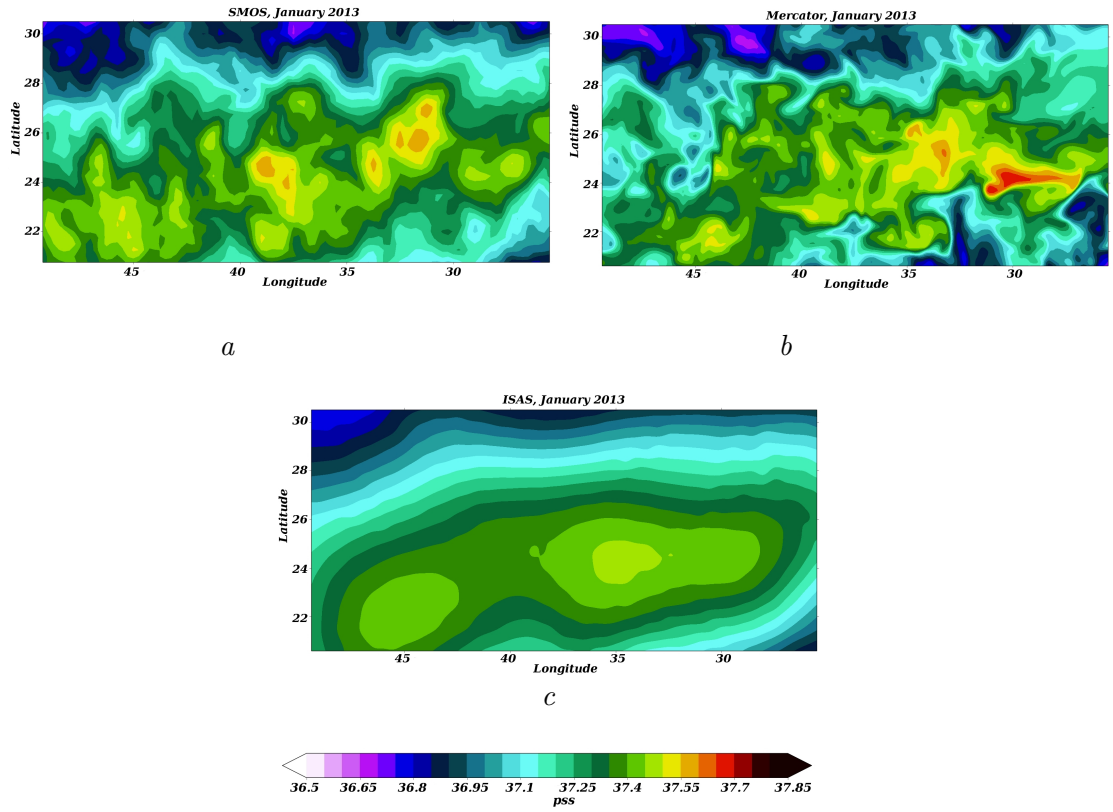

Figure 2.9: Monthly averaged SSS in region $20.5^0N - 30^0N$ $50^0W - 25^0W$, January 2013: a – SMOS, b – Mercator, c – ISAS

But in other instances, we find that Mercator presents rather realistic distribution of local maxima: for example, in August 2012 high salinity concentration were found in the East of the region ($26^0 - 27^0$N/$27^0 - 32^0$W) in Mercator (Fig. 2.10b), that were not found in SMOS or ISAS (Fig. 2.10a and c). The presence at that time of a TSG transect (and a few CTD casts) from the RV Thalassa (Strasse cruise) allows us to state that the Mercator field is more realistic in this region. The absence of drifters in these areas shows the limitations in what can be concluded on the accuracy of SMOS and Mercator from the comparison with drifters. The August 2012 comparisons illustrates that errors in the SMOS fields can also be to some extent at rather large scales, when there is insufficient sampling by the Argo floats that are used in the ISAS fields. The nature of such differences has to be further investigated.

The comparison of temperature fields from Mercator and drifters (Fig. 2.8a, red curve) show RMS differences in range 0.15–0.7^{0}C that is comparable with ones from OSTIA but a little higher (blue curve). The night time (5-11am) (Fig. 2.8c) temperature comparison shows the RMS differences mostly around 0.2^{0}C and we do not see a strong variance as on Fig. 2.8a that was mostly due to the diurnal cycle. RMS differences between Mercator and ISAS SST monthly fields show the results for SST higher in December 2012 to May 2013. It can mean that Mercator does not reproduce

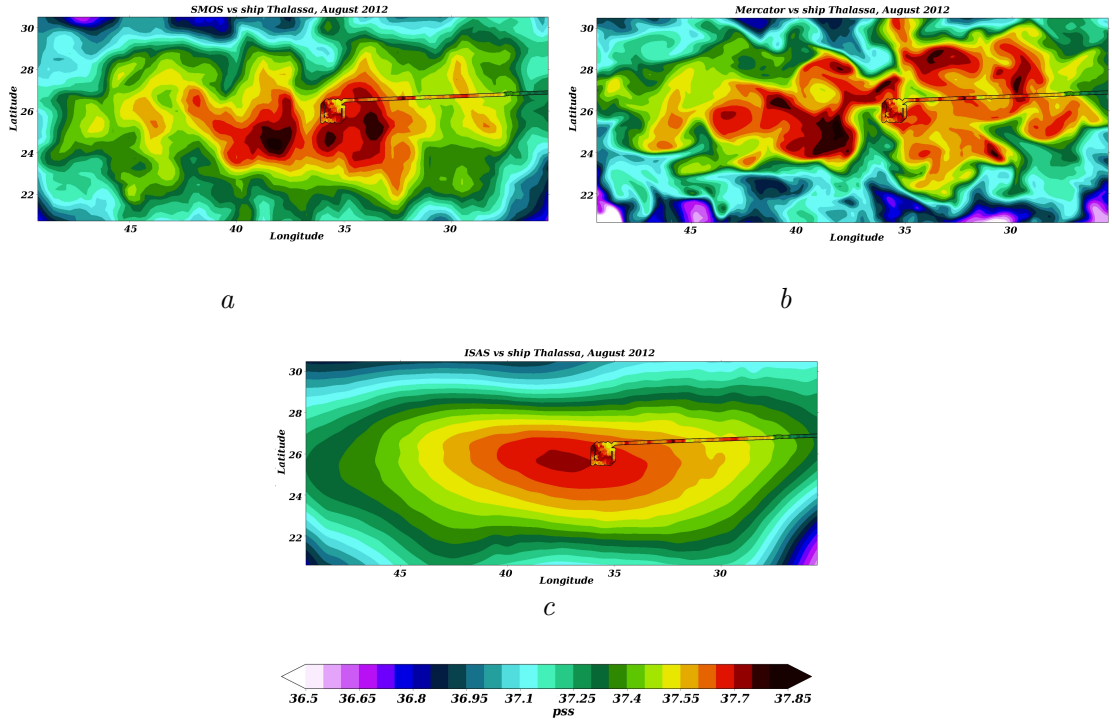

Figure 2.10: Monthly averaged SSS in region $20.5^0N - 30^0N$ $50^0W - 25^0W$ from mapped product and ship measurements of SSS from Thalassa, August 2012 : a – SMOS vs. Thalassa ship measurements, b – Mercator vs. Thalassa ship measurements, c – ISAS vs. Thalassa ship measurements

the temperature field very well in winter and early spring or that there are small scale features not presented in ISAS.

We conclude here that Mercator analysis reproduces the large part of the mesoscale variability: it produces observed salinity to within about 0.15 pss and 0.2^0C for temperature compared with drifters, TSG and ship's measurements. But there are some local differences (mostly at large scales) with monthly averages between Mercator and SMOS salinity fields and Mercator and OSTIA temperature data (through the comparison with ISAS) that might result in different budgets for SSS and SST variability. The use of Mercator analysis will be valuable to better understand the role of small scales in salinity variability as well as the influence of different data used and their uncertainties.

2.7 AVISO altimetry

A regional AVISO 2014 altimetry product (daily product with $1/8^0$ spatial resolution) was constructed to estimate the geostrophic velocity field (Dussurget et al., 2015, D15 product). Measurements from Jason-2, AltiKa, Cryosat-2 and Jason-1 altimeters were used to generate the Sea Level Anomaly (SLA) product. To reduce the inhomo-

geneity of altimeter measurements from different missions, the multi-missions cross-calibration approach was applied (Bosch et al., 2014). Then, compared to the standard Ssalto-Duacs product (AVISO 2010), less along-track filtering was used in AVISO 2014, which is optimized in this region and for the different satellites. The along-track filtering parameters remove wavelengths shorter than 50 to 60 km in SPURS region (for the same region the global product is generated with wavelength filtering from 100 to 150 km). The last step is the mapping process that was done based on an Optimal Interpolation of the along-track measurements from all altimeters onto a regular grid ($1/8^0 \times 1/8^0$). It also uses an updated Mean Dynamic Topography (MDT). The first step is the computation of the difference between Mean Sea Surface and geoid height – so-called "geodetic MDT". To remove the omission and commission errors an optimal filter is applied based on the objective analysis method[2]. At the last step the *in situ* data are used to improve the small-scale features in the obtained "geodetic MDT". The *in situ* data have the same physical content as MDT: mean heights and mean geostrophic velocities are constructed from *in situ* measurements of the ocean dynamics heights (from *in situ* steric dynamic heights) and current velocities (from drifters with drogues at 15 m) from which ageostrophic component and temporal variability estimated from altimetry are removed (Rio et al., 2014). (See Appendix A.4: What are the SLA, the MDT, a multi-mission cross-calibration?)

The ocean currents from the AVISO 2014 regional product fit reasonably well the

[2]Objective analysis is a procedure usually used to map spatially non-uniform data to a regular grid (optimal interpolation) (Emery and Thomson, 1997).

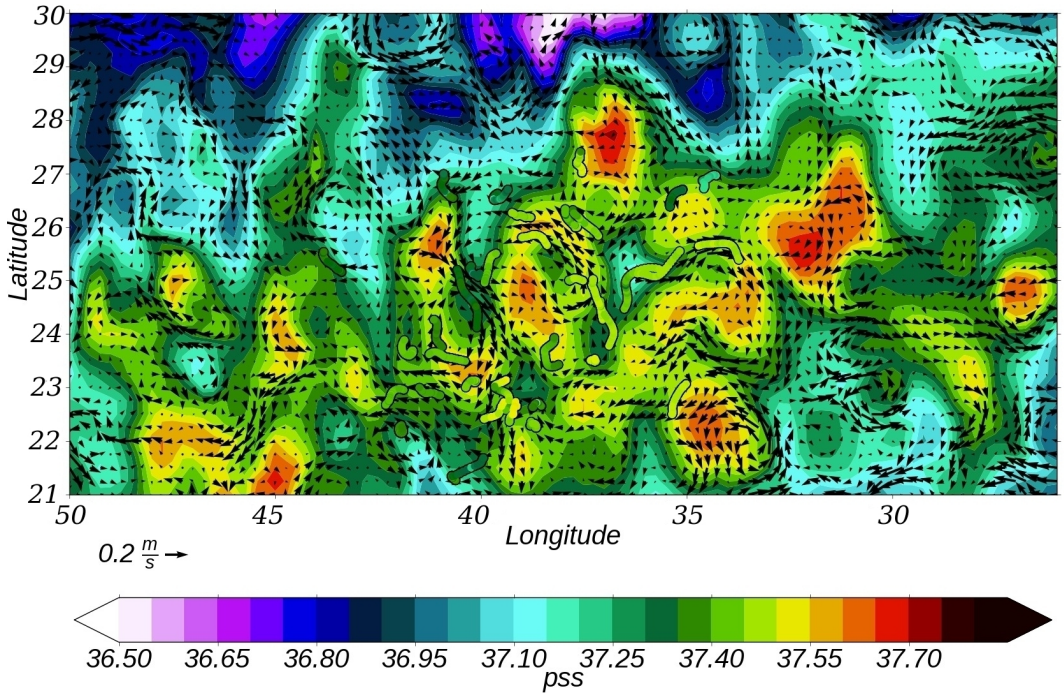

Figure 2.11: SMOS SSS vs. SPURS drifters and AVISO geostrophic velocity field, 8–14 January 2013, Sommer et al. (2015) (Fig. 3)

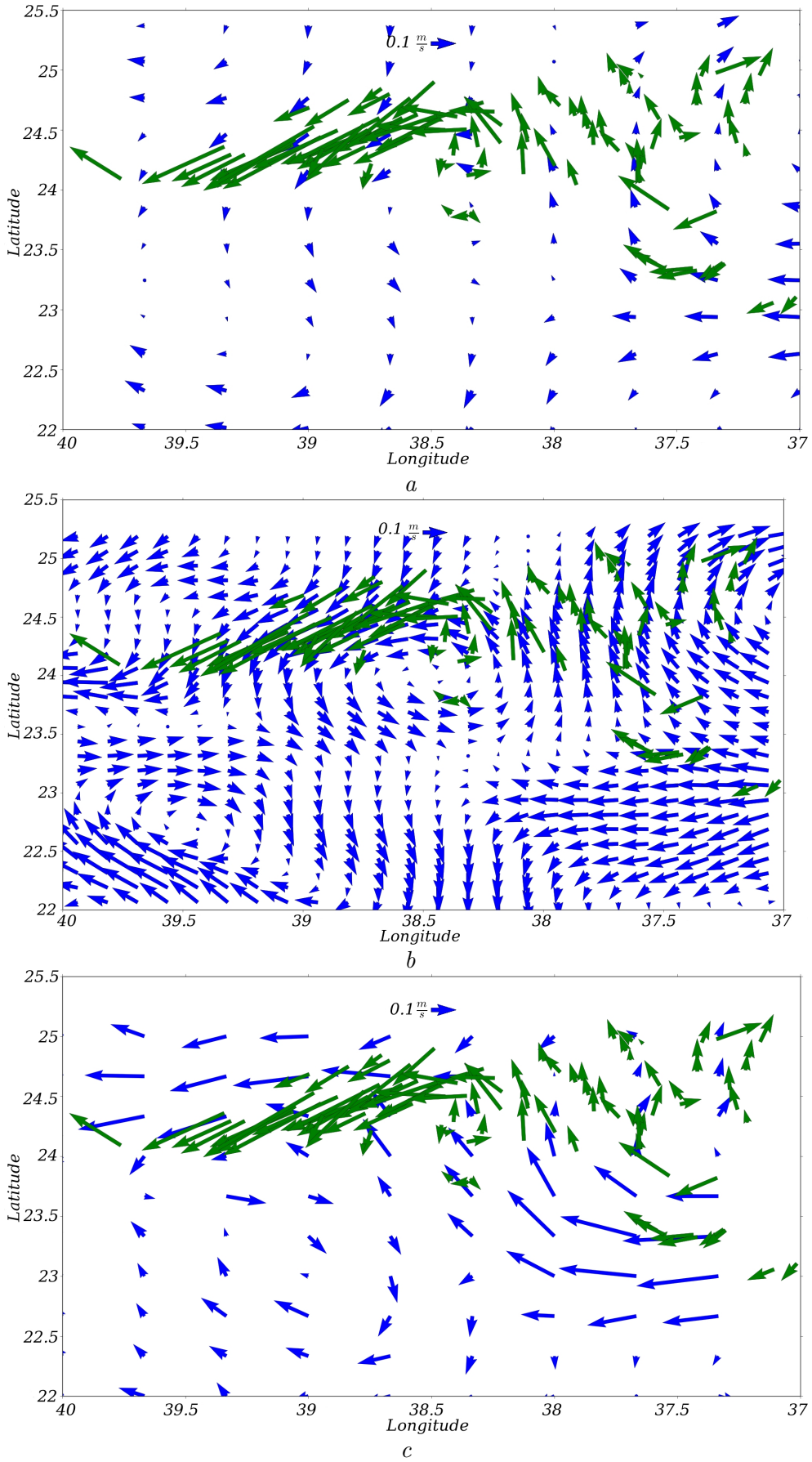

Figure 2.12: 2nd April 2013, vector velocity field from drifters (green vectors, total drifter velocity) and (blue vectors): *a* - AVISO 2010 altimetry product, *b* - AVISO 2014 regional altimetry product, *c* - Mercator total velocity field at 15m plotted at each 0.33^0

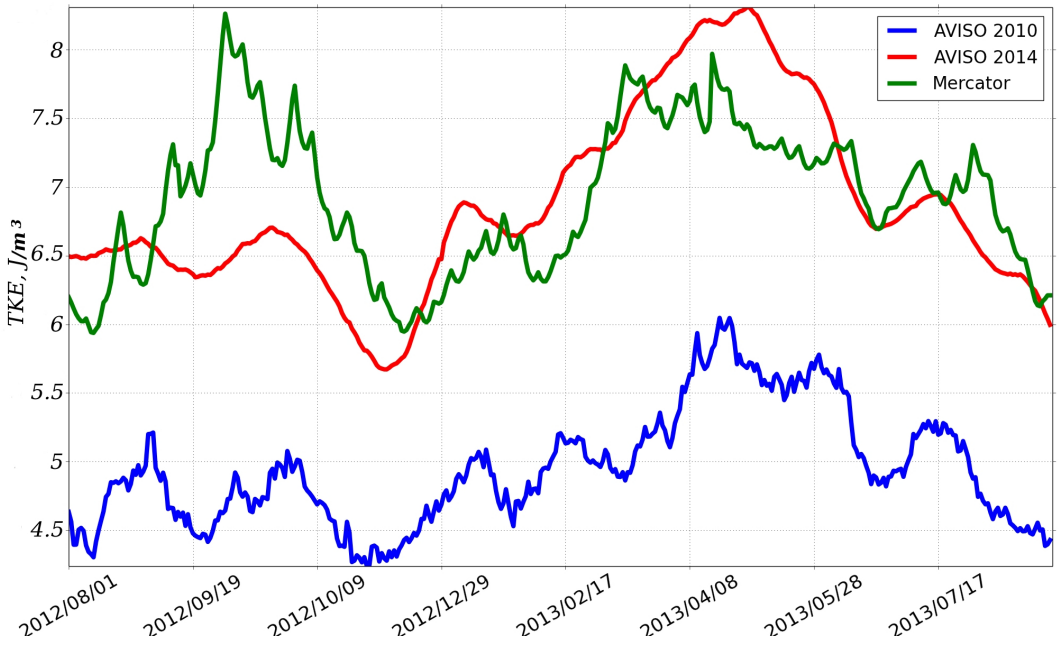

Figure 2.13: Total Kinetic Energy in the region $20.5^0 - 33.5^0$N $49.5^0 - 25.5^0$W from AVISO 2010 altimetry product (blue), AVISO 2014 regional altimetry product (red) and geostrophic velosity estimated from Mercator SSH (green)

drifter trajectories (example in Fig. 2.11) and seem to be associated with deformations of the large scale SSS fields. Salinity gradients tend to align along the streamlines. For example, in the north of the area, the fresh water penetrating towards the salty region at 27^0N 46^0W could be the result of horizontal advection by geostrophic AVISO currents. The eddies inside the high SSS area usually correspond to local SSS maxima or minima: 22^0N 34^0W, 23^0N 30^0W or 26.5^0N 44^0W.

This product was validated with the drifter data. Fig. 2.12 presents velocity fields (blue vectors) of AVISO 2010 daily global product ($1/3^0$ spatial resolution; Fig. 2.12*a*), AVISO 2014 (Fig. 2.12*b*) and Mercator PSY2V4R2-R4 analysis total ocean current at 15m (Fig. 2.12*c*, plotted only at each 0.33^0 (each 4th Mercator grid point) to make a comparison and Mercator current more visible) vs. drifters' total velocity field (green vectors) the 2nd April 2013 (this date was chosen because enough drifters were present in the region and the geostrophic velocity field presented large spatial variability). All these products reproduce well the meso-scale ocean circulation responsible for the drifters' trajectories. Mercator PSY2V4R2-R4 assimilates the AVISO altimetry that results in a similarity between the two velocity fields (Fig. 2.12*a* and *b*). However Mercator PSY2V4R2-R4 analysis (estimated from SSH) shows stronger total kinetic energy (TKE) (7 J/m^3 – averaged value) than assimilated AVISO 2010 (5 J/m^3) (Fig. 2.13, green and blue curves, respectively). The TKE of the new AVISO 2014 product (6.8 J/m^3) (red curve) is close to the Mercator one. AVISO 2014 shows more spatial variability than AVISO 2010. However, both of them produce smaller velocity amplitudes compared to drifters that also suggest a contribution on those of Ekman currents.

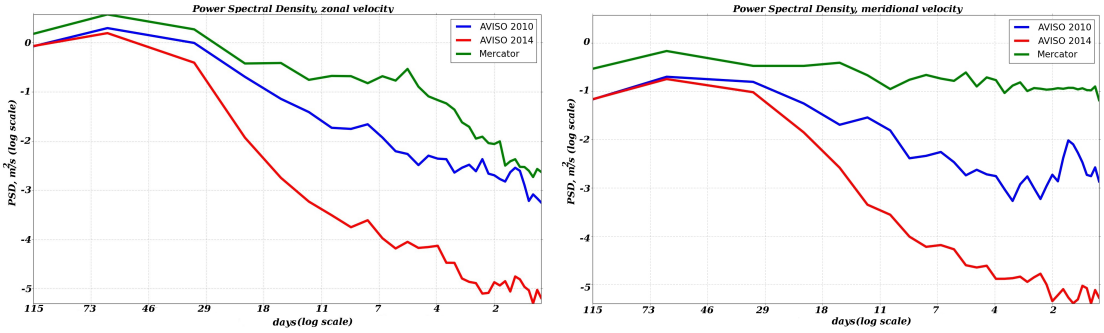

a *b*

Figure 2.14: Power Spectral Density (log scale) for velocity components from AVISO 2010 altimetry product (blue), AVISO 2014 regional altimetry product and Mercator geostrophic velocity estimated from SSH (green) in the region $20.5^0N - 33.5^0N$ $49.5^0W - 25.5^0W$: *a* - zonal velocity component, *b* - meridional velocity component

Fig. 2.14 show the detrended Power Spectral Densities for the spatially averaged zonal (*a*) and meridional (*b*) geostrophic velocity components in logarithmic scale in the region $\sim 20.5^0 - 33.5^0$N $\sim 49.5^0 - 25.5^0$W. At low frequencies, AVISO 2010, AVISO 2014 and Mercator power density lie close to each other around 0 m^2/sec that means that they produce the same variability at time scales of 10 days and longer. At these frequencies the ocean takes energy from the atmosphere that is redistributed (exponentially) through non-linear processes. However, even at these low frequencies there is a small difference between Mercator and the two AVISO altimetric products: Mercator shows larger PSD than AVISO 2010 and AVISO 2014, the differences are $\sim 1.15m^2/s$ in zonal velocity and $\sim 1.65m^2/s$ in meridional. At the high frequency (∼1–2 days) AVISO 2014 shows high negative (in logarithmic scale) PSD (down to 0.006 m^2/s) while Mercator and AVISO 2010 lie close to each other with PSD down to ∼0.05 m^2/s. It means that AVISO 2010 and Mercator have more variability at 1 or 2 day periods than AVISO 2014. The energy at these frequencies is transferred from lower frequencies by non-linear processes (http://www.cygres.com/OcnPageE/Glosry/SpecE.html). The difference between the three products at high frequency can also be associated with large scale Ekman pumping influence on geostrophic velocity that may be estimated differently in the different products. Moreover, the assimilation processes can play a role in the case of Mercator, but we think this effect is minor at high frequency as the assimilation cycle in Mercator analysis is about one week. AVISO 2014 does not show a lot of variability at these frequencies as the spatial averaged time series of this product is smooth probably due to the mapping process and how it manages transitions between successive days.

2.8 Argo floats and Mixed Layer Depth

The Mixed Layer Depth (MLD), as shown in Introduction, varies seasonally from a meter or less to maximum values (∼150 m) (Boyer Montégut et al., 2004; Sutherland

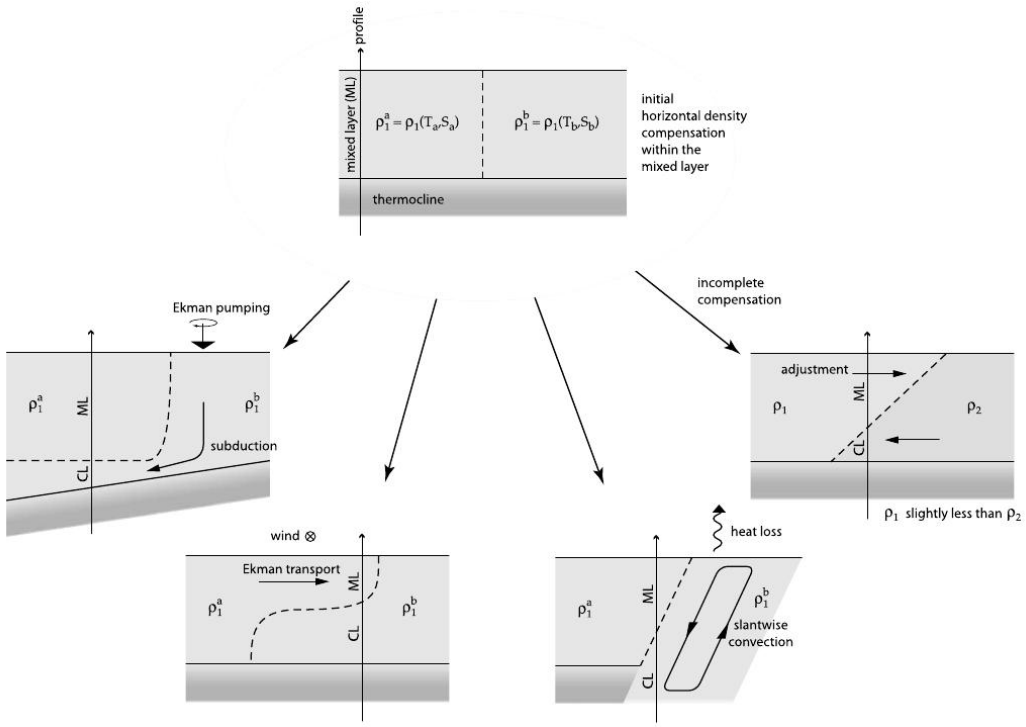

Figure 2.15: Schematics of the different three-dimensional mechanisms proposed to explain the occurrence of vertically compensated layers in the upper ocean. Source: de Boyer Montégut et al. (2004) (Fig. 11)

et al., 2016). Thus, the knowledge of the variability of the MLD is critical in any study of SSS and SST variability.

We estimate MLD on individual Argo temperature-salinity profiles (Gould et al., 2004). The MLD is estimated, when a threshold value for either temperature or salinity is reached compared with a near-surface value at 10 m depth (to avoid the effect of strong diurnal cycle in the top few meters of the ocean): $\Delta T = 0.1^0$C, $\Delta S = 0.03$ pss. Actually, during night time mixing brings MLD deeper than 10 m most of the time. Thus, this choice is relevant mostly for night time and lower frequency MLD variability. The choice of two criteria on T and S, instead of a single one on density stratification was motivated by the need to have conditions with active homogenization both on T and S. As was shown in de Boyer Montégut et al. (2007) and Mignot et al. (2007) there are three layers in the vertical structure in some regions of the upper subtropical ocean: the MLD that is controlled by salinity profiles, the barrier layer (BL) (the difference between the depth of density-based MLD and the depth of temperature-based MLD) and the deeper ocean. BL phenomena protect the surface layer from the heat exchanges with the deep ocean, and have potential climatic impacts, for example they are involved in the development of temperature anomalies that can start the El Niño-Southern Oscillation (ENSO) events or the Indian monsoon. The mechanism responsible for the BL formation in the tropical North Atlantic ($10^0 - 25^0$N) strongly depends on Ekman advection, heat loss in winter and atmospheric heating in

summer that support a salinity domination in the MLD criteria (Mignot et al., 2007). Moreover, there can also be an effect of "compensated layer" (CL) that happens when the density-based MLD is deeper than one from temperature-based criteria due to the compensation of salinity and temperature stratifications. The mechanisms of the vertical compensation are linked to the horizontal compensation: subduction processes of cold and fresh (warm and salty) surface waters or Ekman transport of the upper slides (Fig. 2.15). In the present work, the respective choices for dT and dS were such that they correspond independently to changes in density on the order of $\sim 0.03 kg/m^3$ in the North subtropical Atlantic (de Boyer Montégut et al., 2004). We group these estimates monthly to provide a monthly mixed layer depth distribution (in the standard case, it is the average of the distribution that is retained). We use data from Coriolis web site with the flag "good data". Because of insufficient data distribution, we only use them as providing a large scale average. Figure 2.16 presents three MLDs estimated separably from salinity (red), temperature (green) and density (blue) criteria. The isothermal (temperature-based) MLD (green) is close to the MLD with quasi-uniform density (blue). On the other hand, the halocline MLD is much deeper in spring and summer. This can be explained by the Shallow Meridional Overturning Circulation that brings subducted salty water from the North-East and induces an increase in halocline depth that with the chosen salinity criteria can be very different from MLD with the other criteria. An example of this situation is presented on Fig. 2.17*a* that illustrates a much deeper halocline than MLD estimated from the isothermal or density criteria (17.8 m). Thus, the use of two separate criteria for dS and dT allows us to estimate the layer where both characteristics are well mixed

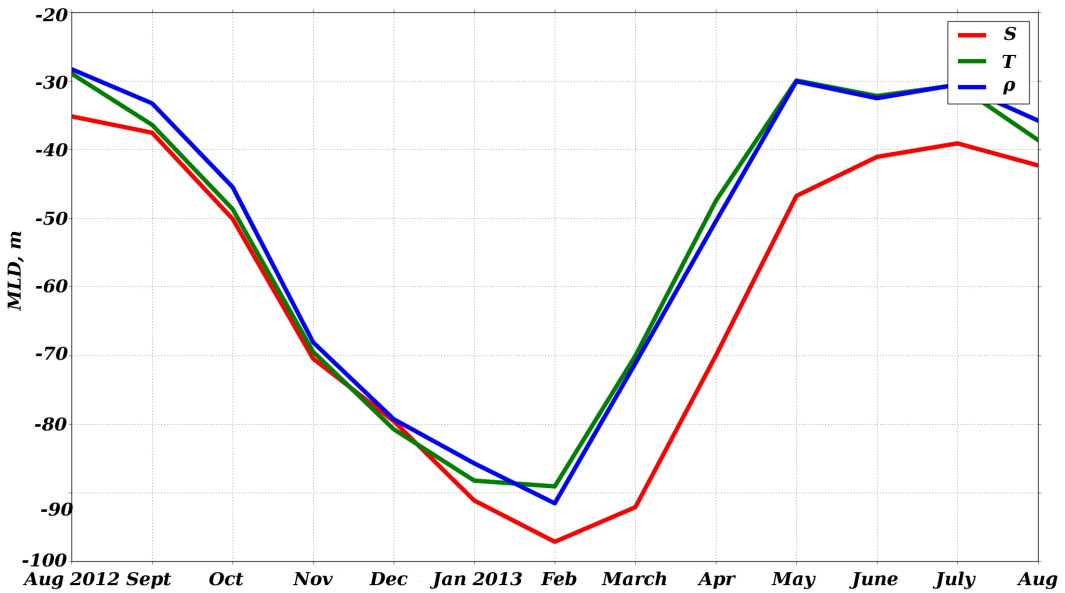

Figure 2.16: MLD from Argo profilers estimated with different MLD criteria for period August 2012 –August 2013 in region $21^0N - 30^0N$ $50^0W - 26^0W$: red – salinity-based criteria $\Delta S = 0.03$ pss; green – temperature-based criteria $\Delta T = 0.1^0$C; blue – density-based criteria $\Delta\rho = \sim 0.03 kg/m^3$

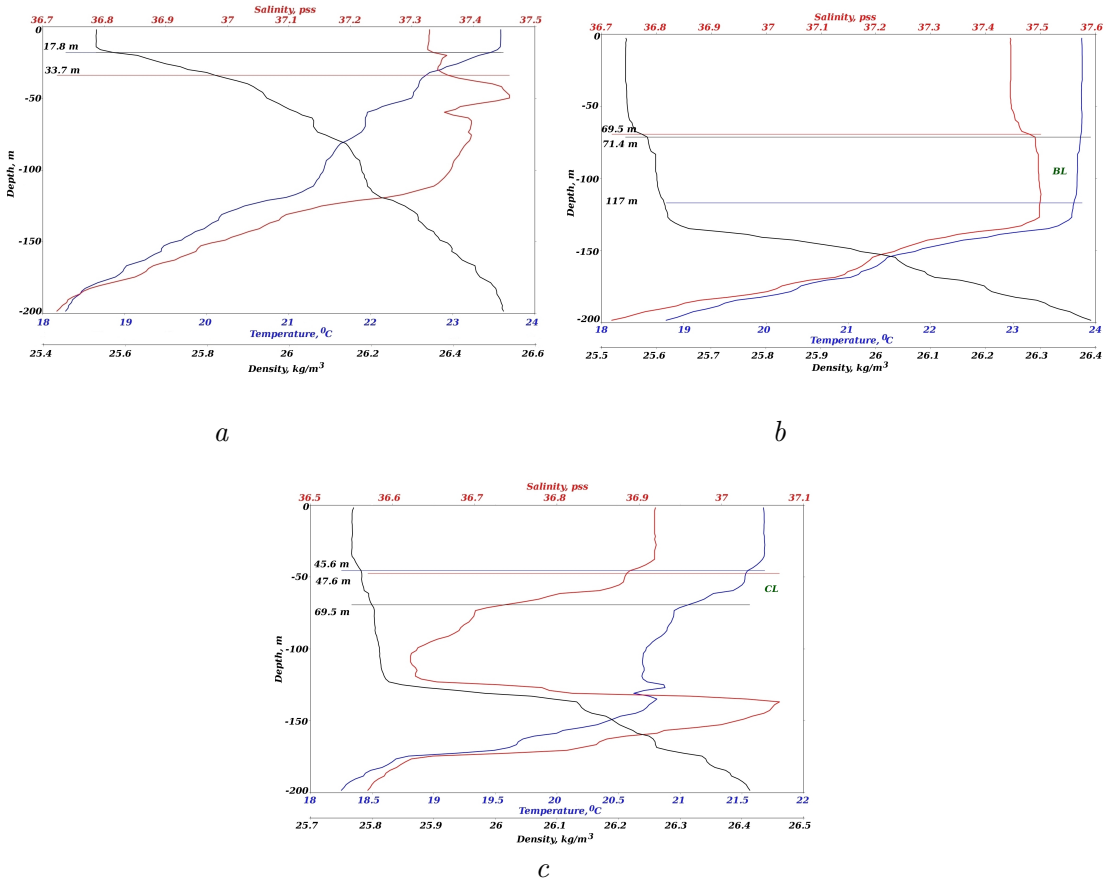

Figure 2.17: Density (black), salinity (red) and temperature (blue) profiles from Argo profilers: a – profiler at 26.8^0N 29^0W 14/05/2013, example of the effect of Shallow Meridional Overturning Circulation, b – profiler at 23.1^0N 36.6^0W 10/01/2013, example of BL, c – profiler at 28.9^0N 41.4^0W 20/01/2013, example of CL

and as it is mentioned before and shown on Fig. 2.17a corresponds to density criteria $\Delta\rho =\sim 0.03 kg/m^3$. Figure 2.17$b$ illustrates an example of the weak BL in autumn and winter from Figure 2.16 (Sprintall and Tomczal, 1992); whereas Fig. 2.17c is a case of weak CL in spring. These results are in a good agreement with the ones presented in de Boyer Montégut et al. (2004) for the North Atlantic. These layers average no more than a few meters in this area (max $\sim$ 3 m). These results are also valid for the later period September 2013 – December 2014.

Further, Fig. 2.18 compares this MLD from individual profiles with the MLD derived from the monthly gridded ISAS T and S fields (spatial resolution 0.5^0), an optimal estimation tool designed for the synthesis of the Argo global data sets (Gaillard et al., 2009). It is extracted at the Argo profile positions (blue curve) or averaged over the domain $21^0 - 30^0$N $50^0 - 26^0$W (green curve). Both show a shallower MLD than the Argo data (red curve) throughout the year, with the maximum difference of $\sim$25m in December. This can result from spatial interpolation of Argo data that would smooth the local vertical gradient, when there is a large spatial variability in MLD, especially

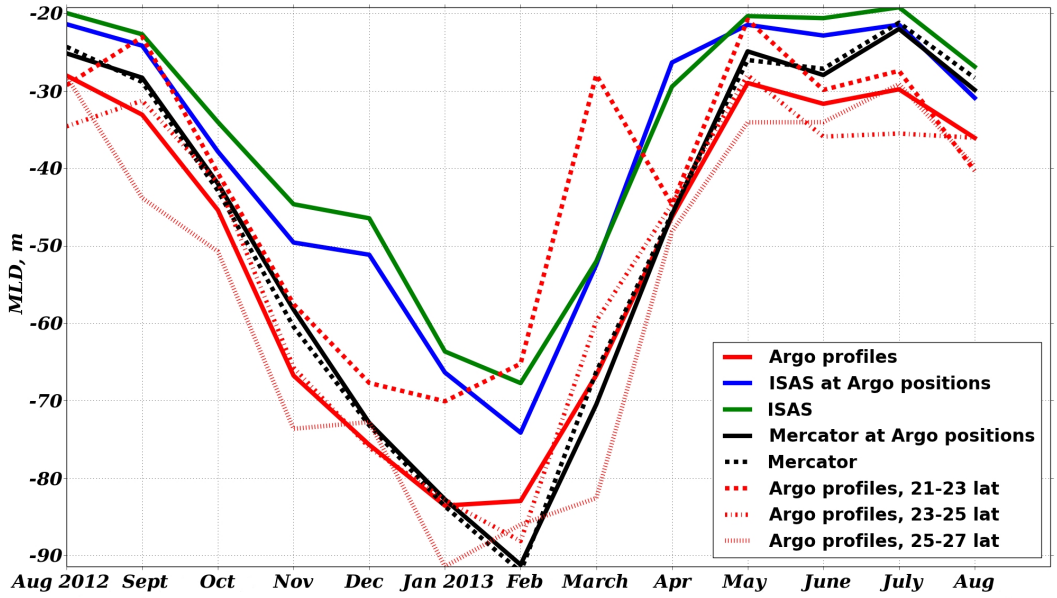

Figure 2.18: MLD from Argo (red) and ISAS interpolated product (blue and green) for period August 2012 –August 2013 in region $21^0N - 30^0N$ $50^0W - 26^0W$. MLD from Argo profiles for different latitude bands (red dashed lines)

in December 2012 when there were more local rain events in this region. Argo data can also be grouped in different latitude bands. This (Fig. 2.18, red dashed curves) shows a horizontal gradient (from shallower MLD in the South to deeper MLD in the North) and a different timing of restratification (March in southern regions and March–April in northern regions; Kolodziejczyk et al., 2015b; Kolodziejczyk et al., 2015c).

The comparison with Mercator analysis (Fig. 2.18, black curves) shows a good agreement with the Argo product (red solid curve) that was expected as Argo data were assimilated in Mercator. The biggest difference was found in February and July ($\sim 9m$) that probably results from inhomogeneous distribution of Argo profiles during these months that include gaps in areas with the deeper MLD in February and shallowest MLD in July. Except for these two months the differences between two products are almost never larger than 5 m. Thus, using Mercator analysis provides the opportunity to test further the effect of horizontal gradient of MLD in SSS or SST budgets (Chapter 4).

2.9 Atmospheric fluxes

As mentioned before, SSS and SST are strongly dependent on the freshwater and heat fluxes (Chapter 1. Introduction; Schmitt, 1995; Yu, 2011; Durack, 2015). Thus, the choice of the atmospheric data and the analysis of their accuracy are critical for our study.

2.9.1 Freshwater flux

Daily ERA-Interim reanalysis (Simmons et al., 2007; Dee et al., 2011) from ECMWF (spatial resolution 0.25^0x0.25^0), widely used daily OAFlux product (1^0x1^0) from WHOI for evaporation field and daily ERA-Interim reanalysis, TRMM TMI (3B42) ($0.25^0 \times 0.25^0$) and GPCP (1^0x1^0) satellites for precipitation field were tested. Precipitation is not a control variable of the analysis procedure in ERA-Interim reanalysis, assimilated rain-rate observations have a weak impact on increments in control variables, and humidity observations have a stronger influence on precipitation in reanalyses than the precipitation observations themselves (Rienecker et al., 2001). GPCP precipitation is strongly based on satellite retrievals, such as TRMM TMI, and surface rain gauges (Adler et al., 2012). GPCP uses the passive emission microwave retrievals (SSM/I) while TRMM satellite uses active microwave measurement (TRMM Precipitation Radar) in addition to TMI passive microwave sensor. This TRMM Radar allows to identify rain type, transformation rain into snow and information about intensity and rain distribution. The serious problems of SSM/I are the distinction of rain on snow-cover and detection of rain in case of significant ice particles in clouds when algorithms may not detect the rainfall (since the weak 85-GHz scattering signature may be swamped by variations in background emission) or precipitation rates may be significantly underestimated (Conner and Petty, 1998). These should not be issues in this subtropical region.

The OAFlux project uses objective analysis to obtain optimal estimates of flux-related surface meteorology and then computes the global fluxes by using state-of-the-art bulk flux parameterizations (OAFlux web site: http://oaflux.whoi.edu/; Yu et al., 2007). OAFlux evaporation is estimated from the relation between latent heat flux Q_{LH} and latent heat of vaporization L_e : $Evp = \frac{Q_{LH}}{\rho_w L_e}$, where $L_e = (2.501 - 0.00237 * SST) * 1.0^6$ (Yu et al., 2008).

The comparison of evaporation fields from ERA-Interim (Fig. 2.19*a*, black curve) with the ones from OAFlux (Fig. 2.19*a*, blue curve) indicates small differences between ∼0 to 0.5 mm/day. The comparison with the mooring data at 24.5^0N 38^0W (see 2.3, Fig. 2.19*a*, low-passed filtered data with 30 days cut-off) shows that ERA-Interim product sometimes (October, November, June) overestimates evaporation (max ∼0.5 mm/day) but usually in the confidence interval from the mooring data (0.16 mm/day) with a high correlation, while OAFlux product underestimates a little (max ∼0.7 mm/day and it is out of the mooring confidence interval in spring and summer) evaporation during most of the period. This is in line with the expectation that OAFlux might slightly underestimate the evaporation (from ERA-Interim and buoys) in the subtropical gyre of the North Atlantic (Yu et al., 2008). Thus, ERA-Interim evaporation data was chosen for the estimation of MLS budget based on observations (Chapter 4).

On the other hand, ERA-Interim reanalysis produces larger precipitation events over the North Atlantic compared with the satellite data (Fig. 2.19*a*, green curve). TRMM satellite precipitation (Fig. 2.19*a*, orange curve) is stronger than in GPCP (Fig. 2.19*a*, red curve) (Huffman et al., 2009). The comparison with the mooring data does not show a good agreement between the different products, even after monthly averaging (Fig. 2.19*b*). As shown in Sommer et al. (2017, in submission), daily-

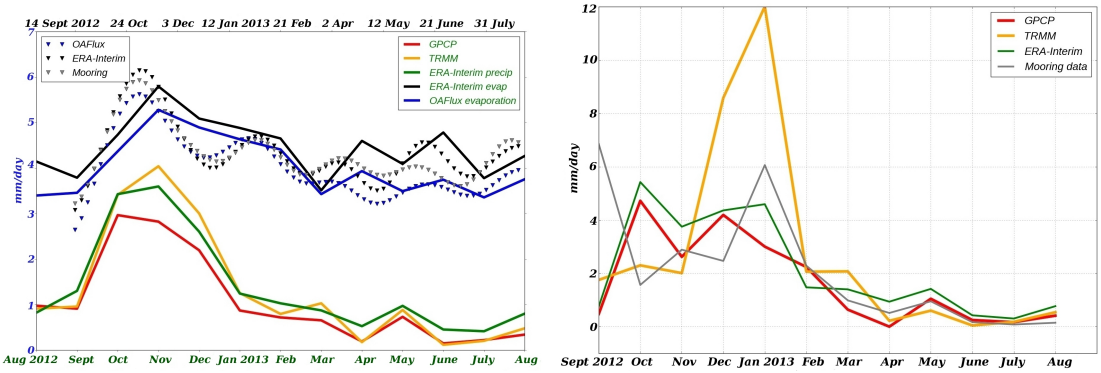

a *b*

Figure 2.19: Comparison of freshwater flux components: *a* – evaporation (ERA-Interim – black curve, OAFlux – blue) and precipitation (GPCP – red, TRMM – orange, ERA-Interim – green) data averaged over the month and over the domain $21^0N - 30^0N$ $50^0W - 26^0W$ (solid lines) and evaporation filtered with cut-off period 30 days at mooring position 24.5^{0}N 38^{0}W (dashed lines, mooring data – gray curve); *b* – precipitation data at mooring position; Sommer et al. (2015) (Fig. 5)

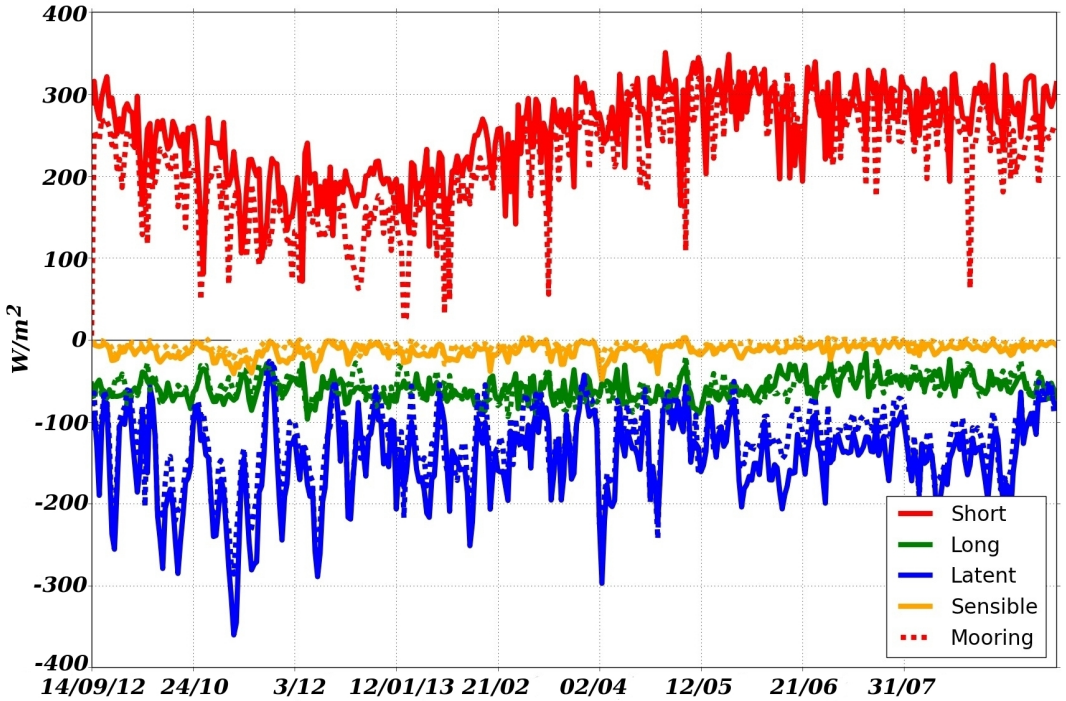

Figure 2.20: Surface heat flux for the period September 2012 – August 2013; solid curves – ERA-Interim reanalysis, dashed curves – mooring data at 24.5^{0}N 38^{0}W: red – net short wave radiation, green – net long wave radiation, blue – latent heat, orange – sensible heat; Sommer et al. (2015) (Fig. 6)

averaged, precipitation data from different sources (different reanalyses or satellite-based datasets) do not show a good agreement. This is due to difficulties in reproducing both light and heavy precipitation, especially in reanalysis, that is less important for climatological means but has large effects at synoptic scales. In our comparison, ERA-Interim shows much higher total precipitation (2.58 mm/day) compared with mooring data (1.86 mm/day $\pm$ 10%), TRMM also overestimates high precipitation events (total precipitation 2.76 mm/day). GPCP does not correlate well with the mooring time series, but presents a very close total precipitation average (1.69 mm/day). We retain GPCP in this work, and it was also proposed as a good reference at the daily scale in Sommer et al. (2017, in submission).

2.9.2 Heat fluxes

The latent heat, sensible heat, net downward short and long wave radiations from ERA-Interim with the resolution 0.25^0x0.25^0 are used to estimate surface heat flux. ERA-Interim net surface heat flux presents a satisfactory agreement with the one from mooring data at 24.5^0N 38^0W (Fig. 2.20). The average over the year for the incoming short wave radiation is 220.3 Wm^{-2} with mooring data and the net downward short wave radiation is 252.06 Wm^{-2} with ERA-Interim, for the long wave radiation it is respectively -58.84 Wm^{-2} and -58.9 Wm^{-2}, for the sensible heat flux it is respectively -6.37 Wm^{-2} and -13.19 Wm^{-2}, and for the latent heat flux it is -124.08 Wm^{-2} and -144.37 Wm^{-2} respectively, so that the net heat flux across the sea surface of the two products differ by less than 6 Wm^{-2}.

Chapter 3

Method

3.1 Introduction

In chapter 2, I presented the data used to estimate MLS and MLT budgets. I compared different types of data (*in situ*, satellite, reanalysis, analysis and model data) to estimate the accuracy of different products. Now I will analyze the effect of each term of mixed layer salinity (MLS) and temperature (MLT) budgets on salinity and temperature variability, respectively. In this chapter at first I will present a method to choose the region and volume for estimation of MLS and MLT budgets. Then the MLS and MLT budget equations and the methods retained to estimate the different terms of these equations are discussed. This depends on the data used as spatial and temporal resolution of the available data constrains what can be estimated.

Data uncertainties are also estimated to understand their effect on the final results and the effect of processes that are not included in the budget's equations.

In many previous studies (Büsecke et al., 2014; Dong et al., 2015) it was noted that horizontal advection is one of the most important components for the MLS budget. Thus, detailed analysis of surface currents is needed. This includes the development and validation of method for estimation of Ekman currents as well as the further investigation of geostrophic currents in particular at meso-scale that was started in Chapter 2. I discuss it further in this chapter.

3.2 Estimation of mixed layer salinity and temperature budgets

As discussed in 2.8, in the North Atlantic subtropical gyre, there is usually a well-mixed and turbulent (at least at night) surface layer. The depth of this layer varies throughout the year from 20 to 150 m. Properties in the mixed layer evolve as a result of ocean processes as well as of the air-sea fluxes. Thus, unusual weak or strong air-sea flux for a particular season can generate strong anomalies in MLD. For example, due to the weak air-sea buoyancy flux in late winter 2010 the MLD was very shallow (Kolodziejczyk et al., 2015c).

Evaporation is a dominant component of the salinity budget (Fig. 3.1*b*). To balance the effect of this water loss due to excess of evaporation flux on salinity, fresh water

transport is contributed by eddies, mixing processes, and Ekman transport (Gordon and Giulivi, 2014). Fig. 3.1 shows the effect of ocean dynamics on moving salinity from the region of the maximum $E-P$ (Fig. 3.1*b*, a little south of red box) further north to the region where the maximum salinity concentration is located (Fig. 3.1 *a*, red box). In winter 2012–2013 (especially in December) a rain band was found in the middle of this region which resulted in two separate local maxima on Fig. 3.1*b*. The figure illustrates the important role of ocean processes on the formation of the salinity maximum region in the subtropical gyre. Ekman transport brings fresh and cold water from the North and fresh and warm water from the tropics. Vertical entrainment of deeper water is expected to be a major contributor to the changes in surface salinity (Dong et al., 2015) and surface temperature in particular during the winter. At large-scale, the change of SSS in salinity maximum region is small compared with the amplitude of the sea surface forcing and "residual terms" (subduction, vertical shear, vertical motions, internal waves and all small-scale and fast dynamics (Dohan et al., 2015)) that close the budget. Furthermore, Dong et al. (2015) found that for SSS (or fresh water) budget the Ekman component dominates the total horizontal advection in this North Atlantic region. The turbulent advection contributes to freshening and warming/cooling mainly by eddies at meso-scales (Büsecke et al., 2014).

Furthermore, the contribution in the SSS variability of one component of the budget or another strongly depends on the time scales. For example, the advection term in the region of SSS–max shows a weak seasonal cycle but is very variable at interannual scale (Dong et al., 2015).

Next I present equations of time evolution of salinity and temperature based on the fundamental conservation theory. We will consider monthly time series of the SSS and SST variability and evaluate the components responsible for this variability during almost 2 years.

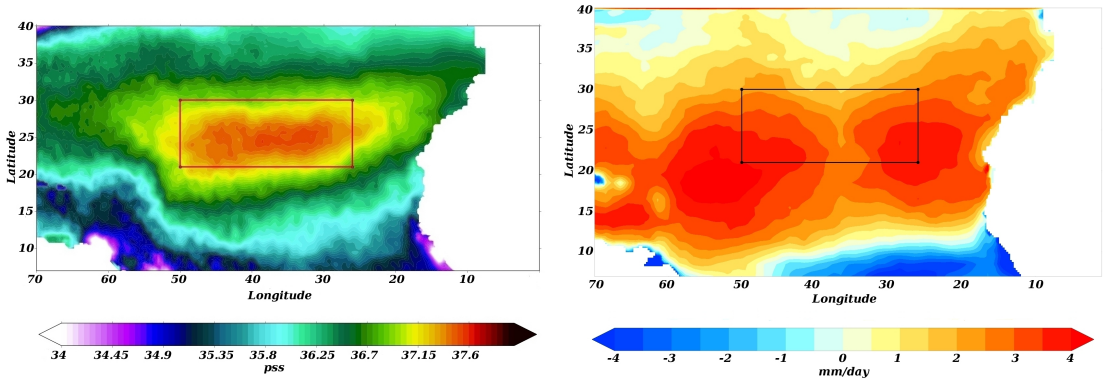

a *b*

Figure 3.1: Annual SMOS SSS (*a*) and E-P (OAFlux - GPCP) (*b*) mean with the selected region for SSS budget estimation (red box) in the salinity maximum region over the August 2012–August 2013

3.2.1 Domain

The important choice for the estimation of the SSS or SST budgets is the choice of the region and volume over which to integrate the equations. One can choose a rather shallow surface layer. In this case, the lateral variations are ignored as they are negligible compared to large scale atmospheric variability and vertical fluxes through the very thin layer dominate the budget. Thus, there is a freshwater flux at the surface that has to be compensated by vertical flow through the bottom of the box as there is no significant transport of salt across the surface. And as shown in Warren (2009) the net flux of salt into or out of thin box must be compensated by an equal and opposite turbulent advection through the bottom of the box.

Schmitt and Blair (2015) propose another method, "control volume approach". It is based on the fact that the SSS–max is deepening and spreading to the West and represent the form of "sock" in three-dimensional view. This maximum is bounded by contours of S = 37 pss that constrain the investigated volume. In this case we have to consider the lateral flow and eddy transports through the sides of this volume. The boundary of the volume by the contour S = 37 pss sets the boundary conditions: velocity across the surface is carrying the same salinity in and out. Thus, this approach allows us to find a connection between ocean mixing processes and surface fluxes (Schmitt and Blair, 2015). The problem of this method is how to define this isohaline: over which time and space scales is it averaged, and thus what are the scales considered in the eddy term. It is clear that the isohaline volume will need to vary at least seasonally and inter-annually, thus it complicates the analysis of results. The surface chosen is also not necessarily relevant for the heat budget. We can find already in the literature the analysis of the variability of the surface contour of S = 37 pss (or other relevant isohaline) and the different processes contributing to it, such as was done for the tropical Pacific in Hasson et al. (2013) and in the subtropical North Atlantic in Dohan et al. (2015).

In the present work we chose the widely used approach which consists of selecting fixed horizontal domains bounded vertically by the bottom of the mixed layer, thus investigating an averaged mixed layer budget. The bottom of this box can vary spatially when horizontal gradients of MLD can be estimated or stay spatially homogeneous if this information is lacking. This method provides the estimations of salinity variability in ML as well as the estimations of processes at the surface and at the bottom of ML which are strongly responsible for salinity variability.

The region investigated is chosen within the latitudes/longitudes range $21^0-30^0N \times 50^0 - 26^0W$ near subtropical Atlantic salinity maximum (Fig. 3.1, red/black box). It encompasses the region of largest SSS and strong SSS horizontal gradients just out of the domain (Fig. 3.1*a*). In particular in the South one expects a strong SSS gradient due to a very large contribution from Ekman currents. Moreover, the chosen SSS–max region presents the Ekman convergence zone and, in the same time, the divergence zone of eddy horizontal advection and the region with a small eddy activity. Furthermore, the spatial concentration of drifters and Argo data is larger in the center of the region and thus the realism of the analysis can be better checked there.

I also tested how different components of the MLS/MLT budget depend on the region chosen. It gives the opportunity to compare our results with earlier studies that

have considered other regions and found results different from ours. This will be done in the next Chapter.

3.2.2 Estimation based on observations

We consider the MLS budget integrated spatially that can be written as

$$\underbrace{\frac{\partial\langle S\rangle}{\partial t}}_{\text{MLS tendency (I)}} = \underbrace{-\langle u'\nabla S'\rangle - \langle\overline{u}\nabla\overline{S}\rangle}_{\text{Advection (II)}} \underbrace{-\frac{(\langle S_{10m}\rangle - \langle S_{-entr}\rangle)}{h}\left(\frac{\partial h}{\partial t} + \langle w_{-h}\rangle\right)}_{\text{Entrainment (III)}} + \underbrace{\left\langle\frac{(E-P)S}{h}\right\rangle}_{\text{Surface Forcing (IV)}} + R, \quad (3.2.1)$$

where $\langle S\rangle$ denotes SSS averaged over the domain for each time step (week), $\overline{S}$ is the mean salinity over a 90 days period for each grid point, h is MLD monthly averaged over the domain, w_{-h} is the Ekman vertical velocity calculated with the ERA-Interim wind, u ($u = \overline{u} + u'$) is the horizontal velocity vector, the sum of geostrophic AVISO velocity field and Ekman velocity that was calculated as $\frac{\overrightarrow{\tau} e^{i*90}}{\rho f h}$, $\overline{u}$ is the mean velocity over a 90 days period and $u' = u - \overline{u}$ for a week in a middle of a 90 days period. $\overline{u}$ can be also estimated as the as a smooth spatial field. Thus, u' would be the residual that presents a smaller spatial scale. The 90-days average should be equivalent to the last method as it seems to be enough to limit the effect of individual eddies from the $\overline{u}$ field. We did not use the spatial filtering/smoothing because we were limited by the spatial domain that poses a problem due to the domain boundary effect. $(E - P)$ is the difference between evaporation and precipitation. After these terms are monthly averaged. In term of entrainment S_{10m} is the salinity at 10m depth (that is assumed the average salinity of MLD), S_{-entr} is the salinity at the depth $\left(\frac{\partial h}{\partial t} + \langle w_{-h}\rangle\right) \times \triangle T$ (with $\triangle T = 1$ month) that scales the layer of entrained water during a month (a month is the elementary time step in the mixed layer depth analysis). The left side of the equation presents the MLS tendency. The first term of the right side of the equation is turbulent horizontal advection estimated for each week at each grid point and then monthly averaged over domain; the second one is mean horizontal advection averaged by the same way as the previous term. The terms $u'\nabla\overline{S}$ and $\overline{u}\nabla S'$ are negligible when the monthly average over domain is applied. The third term presents the entrainment component (here we used Argo profile salinity, and neglect horizontal gradients when estimating this term as the MLD was chosen the same over whole domain for the considered month; see discussion for Mercator analysis). The fourth term is the surface forcing that was estimated in the same manner as advection terms. The last one R is a residual term that includes the sum of all unresolved physical processes and the accumulated errors from the other terms.

Similarly, the ML temperature (MLT) budget can be written as Moisan and Niiler (1998)

$$\underbrace{\frac{\partial\langle T\rangle}{\partial t}}_{\text{MLT tendency (I)}} = \underbrace{-\langle u'\nabla T'\rangle - \langle\overline{u}\nabla\overline{T}\rangle}_{\text{Advection (II)}} \underbrace{-\frac{(\langle T_{10m}\rangle - \langle T_{-entr}\rangle)}{h}\left(\frac{\partial h}{\partial t} + \langle w_{-h}\rangle\right)}_{\text{Entrainment (III)}} + \underbrace{\left\langle\frac{Q}{\rho C_p h}\right\rangle}_{\text{Surface Forcing (IV)}} + R, \quad (3.2.2)$$

where $\langle T\rangle$ is SST averaged over the domain for each time step (month), Q is the surface heat flux, C_{-p} is the specific heat capacity, ρ is density, all other terms are the same as for salinity budget. The surface heat flux can be calculated as $Q = Q_l + Q_s + Q_{lw} + (1-\alpha)Q_{sw}[1 - I(h)]$ (Morel and Antoine, 1994; Sweeney et al., 2005), where Q_l is latent heat, Q_s is sensible heat, Q_{lw} is net long wave radiation, Q_{sw} is net short wave radiation, $\alpha = 0.04$ is the ocean surface albedo, $I(h) = Re^{-h/D_1} + (1-R)e^{-h/D_2}$ is the penetrative solar irradiance with the fraction solar flux for wavelengths longer than 700 nm $R = 0.58$, it is assumed to penetrate the ocean with a decreasing exponential profile, with an e-folding depth scale $D_1 = 0.35m$; $D_2 = 23m$ is the second extinction length scale associated with the shorter wavelength (Madec and the NEMO team, 2014).

All data used (except the data for entrainment term) are weekly averaged and interpolated to the same time and space resolutions as the SMOS product that is the main data of the research.

The error bars for salinity tendency $\frac{\partial\langle S\rangle}{\partial t}$ (I) and terms of advection $(II$ and $III)$ were estimated as standard errors of the sampling distribution over domain and over considered month with size of samples (number of observations) n :

$$\delta_{standard}(x) = \frac{1}{\sqrt{n}}\sqrt{\frac{1}{n}\sum_{i=0}^{n}(x_i - \overline{x})}$$

The method chosen to estimate entrainment term limits the estimation of its errors. This term is estimated directly over domain and over a month. Thus, I could only provide general estimation on MLD uncertainties that were also estimated as standard errors (assuming that individual estimates are independent from each other).

Equations (3.2.1) and (3.2.2) contain terms that combine different variables with their individual uncertainties, for example the terms of freshwater or heat fluxes; in a space-time varying field, the error thus represents the uncertainty on the average due to its variability, as sampled by the fields. To estimate the uncertainty on each term of the equations we use an error propagation method (Emery and Thomson, 1998). If F (the interested us term) is the function of X, Y etc. $F(X, Y, ...)$, the absolute error is estimated as:

$$\varepsilon_a = \delta F = \sqrt{\left(\frac{\partial F}{\partial X} * \delta X\right)^2 + \left(\frac{\partial F}{\partial Y} * \delta Y\right)^2 + ...}$$

or relative error:

$$\varepsilon_r = \frac{\delta F}{|F|} = \frac{1}{|F|}\sqrt{\left(\frac{\partial F}{\partial X} * \delta X\right)^2 + \left(\frac{\partial F}{\partial Y} * \delta Y\right)^2 + ...}$$

Thus, in the case of the surface forcing term $F = \frac{(E-P)S}{h}$ the error bars were estimated as the relative errors using error propagation method:

$$\varepsilon_r = \frac{\delta F}{|F|} = \frac{1}{|F|}\sqrt{\left(\frac{\partial F}{\partial (E-P)} * \delta(E-P)\right)^2 + \left(\frac{\partial F}{\partial S} * \delta S\right)^2 + \left(\frac{\partial F}{\partial h} * \delta h\right)^2} = \frac{1}{|F|}\sqrt{\left(F\frac{\delta(E-P)}{|E-P|}\right)^2 + \left(F\frac{\delta S}{|S|}\right)^2 + \left(F\frac{\delta h}{|h|}\right)^2} = \sqrt{\left(\frac{\delta(E-P)}{|E-P|}\right)^2 + \left(\frac{\delta S}{|S|}\right)^2 + \left(\frac{\delta h}{|h|}\right)^2}$$

This method was not applied to other terms because they contained an differential operator that is hard to interpret.

3.2.3 Estimation based on analysis

Extensive analysis can be done on numerical simulations. Numerical models provide products with the high horizontal resolution together with a refined vertical grid. I used Mercator PSY2V4R2-R4 analysis. It has a daily time spatial resolution and ∼10 km spatial resolution. The spatial resolution if higher than in the case of SMOS (∼45 km) and the comparison of two products gives the opportunity to test the ability of SMOS to resolve the meso-scale variability.

The equations (3.2.1) and (3.2.2) in case of the numerical model has an additional term – horizontal eddy diffusion (to represent subscale transports), and the MLD can be estimated at each grid point that gives an opportunity to estimate the effect of the horizontal gradient of the MLD.

The equations of MLS and MLT can then be written as:

$$\underbrace{\frac{\partial\langle S\rangle}{\partial t}}_{\text{MLS tendency (I)}} = \underbrace{-\langle u'\nabla S'\rangle - \langle\overline{u}\nabla\overline{S}\rangle}_{\text{Advection (II)}} \underbrace{-\left\langle\frac{(S_{10m}-S_{-entr})}{h}\left(\frac{\partial h}{\partial t} + w_{-h} + u * \nabla h\right)\right\rangle}_{\text{Entrainment (III)}} \underbrace{+\left\langle\frac{(E-P)S}{h}\right\rangle}_{\text{Surface Forcing (IV)}} \underbrace{+\left\langle\langle K_h\rangle\nabla^2 S\right\rangle}_{\text{Diffusion (V)}} + R \quad (3.2.3)$$

$$\underbrace{\frac{\partial\langle T\rangle}{\partial t}}_{\text{MLT tendency (I)}} = \underbrace{-\langle u'\nabla T'\rangle - \langle\overline{u}\nabla\overline{T}\rangle}_{\text{Advection (II)}} \underbrace{-\left\langle\frac{(T_{10m}-T_{-entr})}{h}\left(\frac{\partial h}{\partial t}+w_{-h}+u*\nabla h\right)\right\rangle}_{\text{Entrainment (III)}} \underbrace{+\left\langle\frac{Q}{\rho C_p h}\right\rangle}_{\text{Surface Forcing (IV)}} \underbrace{+\left\langle\langle K_h\rangle\nabla^2 T\right\rangle}_{\text{Diffusion (V)}} + R \quad (3.2.4)$$

With this spatially resolved fields, the entrainment terms (third terms in the right sides of equations) are estimated at each grid point and then averaged over domain. An additional term presents the horizontal eddy diffusion (fifth terms), where K_h is the diffusion coefficient that is estimated at each grid point as $K_h \approx \frac{u'^2+v'^2}{2} \times t$, $t = 1$ day (Siedler et al., 2013) to include the effect of submeso-scale processes, and then averaged over domain to avoid the effect of strong diffusion variability. In Mercator analysis the horizontal diffusion is estimated by the same isopycnal Laplacian as in (3.2.3) with the constant horizontal diffusion coefficient (125 m^2/s) which has the same magnitude that was found in our estimation.

As done previously, all data used in equations (3.2.3) and (3.2.4) are weekly averaged to the same time resolution as SMOS product and interpolated to the Mercator spatial grid ($1/12^0 \times 1/12^0$). It means that each particular term (salinity, total velocity, MLD, entrainment velocity, $(E-P)$ etc.) are weekly averaged before their use in equations. It will simplify the comparison and, moreover, reduce the effect of one particular day with strong evaporation or precipitation. The effect of daily variability is briefly discussed in Chapter 4.

It is worth to note that now the error bars of entrainment term can be estimated as the standard errors.

3.3 Analysis and estimation of sea surface currents

As was mentioned before, the surface ocean currents play a significant role in controlling SSS variability but different data, for example geostrophic velocity suffer from various inaccuracies (see Chapter 2). Here I present a method to estimate the uncertainties and make a comparison between different data sets. This method will be expanded further in Chapter 5.

The comparison will be done between Mercator ocean currents (daily resolution on $1/12^0 \times 1/12^0$ grid), AVISO 2010 altimetry (daily data, $1/3^0 \times 1/3^0$), AVISO 2014 regional altimetry product (daily data, $1/8^0 \times 1/8^0$) and ERA-Interim wind (daily data, $0.25^0 \times 0.25^0$). All data will be considered on their own spatial grids despite the ERA-Interim wind that is integrated in the Mercator grid. Thus, this comparison will give an idea on the effect of spatial resolution used in the horizontal advection.

I used drifter current data to estimate the errors in altimetry-derived and model current products. Some of these results were already presented in Chapter 2; they can give an idea of accuracy of these data and can be expanded to velocity fields in the ML. To investigate meso-scale variability from the drifters the drifter velocity is decomposed

into a geostrophic (or cyclostrophic) velocity, Ekman velocity and ageostrophic velocity residuals.

$$U_{drifter} = U_{Ekman} + U_{geostr} + U_{ageostr}. \tag{3.3.1}$$

The drifter velocity time series are filtered with a Butterworth low-pass filter of order 4 to remove noise and high-frequency ageostrophic components (inertial oscillations, tidal currents, internal ocean dynamics, etc.). The cut-off frequency is 0.032 h^{-1} that corresponds to 30 hours (a little larger than the inertial period in the region).

The Ekman current component of the drift is difficult to evaluate directly, as we do not know precisely the dependence with depth and time of diffusivity/viscosity in the upper ocean layer. A model fitted to the data will be used for deriving an estimate of this component, as done in Rio (2012). It first involves removing estimates of the geostrophic (cyclostrophic) currents.

For that, we have estimates of the geostrophic (cyclostrophic) currents from Ssalto-Duacs or other altimetric products and from Mercator PSY2V4R2-R4 analysis currents (articles from "Mercator Ocean – Coriolis Quarterly Newsletter", Special Issue, #52, May 2015). We used two AVISO products Ssalto/Duacs Gridded Absolute Dynamic Topography and absolute geostrophic velocities product of 2010 and new regional product of 2014 (Chapter 2). Mercator geostrophic currents at 50 m are tested as well as geostrophic currents estimated from SSH of Mercator analysis. We expect that the Ekman effect will be small at 50 m.

The Ekman model proposed by M.-H. Rio (2012) has the form:

$$u_{ekm} = \beta\tau e^{i\theta}, \tag{3.3.2}$$

where $\beta = \frac{\pi\sqrt{2}}{\rho f D_e}$, $\theta = \frac{\pi}{D_e}z - \frac{\pi}{4}$, $D_e = \sqrt{\frac{2\nu}{f}}$, and ρ is density, z is the depth, D_e is Ekman depth, ν is eddy viscosity, f is Coriolis parameter.

Wind stress τ is calculated from ERA-Interim wind data, velocity in the left side of the equation is estimated as drifter velocity without the geostrophic current estimates from the products mentioned above. ERA-Interim data are interpolated to drifter positions. Afterwards for each drifter, the collocated wind data were filtered with the same filter as the drifter velocities. Then parameters β and θ are estimated through least square fit on monthly subsets of the drifter data.

These β and θ are compared with their analogs in Mercator surface currents at 15 m. Validated parameters β and θ will be used to estimate the uncertainties in the Ekman current in the ML that is used to estimate MLS and MLT variability and in the formula that is widely used for estimation of Ekman velocity in ML:

$$u_{ekm} = \frac{\tau}{\rho f h} e^{i*90^0},$$

where h is MLD. This formula represents the Ekman transport that occurs at 90^0 clockwise from wind direction. The division by the depth h represents its average over h (Venables and Meredith, 2009). The Ekman velocity exponentially reduces with the depth. At the depth where the the Ekman current has a opposite direction to that at the surface (Ekman depth) the current presents 4% of the surface current. In the North Atlantic subtropical gyre the Ekman depth is not very different from MLD

(Rio and Hernandez, 2003). If the Ekman depth is shallower than MLD the average will be estimated over the MLD and represent the vertical transport of parcels over the MLD. If the MLD is shallower than Ekman depth we expect that it will not have a strong effect on the estimation owing to exponentiation reduction of Ekman velocity with the depth.

The detailed analysis is presented in Chapter 5.

3.4 Sensibility to data and methods used

In this section I would like to show the sensibility of terms in SSS budget equation to data and methods used for their estimations. All data and methods, which I will include, were already presented in the previous and present chapters. Figure 3.2 summarizes the different tests that will be detailed in the two following chapters. On this figure I presented the time and spatial averages of equation's terms over the SSS–max region and the period August 2012 – December 2014. Figure 3.2 shows a large spread of averaged values of terms (x-axis) and residuals R (y-axis). The test of different combinations of precipitation and evaporation data for Mercator or SMOS salinity fields (blue rounds) shows the variation of residual term from -0.43 pss/yr to 0.15 pss/yr. The largest R, -0.43 pss/yr, corresponds to the surface forcing term estimated with Mercator MLS, ERA-Interim evaporation and GPCP precipitation. It is worth to note that the surface forcing term also varies in a large range, 0.85 – 1.42 pss/yr. The advection term (red stars) is also sensitive to the data used: residual varies from -0.55 pss/yr to -0.05 pss/yr with the largest value in the case of combining Mercator MLS with AVISO altimetry product for geostrophic velocity and Ekman current estimated with ERA-Interim wind. But what is more important here is the large spread of averaged values of advection terms that could complicate the evaluation of the impact of this term on salinity variability. This also applies to mean (purple squares) and turbulent (grey triangles) components of advection. The entrainment term (green rhombus) is sensitive to the choice of the depth at which the entrained salinity S_{-entr} can be estimated that was mentioned before. Thus, for example, taking the S_{-entr} at 10 m below MLD, that different from the method proposed in the present PhD work, increases R from -0.3 pss/yr to -0.38 pss/yr in the case of SMOS and Argo profilers and reduces the entrainment term from -0.56 pss/yr to -0.48 pss/yr.

Altogether the small residual is presented by Mercator analysis with combination of GPCP and OAFlux data for precipitation and evaporation, -0.05 pss/yr. SMOS combined with GPCP, ERA-Interim, AVISO and Argo data shows a residual term almost in a middle of its range, -0.3 pss/yr.

In the next section, I will present a detailed analysis of different cases.

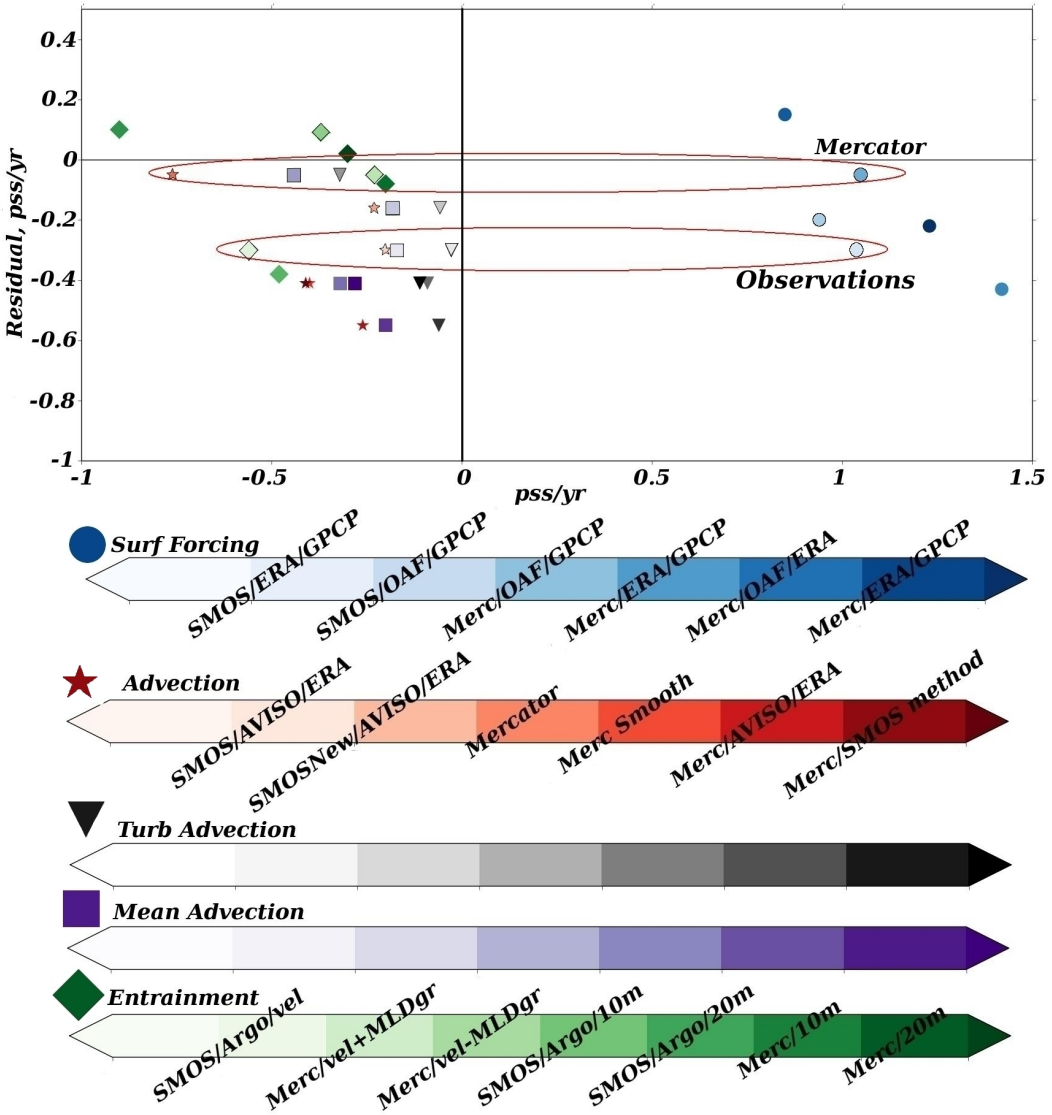

Figure 3.2: Test of sensibility of terms in SSS budget equation to different data and methods used. x-axis represents the variability of SSS budget terms, y-axis represents the variability of residual R, both depend on the combination of different data used and methods as in case of entrainment. Blue rounds – surface forcing term estimated with different combination of SSS and E and P data; red stars – advection term estimated with different combination of SSS and ocean current fields; grey triangles – turbulent advection; purple squares – mean advection; green rhombus – entrainment estimated with different combination of SSS and salinity data at different depth as well as by different method of estimation for entrained salinity S_{-entr}

Chapter 4

Mixed layer salinity and temperature budgets in the North Atlantic subtropical gyre

This chapter is devoted to the investigation of the sea surface salinity and temperature variability. It includes the analysis of mechanisms responsible for this variability, detailing their relative importance throughout the period of studies. As mentioned before, the analysis is done for the period August 2012 – December 2014 in the region of SSS maxima $21^0 - 30^0N \times 50^0 - 26^0W$. These period and region present enough *in situ* data used for "data control" of mapped products (see Chapter 2). In addition, this region does not experience the strongest influence of Ekman or eddy currents which simplifies the analysis (see Chapter 3).

Part of this Chapter was published (Sommer et al., 2015; Appendix B). It included the period from August 2012 to August 2013 of SMOS mapped product. Here, in the present work, I have expanded the investigation until December 2014. This inclusion of more than one extra-year confirmed the main results and hypotheses made in the article.

This chapter first outlines the analysis of SSS and SST budgets from SMOS and OSTIA mapped products. Then I address the analysis of SSS and SST budgets from Mercator analysis. Afterwards I present the SSS budget for regions further south and further north of the SSS-max region to test how the budgets evolve in the presence of stronger SSS gradients and more intense ocean dynamics. An overall conclusion is then provided.

4.1 Mixed layer salinity and temperature budgets based on observations

Salinity budget. The terms in Equation (3.2.1) were estimated and averaged over the whole domain (Fig. 4.1*a*). As expected, there is a strong response of the surface ocean to the evaporation flux (blue curve) on the salinity change term (green curve). They have the same seasonal cycle with a strong increase in spring and summer and decrease in autumn and winter. The error bar on surface forcing term is large during

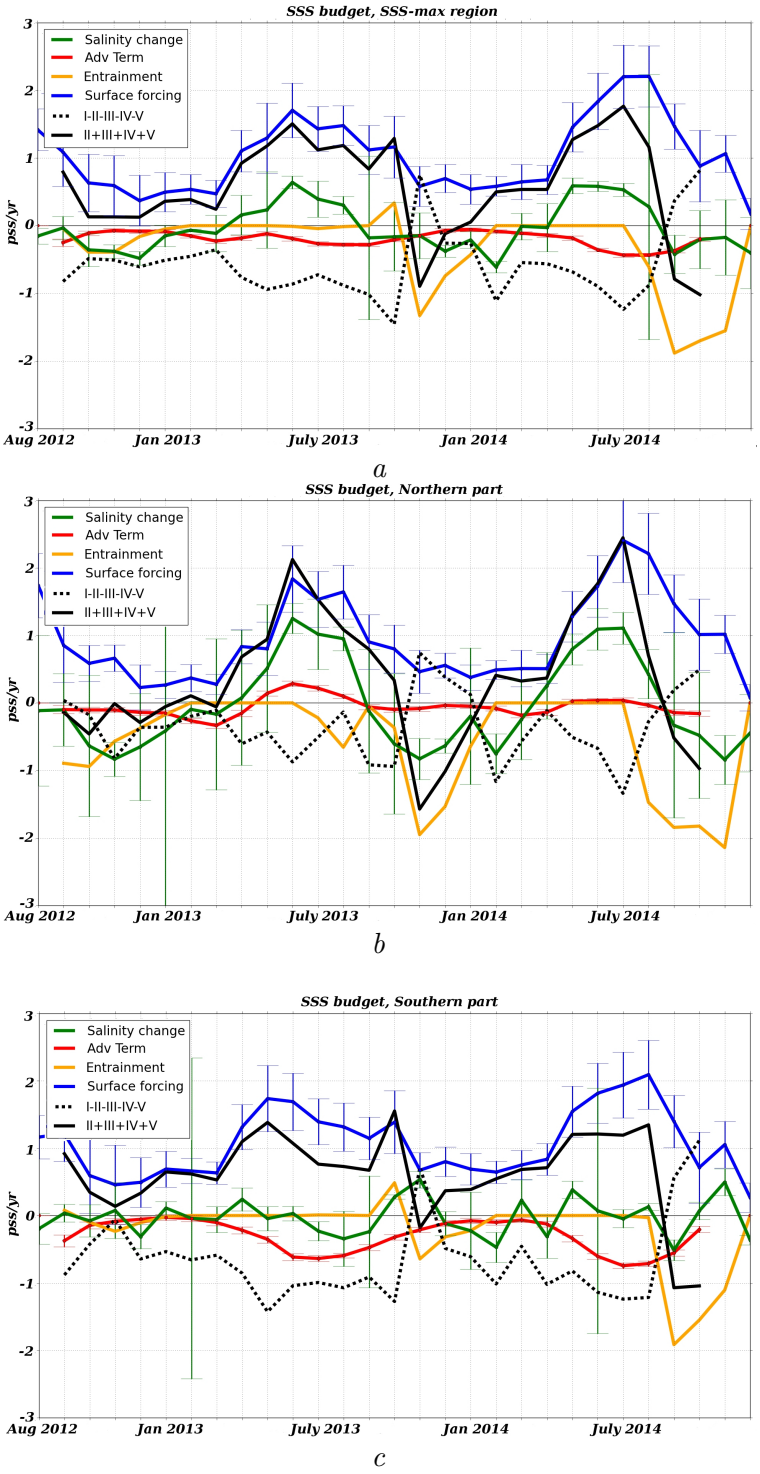

Figure 4.1: Components of salinity budget, residual (black dashed curve) and the sum of all estimated components of the right side of the equation (3.2.1) (black curve): a – SSS–max region $21^0N - 30^0N$ $50^0W - 26^0W$, b – northern part of SSS–max region $25.5^0N - 30^0N$ $50^0W - 26^0W$, c – southern part of SSS–max region $21^0N - 25.5^0N$ $50^0W - 26^0W$

autumn and early winter months for both year. This is due to local precipitation events (especially in 2012) and fast temperature changes, which result in evaporation changes that are not well reproduced (see Chapter 2). The freshwater flux is the dominant component in the salinity budget (1.04 ± 0.34 pss/yr, averaged over the period August 2012 – December 2014 and over $21^0 - 30^0$N/$50^0 - 26^0$W region) (Table 4.1). SSS does not show a strong tendency -0.015 ± 0.32 pss/yr over the period, similar to the results averaged over the 10-years (2004-2013) period and over the SPURS-1 region in Dong et al. (2015). Dong et al. (2015) find a 1-month lag between the salinity change and the seasonal cycles of the surface forcing term, which might be the result of slightly different region retained in their analysis (notice that Dong et al. (2015) domain is 5^0 further south than the region in Fig. 2.2 (red box)).

The entrainment term contributes only during autumn and winter months when MLD is deepening (Fig. 4.1*a* and Fig. 4.3*a*, orange curve). During the winter months entrainment plays a smaller role than in autumn as the deepening of the ML is weaker and MLS is closer to the salinity that is found deeper (S_{-entr}). In November 2012 and December 2013 when there is a small increase in the surface forcing term (evaporation increases) salinity continues to lower due to entrainment as one of the re-freshening mechanisms at that time. This example shows the small changes of components in MLS budget and its minor role compared to the residual term (black dashed curve) but it demonstrates an importance of the ocean dynamics in the salinity variability. In

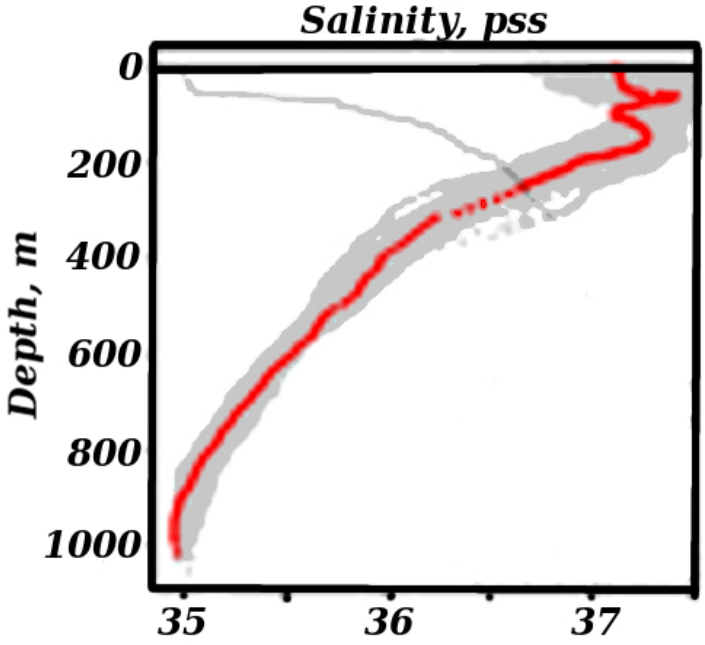

Figure 4.2: Salinity profile from OAO (Oceanographic Autonomous Observations, http://www.oao.obs-vlfr.fr), 19 October 2014 at ~21.2^0N 39.7^0W. This example demonstrates the presence of layer with high salinity bellow the MLD at first 100 m that comes from the North with the Shallow Meridional Overturning Circulation

December 2012, a month with a larger amount of precipitation and small entrainment, the salinity changes are predominantly governed by surface freshwater flux (Fig. 4.1*a*). The same behavior was found for March 2013. In October 2013 the entrainment is positive together with a small increase in surface forcing term: salty water from E-P–max region arrives in the SSS–max region and then as subducted water due to the vertical gradient of temperature appears again in the South (Fig. 4.2). Due to the difficulty in estimating the error on entrainment, only the error bars (standard error) on MLD are shown (Fig. 4.3*a*). In the salinity budget the mean effect of entrainment is equal to -0.56 pss/yr (Table 4.1).

For the whole domain the spatially averaged advection is negative throughout the period with a relatively small amplitude (mean average is -0.19 $\pm$ 0.02 pss/yr) (Fig. 4.1*a* and 4.4*a*). The turbulent and mean advections are both mostly negative with the stronger magnitude for the mean component, -0.17 $\pm$ 0.02 pss/yr and -0.02 $\pm$ 0.02 pss/yr, respectively. It shows a moderate seasonal cycle associated with a maximum freshening during summer and early autumn. Compared to results previously found (Büsecke et al., 2014; Gordon and Giulivi, 2014; Amores et al., 2015) the role of horizontal advection has to be more important. It is important to understand differences between these results and the ones presented in this PhD thesis work.

To better understand the effect of advection we separate the region into two boxes: $21^0 - 25.5^0$N $50^0 - 26^0$W and $25.5^0 - 30^0$N $50^0 - 26^0$W. The dividing latitude was chosen based on the seasonal means and seasonal variability maps of the first year (August 2012 – August 2013; Sommer et al., 2015) of the equation's terms (Fig. 4.5). During winter (December 2012 – February 2013), the SSS variability term (Fig. 4.5*a*) is characterized by a salinity decrease north of 25.5^0N, while a region with variable salinity changes (salinity can increase as well as decrease) is found in the South. For the SSS variability in the summer season (Fig. 4.5*b*) (June – August 2013) the latitude 25.5^0N separates a region of dominant increase in the North from a dominant decrease in the South. It means that during summer the strong increase of SSS takes place in the northern region, while the largest decrease takes place during winter. Autumn and spring (not presented) present similar features for these two regions. The advection variability maps (Fig. 4.5*c*, *d*) (std of time series at each grid point) show two different structures in the southern part. During late summer –autumn (Fig. 4.5*c*) (September – November 2012) some freshwater originating from the Amazon basin enters this region (also see Fig. 4.5*b*) and is mixed through the domain, inducing a strong variation of turbulent advection in the south–western part (the std of turbulent advection is up to 10 pss/yr in this region). During spring (Fig. 4.5*d*) (March – May 2013) mean advection plays a significant role in the salinity change with significant variability in time both in the northern as well as in the southern parts (std up to 3 pss/yr). It is especially stronger on the borders of the region than in its center. Surface water flux (Fig. 4.5*e*, *f*, *g*) shows strong variability (temporal std) in both regions during the autumn (Fig. 4.5*e*) (up to 3 pss/yr) and in the South during the spring (Fig. 4.5*f*) when evaporation largely dominates there (up to 1.5 pss/yr). The mean surface forcing (Fig. 4.5*g*) also exhibits different regimes on either side of 25.5^0N that identify the southern region as the region of maximum E-P field. Thus, 25.5^0N separates two regimes in the SSS budget variability in agreement with Dong et al. (2015).

In the southern part (Fig. 4.4*c*), during spring and summer the mean advection

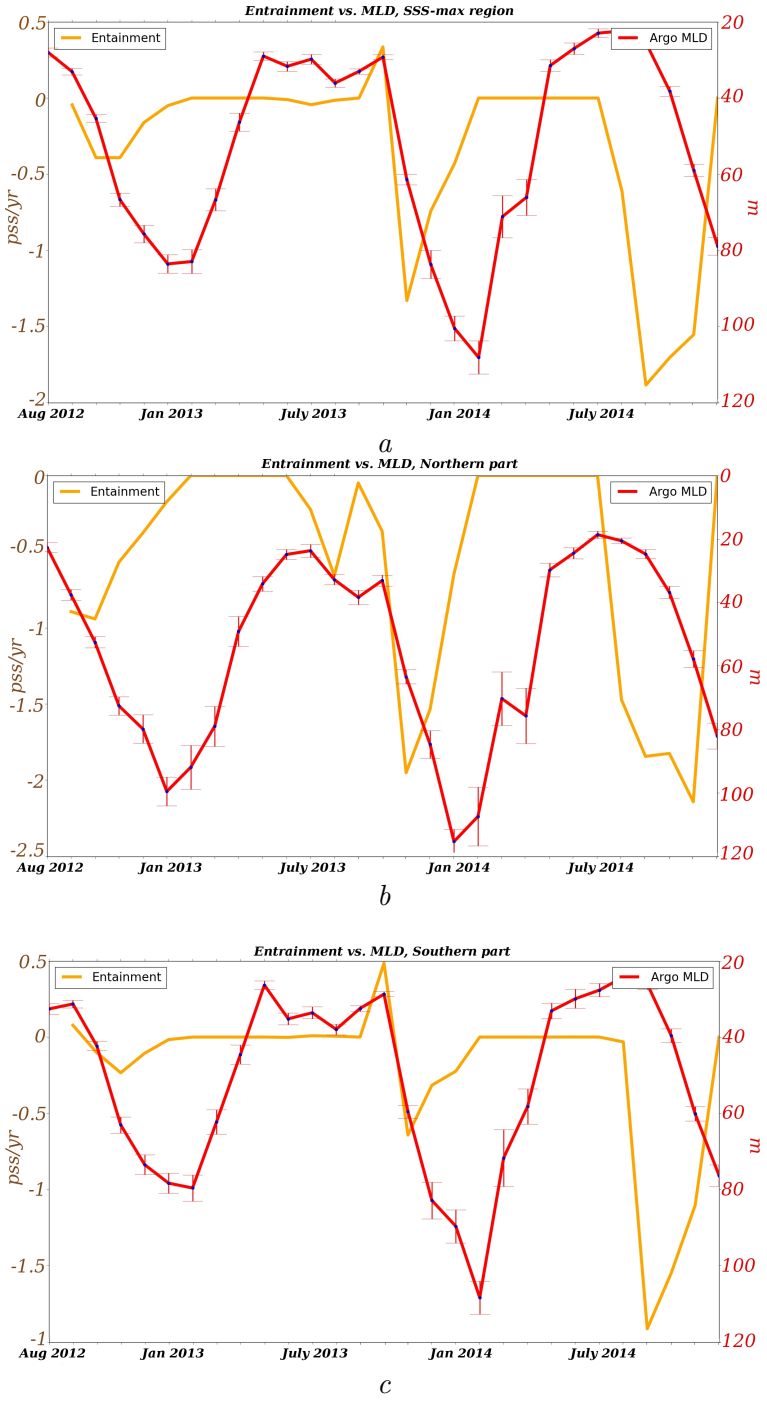

Figure 4.3: Entrainment component (orange curve) and MLD (red): a – SSS–max region 21^0N-30^0N 50^0W-26^0W, b – northern part of SSS–max region 25.5^0N-30^0N 50^0W-26^0W, c – southern part of SSS–max region $21^0N-25.5^0N$ 50^0W-26^0W

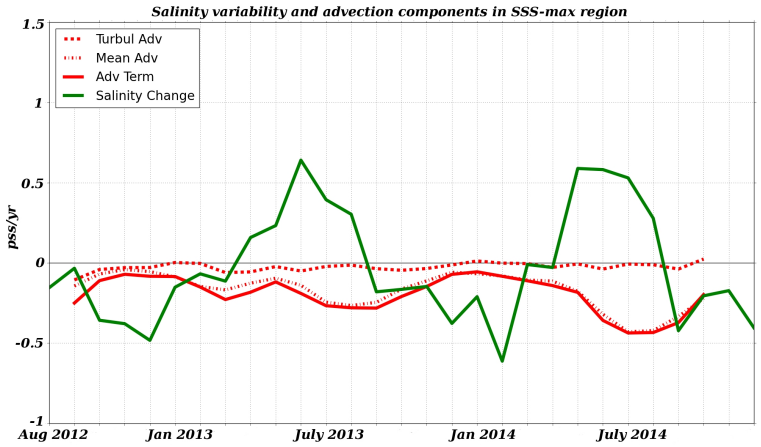

a

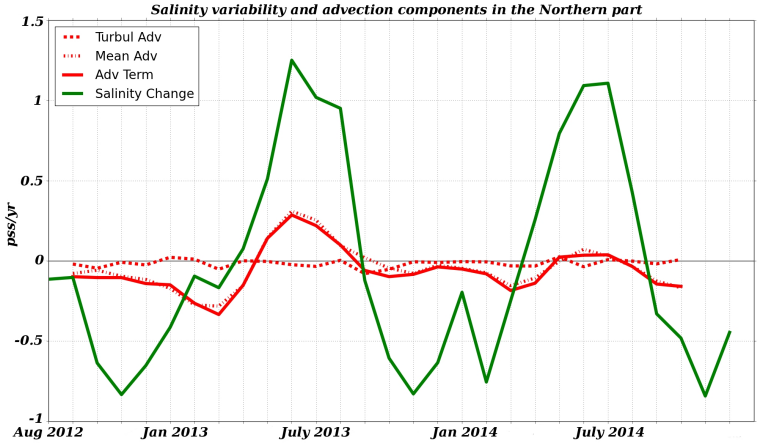

b

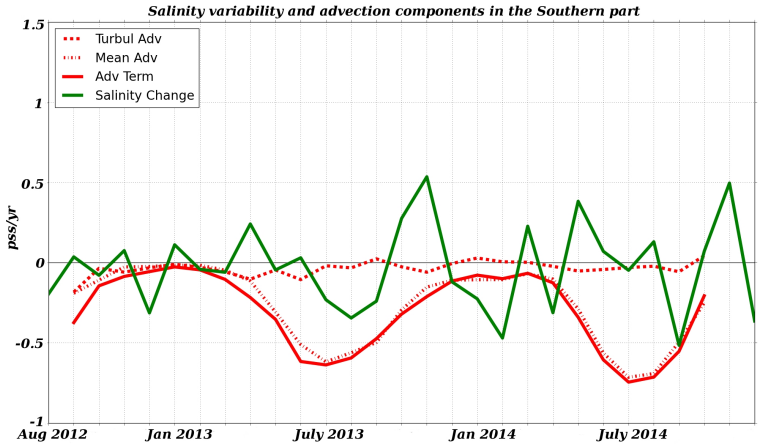

c

Figure 4.4: Salinity change (green curve) and advection components (red curves): a – SSS–max region $21^0N - 30^0N$ $50^0W - 26^0W$, b – northern part of SSS–max region $25.5^0N - 30^0N$ $50^0W - 26^0W$, c – southern part of SSS–max region $21^0N - 25.5^0N$ $50^0W - 26^0W$

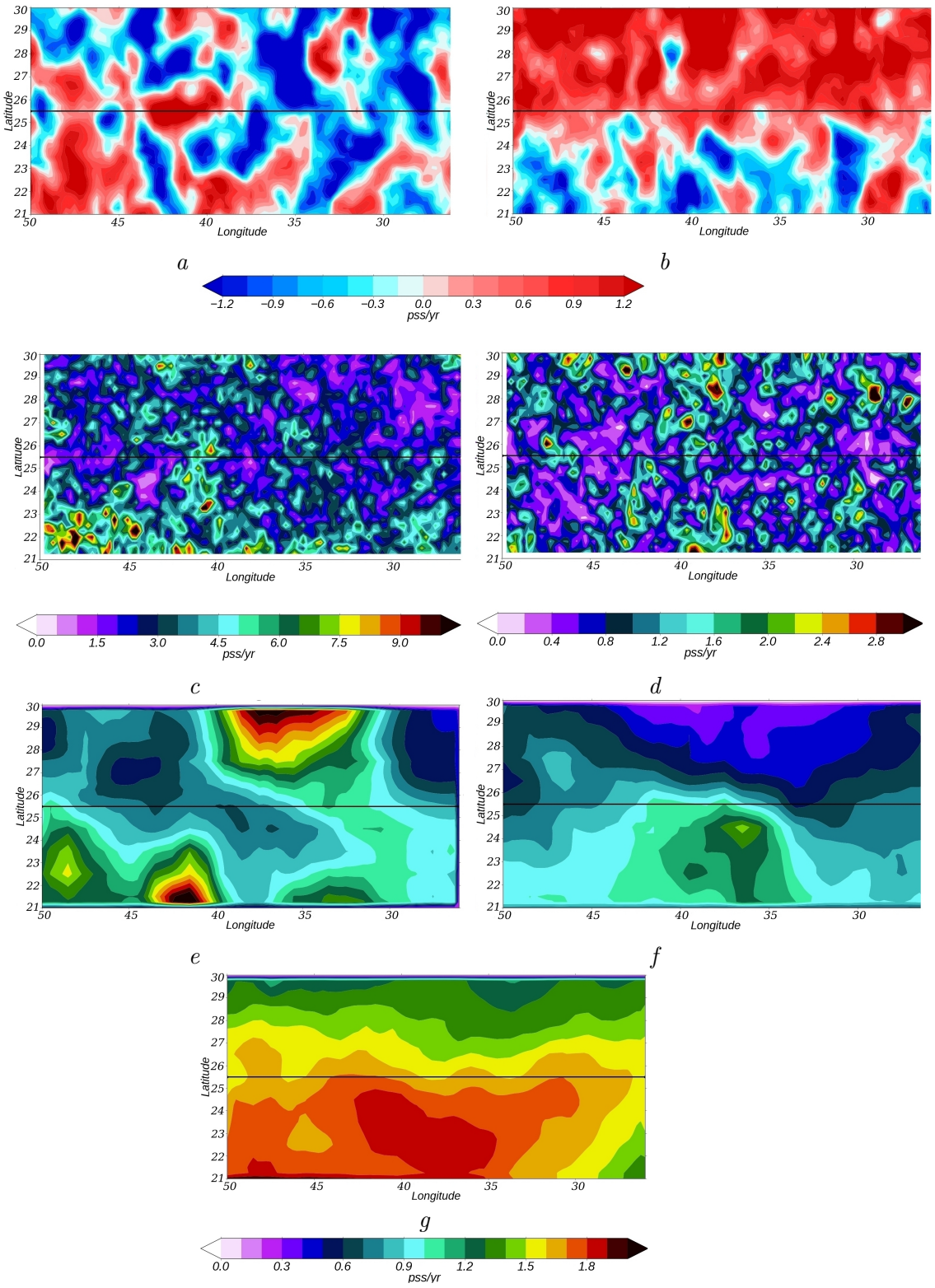

Figure 4.5: Estimation was done over period August 2012 – August 2013. *a* – SSS change in winter, *b* – SSS change in summer, *c* – turbulent advection standard deviation (std) in autumn, *d* – mean advection std in spring, *e* – surface forcing std in autumn, *f* – surface forcing std in spring, *g* – surface forcing mean in summer; Sommer et al. (2015) (Fig. 10)

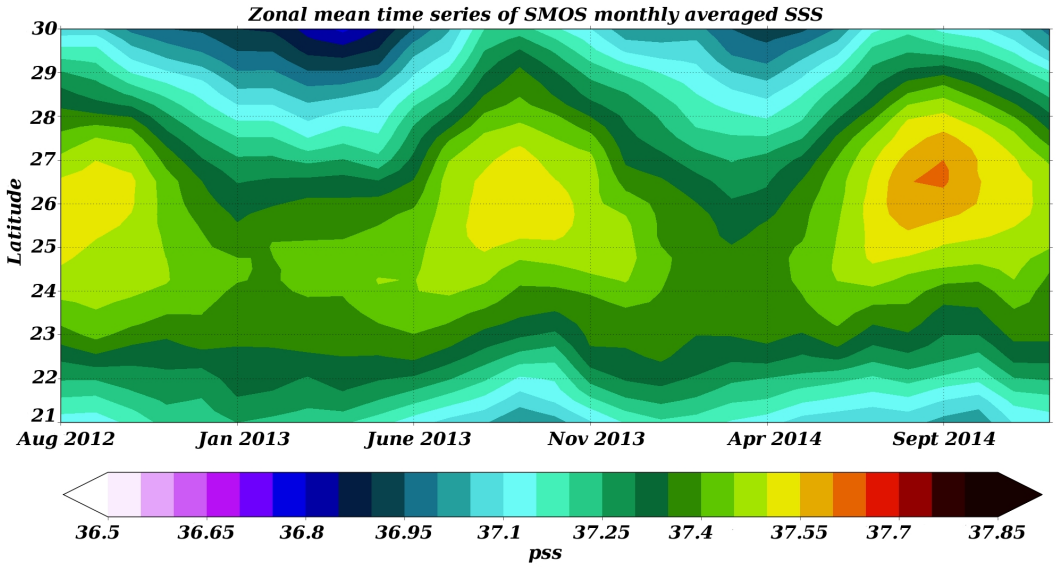

Figure 4.6: Zonal mean of SMOS SSS for the period August 2012 – December 2014 in SSS–max region $21^0N - 30^0N$ $50^0W - 26^0W$

brings freshwater from the tropical regions. In this season, the turbulent advection is small and varies around 0 pss/yr, whereas it has a significant contribution in autumn 2012 and spring 2013 when it participates in freshening along with mean advection. However, this is not reproduced in the second year. There is a strong contribution of mean component in this region, -0.27 ± 0.04 pss/yr compared to -0.035 ± 0.04 pss/yr for the turbulent advection. In the northern part (Fig. 4.4*b*), advection shows a strong seasonal cycle with maximum in summer when mean advection brings salty water from the South and contributes to the salinity increase. It is almost four times stronger in summer 2013 than in summer 2014.

To understand the differences between these two years we consider the zonal means of monthly averaged SSS (Fig. 4.6) and of geostrophic velocity variability (Fig. 4.7). Zonal mean of SSS (Fig. 4.6) shows the seasonal cycle with the movement of maximum salinity further north during the summer when the freshwater comes from the tropics. In the South the meridional gradient of salinity is sharper in summer 2013 than in summer 2014 (Fig. 4.7): the freshwater penetrates further north in 2013 that could be due to a stronger effect of eddy advection (Fig. 4.4*b*). The zonal component of AVISO geostrophic velocity variability (Fig. 4.7*a*) shows variability maxima on the order of 0.01 m^2/s^2 in summer 2013 and of 0.005 m^2/s^2 in 2014. The same tendency was found for the meridional component (Fig. 4.7*b*): the variability reaches 0.006 m^2/s^2 in 2013 and 0.003 m^2/s^2 in 2014. Also there is a maximum of variability in both velocity components during the autumn 2012 that explains the negative contribution of turbulent advection found in the South during this period (Fig. 4.4*b*). In the North the northward Ekman velocity is only a little stronger in 2014 (Fig. 4.8). Thus, the difference in mean advection is mostly explained by the fact that in the North the SSS maximum in 2014 was larger than in 2013. It seems that this is associated with somewhat larger positive $E-P$ fluxes in the northern region (as well as in the southern

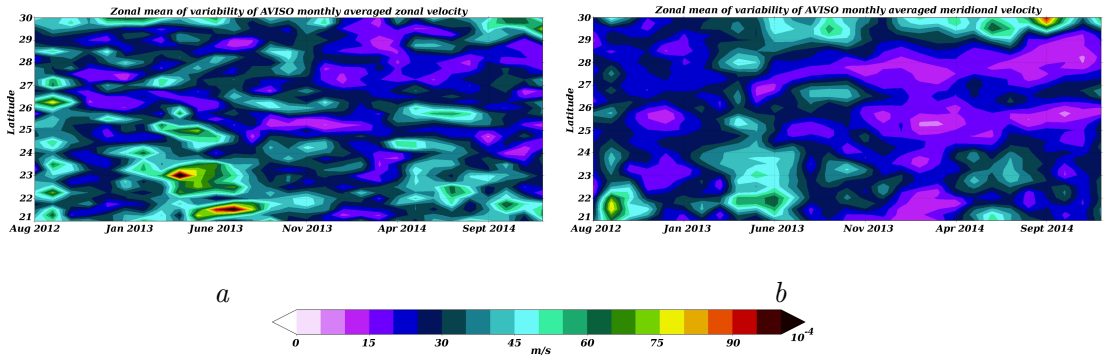

Figure 4.7: Zonal mean of AVISO geostrophic velocity variability (m^2/s^2) for the period August 2012 – December 2014 in SSS–max region $21^0N - 30^0N$ $50^0W - 26^0W$: a – zonal velocity component, b – meridional velocity component

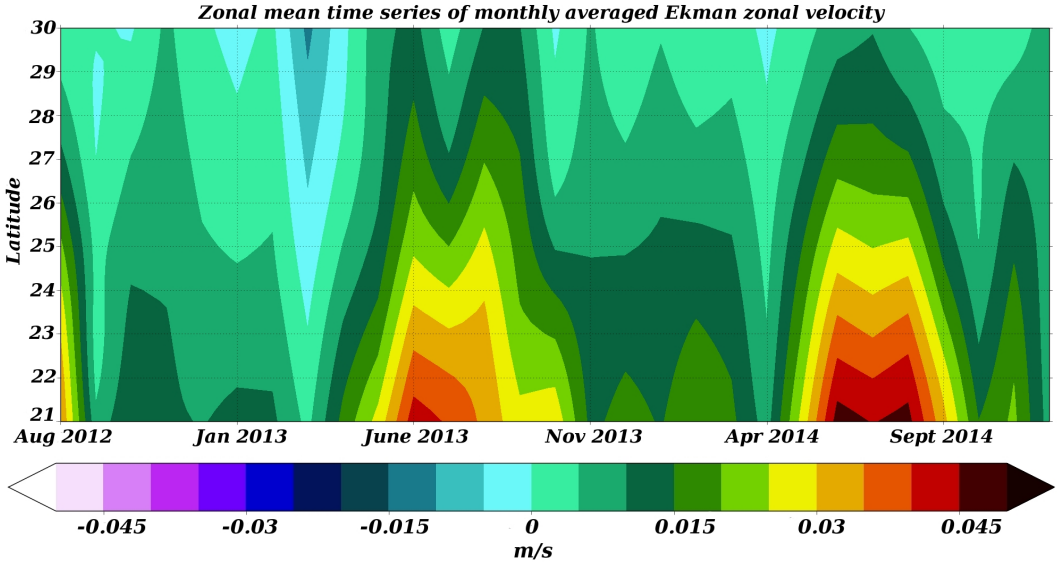

Figure 4.8: Zonal mean of meridional Ekman velocity for the period August 2012 – December 2014 in SSS–max region $21^0N - 30^0N$ $50^0W - 26^0W$

region) from December 2013 to July 2014 than a year earlier (Fig. 4.9). We also commented on larger Ekman advection in the southern part of the domain for the same period. This larger northward Ekman advection could also contribute to further displace the salinity maximum to the north in the late spring/summer 2014 than a year earlier. Thus, as the E-P–max region was extended further north in 2014 it could reduce the salinity gradient and, as consequence, the mean salinity advection term.

In general, the domain-averaged salinity presents large month-to-month changes throughout the year (intraseasonal variability) in the southern part (Fig. 4.1c) and a strong seasonal cycle in the northern part (it decreases in winter and increases in summer) (Fig. 4.1b). In the southern part, SSS decreases until October due to a small

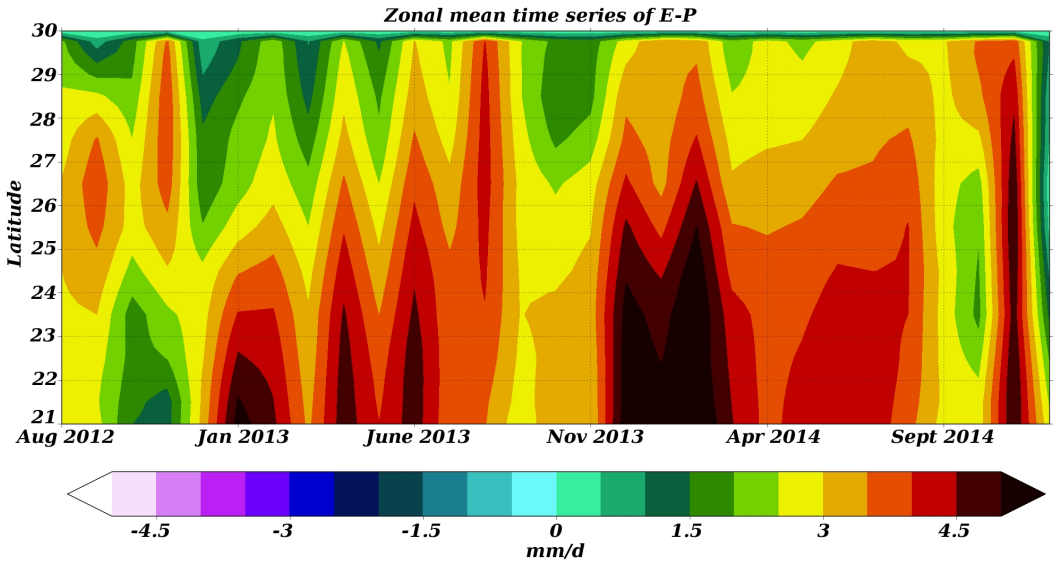

Figure 4.9: Zonal mean of E–P difference (OAFlux – GPCP) for the period August 2012 – December 2014 in SSS–max region $21^0N - 30^0N$ $50^0W - 26^0W$

surface forcing, the effect of the advection and the entrainment terms. Afterwards there is a salinity increase in November. At this time the surface flux continues to decrease and the advection term diminishes in absolute value, thus, reducing its freshening effect on the salinity. At that time even strong entrainment cannot significantly refresh the surface water. A similar situation was found in March 2014. In December 2012 the salinity again decreases while both freshwater flux and the effect of advection are small. In this month, it is likely that entrainment, that lags by one month from $\frac{\partial \langle S \rangle}{\partial t}$, has the largest influence on salinity. The same feature is found in October–November 2013. However, the large residual term (black dashed curve) for these month lets us think that either other processes (vertical processes, horizontal diffusion, filaments) get more important and they are not presented in the data used (due to the resolution), or the data used have a worse accuracy (especially, evaporation and precipitation), or the errors in the estimation of entrainment are more significant during this period. The increase of entrainment that we found before (Fig. 4.1*a*, Fig. 4.3*a*) appears in the southern part of the domain (Fig. 4.1*c*, Fig. 4.3*c*). It confirms our previous explanation that the increase in evaporation produces the increase in SSS that advances further south as subduction water (Shallow Meridional Overturning Circulation) (Fig. 4.2).

In the South during the summer months, the salinity change is controlled by advection associated with transport of fresher water from the tropics that partially counterbalances the gain from evaporation. In April 2013 and May 2014 (months when advection starts to contribute more) salinity increases according with an increase in evaporation, advection term participates in decrease of salinity only in the following months.

In the northern domain (Fig. 4.1*a*) during winter the salinity change is strongly influenced by entrainment of deeper water (Fig. 4.3*a*) and horizontal advection that contribute to a decrease of SSS (Fig. 4.4*a*). It is worth noting that the entrainment

in the North starts earlier (June–July) than in the South (August–September) due to colder (and fresher) water found under the sea surface in this region. The months of local minima of SSS in winter 2013 and 2014 correspond to the local maxima of the residual term.

In the North during summer, the strong increase in salinity depends on advection which brings salty water from the E-P maxima region (it is stronger in summer 2013 than in 2014, see explanation before), and on the freshwater flux which also increases. The residual terms are larger than the ones in winter time (max -1 pss/yr).

The sum of the terms on the right side of the Equation (3.2.1) (from here on, this excludes R) (Fig. 4.1*a*, black curve) is very close to the surface forcing term and its difference with $\frac{\partial \langle S \rangle}{\partial t}$ results in a large residual term R, ∼-0.3 pss/yr (Fig. 4.1*a*, black dashed curve). It presents 47% of the average modulus of $\frac{\partial \langle S \rangle}{\partial t}$ which varies in the range ±0.63 pss/yr (see Table 4.1). The advection can be the most important component for the salinity budget in this region and can be the main source of errors due to the uncertainties in salinity field and underestimation of velocity field (compared to Mercator and drifters) that was discussed in Chapter 2. In some studies the mismatch (residual) is parameterized by horizontal diffusion terms, as in Dong et al. (2015) when such a term contributes to the MLS changes with the averaged magnitude of -0.28 ± 0.01 pss/yr thus comparable with our residual term (-0.3 pss/yr). The effect of this term is mostly represented by the turbulent advection in the present work that is small. Moreover it is thus difficult to blame a choice of a too shallow mixed layer in the summer months, as it would contribute to a negative residual in the SSS budget.

Residual R as a function of total averaged values of MLS components presented in Table 4.1 is shown on Fig. 3.2. Results of this section are emphasized by red ellipse "Observations" that corresponds to a residual -0.3 pss/yr and to the first bars of the colorbars.

Heat budget. The estimation of the temperature budget based on Equation (3.2.2) in the subtropical gyre of the North Atlantic (Fig. 4.10) indicates a near-balance between the terms retained, i.e. the error bar range of the two sides of the equation overlap (black solid (the sum of all elements in the right part of the equation (3.2.2)) and green (temperature change) curves). The different components of the temperature budget present the same variability irrespective of the domain (total region (Fig. 4.10*a*), northern (*b*) and southern (*c*) parts). SST (green curve) decreases in late autumn and winter and increases in spring and summer. The term of surface heat flux (blue curve) shows comparable variability in the two regions being largely responsible for the temperature change. The heat flux is the dominant component in the temperature budget (3.36 ± 1.4^0C/yr). SST as SSS shows small tendency over the period, -1.27^0C/yr (Table 4.1). The entrainment term (orange curve) is large during late autumn and winter and contributes to lower SST. As for SSS the entrainment of temperature starts earlier in the northern part of the domain (Fig. 4.10*b*) (June–July) than in the southern part (Fig. 4.10*c*) (August–September). In the northern part, both for SSS and SST budgets, there is an increase of entrainment in September 2013 after a decrease in August. Entrainment in September is very small due to the competition of warm and salty water from the South and cold and fresh water from the North, when the autumn

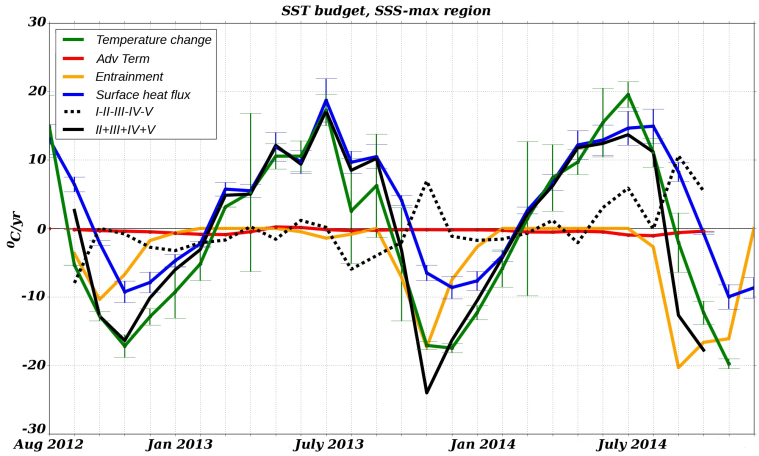

a

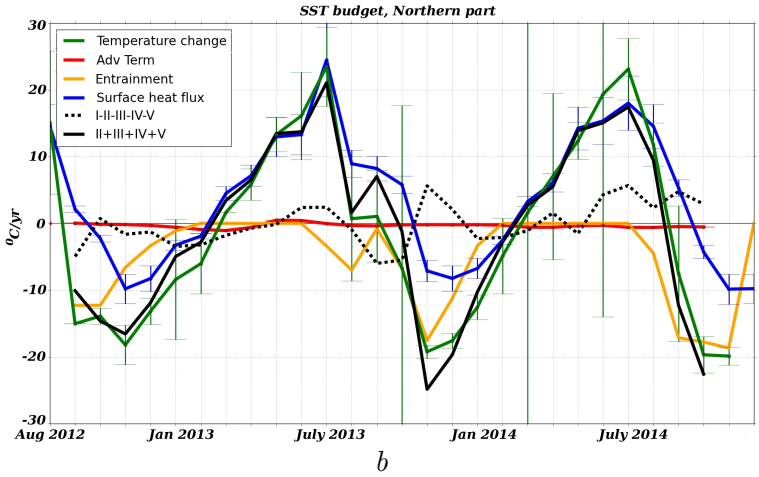

b

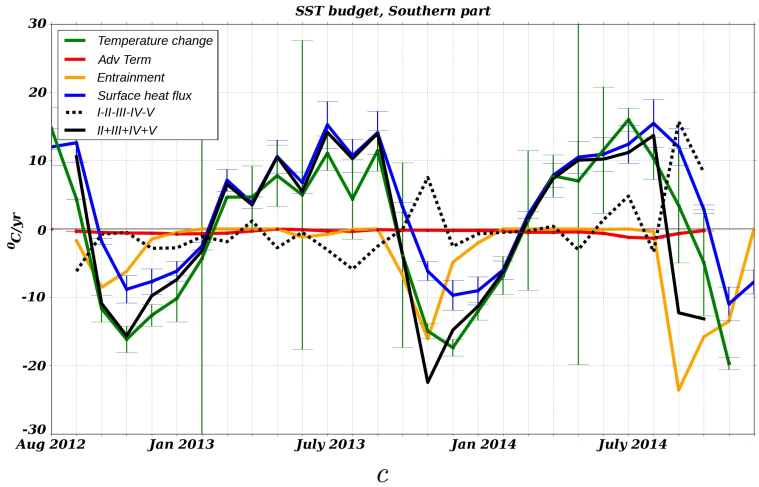

c

Figure 4.10: Components of temperature budget, residual (black dashed curve) and the sum of all estimated components of the right side of the equation (3.2.2) (black curve): *a* – SSS–max region $21^0N - 30^0N$ $50^0W - 26^0W$, *b* – northern part of SSS–max region $25.5^0N - 30^0N$ $50^0W - 26^0W$, *c* – southern part of SSS–max region $21^0N - 25.5^0N$ $50^0W - 26^0W$

Table 4.1: Time averaged mean of the components in Equations (3.2.1) and (3.2.2) in the SSS–max region and its northern and southern parts

	SSS var	Turb adv	Mean adv	Entr	Surf forc	Hor Diff	Res
SSS-max							
pss/yr	-0.015 ± 0.32	-0.026 ± 0.2	-0.17 ± 0.2	-0.56	1.04 ± 0.34	–	-0.3 ± 0.35
North							
pss/yr	-0.017 ± 0.66	-0.016 ± 0.2	-0.044 ± 0.2	-0.97	0.95 ± 0.34	–	0.063 ± 0.35
South							
pss/yr	-0.013 ± 0.36	-0.03 ± 0.2	-0.27 ± 0.2	-0.31	1.09 ± 0.36	–	-0.47 ± 0.36
	SST var	Turb adv	Mean adv	Entr	Surf forc	Hor Diff	Res
SSS-max							
^{0}C/yr	-1.27 ± 3.33	-0.06 ± 0.03	-0.34 ± 0.03	-7.27	3.37 ± 1.4	–	3.04 ± 3.37
North							
^{0}C/yr	-1.67 ± 7.2	-0.07 ± 0.04	-0.25 ± 0.04	-8.98	3.7 ± 1.9	–	3.91 ± 7.2
South							
^{0}C/yr	-0.88 ± 6.32	-0.04 ± 0.03	-0.4 ± 0.03	-6.1	3.3 ± 1.9	–	2.36 ± 6.3

season has started, and to the fact that the averaged over domain MLD was used. In the temperature budget it is the major component that compensates the effect of the heat flux (-7.27^0C/yr).

The advection term has a small effect on SST variability. Compared to the SST tendency term and heat flux the advection is rather small (-0.4 $\pm$ 0.02^{0}C/yr). It presents a small seasonal cycle with the maximum in summer. It is negative throughout most of the period, bringing colder water mostly from the North, whereas it is positive during spring and summer, the period of large warming. It is the case for the full region as well as for the both part of it, the northern and southern parts.

The net residual terms are relatively small with a total positive average, 3.04^{0}C/yr (15% of the average magnitude of $\frac{\partial \langle T \rangle}{\partial t}$ which varies in the range $\pm 20^0$C/yr) (see Table 4.1). It is probably due to the strongest effect of the heat flux on the temperature change that simplifies the estimation of temperature budget, while the salinity variability strongly depends on the ocean dynamics.

Small scale processes such as are found near filaments or fronts, could be a source of asymmetry between the SST and SSS budgets. Indeed, in the southern part of the domain, Kolodziejczyk et al. (2015c) showed that SSS spatial variability dominates the surface density gradients. This was also witnessed in summer during the Strasse cruise

(Reverdin et al., 2015), and in early spring during the Midas cruise (Büsecke et al., 2014). Dynamical processes that induce mixed layer restratification would thus contribute to an average SSS decrease, but with little notable effect on SST (Shcherbina et al., 2015). But even for SST we found that the residual term is higher during the entrainment months. The residual is higher in the North (3.91^0C/yr) where the contribution of entrainment is larger (-8.98^0C/yr) (see Table 4.1). In addition, vertical mixing with salt fingering at the lower boundary of the mixed layer would also contribute to a larger SSS negative term compared with SST, but this would happen preferentially when there is a large salinity vertical stratification compared to temperature, and thus probably not in the summer months.

Using other data sets (for precipitation, evaporation, MLD, etc.) to estimate the salinity budget could help better understand the mechanism of formation of the salinity maximum of the subtropical North Atlantic and its seasonal variability. Further testing other ways to estimate entrainment or a relevant mixed layer depth would also improve the reliability of these results. Thus, in the next section I will also estimate the SSS and SST budget based on Mercator PSY2V4R2-R4 analysis data to improve the entrainment estimation method, to validate the model data on the mesoscale (as Mercator has a higher spatial resolution ∼10 km than SMOS ∼75 km) and to estimate subscale horizontal diffusion.

4.2 Mixed layer salinity and temperature budgets based on Mercator analysis

Salinity budget. As in the previous section, the terms in equation (3.2.3) were estimated and averaged over the domain $21^0 - 30^0$N/$50^0 - 26^0$W during the period August 2012 – December 2014 (Fig. 4.11). As input data we used Mercator PSY2V4R2-R4 analysis data of sea surface height, as well as salinity, temperature and ocean currents at different depth. To estimate the surface forcing term GPCP satellite precipitation and OAFlux analysis evaporation were chosen as will be explained later (it is important to realize that these are not the ones used to force the Mercator analysis).

In general, Mercator shows the same variability of budget components as in the case of SMOS (previous section) (Fig. 4.11*a*). MLS (green curve) has a seasonal cycle with the minimum in winter and maximum in summer (-0.015 ± 0.036 pss/yr, Table 4.3). The freshwater flux at the surface (blue curve) has a strong effect on SSS and shows the same seasonal cycle as the salinity variability (1.05 ± 0.4 pss/yr). Error bars are large (∼0.8 pss/yr) during the spring and summer that indicates the problem of evaporation data used. There is also an increase in error values (∼0.5 pss/yr) during the autumn–winter 2012 when the rain front was located in the region.

Using the Mercator analysis, GPCP satellite for precipitation and OAFlux analysis for evaporation the residual term is extremely small (-0.05 ± 0.036 pss/yr, Table 4.3) compared to the one when SMOS SSS was used. In previous section GPCP precipitation and ERA-Interim evaporation were used. The test with these data and Mercator gave a much stronger residual -0.43 ± 0.4 pss/yr (66%), even larger than the one found for SMOS. The opposite test (GPCP and OAFlux for SMOS) showed that the residual

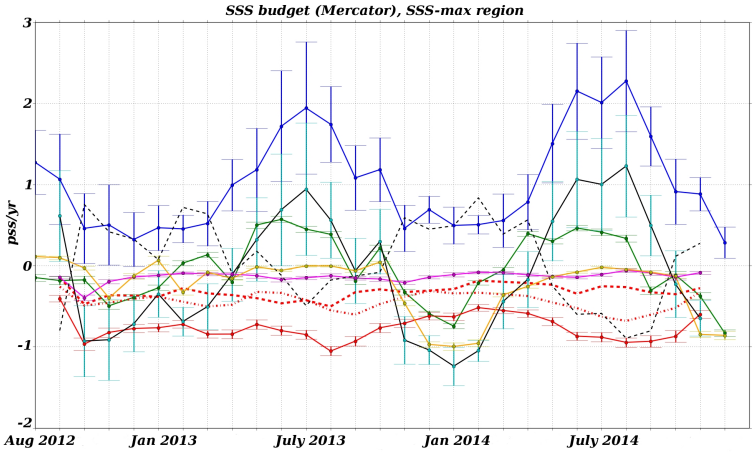

a

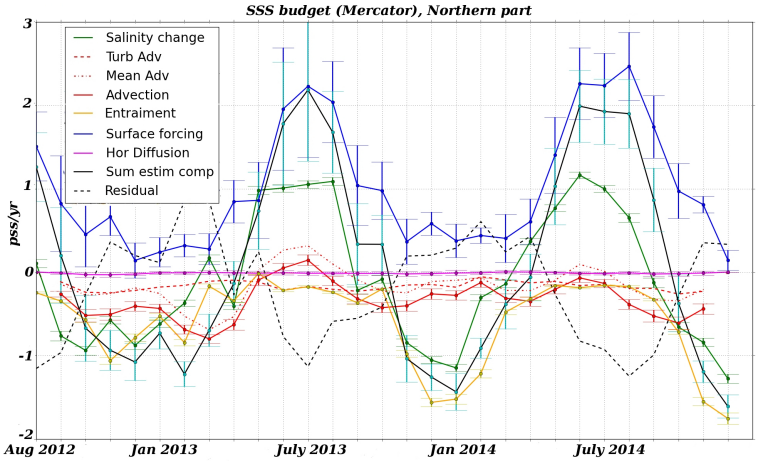

b

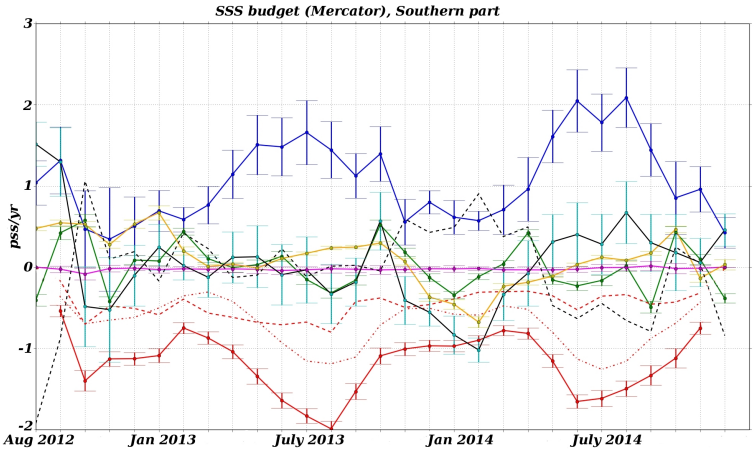

c

Figure 4.11: Components of salinity budget, residual (black dashed curve) and the sum of all estimated components of the right side of the equation (3.2.3) (black curve) based on Mercator analysis: a – SSS–max region $21^0N - 30^0N$ $50^0W - 26^0W$, b – northern part of SSS–max region $25.5^0N - 30^0N$ $50^0W - 26^0W$, c – southern part of SSS–max region $21^0N - 25.5^0N$ $50^0W - 26^0W$

Table 4.2: The effect of precipitation and evaporation data on residual in SSS budget

SSS field var	Precip/Evap	Residual
SMOS	GPCP/ERA-Int	-0.3 pss/yr
	GPCP/OAFlux	-0.2 pss/yr
Mercator	GPCP/OAFlux	-0.05 pss/yr
	GPCP/ERA-Int	-0.43 pss/yr
	ERA-Int/OAFlux	0.15 pss/yr
	ERA-Int/ERA-Int	-0.22 pss/yr

-0.3 pss/yr found previously reduced to -0.2 pss/yr (32%). Thus, the uncertainties from precipitation and evaporation data can be significant and responsible for more than 50% of errors in MLS budget as in the case of Mercator.

As the data for evaporation and precipitation were the only data not used in the numerical analysis (note that one could also consider the "data assimilation" process as forcing data), one can expect a large influence of this choice on the residual of the budget. Thus, four different combinations of evaporation and precipitation data and their effect on the salinity budget were tested (Fig. 4.12). Combination of "GPCP precipitation and ERA-Interim evaporation" (red curve) results in the largest residual during the summer, whereas the combination "ERA-Interim precipitation and OAFlux evaporation" (orange curve) shows the largest residual during the winter. It is probably due

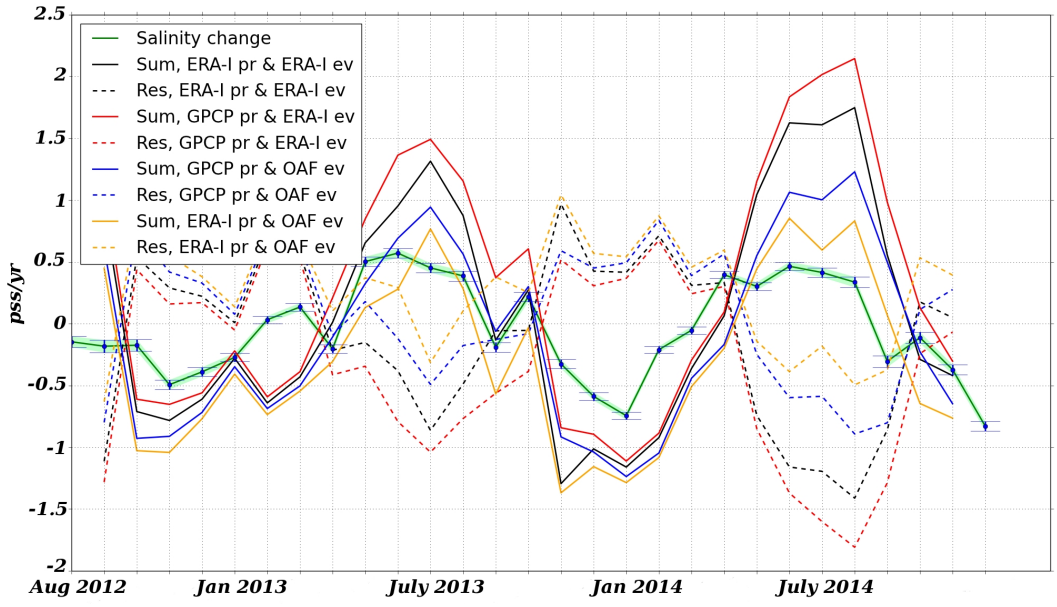

Figure 4.12: Salinity variability (green) and residual (dashed curves) and sum of SSS budget components (solid curves) based on Mercator analysis from equation (3.2.3) for different combinations of evaporation and precipitation data sets

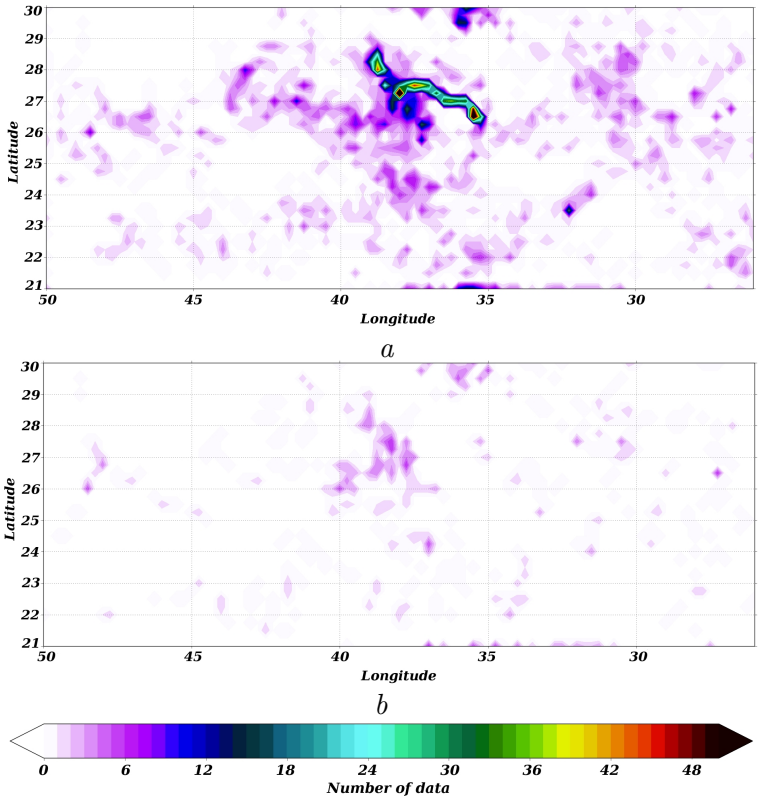

Figure 4.13: Distribution of Argo profilers used in this thesis work on $0.25^0 \times 0.25^0$ grid for the total period August 2012 – December 2014 (a) and for the winter season (b)

to the overestimation of both precipitation and evaporation by ERA-Interim reanalysis (that can be overemphasized when combining with other data sets with lower values, such as GPCP and OAFlux). The combinations "ERA-interim precipitation and evaporation" (black curve) and "GPCP precipitation and OAFlux evaporation" (blue curve) lie close to each other during the winter with a small preference for the first one. However, during the summer months ERA-Interim strongly overestimate the freshwater flux (residual ∼-1.5 pss/yr compared to ∼-0.9 pss/yr for GPCP and OAFlux). Thus, GPCP precipitation and OAFlux evaporation were chosen as the less erroneous combination. Table 4.2 and Fig. 3.2 (blue rounds) summarizes this analysis.

It is worth to note that I did not test the atmospheric forcing data used in Mercator data assimilation procedure. The atmospheric fields in Mercator was taken from ECMWF Integrated Forecast System (Lellouche et al., 2013). I made a request to Mercator to get the assimilated data of freshwater and heat fluxes. At the time of writing the thesis I was waiting for a response from Mercator Ocean team.

Entrainment (Fig. 4.11a, orange curve), as previously, plays a major role during the winter. Its effect is stronger in winter 2013–2014 than in winter 2012–2013 in agreement with our previous results (Fig. 4.1a). There is not anymore the strong positive entrainment in October 2013. The first difference between the two estima-

tion is that in the case of Mercator analysis MLD was estimated in each grid point. And, thus, in the average over the domain the strong negative entrainment in the North (-0.56 ± 0.03 pss/yr) (Fig. 4.11*b*) is balanced by positive entrainment in the South (0.1 ± 0.03 pss/yr) (Fig. 4.11*c*) that could be missed by Argo profilers in previous section. It can result from a nonhomogeneous distribution of Argo profilers, and the concentration of instruments was far from the region where the subducted water enters (Fig. 4.13*a*). In particular, it is significant during winter when most of the profilers have been in the northern part of the domain (Fig. 4.13*b*). The second difference is the use of horizontal gradient of MLD in our estimation. Its contribution diminishes the entrainment values for MLS budget by ∼35% (Fig. 4.14*a*, orange solid curve for entrainment with horizontal gradient of MLD and orange dashed curve – without). It diminishes a little the residual term in MLS budget (black dashed curve) during the

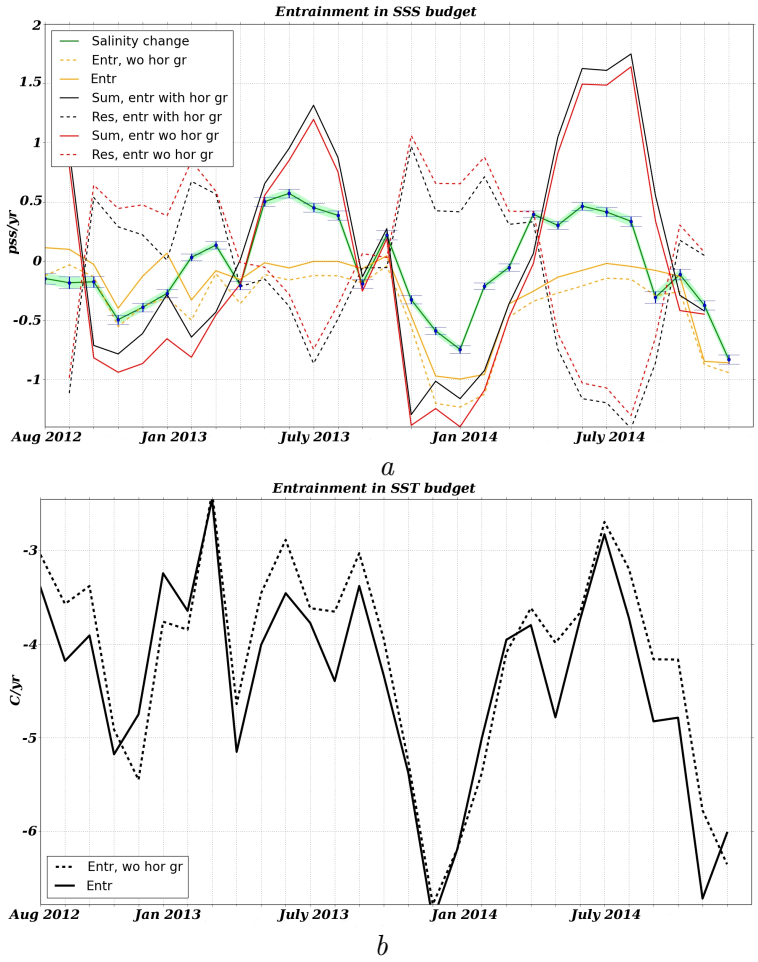

Figure 4.14: Entrainment component for SSS budget (*a*, orange curves) and SST budget (*b*, black curves) with (solid curves) and without (dashed curves) the horizontal gradient of MLD; influence of the horizontal gradient of MLD on residual (dashed curves) and sum of SSS budget components (solid curves) from equation (3.2.3) (*a*, red and black curves)

winter (by ∼35%) and insignificantly increases it in summer (by ∼12%). It is summirezed on Fig. 4.15, an extraction from Fig. 3.2. For MLT budget, as was expected in previous section, the introduction of the horizontal gradient of MLD does not change much the effect of entrainment (Fig. 4.14*b*). Mostly it increases the entrainment by 1–15%.

I also compared the entrainment terms estimated with the entrained salinity S_{-entr} based on entrainment velocity as was proposed in Chapter 3 with the entrainment terms estimated with S_{-entr} averaged over 10 or 20 m below the MLD (Fig.4.15). The last methods are often used in literature. The comparison shows that in case of observations and Mercator analysis the choice of 10 m provides results close to the previously found in the present work but with smaller entrainment terms and a little larger residuals: -0.48 pss/yr and -0.38 pss/yr, respectively for observations, and -0.2 pss/yr and -0.08 pss/yr for Mercator analysis. The choice of 20 m results in larger entrainment and small positive residual: -0.9 pss/yr and 0.1 pss/yr for observations and -0.3 pss/yr and 0.02 pss/yr for Mercator analysis.

Horizontal diffusion (Fig. 4.11*a*, purple curve) has a small negative effect on the salinity variability, -0.02 ± 0.025 pss/yr. The variability of horizontal eddy diffusion is weak throughout the period.

The most interesting difference is presented by the advection term (Fig. 4.11*a*, red curve). The advection is almost twice larger than the one from SMOS and AVISO. It has the same small seasonal cycle with the freshening effect that plays a role during the late spring and summer. It varies in the range -0.6 – -1 pss/yr and has an average value equals to -0.76 ± 0.05 pss/yr. The mean and turbulent advection have almost the same magnitude with a stronger contribution from the mean advection, -0.44 ± 0.05 pss/yr and -0.32 ± 0.05 pss/yr, respectively. Mean advection contributes mostly in freshening during the summer bringing the fresh water from the tropics. Turbulent advection does not vary significantly through the year.

As in previous section, the region was separated into two parts by the latitude band 25.5^0 N (Fig. 4.11*b*, *c*). The influence of MLS budget terms remains mostly the same, as was found in the earlier analysis of the data. Salinity presents a seasonal cycle in the northern part (Fig. 4.11*b*) whereas it varies a lot at higher frequencies in the southern part (Fig. 4.11*c*). In the North the SSS seasonal cycle is controlled mostly by the surface forcing term while in the South the variability of salinity is the complex interrelation between the oceanic and surface processes.

The horizontal diffusion is small in both cases and seems to be constant through the period. It is a little larger in the South (Fig. 4.11*c*) due to the stronger contribution of eddy activity: -0.012 ± 0.02 pss/yr in the North and -0.02 ± 0.04 pss/yr in the South.

The entrainment participates in a decrease of salinity in the North (Fig. 4.11*a*). It is negative for the whole period with a minimum in winter when more cold and fresh water comes from the north. This is contrary to its behavior in the South (Fig. 4.11*b*). As mentioned before, here the entrainment is mostly positive which results from the subduction of salty water from further north-east and participates in an increase of MLS.

The results for advection qualitatively confirm the conclusions in the previous section: there are two regimes in the North and the South of the domain. In the North turbulent advection is small while the mean advection contributes in summer to in-

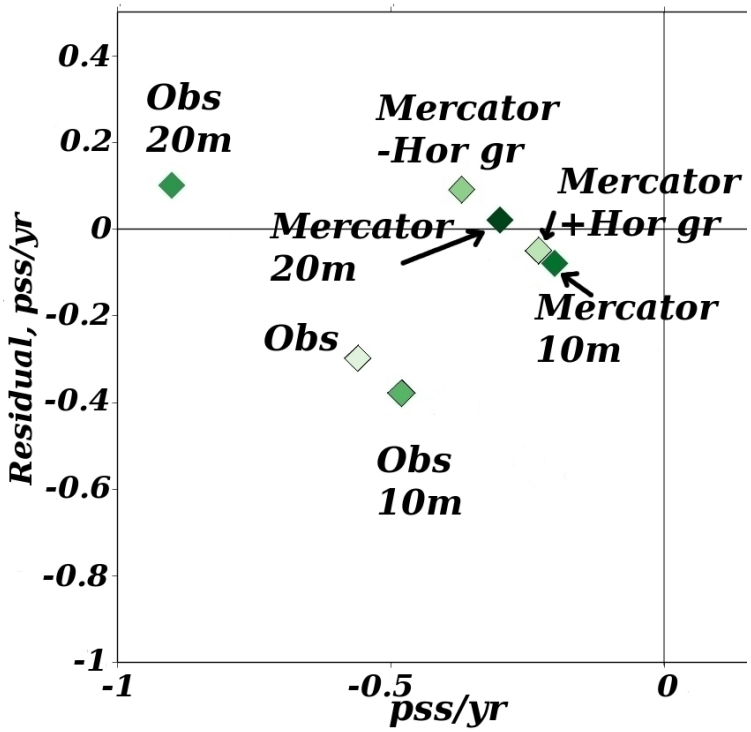

Figure 4.15: Sensitivity to the method of estimation of entrainment term. This figure presents the effect of horizontal gradient of MLD on the entrainment term and residual R in MLS budget: two rhombus labeled "Mercator +Hor gr" and "Mercator -Hor gr". The entrainmlent terms from standard cases (red ellipses on Fig. 3.2) (the depth below MLD over which the entrained salinity averaged was estimated based on entrainment velocity) are compared with the entrainment terms estimated with the entrained salinity averaged over 10 or 20 m below MLD (details in Chapter 3 and 4)

crease the salinity (Fig. 4.11*b*). This increase is higher in 2013 than in 2014, as was also found for SMOS and AVISO. The influence of turbulent advection is significant in the South (Fig. 4.11*c*). It is almost five times stronger than was found in the case of observations and shows a small seasonal cycle with a weak increase in absolute value during summer (contributing to freshening). The mean advection strongly influences the decrease of salinity in summer bringing fresh water from the tropics. Thus, in the North the advection and entrainment terms contribute to balance the effect of surface forcing, while in the South the advection is the largest term that balances the joint influence of surface forcing and entrainment. These results are consistent with the ones from Dong et al. (2015): the advection is responsible for more than a half of the balance after the water loss. Furthermore, the turbulent (eddy) advection plays an important role that is increasing further south as was found by Büsecke et al. (2014) and Gordon and Giulivi (2014).

The residuals are smaller compared with results previously found in Section 4.1. Now the residual for MLS budget is -0.05 $\pm$ 0.036 pss/yr that is $\sim$9% of the averaged

magnitude of $\frac{\partial \langle S \rangle}{\partial t}$ and varies, as in SMOS, in the range ±0.65 pss/yr (see Table 4.3). As shown previously, this difference originates from the estimation of freshwater flux, entrainment and horizontal advection terms. The horizontal advection can be the more important reason for the large residual term in MLS budget using SMOS SSS. This can be due to an underestimation of ocean velocity (AVISO geostrophic, ERA-Interim wind for Ekman current) as well as to a too weak eddy activity that is better represented in Mercator analysis or it could be due to the inability of SMOS to well reproduce the small features of salinity (filaments and fronts; due to the smaller spatial resolution of SMOS compared with Mercator) at the sea surface in the SSS–max region.

To test the capacity of SMOS in the next section I will discuss the results for regions further north and south from the SSS–max region. These regions include the strong salinity gradient that can allow to verify how SMOS works in the presence of strong salinity horizontal gradient and eddy activity.

The results of this section are summarized on Fig. 3.2 (red ellipse labeled "Mercator").

Heat budget. We estimated the temperature budget based on Equation (3.2.4) and Mercator analysis (Fig. 4.16). The MLT budget is almost closed: the sum of all elements on the right part of the equation (3.2.4) (Fig. 4.16*a*, black solid curve) and temperature change (green curve) are very close to each other. For the MLT budget the residual is 5.4% (-1.08 ± 2.23^{0}C/yr) of the averaged magnitude of $\frac{\partial \langle T \rangle}{\partial t}$ that varies in the range ±20^{0}C/yr (see Table 4.3). The largest difference was found for the winter months for the SSS–max region as well as for its northern and southern parts (Fig. 4.16*b* and *c*, respectively). As before (Section 4.1.) the different components of the temperature budget have the same pattern irrespective of the domain (Fig. 4.16*a*, *b*, *c*). SST (green curve) decreases in late autumn and winter and increases in spring and summer. The surface heat flux (blue curve) is the dominant component of the budget and strongly responsible for the temperature change, 4.23 ± 2.23^{0}C/yr. The entrainment term (orange curve) is large during late autumn and winter and contributes to lower SST. The entrainment of temperature is negative (-3.5 ± 0.09^{0}C/yr) and starts earlier in the northern part of the domain (Fig. 4.16*b*)) (July–August) than in the southern (Fig. 4.16*c*)) (September–October). Thus, results are similar to what was found for OSTIA analysis. However, as in the MLS budget there is no contribution of positive entrainment of salty and warm water in September 2013. It is mostly due to the dominant effect of the deepening of MLD during this period that can be observed when averaging Argo profiles.

The advection term again has a small effect on SST variability. It is negative through the period with a small seasonal cycle, -0.7 ± 0.07^{0}C/yr. It tends to compensate the heating during the summer (Fig. 4.16*a*, *b*, *c*).

4.3 Spatial dependency of the mixed layer salinity and temperature budgets

In this section, I present the MLS budget further north and further south from the SSS–max region based on the Mercator analysis and SMOS satellite data. This

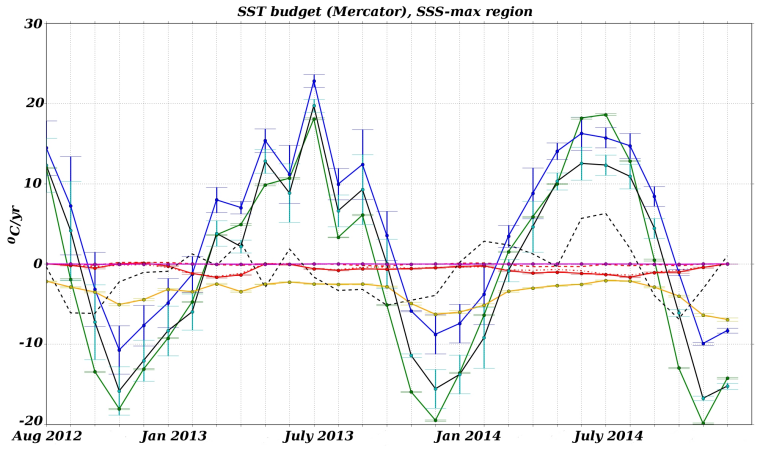

a

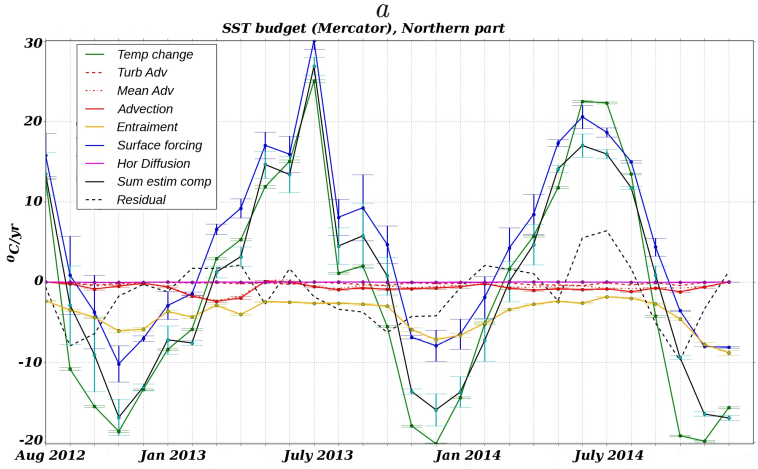

b

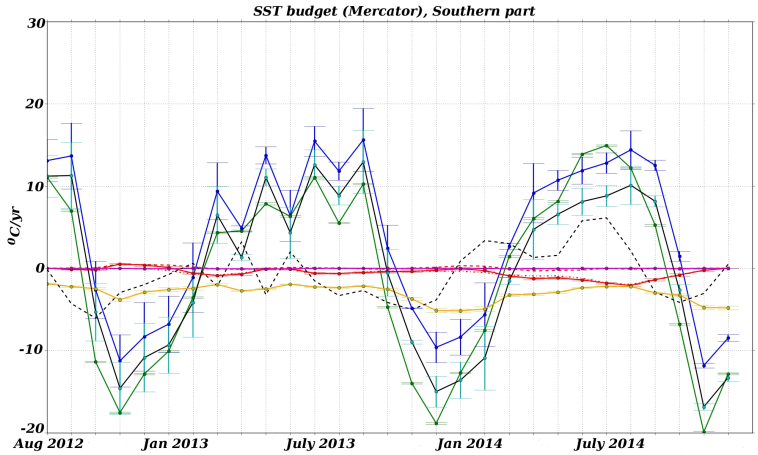

c

Figure 4.16: Components of temperature budget, residual (black dashed curve) and the sum of all estimated components of the right side of the equation (3.2.4) (black curve) based on Mercator analysis: a – SSS–max region $21^0N - 30^0N$ $50^0W - 26^0W$, b – northern part of SSS–max region $25.5^0N - 30^0N$ $50^0W - 26^0W$, c – southern part of SSS–max region $21^0N - 25.5^0N$ $50^0W - 26^0W$

effort was done to test the ability of SMOS to reproduce the SSS in the region of strong salinity gradient and strong eddy activity. SMOS SSS field is averaged over ∼75 km and corrected by using monthly ISAS product that does not represent meso-scales. The issue with the SSS–max region is that SSS does not varies a lot (tendency

Table 4.3: Time averaged mean of the components in Equations (3.2.3) and (3.2.4) in SSS–max region and its northern and southern parts

	SSS var	Turb adv	Mean adv	Entr	Surf forc	Hor Diff	Res
SSS-max							
pss/yr	-0.015 ± 0.036	-0.32 ± 0.05	-0.44 ± 0.05	-0.23 ± 0.023	1.05 ± 0.4	-0.02 ± 0.02	-0.05 ± 0.036
North							
pss/yr	-0.06 ± 0.04	-0.17 ± 0.05	-0.17 ± 0.05	-0.56 ± 0.03	1.01 ± 0.33	-0.012 ± 0.02	-0.16 ± 0.33
South							
pss/yr	0.03 ± 0.05	-0.47 ± 0.08	-0.71 ± 0.08	0.1 ± 0.03	1.09 ± 0.32	-0.02 ± 0.04	0.04 ± 0.32
	SST var	Turb adv	Mean adv	Entr	Surf forc	Hor Diff	Res
SSS-max							
^{0}C/yr	-1.1 ± 0.08	-0.08 ± 0.07	-0.6 ± 0.07	-3.5 ± 0.09	4.23 ± 2.23	-0.02 ± 0.03	-1.08 ± 2.23
North							
^{0}C/yr	-1.42 ± 0.12	-0.19 ± 0.11	-0.63 ± 0.11	-3.9 ± 0.13	4.82 ± 1.67	-0.015 0.04	-1.48 ± 1.68
South							
^{0}C/yr	-0.78 ± 0.09	0.03 ± 0.1	-0.62 ± 0.1	-3 ± 0.13	3.65 ± 2.22	-0.02 ± 0.05	-0.82 ± 2.22

Table 4.4: Time averaged mean of the components in Equations (3.2.1) and (3.2.3) further north and south from SSS–max region

	SSS var	Turb adv	Mean adv	Entr	Surf forc	Hor Diff	Res
Mercator, N							
pss/yr	-0.05 ± 0.035	-0.15 ± 0.07	-0.25 ± 0.07	-0.44 ± 0.025	0.89 ± 0.4	-0.01 ± 0.04	-0.087 ± 0.4
Mercator, S							
pss/yr	0.06 ± 0.05	-0.58 ± 0.08	-1.06 ± 0.08	0.53 ± 0.03	1.09 ± 0.36	-0.013 ± 0.04	0.09 ± 0.36
SMOS, N							
pss/yr	-0.03 ± 1.2	0.001 ± 0.2	-0.06 ± 0.2	-0.8	0.87 ± 0.35	–	-0.041 ± 0.35

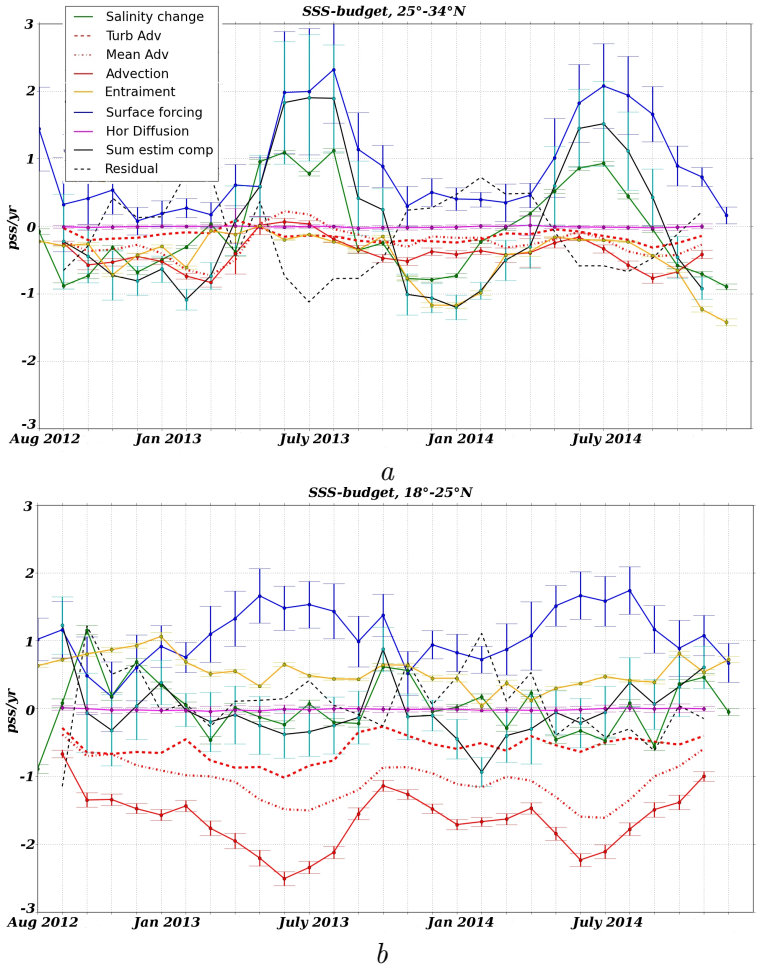

Figure 4.17: Components of salinity budget, residual (black dashed curve) and the sum of all estimated components of the right side of the equation (3.2.3) (black curve) based on Mercator analysis: a – further north from SSS–max region $25^0N - 34^0N$ $50^0W - 26^0W$, b – further south from SSS–max region $18^0N - 25^0N$ $50^0W - 26^0W$

is -0.015 pss/yr for the period August 20102 – December 2014) and probably SMOS cannot catch the small filaments and fronts of salinity that are important at meso-scales. Moreover, the eddy activity is weak (Riser et al., 2015) and the combination SMOS and AVISO to estimate the turbulent advection can underestimate this term.

SMOS was tested only in the region further north because, unfortunately, the AVISO data are limited in latitude further south.

As shown on Fig. 4.17 and Fig. 4.18 and in Table 4.4 the effect of most of the terms of MLS budget is similar to what was found earlier. In this section I will concentrate more on the advection of salinity (red curves).

Further north ($25^0 - 34^0$N) (Fig. 4.17a) Mercator shows similar results for advection to what was found in the North of the SSS–max region ($25.5^0 - 30^0$N). The turbulent advection has the same contribution (-0.15 $\pm$ 0.07 pss/yr) while the mean advection is a little larger (-0.25 $\pm$ 0.07 pss/yr) than it was in the North of the SSS–max region

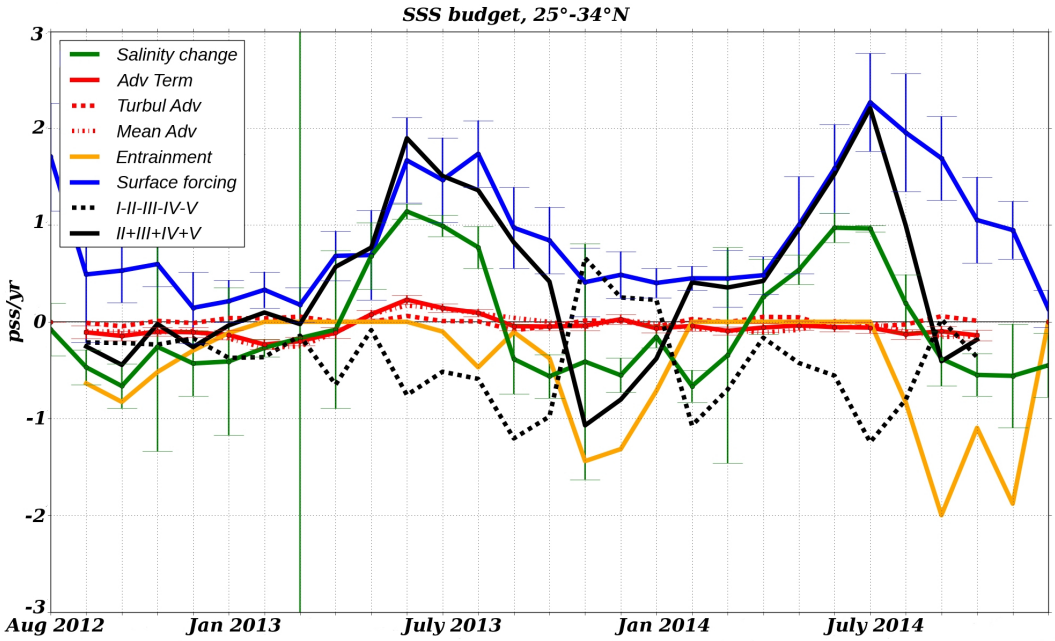

Figure 4.18: Components of salinity budget, residual (black dashed curve) and the sum of all estimated components of the right side of the equation (3.2.1) (black curve) further north from SSS–max region $25^0N - 34^0N$ $50^0W - 26^0W$

(-0.15 ± 0.07 pss/yr). It is due to the stronger effect of Ekman currents further north: as mentioned in the introduction, the SSS–max region is the convergence region of the Ekman currents coming from south and north. The southern Ekman velocity is much stronger than the one from the North, but advancing further north, its effect is enhanced. As found previously, in the North the advection works with entrainment to neutralize the effect of surface forcing.

Further south (18^0-25^0N) (Fig. 4.17*b*) the role of advection is larger. The turbulent and mean advection are larger than they were in the South of the SSS–max region, -0.58 and -1.06 ± 0.08 pss/yr, respectively. Their increase is in direct ratio with the increase in surface forcing term and entrainment that advection tries to balance. The larger mean advection is explained by its strong contribution in summer when Ekman current brings fresh water from the tropics (Fig. 4.17*b*).

Thus, it would be a good test for SMOS to estimate the MLS budget in this southern region ($18^0 - 25^0$N), where the role of eddy advection is so strong. Due to the limitation of geostrophic current data by latitude 20^0 we could not test it at the moment. This stays an important perspective. It can be done with the new global AVISO product that seems to have the required accuracy and TKE in the region of SSS–max.

SMOS was tested in the North ($25^0 - 34^0$N). The role of advection is surprisingly small compared to what was found for Mercator. The turbulent advection shows a weak and positive time-averaged value 0.001 ± 0.2 pss/yr. It varies around zero through the whole period with a positive effect in spring (Fig. 4.18). The more important role here is played by the entrainment that has almost the same value (-0.8 pss/yr) as

the surface forcing (0.87 ± 0.35).

The residual is small both for Mercator and for SMOS (Table 4.4). If OAFlux evaporation is used in case of SMOS, its residual would even be smaller and positive (∼0.03 pss/yr). But as mentioned in section 4.2 the entrainment term in SMOS MLS budget could be smaller due to the effect of horizontal gradients of MLD and estimating this term in each grid point, as was done for Mercator. Thus, the advection term has to be larger (in its absolute values) to close the budget. It confirms the idea that the advection term based on SMOS and AVISO is underestimated and has to play a more important role in the MLS variability.

4.4 Conclusion

In this chapter I have presented the part of my work that was aimed at estimating the MLS budget and the seasonal role of its components using SMOS SSS. SMOS corrected SSS was presented in Chapter 2 and the comparison with *in situ* data showed promising results: the RMS differences with drifter salinity are ∼0.15 pss most of the period. Moreover, I used Mercator PSY2V4R2-R4 analysis with a high spatial resolution to estimate MLS budget based on the model simulations to validate results obtained with SMOS. The use of such a model allows to analyze SSS variability with simulations averaged at the same resolution. It thus avoids the uncertainties related to differences in processing, smoothing or interpolating the data.

The analysis was concentrated in the SSS–max region $21^0 - 30^0$N $50^0 - 26^0$W of the North Atlantic subtropical gyre that is characterized by small SSS variability and weak eddy activity, during the period August 2012 – December 2014.

I have also discussed components of MLT budget. Usually it is easier to close the MLT budget, thus, it could help to better understand possible errors on the MLS budget using the same data sets.

The SSS and SST for SMOS and Mercator show a similar seasonal cycle with the maximum in summer and minimum in winter. Salinity and temperature show a small tendency in the North Atlantic subtropical gyre, -0.015 ± 0.32 pss/yr and -1.27 ± 3.33^0C/yr, respectively (partly, due to the fact that the initial month differs from the final month). The surface forcing is the dominant component in both budgets. Its time-averaged effect on salinity is $\sim 1.05 \pm 0.4$ pss/yr, and on temperature is 4 ± 2.23^0C/yr.

The entrainment was a major contributor to balance the water loss due to evaporation, especially during the winter when ML was deepening. For SMOS MLS budget the entrainment equals to -0.52 pss/yr while for Mercator it is -0.23 ± 0.023 pss/yr. This difference was explained by the inclusion of horizontal gradient of MLD in the estimation of entrainment term. This improvement of entrainment formula reduces the entrainment up to 35%. For temperature it was found that the entrainment participates in the decrease of temperature during the winter enhancing the effect of the heat flux.

Mercator allowed us to estimate the horizontal diffusion term at the daily submesoscales. Its effect on salinity variability was mostly negative and small, ∼-0.02 ± 0.03 pss/yr.

The different results that were most important were found for the advection term. In the case of SMOS, advection is small and does not vary a lot throughout the period (-0.2 ± 0.2 pss/yr). The mean advection is dominant (-0.17 ± 0.02 pss/yr) and the effect of turbulent advection is very weak (-0.026 ± 0.2 pss/yr). Using Mercator analysis the advection becomes the major component of the budget that balances the effect of the water loss on salinity. It is ∼72% higher (-0.76 ± 0.05 pss/yr) than the contribution of advection in the case of SMOS and AVISO. Turbulent (-0.32 ± 0.05 pss/yr) and mean (-0.44 ± 0.05 pss/yr) advection have almost the same magnitudes.

In the North and the South of the region that was chosen for analysis there are two different regimes of advection as was already shown in Dong et al. (2015). Qualitatively they are the same for SMOS and Mercator: mean advection is dominant in the North and strongly contributes in the South (Tables 4.1 and 4.3); the turbulent advection actively participates in the South and, in combination with the mean advection, balances the effect of the surface forcing. However, Mercator shows a stronger contribution of the turbulent advection, especially in the South (-0.03 ± 0.2 pss/yr for SMOS and -0.4 ± 0.08 pss/yr for Mercator). Further North ($25^0 - 34^0$N) Mercator shows that the effect of mean advection will increase (-0.25 ± 0.07 pss/yr). It is due to the stronger effect of Ekman current further north. In the North, the advection works with the entrainment to counteract the effect of surface forcing. The role of advection further north for SMOS is surprisingly small compared to what was found for Mercator. The turbulent advection shows weak and positive time-averaged value 0.001 ± 0.2 pss/yr. It varies around zero through the whole period with the positive effect in spring. The more important role here plays by the entrainment that has almost the same value (-0.8 pss/yr) as the surface forcing (0.87 ± 0.35). But as mentioned before the entrainment term in SMOS MLS budget could be smaller due to the effect of horizontal gradient of MLD and estimation of this term in each grid point. Thus, the advection term has to be larger (in it absolute values) to close the MLS budget.

Unfortunately, I could not study the effect of advection further south ($18^0 - 25^0$N) for SMOS due to the limitation of regional AVISO 2014 altimetry by 20^0N latitude band. Mercator shows here a stronger contribution of eddy advection -0.58 ± 0.08 pss/yr. Their increase is in direct ratio with the increase in surface forcing term and entrainment that advection must balance. Entrainment here is mostly positive (0.53 ± 0.03 pss/yr) in agreement with Dong et al. (2015). The mean advection is larger, it is explained by its strong contribution in summer when Ekman current brings fresh water from the tropics. These results are consistent with the ones from Dong et al. (2015): the advection is responsible for more than half of the balance after the water loss. Moreover, the turbulent (eddy) advection plays an important role that is increasing further south as was found by Büsecke et al. (2014) and Gordon and Giulivi (2014).

In the seasonal temperature budget the advection term is relatively small. It weakly participates in compensating the heating during the summer that results in mostly negative advection (-0.68 ± 0.07^0C/yr). In the South the averaged turbulent advection is positive (0.03 ± 0.1^0C/yr), as it brings a small amount of warmer water from the E-P–max region during the winter. Mercator analysis confirms that for MLT seasonal budget the advection term is small. Thus, the comparison of MLS and MLT budgets cannot be a good test of the accuracy of data used for estimating horizontal advection.

To learn more about the capacity of SMOS and AVISO in the region of strong

eddy activity the analysis of MLS budget further south from the SSS–max region is a promising perspective.

The residual terms in Mercator is much smaller than was found for SMOS in MLS budget, -0.05 ± 0.036 pss/yr and -0.3 ± 0.35 pss/yr, respectively, that is ∼9% and ∼47% of the averaged magnitude of $\frac{\partial \langle S \rangle}{\partial t}$ that varies in the range ±0.65 pss/yr. For the MLT budget the residuals are 5.4% for Mercator and 15% for OSTIA of the averaged magnitude of $\frac{\partial \langle T \rangle}{\partial t}$ that varies in the range $\pm 20^0$C/yr.

I have presented the possible sources of error in the MLS budget and its differences from MLT budget. One of them is the effect of uncertainties in precipitation and evaporation data. Using Mercator analysis, GPCP satellite for precipitation and OAFlux analysis for evaporation the residual term is extremely small compared to the one when SMOS SSS was used. For SMOS the GPCP precipitation and ERA-Interim evaporation were used. The test with these data and Mercator showed a much stronger residual -0.43 ± 0.4 pss/yr (66%) that was even larger than was found for SMOS. The opposite test (GPCP and OAFlux for SMOS) reduced the residual in SMOS MLS budget from -0.3 pss/yr to -0.2 pss/yr (32%). Thus, the uncertainties from precipitation and evaporation data can be large and responsible for more than 50% of errors in MLS budget as shown for Mercator (Table 4.2).

Another source of errors can be the entrainment term. The inclusion of horizontal gradient of MLD was tested, and MLS was considered at each grid point. However, the estimation of this term still presents uncertainties: the residuals in Mercator are large when entrainment is large, and the time averaged residual is higher in the North for both salinity and temperature budgets, where the contribution of entrainment is higher (Table 4.3). It could be due to the method of estimating the salinity entrainment (see Chapter 3). The value of entrainment salinity was considered at the depth of MLD from the next time step (for Mercator it was the next day and then it was averaged over the week) that could be significantly different from the salinity that was really entrained. It can be due to mixing processes that are not properly considered. The estimation of the SSS budget with daily time step showed significant influence on the entrainment and surface forcing terms. The fresh water flux increased from 1.05 pss/yr to 1.46 pss/yr, and entrainment – from -0.23 pss/yr to -1.12 pss/yr. It can be one or two days with the strong precipitation/weak winds (evaporation/strong winds) that can vastly decrease (increase) the MLD and, thus, have an effect on monthly averaged results. In such a case the comparison with weekly SMOS SSS field is not very relevant, and this budget is not very useful.

I concluded in this chapter that the more significant errors in SMOS MLS budget probably come from the advection term. As shown in Mercator it has to be the major component to balance the effect of evaporation. In the case of MLS budget based on observations there is a big unexplained part of surface forcing in the salinity budget that has to be probably compensated by advection. This can be due to the underestimation of ocean currents (AVISO geostrophic, ERA-Interim wind) as well as the effect of this particular region where eddy activity is weak or the inability of SMOS to reproduce well the small features of salinity (filaments and fronts) at the sea surface in this region.

Thus, to understand the problem in advection term more tests of SMOS products

are needed as well as the analysis of ocean currents that I will present in the next Chapter. The further analysis of SMOS salinity fields in other regions and with modified methods of estimation (for example, the method for estimation of entrainment component) are in perspective.

Chapter 5

Sensitivity of the horizontal advection term estimated from observations

In the previous Chapter I presented results for the SSS and SST budgets based on satellite and analysis data sets. Important disagreements were found in advection terms that can result from uncertainties in salinity fields and/or currents. The advection term plays a dominant role in the SSS budget and can balance more than 50% of the effect on salinity of the water loss due to the evaporation in the North Atlantic subtropical gyre. In this chapter I will test the sensibility of the advection term by combining different data of ocean currents and SSS. For example, I will show the effect of AVISO geostrophic currents and Ekman currents from ERA-Interim (that were used in SSS budget based on SMOS) on the SSS budget from Mercator analysis. Further, I will discuss differences in geostrophic and Ekman velocity currents from different data sets that were used to estimate the SSS budget in Chapter 4. This analysis will be done in the SSS–max region as well as further north and south from this region to test data used in presence of stronger salinity gradient and eddy activity.

5.1 Role of advection in the sea surface salinity variability. Sensitivity to different products

This section is devoted to investigating how some characteristics of the current and salinity data sets influence the estimation of horizontal SSS advection.

First of all, the effect of smoothing the daily Mercator data (both currents and salinity) to reproduce what was used for producing the SMOS data sets (see Chapter 2) was tested (Fig. 5.1*a*, blue curve). The smoothing procedure consisted of convolution of the original Mercator data with a Gaussian function scaled to 75 km. The smoothing procedure did not have much effect on the spatial mean of velocity time series, but it reduces the TKE of geostrophic current from 7 J/m^3 to 2.5 J/m^3, and the advection is reduced by a factor 2 compared the original results (red curve, see also Chapter 4). Mostly, the smoothing procedure influences the turbulent advection that was reduced from -0.32 pss/yr to -0.09 pss/yr (Table 5.1). However, the total advection is still large

Table 5.1: Advection of SSS and its turbulent and mean components

	Mercator original	Mercator Smooth	Mercator vs AVISO/ERA-Int	Mercator by SMOS Method	SMOS
Advection	-0.76	-0.4	-0.26	-0.4	-0.196
Turb adv	-0.32	-0.09	-0.06	-0.11	-0.026
Mean Adv	-0.44	-0.32	-0.2	-0.28	-0.17

(-0.4 pss/yr) compared to SMOS advection (-0.196 pss/yr) and can explain about half of the surface flux effect.

The test of Mercator salinity with AVISO 2014 geostrophic and Ekman current from ERA-Interim wind, daily MLD from Mercator and formula $\frac{\overrightarrow{\tau} e^{i*90}}{\rho f h}$ shows a decrease in total advection term from -0.76 pss/yr to -0.26 pss/yr (Fig. 5.1*b*, green curve; Table 5.1). The mean advection decreases by more than half, from -0.44 to -0.2 pss/yr, as well as the turbulent advection that becomes even smaller than using smoothing procedure, -0.06 pss/yr. Those results are close to the ones from SMOS (Fig. 5.1*b*, black curve). These two test are summarized on Fig. 5.3*a*, an extraction from Fig. 3.2 (labeled "Mercator/AVISO/ERA-I" and "Smoothed Mercator"), and compared with the "standard" examples presented in previous chapter (labeled "Mercator" and "Observations"). It shows strong reduction in turbulent advection (grey triangles). These results mean that the big difference in advection term found in Chapter 4 between Mercator analysis and observations is more likely due to the difference in ocean current data sets or to the method of their estimation. Moreover, the other set of currents (AVISO 2014, see Chapter 2) is not well consistent with the eddy positions in Mercator analysis.

It is worth to note that despite these differences all results show good qualitative agreement: in the sense that they present similar variability and seasonal cycle.

The estimation of advection terms in the Mercator SSS budget by the same method as in SMOS SSS budget (geostrophic + Ekman from formula $\frac{\overrightarrow{\tau} e^{i*90}}{\rho f h}$) but with ECMWF wind stress shows results close to the ones in the case of smoothing (Table 5.1, Fig. 5.2, green curves). Both turbulent and mean advection are reduced. It is clear presented on Fig. 5.3*b* (labeled "Mercator SSH + Formula WS ECMWF", dark figures) where two cases lie close to each other.

This result shows that the main issue probably lies in the way we estimate advection terms. It can result from the underestimation of Ekman current from the formula $\frac{\overrightarrow{\tau} e^{i*90}}{\rho f h}$. To better understand this hypothesis the geostrophic and Ekman advection were considered.

Figure 5.4 shows Ekman and geostrophic advections from SMOS SSS budget (black curves) and Mercator SSS budget (blue curves). For the SMOS SSS budget geostrophic advection was calculated with AVISO 2014 altimetry, and Ekman advection was estimated based on the formula $\frac{\overrightarrow{\tau} e^{i*90}}{\rho f h}$ with ERA-Interim wind and MLD from Argo profilers. For Mercator SSS budget, the geostrophic current was estimated from SSH and then Ekman current was considered as the residual of total filtered (from ageostrophic component) ML current without geostrophic component. This "Residual

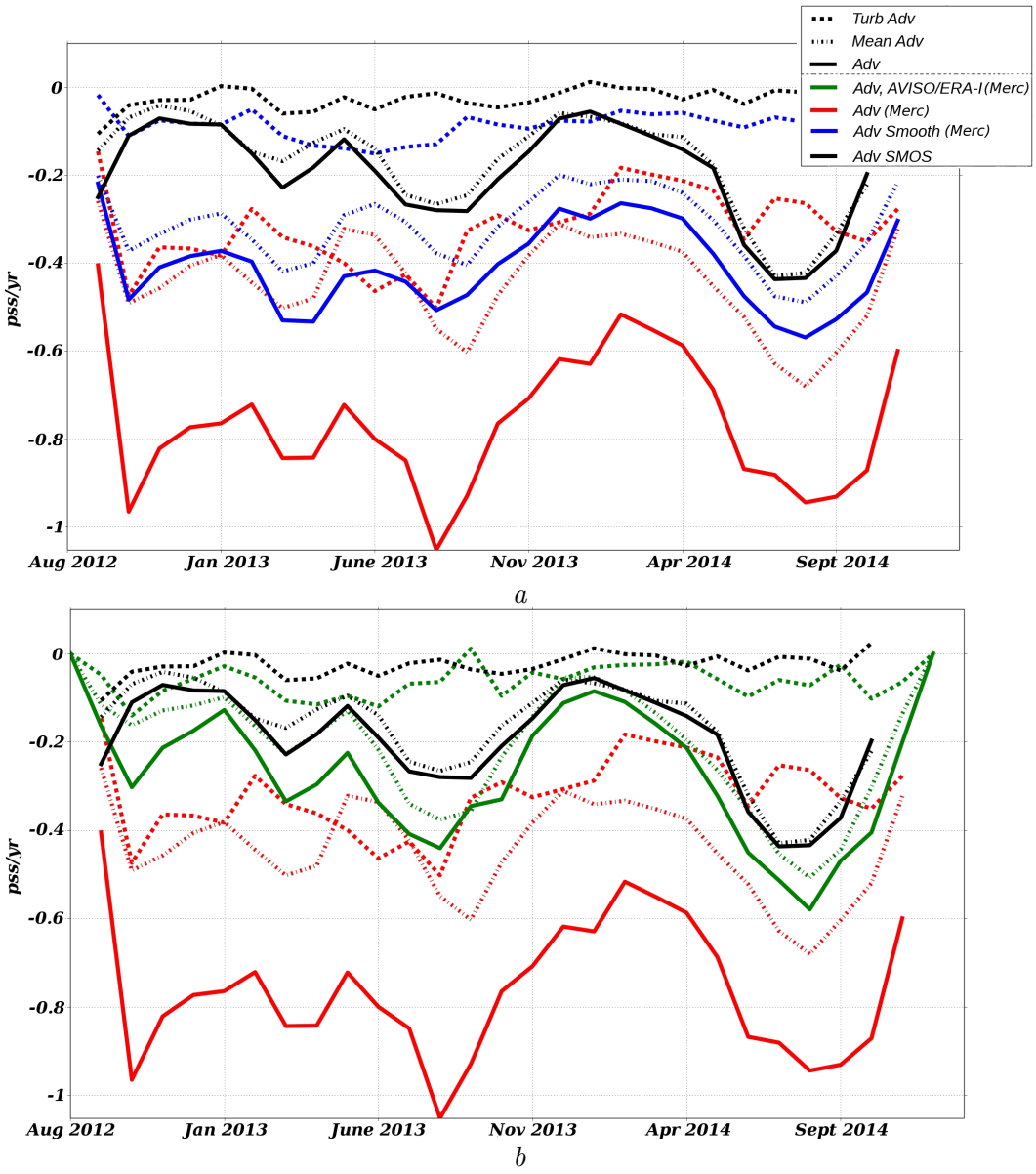

Figure 5.1: Total SSS advection (solid curves) and its turbulent (dashed) and mean (dashed-point) components, red – Mercator analysis, black – advection from SMOS with AVISO geostrophic and ERA-Interim wind: *a* – Smooth Mercator analysis (blue); *b* – advection from Mercator MLS with AVISO geostrophic and ERA-Interim wind (green)

Ekman current" can contain the effect of assimilation increments that have to be estimated separately. But we expect that this effect is small as the assimilation cycle in Mercator analysis is around 7 days that corresponds to time step used in my analysis. The total Mercator advection (blue solid curve) is close to the advection estimated as the sum of its turbulent and mean parts (red curve). The geostrophic advections is very similar in the two cases, SMOS and Mercator (dashed black and blue curves): they have the same seasonal variability with an increase in late summer and autumn and a decrease in winter. Time-averaged values are very similar: -0.03 pss/yr for SMOS and -0.027 pss/yr for Mercator. Although, Mercator (blue dashed curve) shows monthly results a little larger than SMOS/AVISO (black dashed curve) that can result from the effect of the small geostrophic shear in Mercator ML current that has to be further investigated (see next section), or from differences in salinity fields. However, the largest difference is found in the Ekman advection term. For both cases, Mercator and SMOS, it presents the same variability with the strong contribution in summer–early autumn to balance the water loss due to the heating. However, their quantitative difference is huge: in the Mercator analysis the Ekman advection averages to -0.88 pss/yr whereas for SMOS with wind ERA-Interim, itéis equal to -0.17 pss/yr.

For this analysis it is important to show the comparison of SSS fields from Mercator and SMOS. As shown in Chapter 2 the comparison of SMOS (75 km) and Mercator (10 km) fields with *in situ* measurements presents similar RMS differences 0.15 pss. Figure 5.5 presents RMS differences between SMOS and Mercator where Mercator SSS was weekly averaged and interpolated on the SMOS grid $0.25^0 \times 0.25^0$. The RMS

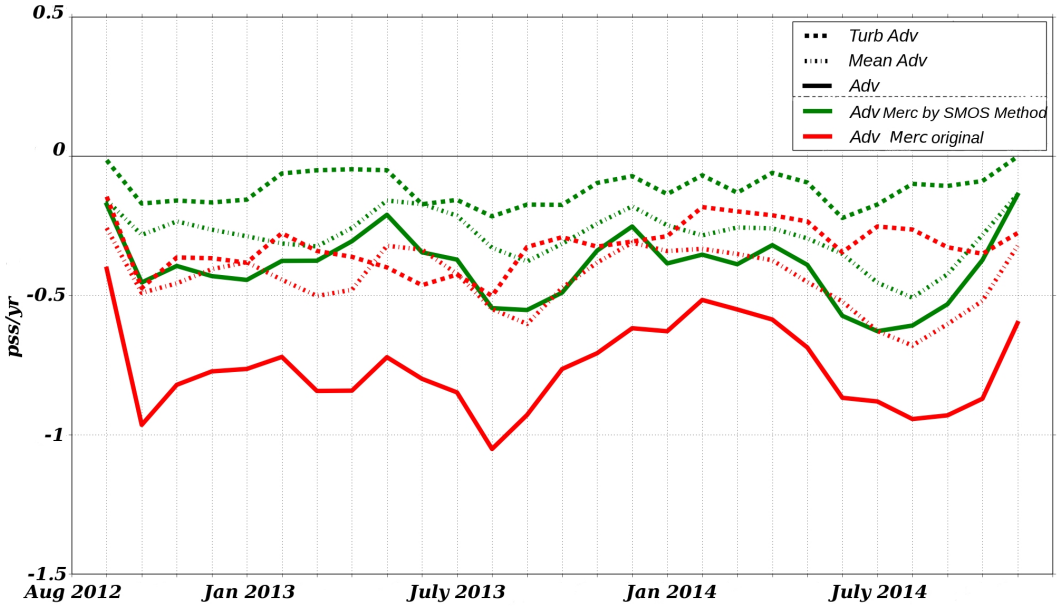

Figure 5.2: Mercator total advection (solid curves) and its turbulent (dashed) and mean (dashed-point) components estimated as in the case of SMOS (geostrophic and Ekman estimated separately) (green) and estimated from the total ocean current in ML (red)

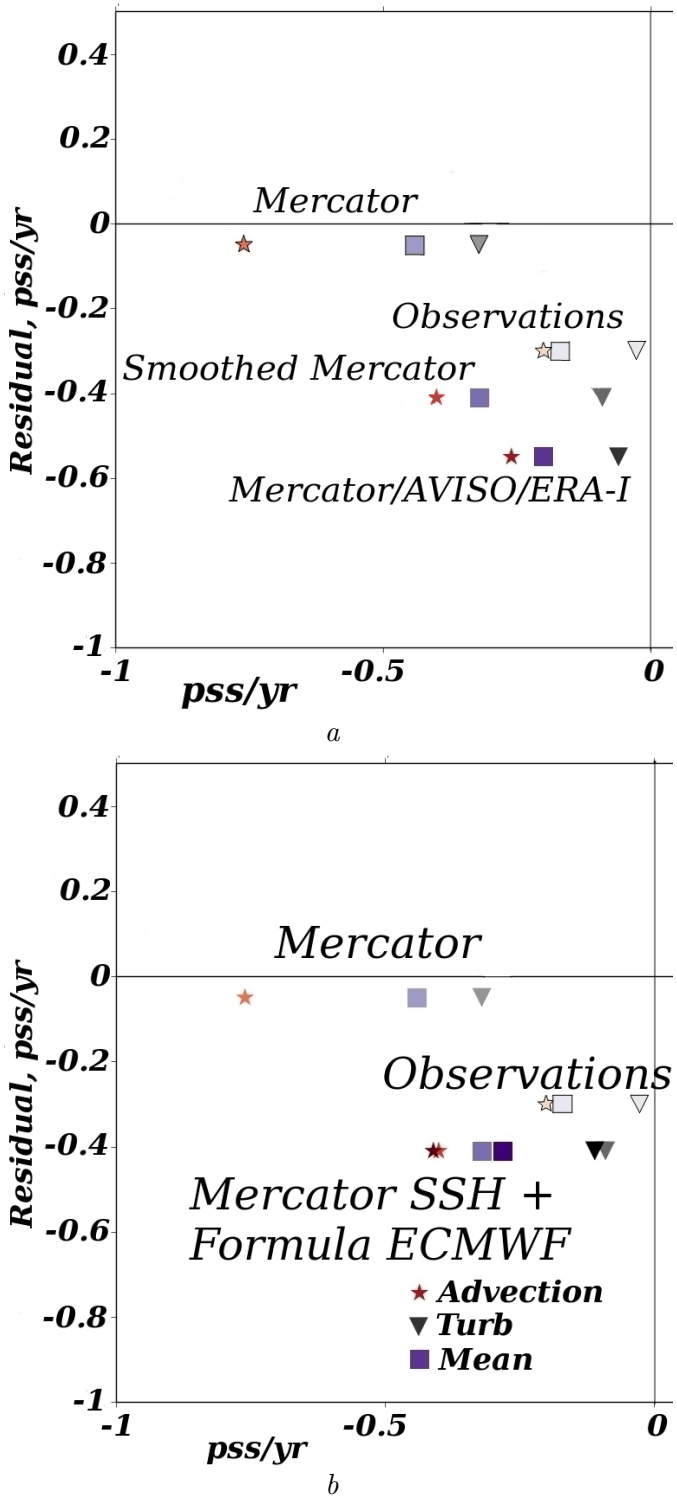

Figure 5.3: Sensitivity of advection terms to data used, extraction from Fig. 3.2, comparison of total advection (star) and its mean (square) and turbulent (triangle) components in two "standard" cases (presented in Chapte 4 and labeled "Mercator" and "Observations") with: *a* – advection terms from smoothed Mercator fields ("Smoothed Mercator") and terms estimated with Mercator salinity, AVISO 2014 geostrophic current and Ekman current from theoretical formula with ERA-Interim wind ("Mercator/AVISO/ERA-I"); *b* – with advection terms estimated with Mercator salinity, geostrophic current from Mercator SSH and Ekman current from theoretical formula with ECMWF wind stress ("Mercator SSH + Formula ECMWF", the dark color figures)

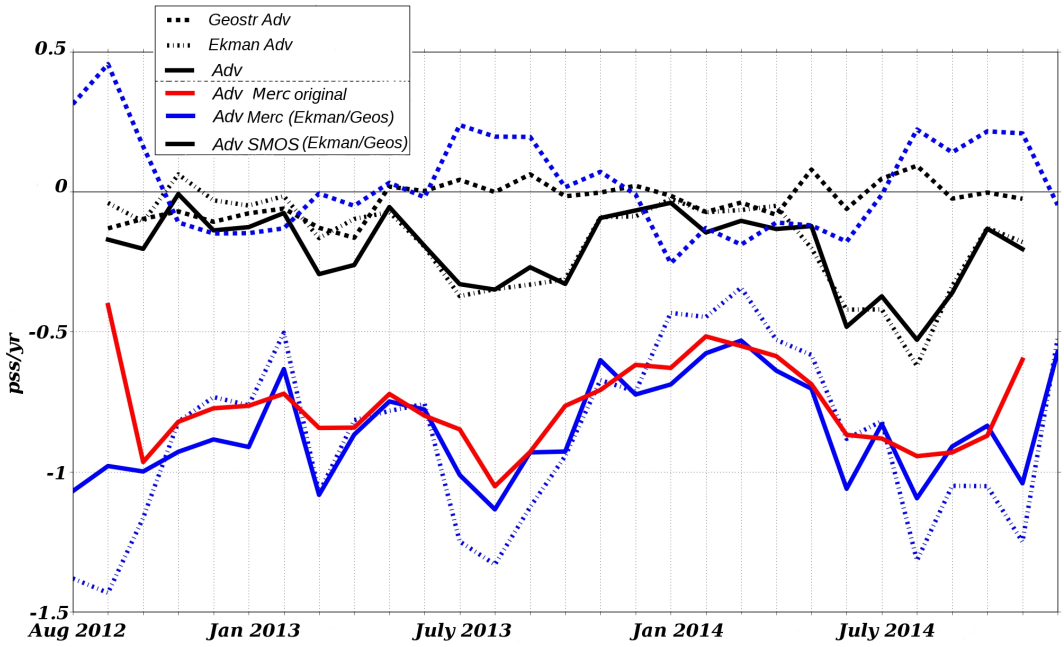

Figure 5.4: Total advection (solid) and its geostrophic (dashed) and Ekman (dashed-point) components: red – total advection from Mercator estimated as in Chapter 4; blue – Mercator advection with Ekman current estimated as the residual from total ocean curent in ML and geostrophic current; black – advection from SMOS with AVISO 2014 and ERA-Interim wind

differences vary in the range 0.15–0.2 pss most of the time. Differences between SMOS and Mercator at its original spatial resolution (10 km) (blue) are a little larger than the differences between SMOS and smoothed Mercator fields (75 km), maximum value is ∼0.03 pss. Thus, the two salinity fields show a good agreement and their differences are not dependent on a too coarse spatial resolution.

I conclude here that the difference in advection term between the Mercator simulation and the combination of SMOS-derived SSS with AVISO altimetry and ERA-Interim reanalysis results mostly from the method used to estimate the Ekman current in the case of SMOS. The widely used formula $\frac{\overrightarrow{\tau} e^{i*90}}{\rho f h}$ seems underestimates the Ekman current in ML. In next two section I will present the daily comparison of geostrophic (5.2) and Ekman currents (5.3) from different data and methods used.

5.2 Geostrophic current from in situ data, altimetry and Mercator analysis

The geostrophic current from AVISO regional 2014, AVISO global 2010 altimetry products and Mercator PSY2V4R2-R4 analysis are compared. I have already presented these data in Chapter 2. AVISO 2014 has a daily resolution on $1/8^0 \times 1/8^0$ regular grid, AVISO 2010 has a spatial resolution $1/3^0 \times 1/3^0$ and Mercator analysis – $1/12^0 \times 1/12^0$. The same period was chosen as previously: August 2012 – December 2014 (for AVISO

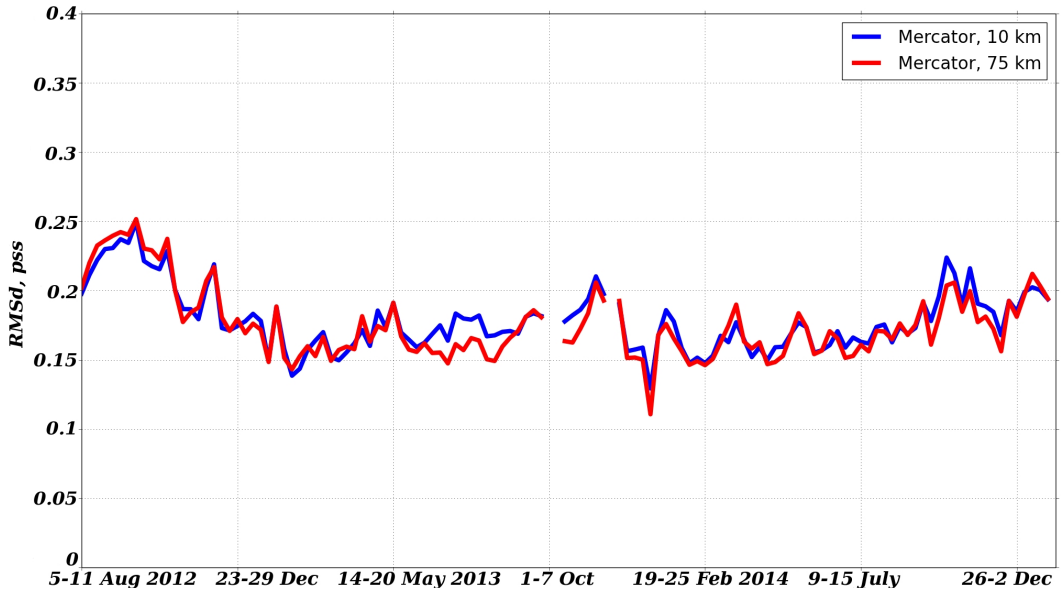

Figure 5.5: RMS differences between SMOS (75 km) SSS fields and Mercator at 10 km resolution (blue) and Mercator at 75 km (smoothing) (red) SSS fields for the period August 2012 – December 2014. Mercator SSS fields were weekly averaged and interpolated in SMOS grid $0.25^0 \times 0.25^0$

2010 the analysis is stopped in October 2013). It is worth to note that the further analysis will be done with a daily time step.

To estimate the geostrophic current (u, v) from Mercator the SSH η was used (geostrophic balance):

$$u = -\frac{g}{f}\frac{\partial \eta}{\partial y}, \qquad v = \frac{g}{f}\frac{\partial \eta}{\partial x},$$

where $f = 2\Omega sin\varphi$ is the Coriolis parameter with $\Omega = 7.2921 * 10^{-5}$ rad/s and latitude φ.

I also considered the ocean currents from Mercator at 50 m. Ekman does not have a strong influence at 50 m, except in winter when the MLD and Ekman Depth can be deeper. The comparison with this deeper current can show the effect of geostrophic shear in MLD (because eddy activity is relatively small and below the Ekman layer, currents are in near-geostrophic balance).

The comparison was done in 5 regions: SSS–max region $21^0 - 30^0N \times 50^0 - 26^0W$, its northern $25.5^0 - 30^0N \times 50^0 - 26^0W$ and southern $21^0 - 25.5^0N \times 50^0 - 26^0W$ parts, then further north $25^0 - 34^0N \times 50^0 - 26^0W$ and further south $18^0 - 25^0N \times 50^0 - 26^0W$. Figure 5.6 presents a zonal (a) and meridional (b) components of AVISO 2014 geostrophic velocity in these regions (except for the region further south due to the limitation of AVISO product by 20^0 latitude). Zonal velocity (Figure 5.6a) has almost the same amplitude in the North (0.0023 m/s) and the South (-0.0038 m/s) but with the opposite sign and amplitudes that increases further north and south (as

expected on the side of the subtropical gyre). That explains that the zonal geostrophic velocity in the SSS–max region (red curve) varies close to zero. The meridional velocity (Figure 5.6*b*) is stronger in the South (black curve) while it reduces further north (green curve) (to some extent, the result of Sverdrup dynamics, and that it is a little to the east of the center of the gyre). Thus one can expect that the influence of geostrophic current will be a little stronger in the South.

Figures 5.7 shows the comparison of AVISO 2014 averaged velocity field with other products in SSS–max region. AVISO 2014 (red curve) and Mercator (SSH) (green) zonal velocities (Fig. 5.7*a*) lie close to each other but with stronger average differences from AVISO 2010 (blue) and Mercator at 50 m (black). Meridional velocity (Fig. 5.7*b*) shows that three products (AVISO 2010, Mercator SSH and Mercator at 50 m) lie together while AVISO 2014 (red) presents a much smaller time average. However,

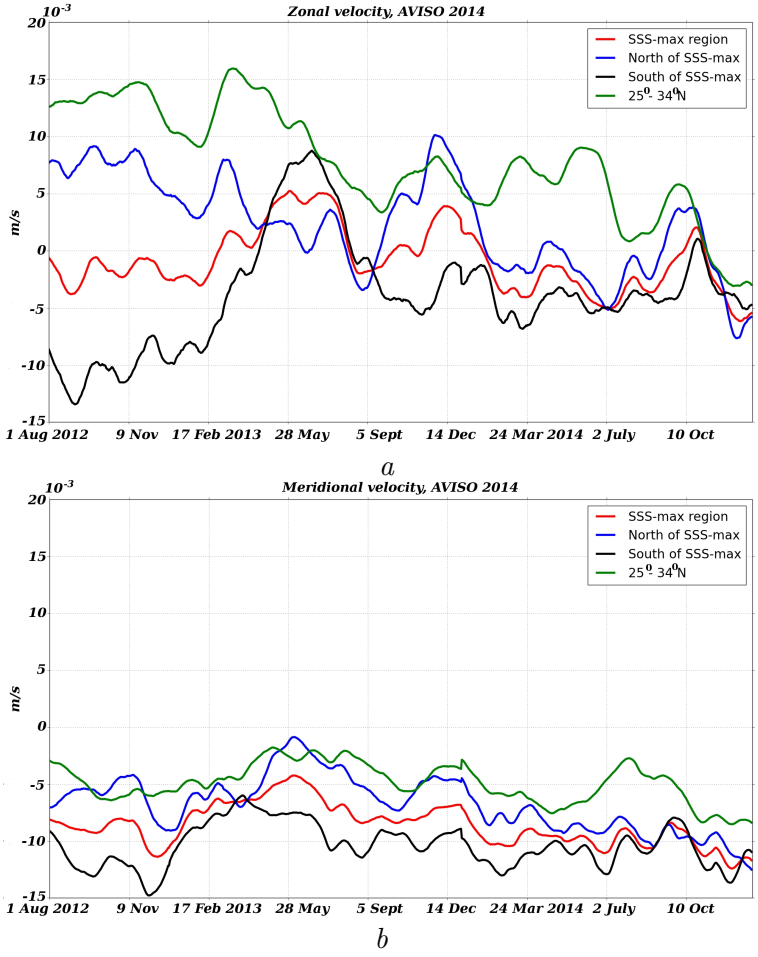

Figure 5.6: Zonal (*a*) and meridional (*b*) velocity from AVISO regional 2014 altimetry in different regions: red – SSS–max region $21^0 - 30^0$N $50^0 - 26^0$W; blue – northern part of SSS–max region $25.5^0 - 30^0$N $50^0 - 26^0$W; black – southern part of SSS–max region $21^0 - 25.5^0$N $50^0 - 26^0$W; green – further north from SSS–max region $25^0 - 34^0$N $50^0 - 26^0$W

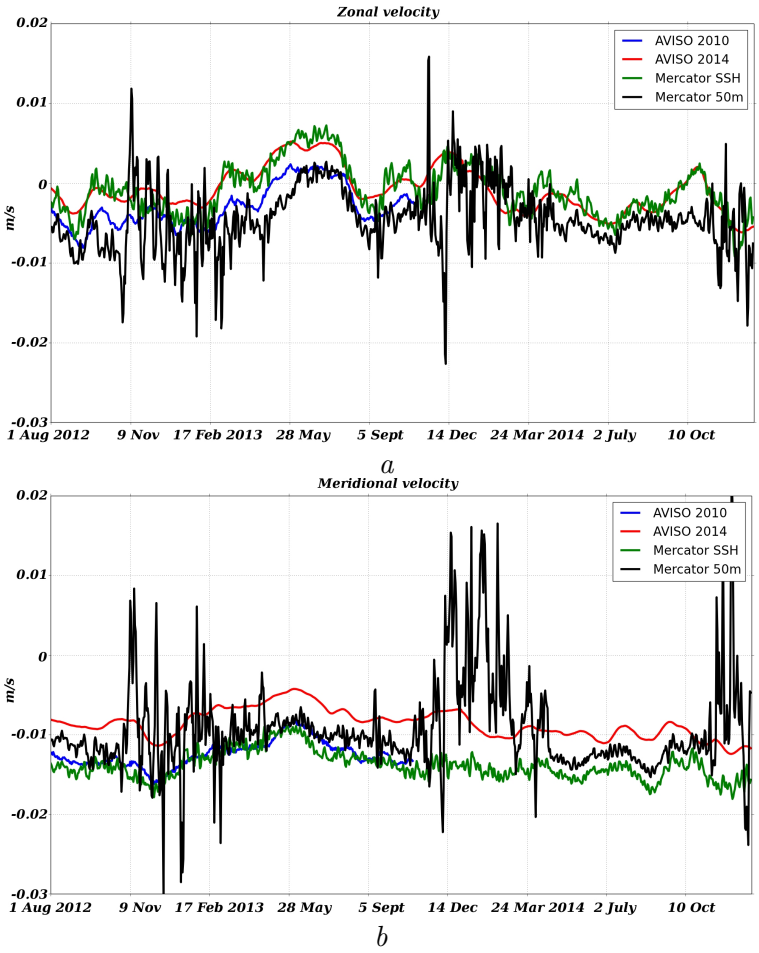

Figure 5.7: Zonal (a) and meridional (b) geostrophic velocity in SSS–max region $21^0 - 30^0$N $50^0 - 26^0$W: blue – AVISO 2010; red – AVISO 2014; green – Mercator geostrophic velocity from SSH; black – Mercator velocity at 50 m depth

Table 5.2: Averaged Total Kinetic Energy (J/m^3) in 5 different regions for AVISO 2010, AVISO 2014 and Mercator SSH geostrophic current (in round brackets the average for period August 2012 – October 2013 common with AVISO 2010)

	SSS–max region	North of SSS-max	South of SSS-max	Further north	Further south
AVISO 2010	3	2.6	3.3	7	3.5
AVISO 2014	4.2 (4.6)	3.8 (4)	4.6 (5.1)	8.6 (8.6)	–
Mercator	5 (5.2)	4.3 (4.4)	5.7 (6.1)	8.6 (8.4)	6.6 (7)

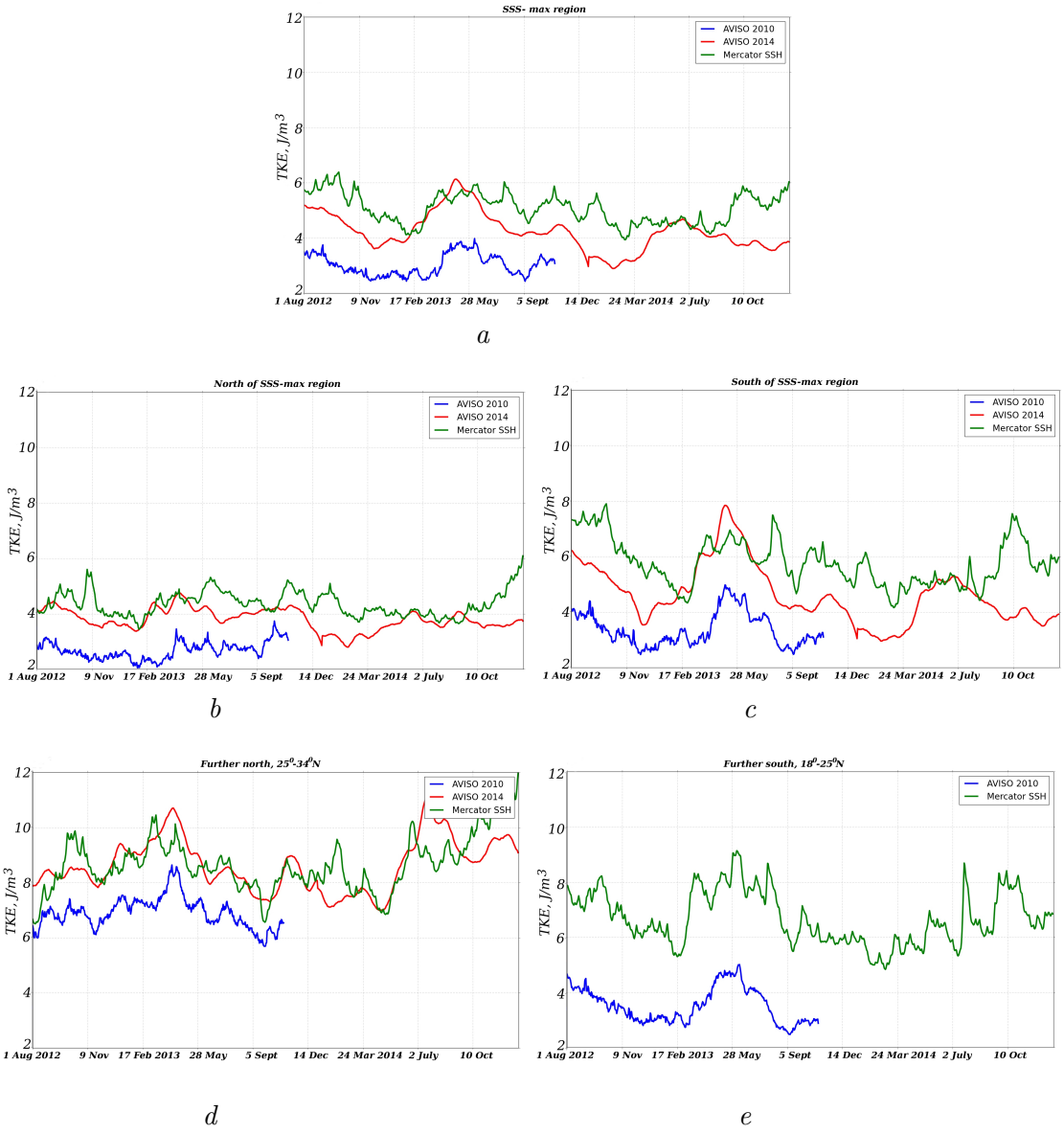

Figure 5.8: Total Kinetic Energy of AVISO 2010 (blue), AVISO 2014 (red) and Mercator (from SSH) (green) geostrophic currents: *a* – SSS–max region 21^0-30^0N 50^0-26^0W, *b* – northern part of SSS–max region $25.5^0 - 30^0$N $50^0 - 26^0$W; *c* – southern part of SSS–max region $21^0 - 25.5^0$N $50^0 - 26^0$W; *d* – further north from SSS–max region $25^0 - 34^0$N $50^0 - 26^0$W; *e* – further south from SSS–max region $18^0 - 25^0$N $50^0 - 26^0$W

at low-frequency (10 days and more) all products are close to each other. Similar results were already demonstrated on the Power Spectral Density maps in Chapter 2 (Fig. 2.14). The difference between Mercator SSH (green) and Mercator at 50 m (black) can be due to the small geostrophic shear (through the horizontal gradient of density: thermal wind, Appendix A.5) as well as to the Ekman current that is evident during

winter months. The possible effect of geostrophic shear that is not taken into accountin SMOS-based MLS budget was mentioned in the previous section. The time-average difference of space-average meridional velocity component between AVISO 2014 and Mercator SSH is on the order of 0.005 m/s. Combining such an error and errors in salinity field from SMOS of about 0.15 pss (see Chapter 2), can result in an uncertainty $\sim$0.15 – 0.2 pss/yr for the advection term in SSS budget (assuming the independence of errors at 0.5^0 resolution). These differences are valid for all regions considered in this section.

The total kinetic energy for the 5 regions is presented on Figures 5.8 with the total averages in Table 5.2 (in round brackets the average for period August 2012 – October 2013 common with AVISO 2010). TKE is a little higher for Mercator in all regions and is very small for AVISO 2010. AVISO 2014 TKE is a little smaller than Mercator TKE, about 15%. These differences were already discussed in Chapter 2.

The southern region of SSS–max region (Fig. 5.8*c*) presents a larger TKE than the northern part (Fig. 5.8*b*). For Mercator (green curve), for example, TKE equals 4.3 J/m^3 in the North and 5.7 J/m^3 in the South. The SSS–max region (Fig. 5.8*a*) is an average of what was found in the North and South (5 J/m^3 for Mercator). However, the TKE shows large increase further north (Fig. 5.8*d*), by 100% for AVISO 2014 and 72% for Mercator (Table 5.2). This region is characterized by stronger eddy activity that might be better captured in the AVISO 2014 product than in the SSS–max region. It is interesting that further south (Fig. 5.8*e*) there is also an increase in TKE compared with SSS–max region and its southern part, but this increase is smaller than in the North (by 32% for Mercator) (Table 5.2). It is mostly due to the difference in the choice for the two regions: the region further north contains more eddies than the region chosen further south. It is likely that the region even further south would give comparable results than the northern part.

The geostrophic contribution (to the SSS budget) in the North and South have almost the same magnitude (a little stronger in the North) but the turbulent advection is also (indirectly) dependent on the Ekman current that is strong in the South. Gordon and Giulivi (2014) with the reference to Cessi (2007) mentioned that Ekman pumping can introduce available potential energy on which eddies can grow. In the South there is a strong meridional salinity gradient caused by Ekman transport that may induce baroclinic instability and eddy generation. These results explain the ones in the previous Chapter, where the net effect of turbulent transport/advection was significantly stronger in the South.

5.3 Ekman current in Mixed Layer and at 15m

Ekman in ML. The second component of ocean current velocity is the Ekman velocity. Ekman current is a combination of the wind at the surface of the ocean and the earth rotation effect. The Coriolis force moves the object to the right from the wind direction (in the northern hemisphere). With depth the angle between Ekman vectors and the wind turns more and more forming the Ekman spiral. The Ekman current was first physically explained by Vagn Walfrid Ekman in 1902.

Figures 5.9 present the zonal (*a*) and meridional (*b*) Ekman velocities of ML in the

SSS–max region estimated from the Mercator analysis and widely used formula $\frac{\overrightarrow{\tau} e^{i*90}}{\rho f h}$ (this formula was already presented in Chapter 3 and it presents the Ekman transport averaged over MLD). "Ekman" velocity from Mercator (green curves) was estimated as a residual from the total filtered ocean current in ML and geostrophic current estimated from Mercator SSH (see previous section 5.1) (quotation marks are used to indicate that the Ekman current estimated as residual from total Mercator current can contain assimilation increments and, thus, does not present the exact Ekman current in ML, but as mentioned before, we expect that this effect is small). Moreover, I presented here the "Ekman" velocity as a residual from the total filtered ocean current in ML and Mercator current at 50 m (black dashed curves). The differences between the two estimated "Ekman" currents are small and result from the small differences of "geostrophic" currents in the previous section (I used quotes because the Mercator currents at 50 m are not only geostrophic currents). The differences between different products that were compared in section 5.1 are small if we compare only velocities and not the advection terms. However, there are large differences in winter months, especially during the winter 2013–2014, between the two "Ekman" currents due to the effect of the deeper ML and deeper Ekman depth (the depth at which the direction becomes opposite to that at the surface). It is worth to note that the geostrophic shear can be stronger during the winter (Fig. 5.7) and, thus, it can also participate in the difference between the different estimates of the Ekman currents.

The comparison with the Ekman current estimated from the formula $\frac{\overrightarrow{\tau} e^{i*90}}{\rho f h}$ with MLD h from Mercator analysis and wind stress $\overrightarrow{\tau}$ from ERA-Interim wind (red curves) shows that the Residual "Ekman" Mercator current (green curve) tends to be larger in its absolute value (Fig. 5.9). RMS differences (Fig. 5.11, green curves) between these "Ekman" currents are around 0.02 m/s for zonal velocity (a) that tend to be smaller at the end of the period ($\sim$ 0.015 m/s) and around 0.015 m/s for meridional velocity (b). With the error 0.15 pss for salinity an error 0.015 m/s in Ekman can result in an error of 2.55 pss/yr in the advection term. Both zonal and meridional RMS differences show a small seasonal cycle with increases in winter due to the stronger geostrophic shear. Furthermore, the larger Residual "Ekman" current in Mercator can be due to the underestimation of MLD used in the formula. Figure 5.10 shows the schematic change of amplitude of the Ekman vector with the depth for three cases. We also have to remember that Ekman vector turns to the right with the depth from the vector at the surface. As presented on Figure 5.10 if we consider the shallower MLD (red line) it will not include in the formula (red vectors) the effect of the Ekman current just below as is possible in Mercator (green vectors). The formula presents the Ekman current averaged in MLD h that coincides with the double Ekman Layer Depth. The amplitude of averaged Ekman current is equal to the amplitude of vector at Ekman layer depth (green line) that is smaller than the one from Mercator. In Mercator, if MLD is shallower, averaging Ekman current in the MLD chosen for the formula will be larger (Fig. 5.10, green line). Thus, the effect of difference between Ekman depth and MLD mentioned in 3.3 can be significant but at the moment it is hard to estimate (role of increments in Mercator, ignorance of exact Ekman depth etc.). For further estimation I continue to consider that MLD and Ekman depth are not significant different.

The choice of constant MLD (no horizontal gradient) h for each day as was done

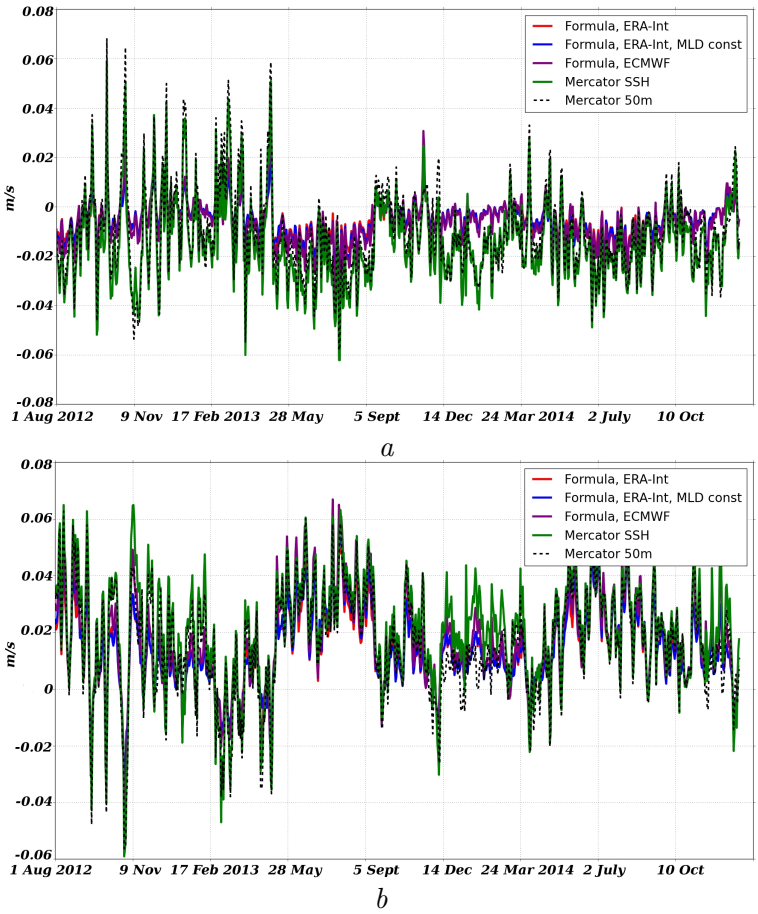

Figure 5.9: Zonal (a) and meridional (b) Ekman velocity in SSS–max region $21^0 - 30^0$N $50^0 - 26^0$W: red – estimation from formula with ERA-Interim wind; blue – formula with ERA-Interim wind and constant MLD; purple – formula with ECMWF wind stress; green – Residual "Ekman" current from Mercator as the difference between total filtered ML current and SSH geostrophy; dashed black – Residual "Ekman" current from Mercator as the difference between total filtered ML current and current at 50 m

to estimate the SSS budget based on SMOS in Chapter 4 (for each month) results in a small effect on the Ekman current $\frac{\overrightarrow{\tau} e^{i*90}}{\rho f h}$ (Fig. 5.9, blue curves). The RMS differences between the Ekman current estimated with variable MLD and constant MLD (Fig. 5.11, blue curves) are small and on the order of 0.005 m/s for zonal velocity (a) and a little large for meridional velocity (b) because of the dominantly meridional Ekman current in the North Atlantic subtropical gyre. There is a small seasonal cycle as was in the case of Mercator but now the small increase is in summer: on Fig. 5.9 blue curves tend to have a larger absolute value than red curves in summer months. During this season the MLD is shallower and meridional Ekman current is larger, thus, if we used the spatial average of MLD we probably will lose the effect of a deeper Ekman Depth (see previous paragraph and Fig. 5.10).

The Mercator analysis is driven by ECMWF winds (NRT) that is a little different

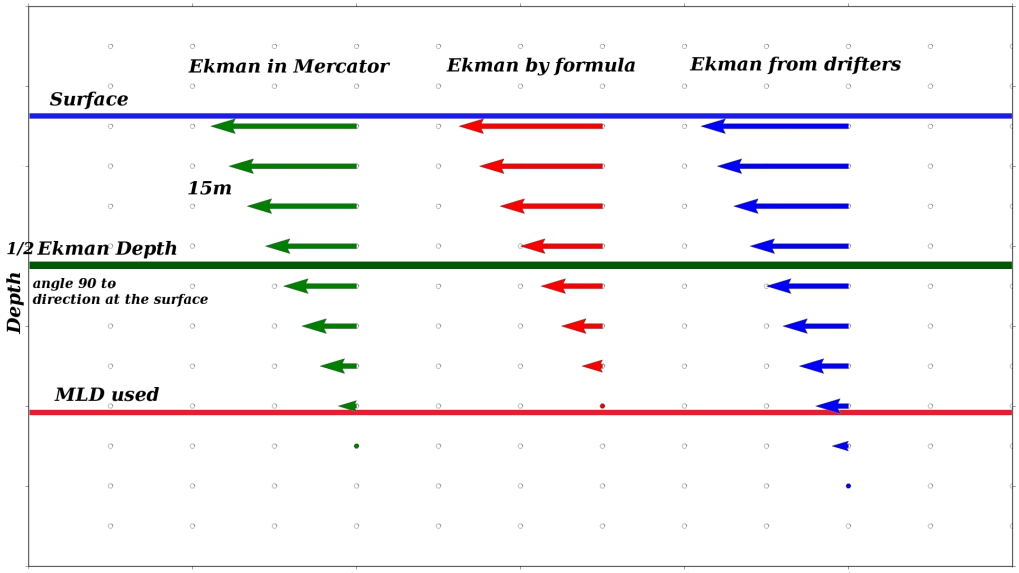

Figure 5.10: Schematic change of vector amplitude with the depth in Ekman spiral considering that MLD equals to Ekman Depth for different cases: green – Ekman spiral from Mercator analysis ($u_{total\_ML} - u_{geostr\_SSH}$) that lies deeper than red – Ekman spiral from formula that depends on the chosen MLD (red line), and blue – Ekman spiral suggested by an analysis of drifter velocity at 15 m. Blue line represent the ocean surface. Green line corresponds to the half of Ekman Depth in the case when Ekman depth coincides with MLD used (red line). At this depth (green line) the Ekman current velocity vector turns 90^0 to the the surface current

from wind ERA-Interim (reanalysis). If we use the wind stress ECMWF (Fig. 5.9, purple curves) in the formula $\frac{\vec{\tau} e^{i*90}}{\rho f h}$, Ekman velocities lie closer to the Residual "Ekman" current from Mercator (green curves). This is in particular apparent for the meridional velocity (Fig. 5.9*b*). It results in a little larger RMS differences with Ekman currents using wind ERA-Interim in winter (Fig. 5.11*b*). However, RMS differences remain small (∼0.005 m/s) compared to the ones from Mercator Residual "Ekman" velocity (green curves).

The difference between Mercator Residual "Ekman" current and Ekman current based on the formula and ERA-Interim wind diminishes further north, RMS differences of zonal and meridional components are around 0.015 m/s. Further south where the Ekman current is stronger, the difference increases up to 0.03 m/s. The large disagreement is still present during winter.

Thus, the difference between the Residual "Ekman" current of Mercator analysis and Ekman current estimated by the widely used formula $\frac{\vec{\tau} e^{i*90}}{\rho f h}$ (expecting that the effect of data assimilation increments in Mercator is small) can be due to *(1)* the overestimation of Ekman current by Mercator, and/or *(2)* uncertainties in MLD estimation and, as a result, underestimation of Ekman current by $\frac{\vec{\tau} e^{i*90}}{\rho f h}$ and/or *(3)* the difference between MLD and Ekman depth. To better understand possible differences, the Ekman current at 15 m is considered. As explained in Chapter 3 we can use the drifters

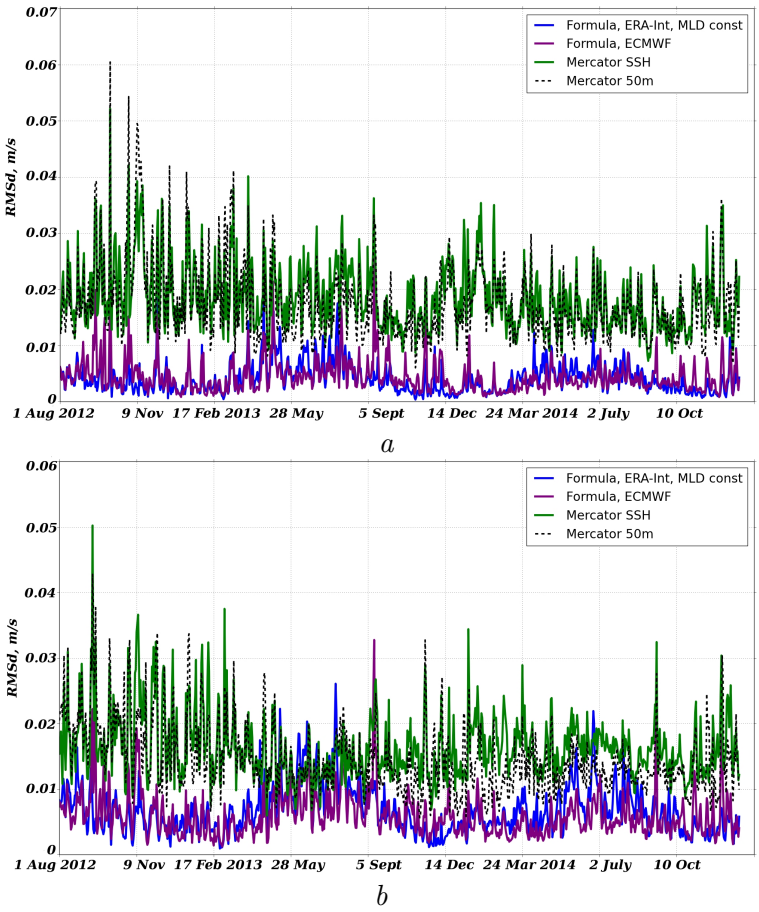

Figure 5.11: RMS differences of zonal (a) and meridional (b) velocity components of Ekman currents estimated by formula 3.3 with wind ERA-Interim and MLD from Mercator analysis and: blue – Ekman from the same formula but with constant MLD; purple – the same formula but with wind stress from ECMWF; green – Mercator Residual "Ekman" current in ML estimated as residual from total filtered ocean current and geostrophic current estimated from SSH; dashed black – Mercator Residual "Ekman" current in ML estimated as residual from total ocean current and current at 50 m

as the references for this analysis because they have their drogues at 15 m depth and, thus, move with the current at this depth.

The use of constant monthly-averaged MLD from Argo data in SMOS-based MLS budget can underestimate the MLD in the North and overestimate in the South. But as the Argo profilers were mostly concentrated in the center of the region we expect that results can be compared with the ones found with daily time step. However, the monthly average of MLD can have some effect on the Ekman advection that are probably one of the reasons for differences in section 5.1.

Ekman at 15 m depth. The geostrophic velocity from AVISO 2014 altimetry was removed from the total drifter velocity (see equation (3.3.1)). Then the residual velocity was filtered by low-pass (30 hours) and high-pass (30 days) filters to remove the ageostrophic component (Van Meurs and Niiler, 1997). The velocity obtained is

the Ekman velocity at 15 m. the same filers were applied to wind ERA-Interim data. Around 80 drogued drifters were used for the period of September 2012 – March 2014, the period of the largest concentration of drifters, which were sufficient for the further analysis in the SSS–max region $20^0 - 30^0$N $50^0 - 26^0$W.

We will use the Ekman model proposed by M.-H. Rio (2012) that can be written as (equation (3.3.2)) $u_{ekm} = \beta\tau e^{i\theta}$.The estimation of β and θ using the theoretical formulas presented in Chapter 3 is difficult to do correctly as it requires the knowledge of varying viscosity (diffusion). To find β and θ parameters I propose here an empirical method that has three steps (Fig. 5.12): for each month *(1)* the most frequent angle θ between the Ekman and wind ERA-Interim vectors is chosen (Fig. 5.12*a*), then *(2)* based on the 2D histogram the most frequent MLD (from Mercator analysis) is chosen according with the angle θ found in (1) (Fig. 5.12*b*), and *(3)* based on this MLD from step (2) β can be chosen (Fig. 5.12*c*). This method allows to find Ekman parameters that have a physical meaning based on the MLD.

Figure 5.12 shows the example of April 2013. At first, from the spread distribution of the angle we chose the angle $\sim 60.8^0$ as the most frequent and comparable with results from Rio et al. (2014). Then on the Figure 5.12*b* the MLD at ∼67.2 m is retained. Furthermore, there is a maximum of distribution at this MLD around 60^0 angle. The 2D histogram does not show a large frequency of the distribution, the maximum number of the cases with the same MLD and angle is 4. It is sensitive to conditions that have been chosen, for example, the angles less than 0^0 were eliminated and β values were kept for the range from 0 to 1 m^{2}s/kg. Afterwards, based on the found MLD we can estimate β (Fig. 5.12*c*). β was estimated as the ratio of Ekman velocity amplitude and amplitude of wind stress $\beta = \frac{\sqrt{u_{Ekm}^2+v_{Ekm}^2}}{\sqrt{\tau_x^2+\tau_y^2}}$. On Figure 5.12*c* the β larger than 0.6 m^{2}s/kg corresponds to 0.014 m^{-1} (1/MLD). The choice of β is more complicated due to the noise in constructed time series of velocities (for geostrophic, wind, residual drifter velocity) as they come from different types of data. Thus, to simplify a little the choice I used the results of Rio et al. (2014) where almost the same analysis was done but θ and β were estimated based on a least square fit method. In their work β is almost never larger than 0.5 m^{2}s/kg at 15 m depth. Thus, for April 2013 based on the Figure 5.12*c* β was chosen equal to 0.42 m^{2}s/kg, whereas the maximum value of the distribution β_{max} equals to 0.83 m^{2}s/kg. The same analysis was done for all the other months.

For some months, this approach is difficult to apply. Figure 5.13 presents such an example for January 2013. This month is characterized by the frequent occurrence of rain and a strong change in the wind that were not well captured by ERA-Interim (see Chapter 2). As a consequence, the distribution of angle θ (Fig. 5.13*a*) is very random and it is difficult to choose one "peak" angle. The 2D histogram "MLD vs. θ" (Fig. 5.13*b*) shows that a dominant MLD is ∼112 m. Based on the results for the preceding and following months and from Rio et al. (2014) the angle of 53^0 was chosen. The β corresponding to 0.009 m^{-1} of 1/MLD (Fig. 5.13*c*) can be equal to 0.45 m^{2}s/kg as well as 0.23 m^{2}s/kg (again based on the preceding and following months and Rio et al. (2014)). The value 0.68 m^{2}s/kg was also stored, the maximum value of the distribution.

Some months can, thus, provide uncertain results and in this case the linear inter-

polation of θ and β from nearby months presents a possible solution.

The same analysis was done for the Mercator residual Ekman current at 15 m that also was filtered at low- and high-frequencies (Fig. 5.14 and 5.15). The wind velocity field was derived from wind stress of ECMWF that was assimilaed in Mercator. The results are less noisy than the ones from drifter velocities. The distribution of angle in April 2013 (Fig. 5.14*a*) shows a maximum at 83^0 that is larger than what was found from drifters. MLD (Fig. 5.14*b*) shows strong variations as April is a month of restrification. The maxima of distribution are all around the angle 83^0 that is in agreement with the angle distribution. We can chose the same MLD as in the case of drifters 67.2 m. From Fig. 5.14*c* using the values of 1/MLD 0.014 m^{-1} we found the

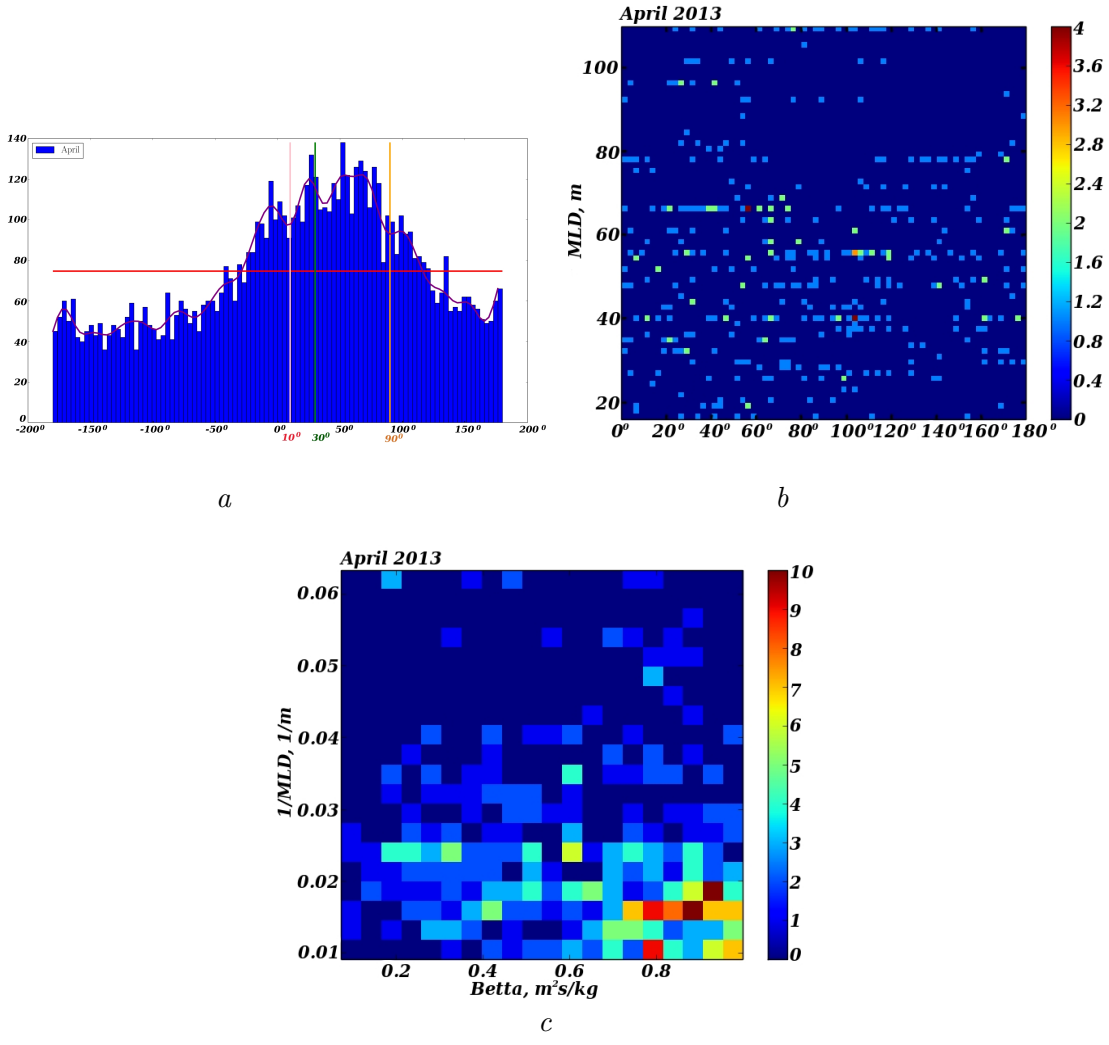

a *b* *c*

Figure 5.12: "Distribution approach" to estimate Ekman current at 15 m in SSS–max region in the North Atlantic subtropical gyre, drifter data, April 2013. *a* – distribution of angle between the wind and Ekman current at 15 m, *b* – 2D histogram of angles between the wind and Ekman at 15 m and MLD at the same time and spatial location, *c* – 2D histogram of parameter β and 1/MLD at the same time and spatial location

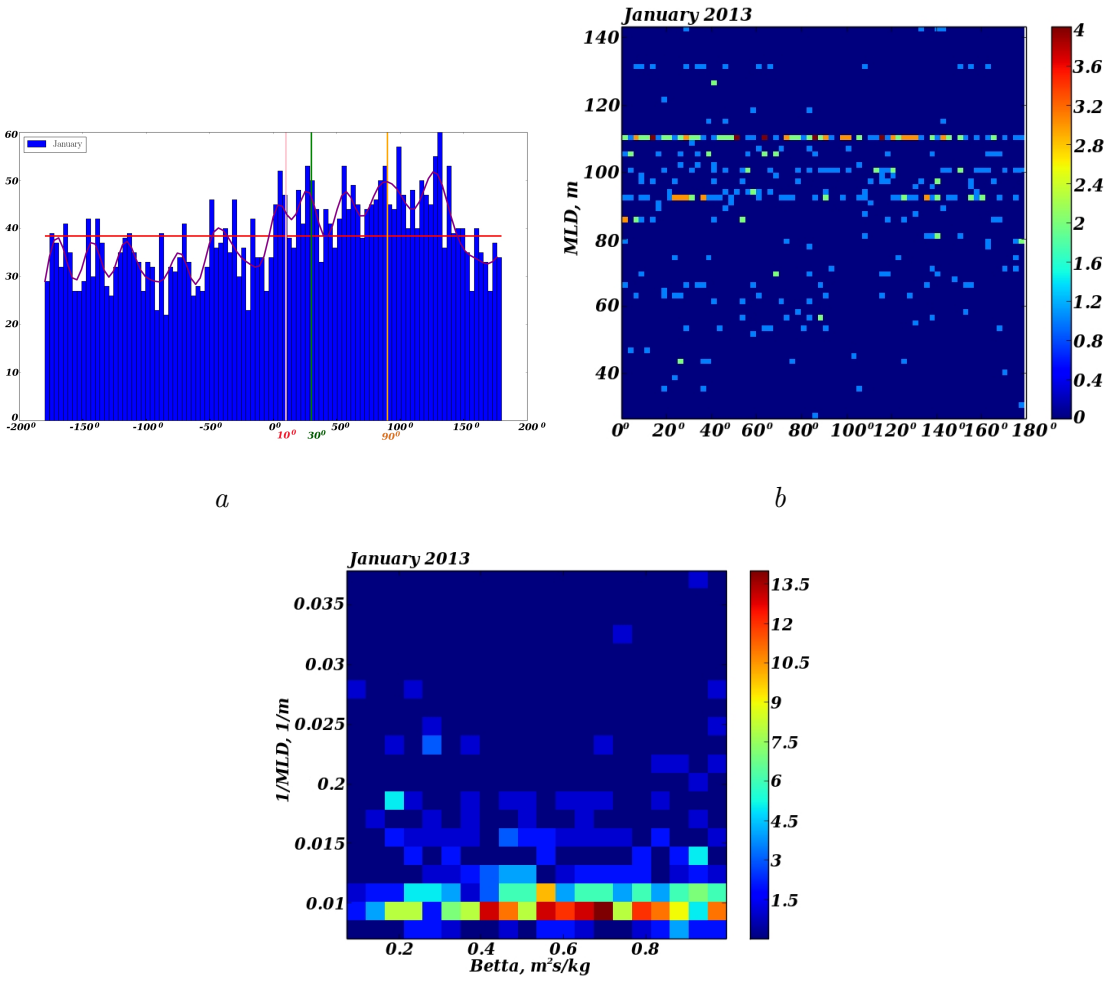

a *b* *c*

Figure 5.13: "Distribution approach" to estimate Ekman current at 15 m in SSS–max region in the North Atlantic subtropical gyre, drifter data, January 2013. *a* – distribution of angle between the wind and Ekman current at 15 m, *b* – 2D histogram of angles between the wind and Ekman at 15 m and MLD at the same time and spatial location, *c* – 2D histogram of parameter β and 1/MLD at the same time and spatial location

β values equals to 0.4 m^2s/kg.

In January 2013 the angle distribution (Fig. 5.15*a*) is less wide than for drifters on the Fig. 5.13*a*. The dominant angle in January 2013 was on the order of 79^0. Fig. 5.15*b* clearly shows one dominant level of MLD close to 112 m of depth with the maximum distribution around the angle of 79^0. The corresponding β is 0.38 m^2s/kg.

Figure 5.16 presents the summary of this analysis. The results obtained are compared with the results from Rio (2012) and Rio et al. (2014) (personal communication with Rio M.-H.) (dashed curves). The angles found by using drifter velocity (red solid curve) lie close to ones from Rio (2012) and Rio et al. (2014). The small difference can be explained by a small difference in the size of the region, period and drifter data

used. There is a seasonal cycle with an increase of the angle in summer when MLD is shallow. The angle from Mercator is much larger (red dashed-point curve). It presents a similar seasonal cycle, but with weaker changes.

The parameter β was difficult to estimate precisely, but we obtained results that are indicative and can provide a qualitative explanation for the differences between Mercator and observations. β from drifter data sets under the additional conditions from results of Rio et al. (2014) (for example, that β can not be larger than 0.5 m^2s/kg) (blue solid curve) is close to β from Rio's model. There is also, as for the angle θ, a seasonal cycle with the absolute maximum in summer. However, the β_{max} from the

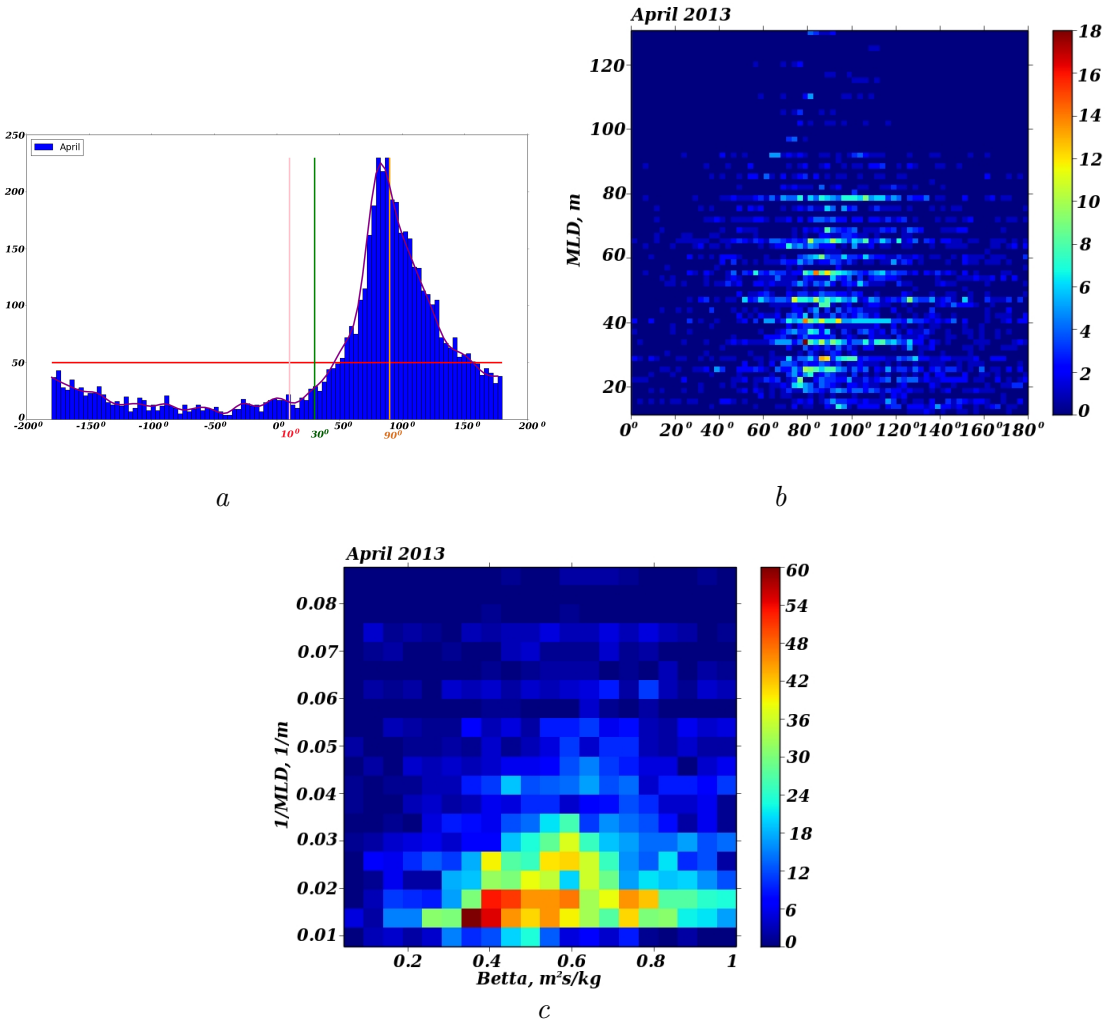

a b c

Figure 5.14: "Distribution approach" to estimate Ekman current at 15 m in SSS–max region in the North Atlantic subtropical gyre, Mercator analysis, April 2013. a – distribution of angle between the wind and Ekman current at 15 m, b – 2D histogram of angles between the wind and Ekman at 15 m and MLD at the same time and spatial location, c - 2D histogram of parameter and 1/MLD at the same time and spatial location

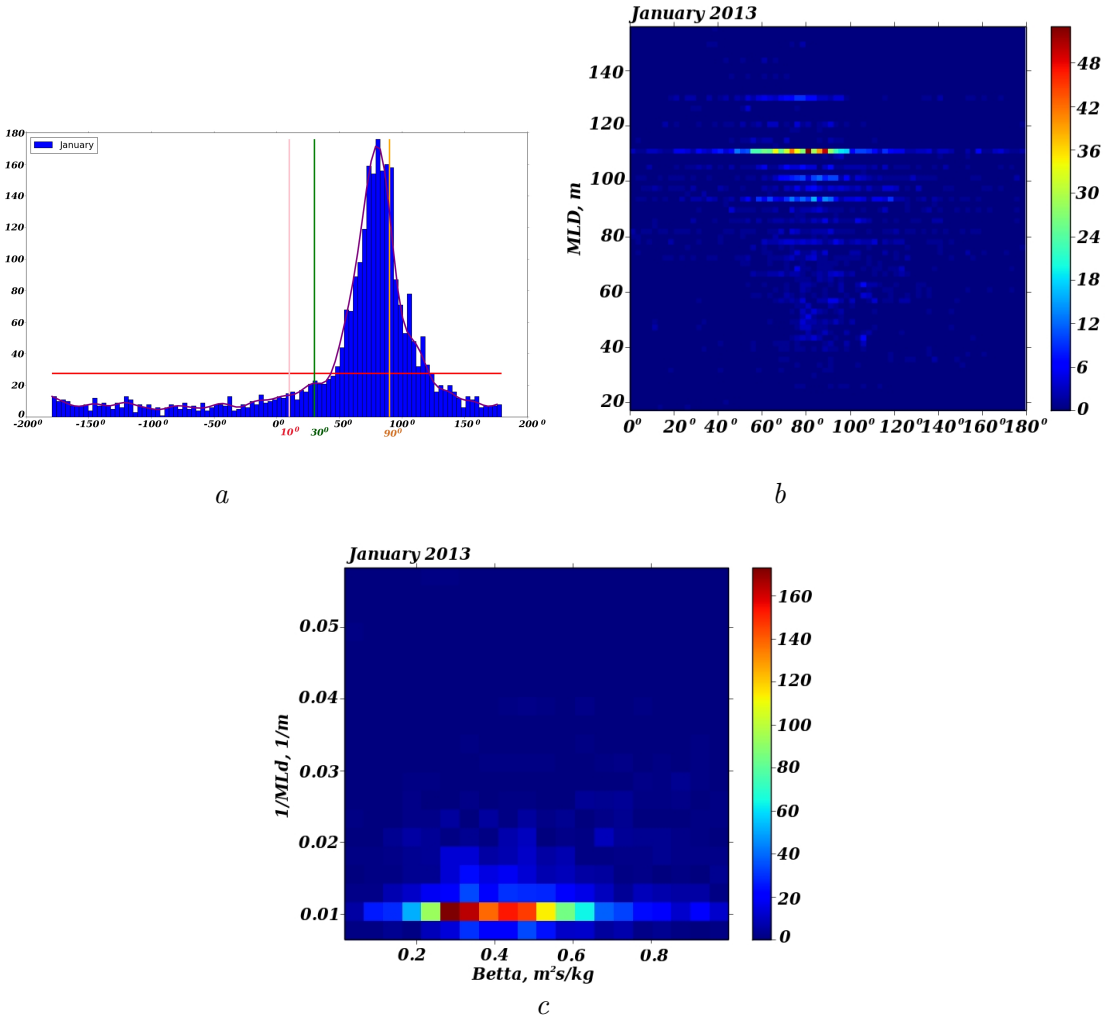

a b c

Figure 5.15: "Distribution approach" to estimate Ekman current at 15 m in SSS–max region in the North Atlantic subtropical gyre, Mercator analysis, January 2013. a – distribution of angle between the wind and Ekman current at 15 m, b – 2D histogram of angles between the wind and Ekman at 15 m and MLD at the same time and spatial location, c - 2D histogram of parameter and 1/MLD at the same time and spatial location

"distribution approach" proposed in this thesis work (black curve) shows large values and almost no seasonal cycle. The parameter β from the Mercator analysis (blue dashed-point curve) does also not show a strong seasonal variability, but lies closer to the Rio's result and much lower than one from drifters (black curve).

Figure 5.10 proposes one explanation for the differences between Ekman currents from Mercator and observations (drifters). As the Mercator estimates present stronger angle but lower amplitude it seems that the observed Ekman spiral is deeper (Fig. 5.10, blue vectors) compared to the one from Mercator (green vectors). Furthermore, the comparison with results from Rio et al. (2014) shows that β from Mercator tends to be lower in summer and larger in winter. The underestimation in summer can be again

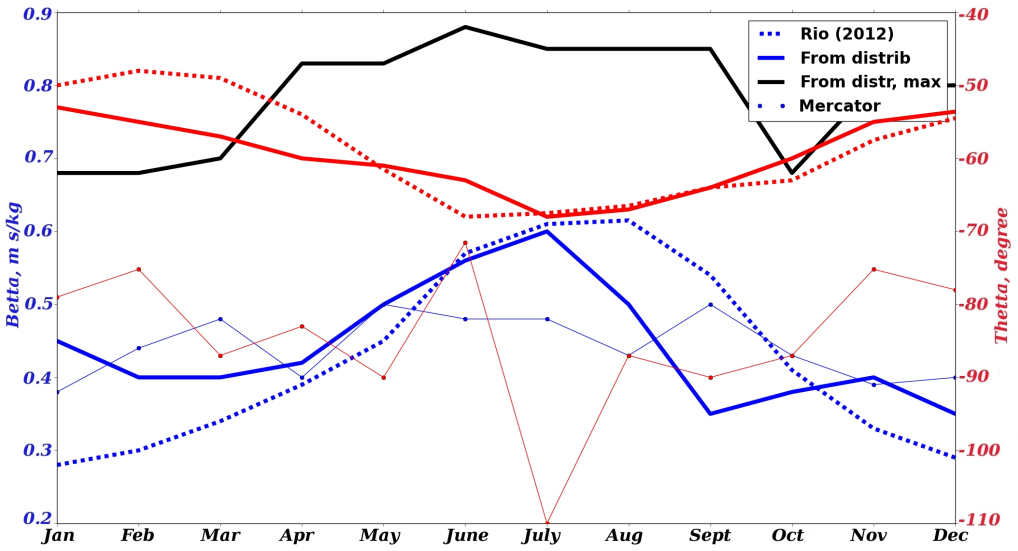

Figure 5.16: β (blue) and θ (red) parameters of Ekman model in SSS–max region $25^0N - 34^0N$ $50^0W - 26^0W$: solid curves – results of "distribution approach" with β under conditions from Rio et al. (2014); black – β_{max} from "distribution approach"; circles – results from Mercator analysis

explained by the shallow MLD while in winter the overestimation of Rio's results is likely due to the geostrophic shear that is more significant in winter due to the deeper MLD.

5.4 Conclusion

In this chapter the main question was: What is the source of such large difference between advection terms from Mercator analysis and from SMOS salinity combined with AVISO 2014 altimetry and ERA-Interim wind that was found in Chapter 4? There were several hypotheses to answer on this question: *(1)* uncertainties in velocity of ocean currents, *(2)* uncertainties in salinity field, and *(3)* imperfections of the method used to estimate the ocean currents. In this chapter the analysis was focused on hypotheses (1) and (3).

I estimated advection terms by combining different products. Thus, Mercator salinity with AVISO 2014 geostrophic velocity and Ekman current estimated by formula $\frac{\vec{\tau} e^{i*90}}{\rho f h}$ with the ERA-Interim wind showed results close to the ones found for SMOS salinity (Chapter 4), -0.26 pss/yr and -0.196 pss/yr, respectively. The small difference can be explained by the difference in salinity fields that seems to be small (RMSd is ∼0.18 pss). SMOS has a spatial resolution ∼45 km (and averaged over ∼75 km) while in Mercator it is ∼10 km. The advection term estimated with Mercator salinity and geostrophic velocity from Mercator SSH and Ekman current again estimated as in the previous case also showed smaller advection than the original Mercator horizontal advection (Chapter 4), -0.4 pss/yr and -0.76 pss/yr, respectively.

The separation of advection term in its Ekman and geostrophic components showed

that the geostophic advection from Mercator analysis is very close to the one estimated from SMOS and AVISO 2014, -0.027 pss/yr and -0.03 pss/yr. At the same time, Ekman advection from Mercator (Ekman current as residual from total ocean current and Mercator geostrophic) and SMOS with ERA-Interim wind in $\frac{\overrightarrow{\tau} e^{i*90}}{\rho f h}$ showed a huge difference. In the case of Mercator it was -0.88 pss/yr and in the case of SMOS it was equal to -0.17 pss/yr. The use of the formula $\frac{\overrightarrow{\tau} e^{i*90}}{\rho f h}$ for Ekman advection with Mercator salinity showed a reduction in its absolute value to -0.44 pss/yr.

The comparison of geostrophic components from AVISO 2014 regional altimetry product and Mercator SSH showed a small difference, 0.005 m/s. The two fields are quite similar: they show the same variability at low-frequency, and their TKEs (J/m^3) are very close, 4.2 J/m^3 for AVISO 2014 and 5 J/m^3 for Mercator in SSS–max region $21^0 - 30^0$N $50^0 - 26^0$W.

A geostrophic shear was found in the Mercator analysis. Geostrophic current derived from SSH and ocean current at 50 m were compared and showed that the velocity has a tendency to turn in the direction of larger density. This shear is small in the North Atlantic subtropical gyre and contributes to a little variation in geostrophic current through the ML. It results in a small monthly difference between the geostrophic salinity advection from observations (SMOS with AVISO 2014) and Mercator analysis.

The most important and interesting results were found for Ekman current. The Ekman current from Mercator (residual from the total ocean current in ML and geostrophic current from Mercator SSH) is larger than ones estimated by the widely used formula $\frac{\overrightarrow{\tau} e^{i*90}}{\rho f h}$ with wind stress $\overrightarrow{\tau}$ from ERA-Interim wind and daily MLD h from Mercator. RMS differences are around 0.015-0.02 m/s. It can be explained by an underestimation of MLD that is used in the formula or overestimation of the Ekman Depth in Mercator. The last reason for this difference could be due to the geostrophic shear in the ML that is not included in the geostrophic current estimated from SSH. The comparison of Ekman current from Mercator and Ekman currents derived from drifter velocity at 15 m showed that the differences can be large in winter. Furthermore, probably the Mercator Ekman Depth is underestimated compared to the "real one" (from drifter estimation) (Fig. 5.10).

The conclusion of this Chapter is that a major source for the difference between advection terms from Mercator analysis and observations (SMOS, AVISO) found in Chapter 4 originates from differences in Ekman currents. The formula $\frac{\overrightarrow{\tau} e^{i*90}}{\rho f h}$ tends to underestimate the Ekman velocity due to the underestimation of Ekman Depth compared to the Mercator and even "real" Ekman Depth (from drifter analysis). Thus, the advection term has to be larger in SMOS SSS budget and its contribution in the balance of water loss in the North Atlantic subtropical gyre can be more than 50% of the effect of surface forcing. The contributions of turbulent and mean advection are almost equal based on results for the Mercator analysis.

These results together with the Chapter 4 for Mercator analysis confirm results of earlier studies dedicated to the importance of eddy advection: turbulent/eddy advection is a critical component in the oceanic fresh water balance of the North Atlantic (Treguier et al., 2012; Büsecke et al. 2014; Gordon and Giulivi, 2014; Treguier et al., 2014; Amores et al, 2015). However its quantitative effect is debated. Thus, Gordon and Giulivi (2014) showed that more than 50% of the water loss in the subtropical

gyre can be compensated by eddy advection, while Amores et al. (2015) in their presentation indicated a smaller contribution between 20 and 40%. Amores et al. (2015) reconstructed in a different part of gyre the vertical eddy structure found from the mean sea level anomaly. Thus, it seems that the reconstruction can increase the effect of eddy advection. Treguier et al. (2012) and Treguier et al. (2014) proposed another method to examine the SSS budget. Separating the volume and salt transport they showed that the eddy and mean advection almost compensate each other in the North Atlantic Ocean and present a significant proportion of freshwater flux (30%). They also showed that there is a divergence of eddy advection in the North Atlantic centered in the SSS–max region with the stronger effect in the South. It is in agreement with our results in Chapter 4 for Mercator analysis: further north the turbulent advection is small -0.15 pss/yr, and even positive in the case of SMOS 0.001 pss/yr, and further south is larger than in SSS–max region and negative -0.58 pss/yr. Thus, in our estimations based on Mercator analysis the eddy turbulent advection explains around 30% of the freshwater flux in the North Atlantic subtropical gyre.

Chapter 6

Conclusions and perspectives

My PhD thesis work was dedicated to the investigation of sea surface salinity variability and processes causing this variability in the North Atlantic subtropical gyre. Salinity plays an important role in oceanography and air-sea interactions: salinity is a water mass tracer, it has an important dynamical role through the ocean density, and its spatial or time variations trace the freshwater fluxes at the interface with continents, ice or atmosphere (Schmitt, 1995; Tomczak, 1999; Ueki et al., 2002; de Boyer Montégut et al., 2004; Qu et al., 2011; Durack, 2015).

The North Atlantic subtropical region is characterized by the strong evaporation that dominates in the SSS budget. Horizontal salinity advection, entrainment and mixing processes contribute to balance salinization due to evaporation. These contributions of ocean dynamics in the MLS budget are strongly dependent on the scale and season: for example, the horizontal turbulent advection dominates at the small spatial scales while the Ekman advection is small at those scales but strongly contributes at large-scales (Dong et al., 2015; Farrar et al., 20105); entrainment is a major contributor to salinity change in winter when the MLD is deepening. There is a number of studies dedicated to the same analysis in the North Atlantic (Table 1.1 in Introduction). They rely on a wide range of data and methods used, and are devoted to different temporal and spatial scales. In this thesis work, for the first time, I presented the seasonal analysis of domain-averaged SSS and SST budgets at meso-scales based on the weekly-averaged data from high-resolution SMOS satellite and Mercator PSY2V4R2-R4 analysis products. The analysis was done for the period August 2012 – December 2014.

I used the corrected weekly SMOS product ($0.25^0 \times 0.25^0$) (Kolodziejczyk et al., 2015a), in which systematic and seasonal errors were removed from original SMOS ESA level 2 SSS v550 (Chapter 2). SMOS was the first satellite mission to measure sea surface salinity from space with the high initial requirements for temporal (at least 5 days) and spatial resolutions (at 50 km). I also used daily Mercator PSY2V4R2-R4 analysis ($1/12^0 \times 1/12^0$). The use of such a model allows to analyze SSS variability with data that are all on the same regular grid. It avoids uncertainties related to differences in processing, smoothing or interpolating the data. Mercator has a higher spatial resolution ($\sim$10 km) than SMOS ($\sim$50 km and then averaged over $\sim$75 km). Thus, the comparison of results from SMOS and Mercator can indicate the influence of small-scale processes that are not captured by SMOS. SMOS and Mercator were compared with

SSS from SPURS drifters, TSG and gridded ISAS product. The comparison showed promising results: RMS difference is on the order of 0.15 pss for SMOS and Mercator. It implies that two SSS fields capture some of the meso-scale salinity variability. However, at large-scales Mercator and SMOS showed large differences in regions where drifters were not present. These differences can indicate uncertainties in SMOS as well as in Mercator (Chapter 2, examples for January 2013 and August 2012). Thus, I concluded that these two products have errors of similar magnitudes, although with different characteristics.

In order to estimate the SSS budget a box with spatially constant (Argo profilers for SMOS) and spatially variable (Mercator) MLD was chosen in the core of SSS–max region $25.5^0 - 30^0$N $50^0 - 26^0$W in the North Atlantic subtropical gyre. This region presents small salinity gradient and a weak eddy activity that simplifies the estimation of SSS budget. To estimate the entrainment component I proposed a different method from the one widely used in literature. Usually, the effect of entrained salinity is estimated as the difference between the MLS and salinity averaged in the 20 or 10 m (Dong et al, 2015) water column below the MLD. In the present PhD work the entrainment velocity was used to estimate the layer of entrained water below the MLD and, thus, the salinity averaged in this layer that would be entrained.

The results found from Mercator analysis and SMOS satellite SSS fields (combined with GPCP, ERA-Interim, Argo products etc., see Chapter 2) showed a good qualitative agreement. Salinity shows a small tendency, -0.015 $\pm$ 0.32 pss/yr. The surface forcing (freshwater flux) is the dominant component in the SSS budget. Its time averaged effect on salinity is $\sim$1.05 $\pm$ 0.4 pss/yr. It shows the same seasonal cycle as salinity with an increase in spring–summer and a decrease in autumn–winter. Further north and south the air-sea freshwater flux shows the same seasonal variability while salinity in the South varies much less seasonally. It means that the contribution of ocean dynamics balancing the surface forcing on seasonal time scales is stronger in the South.

The main components of ocean dynamics that can influence the MLS are an entrainment of deeper water and a horizontal salinity advection, both mean and turbulent. In the case of Mercator the horizontal diffusion at submeso-scale was also estimated. Its contribution is small and negative, -0.02 $\pm$ 0.02 pss/yr, and, thus, contributes to the reduction of salinity. Entrainment shows its large contribution in late autumn–winter when the MLD is deepening. For the MLS budget estimated from SMOS salinity with Argo monthly constant MLD the entrainment is larger than the one from Mercator. This is explained by the inclusion of horizontal gradient of MLD in the entrainment term in the case of Mercator that results in a $\sim$35% reduction of the entrainment term. The effect of entrainment is stronger in the North where the MLD is deeper and contributes in a decrease of salinity. In the South it is lower and in the case of Mercator is positive. Positive entrainment in the South originates from the Shallow Meridional Overturning Circulation that brings subducted salty water from the North. Subducted salty water goes up in the South when the MLD is deepening and entraines some of this water. This entrainment of deep salty water was not present in SMOS ML budget due to the choice of constant MLD from Argos profilers and a too spotty distribution of these profilers over the region.

Advection does not vary a lot throughout the period in the SSS–max region and

strongly depends on its mean part. It is because the SSS–max region is a zone of divergence of eddy advection and convergence of Ekman advection that can result in the small seasonal variability of total advection (Treguier et al., 2012; Gordon and Giulivi, 2014). The mean advection is strong in the South and contributes here in a reduction of salinity especially during summer, period of heating. In the North it participates in a salinity increase in late spring–summer. The turbulent advection increases (in absolute values) further south from the SSS–max region which is in agreement with Treguier et al. (2012). Thus, advection is responsible for the northward shift of the high SSS from the region of E-P–max.

The advection term shows the largest quantitative difference between MLS budgets from SMOS and Mercator. Using Mercator analysis the advection becomes the major component of the budget that balances the salinization due to the water loss. It is three times larger (-0.76 ± 0.05 pss/yr) than the contribution of advection in the case of SMOS and AVISO (-0.2 ± 0.22 pss/yr). Moreover, in Mercator the turbulent/eddy advection has almost the same contribution as the mean advection, -0.32 ± 0.05 pss/yr and -0.44 ± 0.05 pss/yr, respectively, while in the MLS budget based on observations it is small (-0.026 ± 0.2 pss/yr).

Thus, in the North the advection (mostly mean advection) works with the entrainment to counteract the effect of surface forcing and brings salty water further north while in the South in the case of Mercator it strongly contributes (with the large eddy advection) to balance the freshwater flux and positive entrainment. In Mercator MLS budget the advection is responsible for more than a half of the balance after the water loss. Moreover, the turbulent (eddy) advection plays an important role as was found by Büsecke et al. (2014) and Gordon and Giulivi (2014).

However, the MLS budget cannot be closed. The residual terms in Mercator is much smaller than was found for SMOS in MLS budget, -0.05 $\pm$ 0.036 pss/yr and -0.3 $\pm$ 0.35 pss/yr, respectively, that is $\sim$9% and $\sim$47% of the averaged magnitude of $\frac{\partial \langle S \rangle}{\partial t}$ that varies, as in SMOS, in the range $\pm$0.65 pss/yr.

The MLT budget was also estimated and showed a near-balance between the terms retained. Mostly, the variability of SST is under control of the heat flux and entrainment of cold deep water in winter. The horizontal temperature advection is weak. Thus, the comparison of MLS and MLT budgets cannot be a good test of accuracy of data used for estimating of, for example, horizontal advection.

Each term in the MLS budget can be a potential source of errors. The uncertainties in precipitation and evaporation data in the freshwater flux is one of them (Table 4.2). Thus, for example, using different data from GPCP precipitation and OAFlux evaporation in Mercator MLS budget showed a much stronger residual -0.43 $\pm$ 0.4 pss/yr (66%) that was even larger than what was found for SMOS.

Another source of errors can be the entrainment term. The net entrainment term estimated with the horizontal gradient of MLD can be smaller by up to $\sim$35% that reduces residuals in winter. However, the estimation of this term still presents uncertainties: the residuals in Mercator are large when entrainment is large, and the time averaged residual is larger in the North where the contribution of entrainment is higher. It could be due to the method of estimating the salinity entrainment (see Chapter 3). The value of entrainment salinity was considered at the depth of MLD

from the next time step that could be significantly different from the salinity that was really entrained. It can also be due to mixing processes that are not properly considered.

Altogether, the most significant errors in SMOS MLS budget probably come from the advection term. As shown in Mercator it has to be the major component to balance the effect of evaporation. At the moment there is a big unexplained part of surface forcing in the SMOS salinity budget that has to be balanced by advection. This can be due to the underestimation of ocean currents (AVISO geostrophic, ERA-Interim wind) as well as the effect of a particular region where the eddy activity is weak and probably not well captured by data used. Also part of the uncertainties can originate from the difference in salinity fields from SMOS and Mercator and their different spatial resolution. Mercator with the resolution ∼10 km could capture better the small features of salinity (filaments and fronts) at the sea surface in the North Atlantic subtropical gyre.

I presented the comparison of geostrophic and Ekman components of ocean currents from different products and methods of estimation. The geostrophic currents from Mercator SSH and AVISO 2014 are similar in particular for their turbulent kinetic energy. Furthermore, the geostrophic advection from SMOS and Mercator shows almost the same contribution in MLS budget, -0.03 pss/yr and -0.027 pss/yr, respectively. Mercator current also shows the presence of a small vertical geostrophic shear that can have a small influence on the estimation of horizontal advection.

The comparison of daily Ekman current in MLD was made between Ekman current from Mercator (as residual from total ML current and geostrophic SSH current) and Ekman current estimated by $\frac{\overrightarrow{\tau} e^{i*90}}{\rho f h}$. I found that the MLD used in the formula can be underestimated and can explain larger Ekman current and, as consequence, larger Ekman advection in Mercator. Moreover, Ekman currents at 15 m from drifters and Mercator were compared using an empirical "distribution method". This test showed that the "real" Ekman Depth can be even lower than the one from Mercator. The use of the AVISO geostrophic current (that was used in the SMOS MLS budget) with Mercator salinity field showed results close to the ones from SMOS. It confirmed the hypothesis that the difference in advection term from the two products originates largely from the different in ocean currents, particularly the Ekman current component.

Thus, the advection term has to be larger than in SMOS SSS budget and its contribution in the balance of water loss in the North Atlantic subtropical gyre can be more than 50% of the effect of surface forcing. The contributions of turbulent and mean advection are almost equal based on results from Mercator analysis.

This subject still has a number of perspectives for further research. **Further tests of observations and Mercator analysis.** As mentioned before, the comparison of the salinity variability using SMOS and the Mercator PSY2V4 analysis that has a high spatial resolution (10 km) showed that SMOS has a sufficient resolution (50 km) to reproduce the large part of the meso-scale salinity variability in the North Atlantic subtropical gyre, and that the results can be compared with the ones from the Mercator analysis. However, it is worth noting that the smoothing has a large effect on eddy advection mostly due to the too smooth ocean current but also with possible effect on smooth salinity field that has to be further investigated. Thus, as one of the

perspective, SMOS product can be tested in regions of strong salinity gradients and in the presence of small filaments. The new global AVISO altimetry product can be used for this purpose as it seems to have the required accuracy and TKE in the North Atlantic. There are already some studies dedicated to this issue. For example, Reul et al. (2014) showed the strong capability of SMOS to capture cold-core rings in the region of Gulf Stream during warm season. However, it was mentioned that the SMOS SSS field is less accurate during cold season. The good agreement between SMOS SSS and AVISO SSH was also shown. The combination of SSS, SST and SSH can help to better estimate the sea surface density that further can be used to constrain subsurface currents. Nevertheless, the comparison of SMOS and Mercator analysis that has a high spatial resolution (10 km) showed a good agreement with RMS difference ∼0.2 pss/yr.

Control volume approach in estimation of MLS budget. It would be also interesting to estimate the MLS budget by the "control volume approach" proposed by Schmitt and Blair (2015). This approach is based on the fact that the SSS–max is deepening and spreading to the West and presents the form of a "sock" in three-dimensional view. This maximum is bound by contours of S = 37 pss that set the investigated volume. This approach allows to find a connection between ocean mixing processes and surface fluxes. The problem of this method, as mentioned before, is how to define this isohaline: over which time and space scales is it averaged, and thus what are the scales considered in eddy components. Probably a method of adaptive grids can be applied. Nevertheless, we can find already in the literature the analysis of the variability of the surface contour of S = 37 pss (or other relevant isohaline) and the different processes contributing to it, such as was done for the tropical Pacific in Hasson et al. (2013) and in the subtropical North Atlantic in Dohan et al. (2015).

Ekman current in ML. Also improvement in estimating Ekman current in ML is needed. It can be done by using other conditions and/or products for estimation of MLD h used in formula $\frac{\overrightarrow{\tau} e^{i*90}}{\rho f h}$. As mentioned before MLD seems to be underestimated for this particular task. It can result from the differences between MLD and Ekman depth that are considered as equal in this formula. The possible effect of these differences is expected to be smaller in the North Atlantic subtropical gyre, however, it has to be estimated and justified. Another possibility can be the use of products of total ocean current such as OSCAR, or as was done with Mercator. At the moment I proposed to use the formula $\frac{\overrightarrow{\tau} e^{i*90}}{\rho f h}$ but more attention should be devoted to the choice of MLD. The MLD can be estimated with other conditions for salinity and temperature gradient as well as derived from the comparison of several different products (ISAS, Argo, Mercator).

Estimation of entrainment term. The choice of MLD will also help to improve the entrainment term. Furthermore, for entrainment it would be useful to test another method of estimation of entrained salinity in the layer below the MLD.

Improvement of remote sensing SSS fields. The last and important perspective is to further validate and improve remote sensing salinity products (for example, SMOS). It includes as improvement in data of SMOS level 1 (calibration, image reconstruction, etc.) as well as further level 2 and 3 processing of satellite data (Melnichenko et al., 2014; Kolodziejczyk et al., 2015a; Boutin et al., 2016; Kolodziejczyk et al., 2016). There can be also improvements in level 4 products, by merging SSS from different satellite mission, such as SMOS and AQUARIUS or SMOS and SMAP.

Appendix A

Supporting information

A.1 SMOS satellite mission. Technical details of measurement of brightness temperature

Microwave Imaging Radiometer by Aperture Synthesis (MIRAS), a passive microwave[1] 2D interferometric radiometer operating in L-band (1.413 GHz) and used in SMOS satellite mission, produces 2D brightness temperature images without mechanical antenna scanning. This method provides high-resolution radio images (high angular resolution[2]) with an array of small antennas. In comparison, a real aperture radiometer at low-frequency (L-band) requires a very large antenna to reach a moderate resolution. MIRAS consists of a central structure and three deployable arms holding the equally distributed 69 antenna elements (lightweight cost effective front-end (LICEF) receivers). To provide the largest coverage (the best angular resolution) a Y-structure was proposed, with the three arms spaced 120^0 (Fig. 1.6). LICEF are the antenna-received integrated units that measure the radiation emitted from the Earth at L-band. The signal is then transmitted to a central correlator unit, which performs interferometry cross-correlations of the signals between all possible combinations of receiver pairs (SMOS Mission Payload, Last Batch of LICEF Receivers Delivered for SMOS).

The principle of L-band radiometer to measure SSS is based on the salinity sensitivity of sea surface brightness temperature[3] T_B at microwave frequencies. T_B is a product of the sea surface emissivity[4] and the sea surface temperature (SST).

[1]Passive remote sensing system detects Electromagnetic Radiation (EMR) that was naturally reflected or emitted from the surface of the Earth at relatively low energy levels 1–200 GHz. This is different from active remote sensing systems that create their own electromagnetic energy transmitted from the sensor with received signals then recorded by the remote sensor's receiver.

[2]Angular resolution or spatial resolution is the ability of the imaging system to distinguish small details of an object or distinguish objects that are close to each other. Thus, it determines the image resolution. It can also be presented in term of angular distance that is the size of the angle between the two objects.

[3]Brightness temperature is the temperature which a black body in thermal equilibrium with its surroundings would have with the same intensity as an observed grey body object at a frequency ν. A black body is a physical body that absorbs all incident electromagnetic radiation.

[4]The emissivity of the body surface is its effectiveness in emitting energy as spectral (thermal) radiation. Thermal radiation is electromagnetic radiation and it may include both visible radiation (light) and infrared radiation. Emissivity is the ratio of the thermal radiation from a surface to the

$$T_B = e(SSS, SST, roughness, \theta) * SST$$

where θ is an angle of incidence[5]. The surface emissivity is a function (through the water dielectric constant) of the salinity, temperature, and radio frequencies. In SMOS the SSS retrieval algorithm based on an iterative inversion method is used (details in Zine et al., 2008).

As was noted before the SMOS central correlator unit provides cross-correlation V of the signals in $(u, v) = (\Delta x, \Delta y)/\lambda_0$ wavelength coordinate systems (here, Δx and Δy are the distances between antenna positions normalized to the wavelength $\lambda_0 = c/f_0$, f_0 is the center frequency of the receivers). This cross-correlation can be written as the Fourier transformation (Font et al., 2010):

$$V(u, v) = F\left[T(\xi, \eta)\right]$$

Inverse Fourier transformation provides an image of the temperature T that is the difference between the brightness temperature of the object at pq polarization in antenna frame T_B^{pq} and the physical temperature of the instrument in $(\xi, \eta) = (\sin\theta\cos\varphi, \sin\theta\sin\varphi)$ coordinate system defined with respect to the X- and Y-axes of the antenna frame. The temperature of the instrument is normally known, thus, T_B can be derived. This step is called "image reconstruction". Figures A.1 *a*, *b*, *c* show this image reconstruction from (u, v)–domain (Fig. A.1 *a*) (hexagonal grid) to (ξ, η) (Fig. A.1 *b*). If the distance between antennas is from $d = \lambda_0/2$ to $d = \lambda_0/\sqrt{3}$ the image reconstruction is free from aliasing[6]. Otherwise, the closest six replicas overlap with the main one, and there is an aliasing effect (Fig. A.1 *d*, *e*). Thus, the snapshot of the alias-free field of view (AF–FOV) from the SMOS satellite will have a non-uniform hexagonal form (Fig. A.1 *e*).

The brightness temperature derived from inverse Fourier transformation is the T_B^{pq} polarized in antenna frame. Polarization is a direction of the electric (E) or magnetic (H) field in a propagating electromagnetic wave (Randa et al., 2008). Here, p and q are unit vectors oriented perpendicular to a vector of propagating wave $\overrightarrow{r}$ and satisfy $p \times q = \overrightarrow{r}/|\overrightarrow{r}|$. Thus, polarization is applied to estimate the orientation of microwave oscillations. There are six type of polarization: horizontal and vertical polarization, polarization with the linear slant of $\pm 45^0$ and right and left hand circular polarization. An electromagnetic wave at a certain frequency can be completely characterized by four Stokes parameters. In polarimetric remote sensing radiometry the Stokes parameters are expressed in terms of brightness temperature (more details can be found in Appendix A.2; Randa et al., 2008; Yueh et al., 2001).

Polarized T_B^{pq} in antenna reference frame can be transformed to T_B in Earth reference frame that requires knowledge of Faraday and geometric rotation angles (Camps et al. 2005; Appendix A.2).

---

radiation from a black-body surface at the same temperature. The ratio varies from 0 to 1.

[5]Incidence angle is the angle between the incident radar beam and the vertical (normal) to the intercepting surface.

[6]Aliasing is an effect when different signals become indistinguishable when sampled.

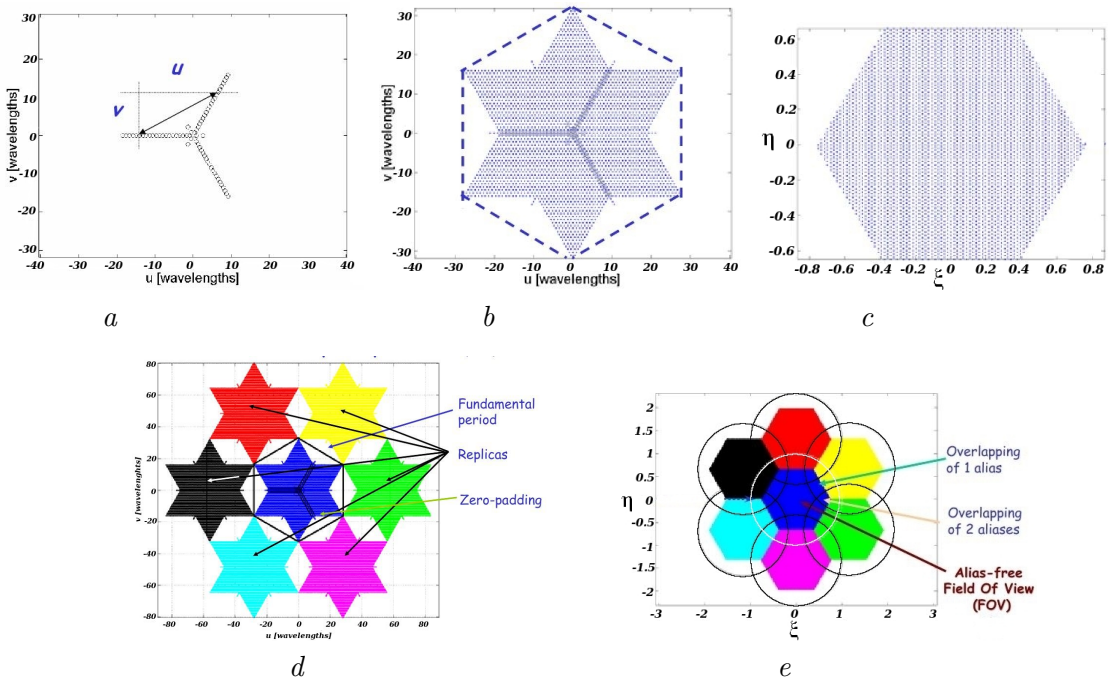

Figure A.1: Image reconstruction process: a – antenna positions, b – (u, v) spatial frequencies sampled by the SMOS Y-array, c – inverse Hexagonal Fourier transformation from (u, v) domain to (ξ, η) domain, d – periodic extension of the "visibility" samples in the (u, v) domain, e – periodic extension of the fundamental reciprocal grid (ξ, η). Source: Camps (2006)

The T_B measured by MIRAS is the apparent brightness temperature $T_{B,Ap}$. This includes the effect of atmosphere, reflections from the sun and the moon, galactic noise etc. These components bring their uncertainties to the sea brightness temperature. Further on, I presented the list of these phenomena and their effect on the brightness temperature.

Surface roughness and wind. $T_{B,sea} = (1-F)(T_{B,flat}+T_{B,rough})+T_{B,foam}$ is the T_B of the sea surface that includes the contribution of the rough ocean ($T_{B,rough}$) and foam ($T_{B,foam}$), F is the fraction of sea foam coverage (Zine et al., 2008; Mecklenburg et al., 2012). The coefficient F depends on the wind amplitude U_{10} that makes a T_B sensible to the wind change: increase of wind speed by 1 m/s leads to T_B increase by tenths of Kelvin degree (Yueh et al., 2001). Thus, the accuracy of data used for wind speed in the SMOS iterative method plays the critical role in the estimation of T_B at the sea surface and it makes the roughness of sea surface is one of the sources of big uncertainties. Yin et al. (2016) proposed a new analysis of foam emissivity model based on SMOS data that improved measurements of T_B but systematic biases of several Kelvins are still observed.

Sea surface temperature. The temperature brightness as mentioned before is sensible not only to surface roughness but also to SST. The tests of T_B sensitivity to SST show that the brightness temperature is less sensitive to the SSS for the cold water: 0.2 K (at 0 ^0C) to 0.8 K (30 ^0C) per pss unit (Yueh et al., 2001).

Atmosphere: *Dry air and water vapor.* The effect of the atmosphere on T_B at 1.4 GHz is very small. Water vapor bring the errors in range 0–0.08 K (Yueh et al., 2001). The effect of the clouds is also not significant at low frequency, the error is lower than 0.05 K (Martin, 2013; Yueh et al., 2001). Molecular oxygen is the radiatively active component in the dry atmosphere. As mentioned in Zine et al. (2008), molecules of oxygen have a permanent magnetic momentum, thus, the absorbation and radiation occur due to the mafnetic interactions with the incident field. Effect of oxygen depends on the pressure and the temperature of the atmosphere. The increase in T_B increases with increasing surface pressure and decreasing surface air temperature (Reul et al., 2012; Yueh et al., 2001). An increase of 10 mbar surface pressure increases T_B at an incidence of 40^0 by about 0.05 K. In low pressure and warm air temperature systems that is characteristic of tropical cyclones, a very large error of 100 mbar can result in a large contribution of the oxygen to L-band T_B that can be about 0.5 K (Reul et al., 2012).

Atmosphere: *Rain.* Meteorological phenomena such as rain, hail and snow participate in the absorption and diffusion of electromagnetic radiation. The effect of hail and snow is small at 1.4 GHz. The rain can change the roughness of the surface, and thus, change the diffusion of the electromagnetic waves, but this remains small as was shown for rain higher than 10 mm/h and wind lower than 7 m/s (Skou and Hoffman-Bang, 2005; Martin, 2013). Over the region of our interest, subtropical gyre of the North Atlantic, strong precipitation events are not common and one expects only a small influence of rain on SSS field.

Ionosphere: *Faraday rotation.* The microwave radiation from the earth propagates through the ionosphere[7] where the polarized components of the brightness temperature are rotated by the angle of Faraday rotation[8]. As it was shown in Yueh et al. (2001) the error due to the passing through the ionosphere is less than 0.1 K for a Faraday rotation of few degrees, and can exceed 10 K for Faraday rotation of 30^0 at 40^0 incidence. The error in $T - B$ at 6 a.m. due to the Faraday rotation can be 1.5 K (Zine et al., 2008).

Solar and galactic radiation. At L-band the sun is an extremely strong radiation source (10^5 to 10^7 K), and with the SMOS orientation, the sun is presented in 97% of the snapshots (Yueh et al., 2001; Font et al., 2010). The solar radiation can be felt both by the direct leakage into the antenna and by the reflection from the earth surface (Yueh et al., 2001). The antenna points towards the ocean, and thus, the influence of direct sunlight is negligible (less than 0.05 K). But when the sunlight is reflected or scattered by the surface of the ocean and reaches the main lobe of theéantenna, the impact varies from 0.5 to 50 K for $T_{sun} = 10^5$ – 10^7. In case of an isotropic diffusion (very rough reflective surface) the impact on antenna temperature is 0.1 K for the quiet sun period (10^5 K) and 10 K during the period of strong sun activity (Yueh et al., 2001). In the North Atlantic SSS retrieved data suffer from sun contamination mostly in winter in descending mode (Hernandez et al., 2014).

[7]The ionosphere is part of the Earth's atmosphere, from near 60 km to 1,000 km altitude. It is ionized by solar radiation, plays an important part in atmospheric electricity and influences radio propagation.

[8]Faraday effect or Faraday rotation is a magneto-optical effect that consists in the rotation of plane of polarized light when it propagates through an optically inactive substance in a magnetic field.

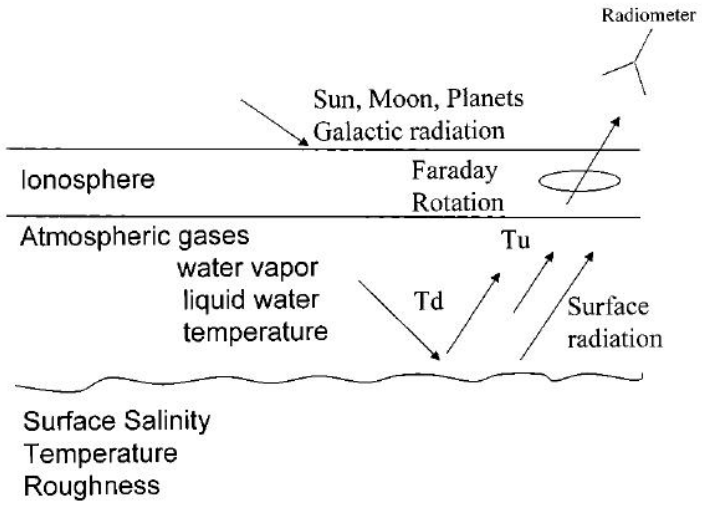

Figure A.2: Geophysical sources influence the microwave radiation from the sea surface. Source: Yueh et al. (2001) (Fig. 1) ©2001 IEEE

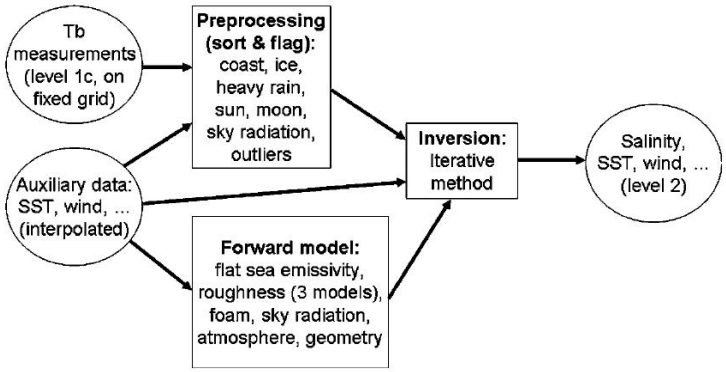

Figure A.3: Block diagram of the SMOS SSS retrieval processor. Source: Font et al. (2010) (Fig. 8) ©2010 IEEE

Sun effect on the average T_B transforms in the image reconstruction biases. The sun-glint-induced image reconstruction biases are weakly dependent on the wind that can change the sea roughness. Thus, the uniform wind speed 7 m/s is used to detect the image reconstruction biases. Furthermore, the center of the sun's glitter is never in the SMOS AF FOV, but during the winter it lies close to the right-hand border of the FOV that produces a significant contamination.

The effect of the Moon and planets in our solar system is negligible. The Moon T_B is about 200 K with a small dependence on the lunar phase. When the lunar radiation affects the antenna boresight, the effect on the apparent antenna T_B is about 5 K. The effect of other planets is negligible because their angular extension are lower than the one from the Moon (0.215 deg^2) with T_B not longer than a few hundreds of a Kelvin degree (Yueh et al., 2001).

Radio-Frequency Interference. RFI originates from man-made emitters on the ground, on aircraft or space-borne systems that emits in the same frequency band as SMOS (Mecklenburg et al., 2012). It was found (Mecklenburg et al., 2012, Oliva et al., 2012) that the SMOS mission is perturbed by RFI especially over continental areas in Europe, south Asia and the Middle East, and over the ocean in the Northern Hemisphere above 55^0 latitude. SMOS on-board processing does not remove the RFI from the acquisition. The data are averaged without filtering over periods of 1.2s for V and H polarization. Several methods to detect this errors were proposed (Oliva et al., 2013; Soldo et al., 2014).

Calibration. Errors in the instrument calibration bring some uncertainties in the final data fields. This was seen both at the beginning of the mission (Mecklenburg et al., 2012; Boutin et al., 2016).

This list gives an idea of the work and overview of some problems in SMOS. I would like to emphasize that the main difficulties in SMOS relay to the image reconstruction (alias problem due to the strong effect of the sun that convert into T_B biases) and the bad controlled modernization of the temperature of the instrument.

To reduce some of the errors presented the independent errors from multiple satellite passes over a fixed grid cell can be averaged temporally. The revisit time can be a few hours for high latitudes and 1–3 days for equatorial regions, as proposed in Yueh et al., 2001. But this mostly helps in case of random errors (sea surface state data, galactic noise, temperature of radiometric , sun radiation etc), with little effect on the systematic errors (calibration, RFI, model problems etc.). Today, large efforts are dedicated to remove these time-constant errors (Melnichenko et al., 2014; Kolodziejczyk et al., 2015(a); Boutin et al., 2016; Kolodziejczyk et al., 2016).

The summary of the error sources is presented on Figure A.2. The SMOS retrieval process is schematically presented on Figure A.3.

In this work we will use corrected SMOS data for which seasonal and coastal systematic errors have been removed (Kolodziejczyk et al., 2015(a); Kolodziejczyk et al., 2016).

A.2 Polarization and Stokes parameters

a) Stokes parameters are the parameters that can completely characterize an electromagnetic wave at a given frequency. The first Stokes parameter (I) denotes the total intensity of the wave. The second Stokes parameter (Q) is the difference between the flux densities polarized in two orthogonal directions in a given polarized frame (vertical polarization and horizontal polarization). The third (U) and fourth (V) Stokes parameters respectively represent twice the real and imaginary parts of the cross-correlation between these orthogonal polarization. The third Stokes parameter can also be defined as a difference between $+45^0$ and -45^0 skewed linearly polarized flux densities, and the fourth parameter as a difference between left-handed and right-handed circularly polarized flux densities:

$$I = \frac{\langle |E_v|^2 \rangle + \langle |E_h|^2 \rangle}{\eta} = S_v + S_h,$$

$$Q = \frac{\langle |E_v|^2 \rangle - \langle |E_h|^2 \rangle}{\eta} = S_v - S_h,$$

$$U = \frac{2 * Re \langle E_v E_h^* \rangle}{\eta} = S_{+45} - S_{-45},$$

$$V = \frac{2 * Im \langle E_v E_h^* \rangle}{\eta} = S_{lc} - S_{rc},$$

where S is the flux density of the wave (W/m^2). The subscriptions v, h, $+45$, -45, lc and rc represent respectively the vertically, horizontally, $+45^0$ skewed linearly, -45^0 skewed linearly, left-handed circularly, and right-handed circularly polarized waves, η is the wave impedance of the medium, and E_v and E_h are the electric field components with vertical and horizontal polarization, respectively.

In polarimetric remote sensing radiometry the Stokes parameters are expressed in terms of brightness temperature (in kelvins):

$$T_I = \frac{\lambda^2}{k_B * B} * I,$$

$$T_Q = \frac{\lambda^2}{k_B * B} * Q,$$

$$T_U = \frac{\lambda^2}{k_B * B} * U,$$

$$T_V = \frac{\lambda^2}{k_B * B} * V,$$

where λ, k_B and B are wavelength, Boltzmann's constant and noise-equivalent bandwidth, respectively. Noise-equivalent bandwidth is the width of an ideal rectangular filter having the same maximum gain as the real filter, and which produces the same output available power as the real one when the input is white noise. These definitions were taken from Randa et al. (2008).

Measurements by earth remote sensing conventional radiometer is expressed as T_h and T_v (the brightness temperature of horizontal and vertical polarization) and for this reason the modified Stokes parameters are used (Ranad et al., 2008; Yueh et al., 2001):

$$T_v = \frac{\lambda^2}{k_B * B} * \frac{I + Q}{2},$$

$$T_h = \frac{\lambda^2}{k_B * B} * \frac{I - Q}{2},$$

$$T_3 = \frac{\lambda^2}{k_B * B} * U,$$

$$T_4 = \frac{\lambda^2}{k_B * B} * V,$$

while the first and second parameters characterize the T_B of vertical and horizontal polarization, the third and fourth parameters characterize the correlation between these two orthogonal polarizations.

b) Since $T_{pq}(\xi, \eta)$ is proportional to $\left\langle E_p E_q^* \right\rangle /2$, the brightness temperatures in the antenna reference frame at a given polarization (X or Y) can be expressed as a linear combination of the brightness temperatures in the earth's pixel reference frame (H or V). Transformation from antenna to earth reference frame for full-mode polarization has a form $T_{antenna} = M_{full-pol} * T_{earth}$ (Camps et al., 2005; Camps, 2006), where:

$$\begin{bmatrix} T_{xx} \\ T_{xy} \\ T_{yx} \\ T_{yy} \end{bmatrix} = \begin{bmatrix} A^2 & AB & AB & B^2 \\ -AB & A^2 & -B^2 & AB \\ -AB & -B^2 & A^2 & AB \\ B^2 & -AB & -AB & A^2 \end{bmatrix} \begin{bmatrix} T_{hh} \\ T_{hv} \\ T_{vh} \\ T_{vv} \end{bmatrix}$$

where $A = \cos(\varphi_{Faraday} - \varphi_{geometry})$, $B = \sin(\varphi_{Faraday} - \varphi_{geometry})$.

A.3 Bulk flux algorithm

The Monin-Obukhov similarity (MOS) theory (Monin and Obukhov, 1954) is used for the bulk flux algorithm to estimate the atmospheric components in the surface layer in the Tropical Ocean-Global Atmosphere Coupled-Ocean Atmosphere Response Experiment (COARE 2.0). This theory describes relationships between non-dimensionalized variables in surface boundary layer and is based on a large amount of the empirical data.

As the basic structure the bulk paramterization of Liu-Katsaros-Businger (LKB) (Liu et al., 1979) is used. This parameterization was modified to improve the accuracy of mooring data from COARE 2.0 (Fairall et al., 1996). COARE 2.0 bulk flux algorithm is also used for the data from the SPURS mooring presented in this thesis work.

The standard bulk expression for the scalar fluxes and stress components are:

$$H_s = \rho_a c_{pa} C_h S(T_s - \theta),$$

$$H_l = \rho_a L_e C_e S(q_s - q),$$

$$\tau_i = \rho_a C_d S(u_{si} - u_i),$$

where H_s and H_l are the turbulent fluxes of sensible and latent heat, τ_i is wind stress; $C_d(z_0)$, $C_h(z_{0T})$ and $C_e(z_{0q})$ are the transfer coefficient fro stress, sensible heat and latent heat, respectively; θ is the potential temperature, q is the water vapor mixing ratio, and u_i is one of the horizontal wind components relative to the fixed Earth; S is the averaged value of the wind speed relative to the sea surface at some atmospheric reference height z_r; T_s is the sea surface interface temperature; u_{si} is the surface current; q_s is the interfacial value of the water vapor mixing ratio.

The first modification is associated with the specification of the roughness/stress relationship. The following formula is used for the roughness length:

$$z_0 = \alpha \frac{u_*^2}{g} + 0.11 \frac{\nu}{u_*},$$

where the first part presents the relationship between oceanic roughness and stress for rough flow (Charnock, 1955) and the second part is this relationship for the smooth flow. The modification consists in the addition of the first term to the widely used second term from the LKB theory. u_* is the related Monin-Obukhov similarity scaling parameter of the horizontal wind, ν is the kinematic viscosity of air, α is the Charnock constant (values between 0.01 and 0.035).

The second modification is related to the MOS profile functions that participate in the transfer coefficients. These functions are modified to alter the dependence on stability of the profiles of temperature, moisture, and momentum in highly unstable conditions.

Another approach is based on the fact that in the standard bulk expressions for the scalar fluxes and stress components the parameter S is the averaged value of the instantaneous wind speed, and not magnitude of the mean wind vector. The horizontal velocity fluctuation in the surface layer of the convective boundary layer do not obey Monon-Obukhov similarity but scale with the convective velocity (Godfrey and Beljaars, 1991). Following Fairall et al . (1996) S can be written as:

$$S^2 = u_x^2 + u_y^2 + w_g^2 = u^2 + w_g^2,$$

where u_x and u_y are the mean wind components, w_g is proportional to the convective scaling velocity

$$w_g = \beta W_*,$$

where β is an empirical constant, of the order of 1.0 and

$$W_*^3 = \frac{g}{T}\left[\frac{H_s(z_{0T}, S)}{\rho_a c_{pa}} + 0.61 T \frac{H_l(z_{0q}, S)}{\rho_a L_e}\right] z_i,$$

with air temperature T, sensible heat H_s, latent heat H_l, specific heat of dry air c_{pa}, density of moist air ρ_a, latent heat of evaporation L_e. The convective velocity presents

the transport of air by the large coherent thermal structures from the surface layer into the interior of the turbulent mixed layer (Stull, 1994).

The cool-skin and warm-layer corrections are applied. As explained in Fairall et al. (1996) the sensible, latent and longwave radiations in the first several millimeters of the surface lead to a "cool skin". It is noted that the difference in temperature between the surface water and the water a millimeter below can be 0.2-0.5K. On the other hand about half the solar radiation is absorbed in the first several meters of the ocean. In the conditions of the light wind the surface temperature warmed by this solar radiation can produce warm layer less than a meter deep. This requires corrections in the bulk algorithm. The correction is based on integrals of the surface energy and momentum budgets and requires additional data input of solar and IR radiative fluxes.

The last correction is associated with the effect of the precipitation on the sensible heat flux (the rain is at the wet-bulb temperature) and modification of the latent heat flux estimated according with Webb correction (Webb et al., 1980) that requires the net dry mass flux be zero.

A.4 Altimetry product. What is SLA and MDT?

Mean dynamic topography (MDT) is the average over a selected period of the height of the sea surface referenced to the geoid. The geoid is a gravity equipotential surface that would correspond with the ocean surface if ocean was at rest (Dussurget et al., 2015).

A sea-level anomaly (SLA) is the difference between the total sea-level and the average sea-level for this time of year.

Cross-calibration is the radiometric comparison of one sensor to another sensor on different satellites. For cross-calibration, sensors have to calibrate to a common target. Thus, cross-calibration of two sensors has to be performed on the same target at the same time and avoiding possible change of target scene (changes in atmosphere, for example) (Bosch and Savcenko, 2007).

A.5 Thermal wind

The geostrophic current changes with depth due to the Coriolis force but also due to the difference in ocean density. Pressure gradient force (PGF) is directed from the region of high pressure to low (or from the region of low density to high). Using geostrophic momentum balances and hydrostatic balance, one can derive the relation between vertical shear in geostrophic velocity and horizontal density derivatives that called Thermal wind:

$$-f\frac{\partial v}{\partial z} = \frac{g}{\rho_0}\frac{\partial \rho}{\partial x}, \qquad f\frac{\partial u}{\partial z} = \frac{g}{\rho_0}\frac{\partial \rho}{\partial y}.$$

In the North Atlantic SSS–max region due to the strong density gradient the geostrophic shear is expected in clockwise direction from the geostrophic current derived from SSH. Figure A.4 shows this effect based on Mercator ocean currents. Blue

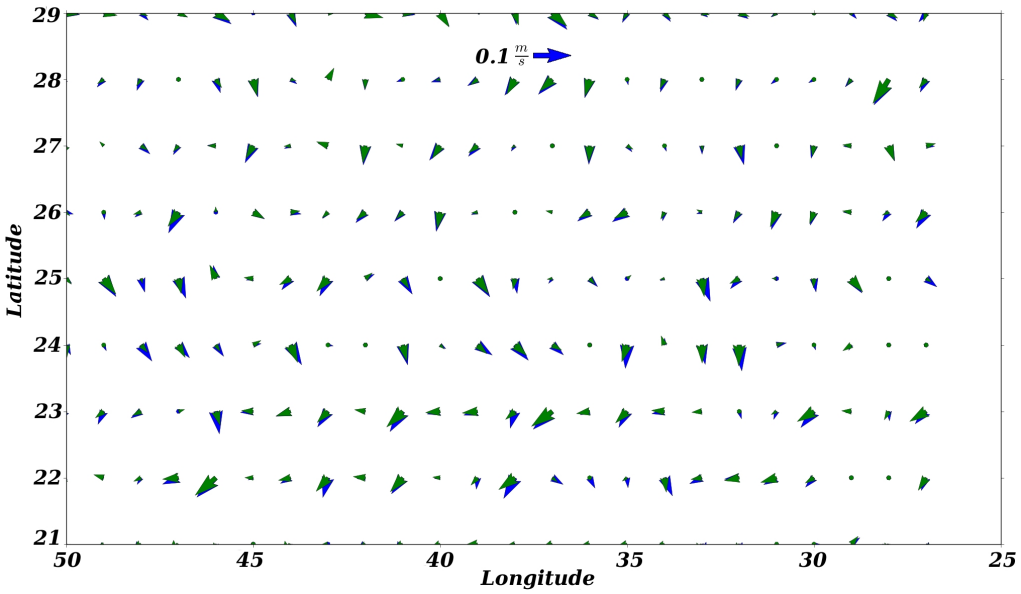

Figure A.4: Effect of geostrophic shear in Mercator simulated ocean current averaged over August 2012 – December 2014 period in SSS–max region: blue – geostrophic current from Mercator SSH; green – Mercator ocean current at 50 m depth

vectors represent the geostrophic current derived from geostrophic balance equations and SSH while green vectors are ocean current from Mercator at 50 m depth. The velocity was averaged over the period August 2012 – December 2014 at each grid point. Most of the time the green vectors turn to the right from the blue ones. In the South of the region the gradient of density (through salinity) is positive in x and y directions (as the SSS maximum core is centered in the region further north). Thus, the vertical gradient of u is positive and negative for v (in agreement with results in section 5.1) that explains this rotation to the right. In the center of the region almost there is not a turn of vector as the salinity gradient is not very different in its x or y directions.

Using equations presented above and density ρ from Mercator analysis and averaged over the ML we obtained the results presented on Fig. A.5. There are geostrophic shears in winter (yellow curves) that were not included in AVISO 2014 geostrophic current (red curves).

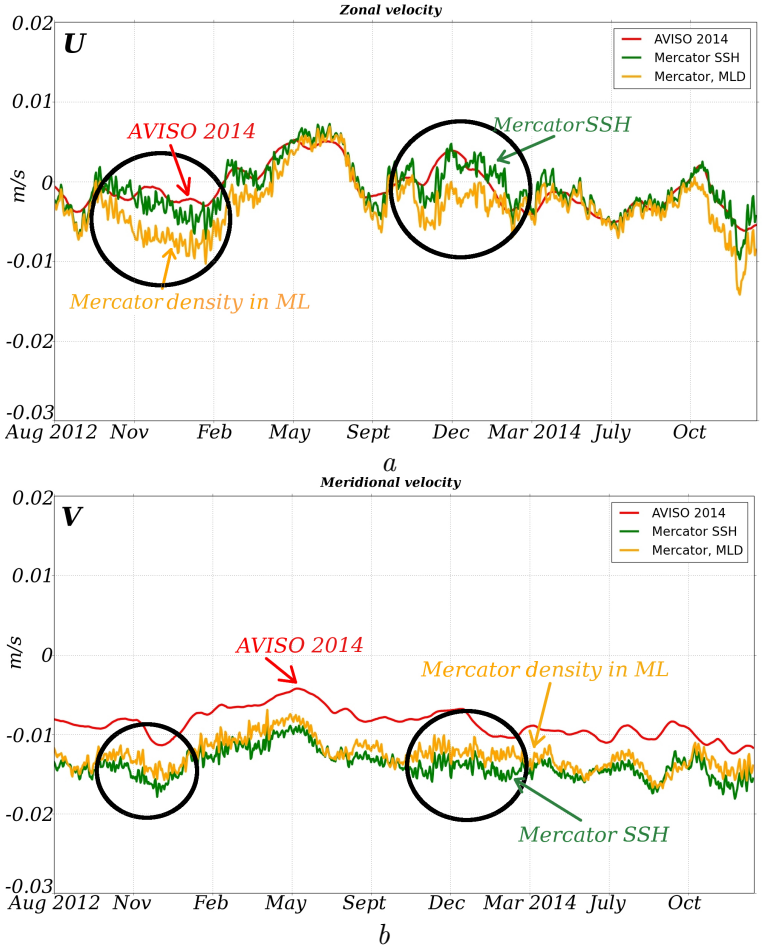

Figure A.5: Zonal (a) and meridional (b) geostrophic velocity in SSS–max region $21^0 - 30^0$N $50^0 - 26^0$W: red – AVISO 2014; green – Mercator geostrophic velocity from SSH; black – geostrophic shear in ML estimated by equations from A.5 based on the density ρ from Mercator analysis

Appendix B
Article: Sommer et al., 2015

frontiers in Marine Science

ORIGINAL RESEARCH
published: 08 December 2015
doi: 10.3389/fmars.2015.00107

Sea Surface Salinity and Temperature Budgets in the North Atlantic Subtropical Gyre during SPURS Experiment: August 2012-August 2013

Anna Sommer[1], Gilles Reverdin[1]*, Nicolas Kolodziejczyk[1,2] and Jacqueline Boutin[1]*

[1] LOCEAN/IPSL, Sorbonne Universités (University Pierre et Marie Curie, Univ Paris 06)-Centre National de la Recherche Scientifique-IRD-Muséum National d'Histoire Naturelle, Paris, France, [2] Laboratoire de Physique des Oceans, UMR Centre National de la Recherche Scientifique/Ifremer/IRD/UBO-IUEM, Brest, France

Variability at large to meso-scale in sea surface salinity (SSS) and sea surface temperature (SST) is investigated in the subtropical North Atlantic Ocean during the Subtropical Atlantic Surface Salinity Experiment Strasse/SPURS in August 2012—August 2013. The products of the Soil Moisture and Ocean Salinity (SMOS) mission corrected from large scale systematic errors are tested and used to retrieve meso-scale salinity features, while OSTIA products, resolving meso-scale temperature features are used for SST. The comparison of corrected SMOS SSS data with drifter's *in situ* measurements from SPURS experiment shows a reasonable agreement, especially during winter time with RMS differences on the order of 0.15 pss (for 10 days, 75 km resolution SMOS product). The analysis of SSS (SST) variability reveals that the meso-scale eddies contribute to a substantial freshening (cooling) in the central high salinity region of the subtropical gyre, albeit smaller than Ekman and atmospheric freshwater (heat) seasonal flux, which are the leading terms in SSS (SST) budget. An error is estimated along with SSS and SST budgets; as well as sensitivity to the different products in use and residuals are discussed. The residuals in the SSS budget are large and can arise from errors in the advection fields and freshwater flux, from neglected small scale or unresolved local processes (salt fingering, vertical mixing, and small scale subduction, etc.). However, their magnitude is similar to what is often parameterized as eddy horizontal diffusion to close large scale budgets.

Keywords: salinity, temperature, budget, meso-scale, advection, SMOS, SPURS

OPEN ACCESS

Edited by:
Chris Bowler,
École Normale Supérieure, France

Reviewed by:
Fabien Roquet,
Stockholm University, Sweden
Shinya Kouketsu,
Japan Agency for Marine-Earth Science and Technology, Japan

****Correspondence:***
Anna Sommer
anna.sommer@locean-ipsl.upmc.fr;
Gilles Reverdin
reve@locean-ipsl.upmc.fr

Specialty section:
This article was submitted to Ocean Observation, a section of the journal Frontiers in Marine Science

Received: *24 September 2015*
Accepted: *20 November 2015*
Published: *08 December 2015*

Citation:
Sommer A, Reverdin G, Kolodziejczyk N and Boutin J (2015) Sea Surface Salinity and Temperature Budgets in the North Atlantic Subtropical Gyre during SPURS Experiment: August 2012-August 2013. Front. Mar. Sci. 2:107. doi: 10.3389/fmars.2015.00107

INTRODUCTION

The water cycle is a predominant element of the Earth's climate which has a specific impact on human society among agriculture, energy and water supply. In the global water cycle, the ocean plays a key role, with ~86% of global evaporation and 78% of global precipitation taking place over the ocean (Schmitt, 1995). Despite growing observing capability, in particular from satellites, our knowledge of precipitation (P) and evaporation (E) over the oceans is still rudimentary (Trenberth et al., 2007; Skliris et al., 2014; Durack, 2015). It is due to coarse available *in situ* measurements and insufficient sampling or systematic errors in satellite retrievals.

The climatological mean of sea surface salinity (SSS) is closely related to the surface E-P flux (Schmitt, 1995; Durack, 2015). Thus, as the ocean salinity is better observed than P or E, its monitoring could also contribute to better understand the pattern and variability of the E-P field. Large salinity trends or multi-decadal variability have been observed in large parts of the world ocean in the last 30–50 years (Durack and Wijffels, 2010; Terray et al., 2012; Skliris et al., 2014). They provide sharper information about a changing global water cycle than terrestrial data (river flows, evaporation or precipitation) which show less trends (Dai et al., 2009; Lagerloef et al., 2010).

The changes in salinity concentration originate from precipitation, evaporation, runoff, ice freezing and melting, as well as changes in ocean circulation and mixing (Talley, 2002). Thus, the ocean dynamics needs to be accurately assessed to link E-P field's variability with change in SSS (Yu, 2011). At meso-scale, recent work in the North Atlantic subtropical gyre (Qu et al., 2011; Busecke et al., 2014; Gordon and Giulivi, 2014; Farrar et al., 2015) shows a significant contribution of horizontal advection in governing surface salinity, with roughly half of the salinity variation being explained by ocean meso-scale dynamics. In the South Pacific, the compensation of fresh water loss is also made by vertical turbulent mixing and horizontal salinity advection (Hasson et al., 2013; Kolodziejczyk and Gaillard, 2013). However, in these studies, the respective contribution of meso-scale advection and vertical mixing is not very well established because of uncertainties in the data sets and also because of the crude horizontal resolution.

In this work we concentrate our investigation on near-surface salinity and temperature budgets in the saltiest region of the world open ocean, the sub-tropical gyre of the North Atlantic Ocean (NSTG, **Figure 1**). In this region, evaporation is a dominant component of the salinity budget, as shown in the E-P climatological map. The eastern subtropical North Atlantic surface area is affected by dry continental air from North Africa. To balance this water loss due to the excess of evaporation flux, fresh water transport is contributed by eddies, mixing processes, and Ekman transport (Gordon and Giulivi, 2014). The Ekman transport from the tropics is large in this region and brings fresh and warm surface water from the tropics, while further north a weaker Ekman transport brings fresh and cold water. The vertical entrainment of deeper water is expected to be a major contributor to the salinity (Dong et al., 2015) and temperature change in particular during the winter. At large-scale, the change of SSS in salinity maximum region is small compared with the amplitude of the sea surface forcing and "residual terms" (subduction, vertical shear, vertical motions, internal waves and all small-scale and fast dynamics, Dohan et al., 2015) that close the budget. Furthermore, Dong et al. (2015) found that for the SSS (or fresh water) budget the Ekman component dominates the total horizontal advection in this North Atlantic region. On the other hand, at the scale of turbulent advection, it is worth to note that the Ekman transport does not play a significant role. The turbulent advection is indeed mainly responsible for the freshening and warming/cooling by eddies (Busecke et al., 2014).

To estimate a regional surface salinity budget during the period August 2012–2013, surface salinity product derived from the Soil Moisture and Ocean Salinity (SMOS) satellite mission, a regional ocean current product produced by AVISO and *in situ* data collected during the SPURS (Salinity Processes in the Upper-ocean Regional Study) experiment are used. The SPURS experiment took place in August 2012–April 2013 (**Figure 1**, black box). Its goal was to better understand the mechanisms responsible for salinity maximum formation in the subtropical

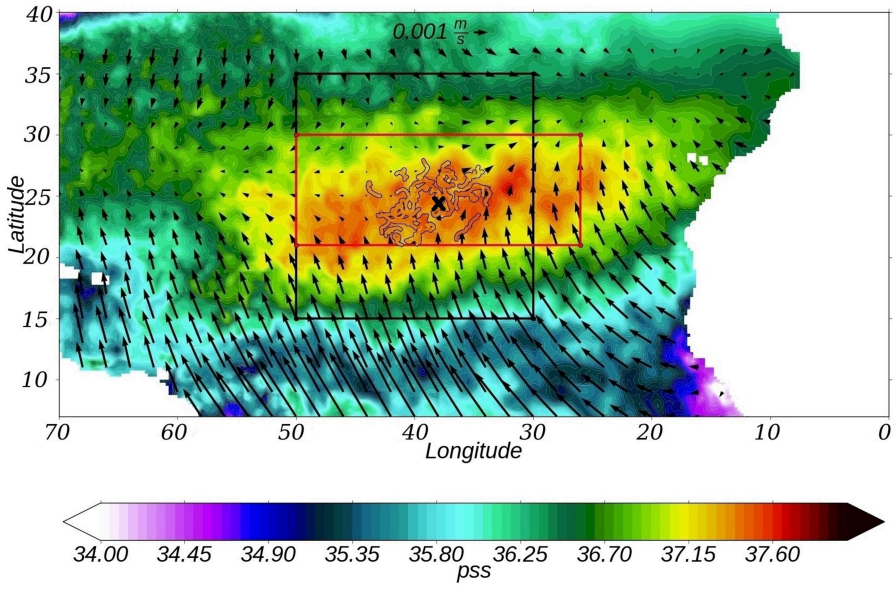

FIGURE 1 | North Atlantic subtropical region, January 2013. Climatological monthly mean SSS from SMOS and Ekman velocity field using ERA-Interim. The black box indicates SPURS region. The red box is the region that was chosen for estimation of salinity budget. Black cross is the mooring position at 24.5°N 38°W.

North Atlantic (Oceanography special issue, 2015, Vol. 28, No. 1). The drifter data collected during SPURS and afterwards are used to validate the SMOS derived SSS and the ocean current products. The SST budget is estimated based on the OSTIA (Operational Sea Surface Temperature and Sea Ice Analysis) data. The SST budget is investigated to compare the meso-scale contribution in this budget to the one in the SSS budget, and better understand their effect on the SSS budget.

We will first describe the data sets and their accuracy in Section Data Sets and Validation before discussing the methodology in Section Method. Results and their discussion are then presented in Sections Results and Discussion and Summary respectively.

DATA SETS AND VALIDATION

We investigate the area of 21°−30°N 50°−26°W. In the next section we will explain why we consider this region.

Spurs Drifters

The SPURS international experiment took place over one seasonal cycle during 2012/2013 (**Figure 1**, black box). Around 150 drifters were deployed in the central NSTG mostly in August–October 2012 and March–April 2013 (Centurioni et al., 2015). SVP-S drifters (Lumpkin and Pazos, 2007; Reverdin et al., 2007; Centurioni et al., 2015) have a battery pack, a satellite transmitter, a conductivity sensor below the surface float as well as a sea surface temperature (SST) sensor located either next to the conductivity cell or at the base of the float to avoid direct radiative heating. The drifters initially have a drogue centered at 15 m to follow the currents at this depth. Most of the drifters had a sensor to identify the presence of the drogue. In this work we use data of drogued SVP-S drifters. The time step of the data records is usually 30 min.

Mooring Data

The surface mooring was deployed as part of the SPURS project by the Upper Ocean Processes Group at WHOI at ∼24.5°N 38°W (**Figure 1**, black cross). Data was collected from September 2012 until September 2013 by the ASIMET (Air-Sea Interaction Meteorology) system. The ASIMET system provides measurements of specific humidity, SST and conductivity, wind speed and direction, barometric pressure, shortwave radiation, longwave radiation, and precipitation. These variables are used to compute air-sea fluxes of heat, moisture and momentum using bulk flux algorithm. The accuracy of the mooring data is 8 Wm^{-2} for the heat fluxes, 6 cm yr^{-1} for the evaporation and 10% for precipitation (Colbo and Weller, 2009; Farrar et al., 2015). We use these mooring data to validate the gridded data sets of heat fluxes, evaporation and precipitation.

SMOS

The SMOS satellite mission was launched in November 2009 on a sun-synchronous circular orbit with a local equator crossing time at 6 a.m. on ascending node and at 6 p.m. on descending node. The SMOS mission carries an L-band (1.4 GHz) interferometric radiometer that allows the reconstruction of a bi-dimensional multi-angular image of the L-band brightness temperatures (Tb) that is used to retrieve the SSS (Kerr et al., 2010).

In the subtropical North Atlantic SMOS SSS suffers from a seasonally varying systematic error (Hernandez et al., 2014), especially strong during boreal winter (RMS close to 0.5, **Figure 2**). Systematic errors in SMOS SSS originate mainly from inaccuracies in instrument calibration, in image reconstruction (in particular the one that depends of the distance to coast, Kolodziejczyk et al., 2015a) and from anthropogenic RFI (Radio Frequency Interferences).

In this work we use a new corrected and optimal interpolated (OI) SMOS SSS products described in Kolodziejczyk et al. (2015a,b, submitted), providing SSS to 75 km and 10 days resolution. The new OI SMOS SSS are derived from ESA level 2 SSS v550, using the same flagging as Boutin et al. (2013). The correction for systematic errors follows a two-step procedure: (1) removal of systematic errors in the vicinity to coast; (2) removal of seasonal systematic errors. First, data are corrected for 4-year mean (07/2010–07/2014) near coastal discrepancies with respect to the ISAS Argo climatology (Gaillard et al., 2009) taking into account that systematic errors depend on the location of the pixel across track and on the orbit orientation. Then, ascending and descending orbit data are mapped separately with an optimal interpolation scheme at large scale (500 km) with a Gaussian shaped correlation function. The seasonal large scale biases are then derived from the comparison with monthly ISAS SSS products. The last step is a noise reduction and mapping of bias corrected SMOS SSS every 7 days on the regular grid of 0.25° using optimal interpolation with a Gaussian correlation function scaled to 75 km over a window of 10 days centered on the day of mapping, using the corresponding monthly ISAS SSS fields as first guess.

In order to improve the horizontal SSS gradient at meso-scale, we also tested the introduction of a small constraint on along-stream-line (from AVISO SSH) orientation of the structures by including it in Gaussian correlation function (Kolodziejczyk et al., 2015a). This method allows to recover spatial scales slightly smaller than 75 km (OI SMOS SSH).

The SMOS OI (**Figure 2**, red curve) shows significant improvement with respect to earlier products (**Figure 2**, black curve, original SMOS product). The RMS difference between SMOS SSS at 10 days 75 km resolution and *in situ* data (TSGs, drifters) is lower than 0.15 almost for the whole period. The introduction of the supplementary correction (OI SMOS SSH) marginally, not significantly, improves the results (**Figure 2**, green curve). In this work we retained this last version of the weekly SMOS products with the spatial resolution of 0.25°.

As expected from the error statistics, the mapped (OI SSH) SMOS SSS field with the drifters' trajectories and data overlaid for the week 8–14 January 2013 (**Figure 3**) suggests that remaining systematic errors are small, and that the product captured a good part of meso-scale variability. Further discussions of the characteristics of the mapped product will be provided in another paper.

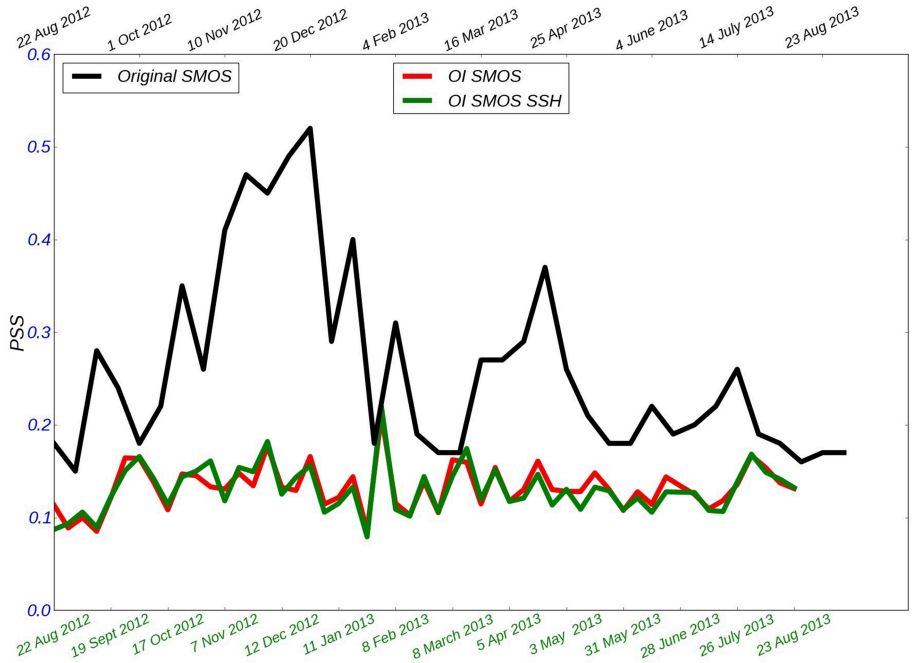

FIGURE 2 | RMS differences at drifter positions (in pss) over the SPURS domain between drifters SSS and 10-day CEC-CATDS SMOS SSS product (black), SMOS-OI with (green) SSH or without (red) constraint.

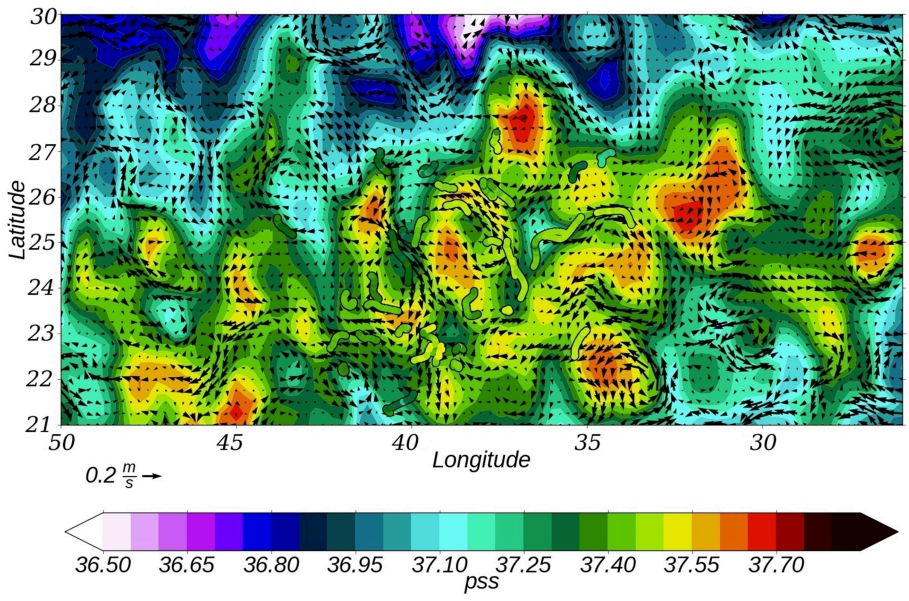

FIGURE 3 | SMOS SSS vs. SPURS drifters and AVISO geostrophic velocity field, 8–14 January 2013.

From **Figure 2** we just note that the error budget seems to remain relatively stationary in time. The small RMS error during August 2012 (**Figure 2**) results from a too small number of data for this period. There is a small peak of larger RMS difference in the week between January and February 2013 which could be due to a rain/wind front across this area inducing larger spatial variability and/or errors. Indeed, the rain front could have generated rapid and small scale wind changes not well captured in ECMWF (European Centre for Medium-Range Weather Forecasts) wind forecasts that are used in the SSS retrieval scheme.

Sea Surface Temperature OSTIA

To estimate the SST we use daily OSTIA SST analysis with horizontal resolution 0.05° (Reynolds and Chelton, 2010; Donlon et al., 2012). The SST product from OSTIA has zero mean bias and an accuracy of ∼0.57 K compared to the *in situ* measurements as noted in Donlon et al. (2012).

AVISO Altimetry

A regional AVISO 2014 altimetric product (daily product with 1/8° spatial resolution) was chosen as the geostrophic velocity field (Dussurget et al., 2015, D15 product). Compared to the standard Ssalto-Duacs product, it uses less along-track filtering, which is optimized in this region and for the different satellites. It uses also an updated Mean Dynamic Topography (MDT). This product was validated with the drifter data. The ocean currents from this product fit reasonably well the drifter trajectories (example in **Figure 3**) and seem to be associated with deformations of the large scale SSS fields. Salinity gradients tend to align along the streamlines. For example, in the north of the area, there is a small advection of fresh water in salty region at 27°N 46°W that is explained by geostrophic AVISO currents. The eddies inside the high SSS area usually correspond to local SSS maxima or minima: 22°N 34°W, 23°N 30°W, or 26.5°N 44°W.

Argo Floats

We estimate MLD on individual Argo temperature-salinity profiles (Gould et al., 2004). The MLD is estimated, when a threshold value for either temperature or salinity is attained compared with a near-surface value at 10 m depth: $\Delta T = 0.1^0C$, $\Delta S = 0.03pss$. We group these estimates monthly to provide a monthly mixed layer depth distribution (in the standard case, it is the average of the distribution that is retained). We use data from Coriolis web site with the flag "good data." Because of insufficient data distribution, we only use them as providing a large scale average. The comparison (**Figure 4**) with the monthly gridded ISAS (*In Situ* Analysis System) fields (spatial resolution 0.5°), an optimal estimation tool designed for the synthesis of the Argo global data sets (Gaillard et al., 2009), at the Argo profile positions (blue curve) and averaged over the domain (green curve) shows a shallower MLD than the Argo data (red curve) throughout the year, with the maximum difference of ∼25 m in December. The interpolation of Argo data can smooth the local MLD deepening, especially in December when there are more local rain events in this region. The consideration of the MLD in different latitude bands (**Figure 4**, red dashed curves) shows a horizontal gradient (from shallower MLD in the South to deeper in the North) and different restratification time (March in southern regions and March-April in northern regions; Kolodziejczyk et al., 2015c).

Atmospheric Fluxes

Freshwater Flux

Daily Era-Interim reanalysis from ECMWF (spatial resolution 0.25° × 0.25°), widely used daily OAFlux product (1° × 1°) from Woods Hole Oceanographic Institution (WHOI) for evaporation field and daily Era-Interim reanalysis, TRMM TMI (3B42) (0.25° × 0.25°) and GPCP (1° × 1°) satellites for precipitation field were tested. GPCP is strongly based on satellite retrievals, such as TRMM TMI, and surface rain gauges (Adler et al., 2012).

The comparison of evaporation field from Era-Interim (**Figure 5A**), black curve) with ones from OAFlux (**Figure 5A**),

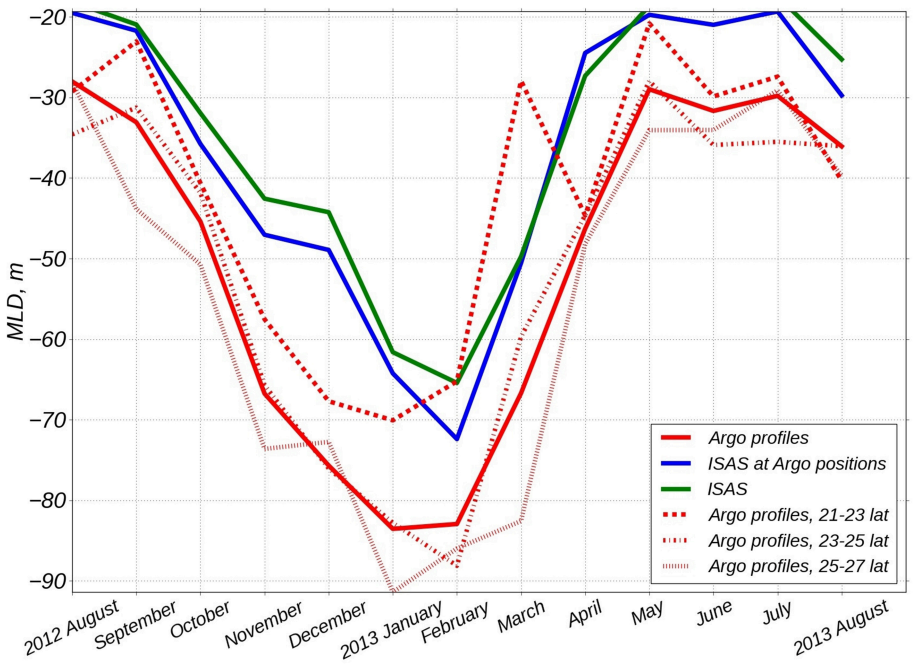

FIGURE 4 | MLD from Argo (red) and ISAS interpolated product (blue and green) for period August 2012—August 2013. MLD from Argo profiles for different latitude bands (red dashed lines).

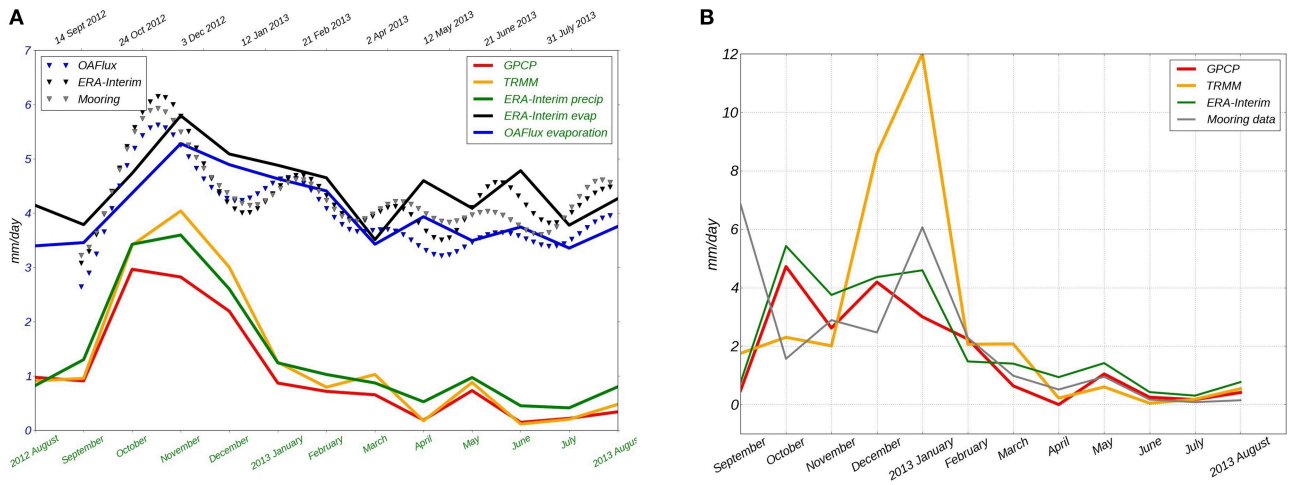

FIGURE 5 | (A) —Evaporation (ERA-Interim—black curve, OAFlux—blue) and precipitation (GPCP—red, TRMM—orange, ERA-Interim—green) data averaged over the month and over the domain (solid lines) and evaporation filtered with cut-off period 30 days at mooring position 24.5°N 38°W (dashed lines, mooring data—gray curve); **(B)** —precipitation data at mooring position.

blue curve) indicates small differences between ∼0 and 0.5 mm/day. The comparison with the mooring data at 24.5°N 38°W (see 2.2, **Figure 5A**), low-passed filtered data with 30 days cut-off) shows that ERA-Interim product sometimes (October, November, June) overestimates evaporation (max ∼0.5 mm/day) but usually in the confidence interval from the mooring data (0.16 mm/day) with a high correlation, while OAFlux product underestimates a little (max ∼0.7 mm/day and it is out of the mooring confidence interval in spring and summer) evaporation during almost the whole period. This is in line with the expectation that OAFlux might slightly underestimate the evaporation (from ERA-Interim and buoys) in the subtropical gyre of the North Atlantic (Yu et al., 2008).

On the other hand, Era-Interim reanalysis produces larger precipitation events over the North Atlantic compared with the satellite data (**Figure 5A**), green curve). TRMM satellite precipitation (**Figure 5A**), orange curve) is stronger than one from GPCP (**Figure 5A**), red curve) (Huffman et al., 2001). The comparison with the mooring data does not show a good agreement between the different products, even after monthly averaging (**Figure 5B**). ERA-Interim shows much higher total precipitation (2.58 mm/day) compared with mooring data (1.86 mm/day ± 10%), TRMM overestimates high precipitation events (total precipitation 2.76 mm/day). GPCP does not correlate well with the mooring time series, but presents a very close total precipitation average (1.69 mm/day). We retain GPCP in this work.

Heat Fluxes

The latent heat, sensible heat, net downward short and long wave radiations from ERA-Interim with the resolution 0.25° × 0.25° are used to estimate the surface heat flux. ERA-Interim net surface heat flux presents a satisfactory agreement with the one from mooring data at 24.5°N 38°W (**Figure 6**). The average over the year for the incoming short wave radiation is 220.3 Wm^{-2} with mooring data and the net downward short wave radiation is 252.06 Wm^{-2} with ERA-Interim, for the long wave radiation it is respectively −58.84 W/m^2 and −58.9 Wm^{-2}, for the sensible heat flux it is respectively −6.37 Wm^{-2} and -13.19 Wm^{-2}, and for the latent heat flux it is −124.08 Wm^{-2} and −144.37 Wm^{-2} respectively, so that the net heat flux across the sea surface of the two products differ by less than 6 Wm^{-2}.

METHOD

We consider the ML salinity (MLS) budget that can be written as (based on the conservation equation of any tracer with additional scale separation) (Delcroix and Hénin, 1991):

$$\frac{\partial \langle S\rangle}{\partial t} = -\langle u'\nabla S'\rangle - \langle \bar{u}\nabla\bar{S}\rangle - \frac{(S_{10\,m} - S_{-entr})}{h}\left(\frac{\partial h}{\partial t} + \langle w_{-h}\rangle\right) + \left\langle\frac{(E-P)S}{h}\right\rangle + \mathrm{R}, \quad (1)$$

where $<S>$ denotes SSS averaged over the domain for each time step (month), $\bar{S}$ is the mean salinity over a 90 days period for each grid point, $u = \bar{u} + u'$, h is MLD averaged over domain, w_{-h} is the Ekman vertical velocity calculated with the Era-Interim wind, u is the horizontal velocity vector, the sum of geostrophic AVISO velocity field and Ekman velocity that was calculated as $\frac{\vec{\tau}}{\rho f h}$, (E-P) is the difference between evaporation and precipitation. In term of entrainment S_{10m} is the salinity at 10 m depth (that is considered as the salinity of MLD), S_{-entr} is the salinity of the entrained water and is estimated as the salinity at the depth $\left(\frac{\partial h}{\partial t} + w_{-h}\right) \times \Delta T$, (with $\Delta T = 1 month \approx 2592000\,s$) that scales the layer of entrained water during the month considered (a month is the elementary time step in the mixed layer depth analysis). The left side of the equation presents

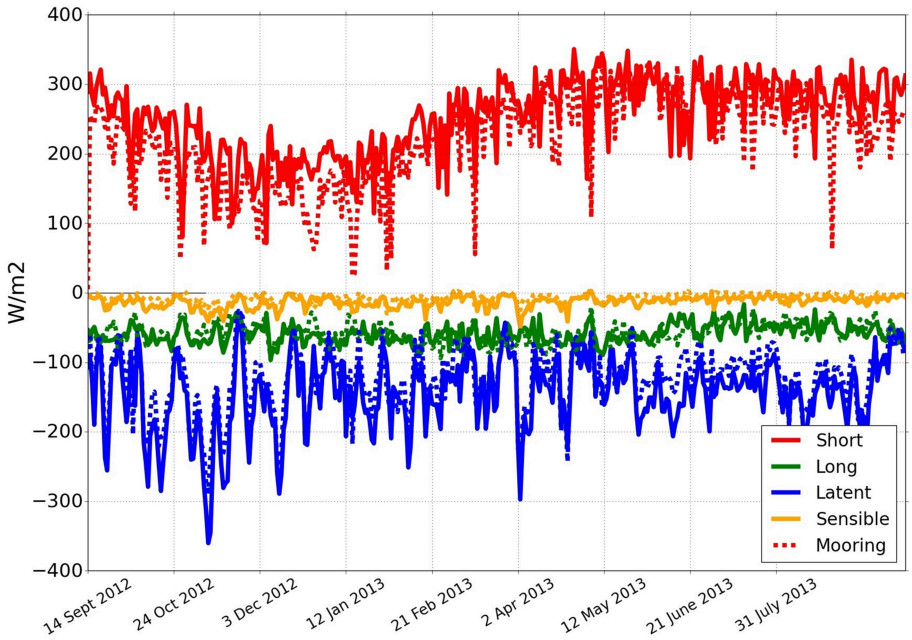

FIGURE 6 | Surface heat flux for the period September 2012–August 2013; solid curves—ERA-Interim reanalysis, dashed curves—mooring data at 24.5°N 38°W, red—net short wave radiation, green—net long wave radiation, blue—latent heat, orange—sensible heat.

the MLS tendency. The first term of the right side of the equation is turbulent horizontal advection estimated at each grid point and then monthly averaged over domain; the second one is mean horizontal advection estimated as the previous term. The third term presents the entrainment component (here we used Argo profile salinity, and neglect horizontal gradients when estimating this term as the MLD was chosen the same over whole domain for the considered month). The fourth term is the surface forcing that was estimated in the same manner as advection terms. The last one R is residual term that includes the sum of all unresolved physical processes and the accumulated errors from the other terms.

Similarly, the ML temperature (MLT) budget can be written as Moisan and Niiler (1998):

$$\frac{\partial \langle T\rangle}{\partial t} = -\left\langle u'\nabla T'\right\rangle - \left\langle \bar{u}\nabla \bar{T}\right\rangle - \frac{(T_{10\,m} - T_{-entr})}{h}\left(\frac{\partial h}{\partial t} + \left\langle w_{-h}\right\rangle\right) + \left\langle \frac{(Q)}{\rho C_p h}\right\rangle + \mathrm{R}, \quad (2)$$

where $<T>$ is SST averaged over the domain for each time step (month), Q is the surface heat flux, C_{-p} is the specific heat capacity, ρ is density, all other terms are the same as for salinity budget. The surface heat flux can be calculated as $Q = Q_l + Q_s + Q_{lw} + (1-\alpha)\,Q_{sw}[1 - I(h)]$ (Morel and Antoine, 1994; Sweeney et al., 2005), where Q_l is latent heat, Q_s is sensible heat, Q_{lw} is net long wave radiation, Q_{sw} is net short wave radiation, $\alpha = 0.04$ is the ocean surface albedo, $I(h) = Re^{-h/D_1} + (1-R)\,e^{-h/D_2}$ is the penetrative solar irradiance with the fraction of total solar flux for wavelengths longer than 700 nm $R = 0.58$, it is assumed to penetrate the ocean with a decreasing exponential profile, with an e-folding depth scale $D_1 = 0.35\,m$; $D_2 = 23\,m$ is the second extinction length scale associated with the shorter wavelength (Madec and the NEMO team, 2014).

All data sets were interpolated to the OI SMOS grid with the spatial resolution 0.25 × 0.25°. The error bars for each term were estimated by propagating the errors on the data (Appendix B in Supplementary Material).

We chose the region within the latitudes/longitudes range 21°−30°N/50°−26°W in subtropical Atlantic salinity maximum. It encompasses the region of largest SSS and strong SSS horizontal gradients just out of the domain (**Figure 7A**). In particular in the south one expects the strong SSS gradient due to a very large contribution from Ekman currents. Moreover, there is a large eddy variability in the North and in the West where the annual mean of SSS variability $\frac{\partial \langle S\rangle}{\partial t}$ reaches more than 0.6 pss/yr which is two times higher than in the center of the box (**Figure 7**; on the southern and eastern boundaries we are limited by the availability of the regional AVISO data). On **Figure 7B** (the annual mean of the turbulent salinity advection) the strong effect of eddy variability is further north, south and west (out of the domain), where it shows higher maximum absolute value larger than 0.6 pss/yr almost everywhere for these regions. On **Figure 7C** (the annual mean of the mean salinity advection) one notes the strong effect of Ekman currents further north and south up to 0.75 pss/yr. Furthermore, the spatial concentration of drifters and Argo data is larger in the center of the region and used to check the realism of the analysis.

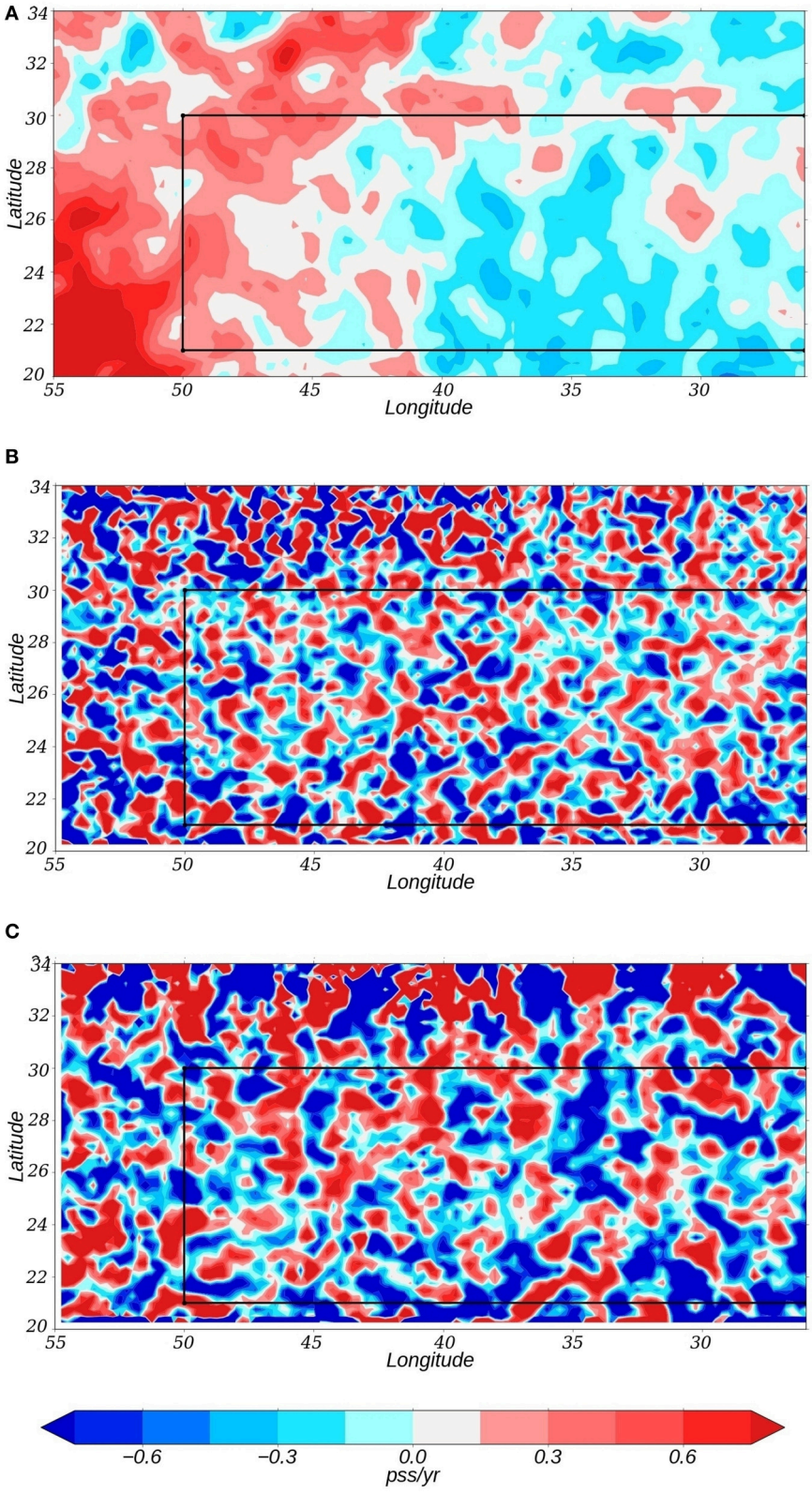

FIGURE 7 | Terms of the Equation (1) averaged over the year August 2012—August 2013; (A) —time salinity change, (B) —turbulent advection term, (C) —mean advection term.

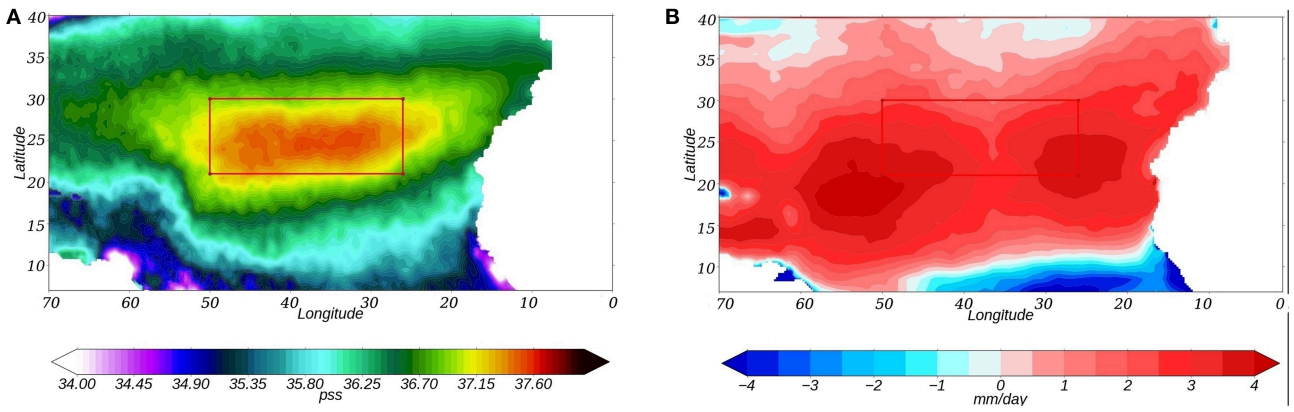

FIGURE 8 | Annual salinity (A) and E-P (B) mean with the selected region for SSS budget estimation (red box) over the August 2012—August 2013.

RESULTS

Salinity Budget

As mentioned before, SSS maximum is located a few degrees to the north of the E-P maxima (**Figure 8**) which shows the importance of the ocean dynamics in this region (Qu et al., 2011), indicating in particular a contribution of Ekman advection, and suggesting a large scale balance between sea surface forcing, advection and mixing processes. In winter 2012–2013 (especially in December) a rain band was found in the middle of the region which resulted in two local maxima on **Figure 8B**.

The terms in Equation (1) were estimated and averaged over the whole domain (**Figure 9A**). As expected, there is a strong response of the surface ocean to the evaporation flux (blue curve) on the salinity change term (green curve). The error bar is large during autumn and early winter months. This is due to local precipitation events and fast temperature changes, as consequences the evaporation changes that are not well reproduced.

The entrainment term contributes only during autumn and winter months when MLD is deepening (**Figures 9A,B**), orange curve). During the winter months entrainment plays a smaller role as the deepening of the ML is weaker and the MLS is closer to the salinity that is found deeper (S_{-entr}). In November when there is a small increase in the surface forcing term (evaporation increases) salinity continues to lower due to entrainment. In December, a month with larger amount of precipitation and small entrainment, the salinity changes are predominantly governed by surface freshwater flux (**Figure 9A**). Due to the difficulty in estimating the error on entrainment, only the error bars (standard error) on MLD is shown (**Figure 9B**).

For the whole domain the spatially averaged advection is negative throughout the year with a relatively small amplitude (**Figures 9A,C**). The turbulent and mean advections are both negative with the stronger magnitude for the mean component. It shows a moderate seasonal cycle associated with a maximum freshening during summer.

The sum of all estimated equation's component in the right side of the Equation (1) (here and after does not include R) (**Figure 9A**), black curve is very close to the surface forcing term and its difference with $\frac{\partial \langle S \rangle}{\partial t}$ gives a large residual term R (**Figure 9A**), black dashed curve.

To better understand the effect of advection we separate the region into two boxes: 21°−25.5°N 50°−26°W and 25.5°−30°N 50°−26°W. The dividing latitude was chosen based on the seasonal means and seasonal variability maps of the equation's terms (**Figure 10**). During the winter, the SSS variability term (**Figure 10A**) is characterized by salinity decreases north of 25.5°N, while a region with variable salinity changes (salinity can increase as well as decrease) is found in the South. For the SSS variability in the summer season (**Figure 10B**) the latitude 25.5°N separates a region of dominant increase in the North from a dominant decrease in the South. It means that during the summer the strong increase of SSS takes place in the northern region, while during the winter there is the largest decrease. Autumn and spring (not presented) show similar patterns for these two regions. The advection variability maps (**Figures 10C,D**) show two different structures in the southern part. During autumn (**Figure 10C**) some freshwater originating from the Amazon basin enters this region and is mixed through the domain, inducing a strong variation of turbulent advection in the south-western part (the std is up to 10 pss/yr in this region). During spring (**Figure 10D**) mean advection plays a significant role in the salinity change with significant spatial variability both in the northern as well as in the southern parts. Surface water flux (**Figures 10E–G**) shows strong spatial variability in both regions during the autumn (**Figure 10E**) and in the South during the spring (**Figure 10F**) when evaporation largely dominates there. The mean surface forcing (**Figure 10G**) also exhibits different regime on either side of 25.5°N that isolate the southern region, the region of maximum E-P field. Thus, 25.5°N separates two regimes in the SSS budget variability in agreement with Dong et al. (2015).

In the southern part, both the turbulent advection and mean advection (**Figure 11A**) play a significant role during the autumn and brings fresh water through eddy transport. On the other hand, during spring and summer it is rather the mean advection that brings freshwater from the tropical regions. In the northern

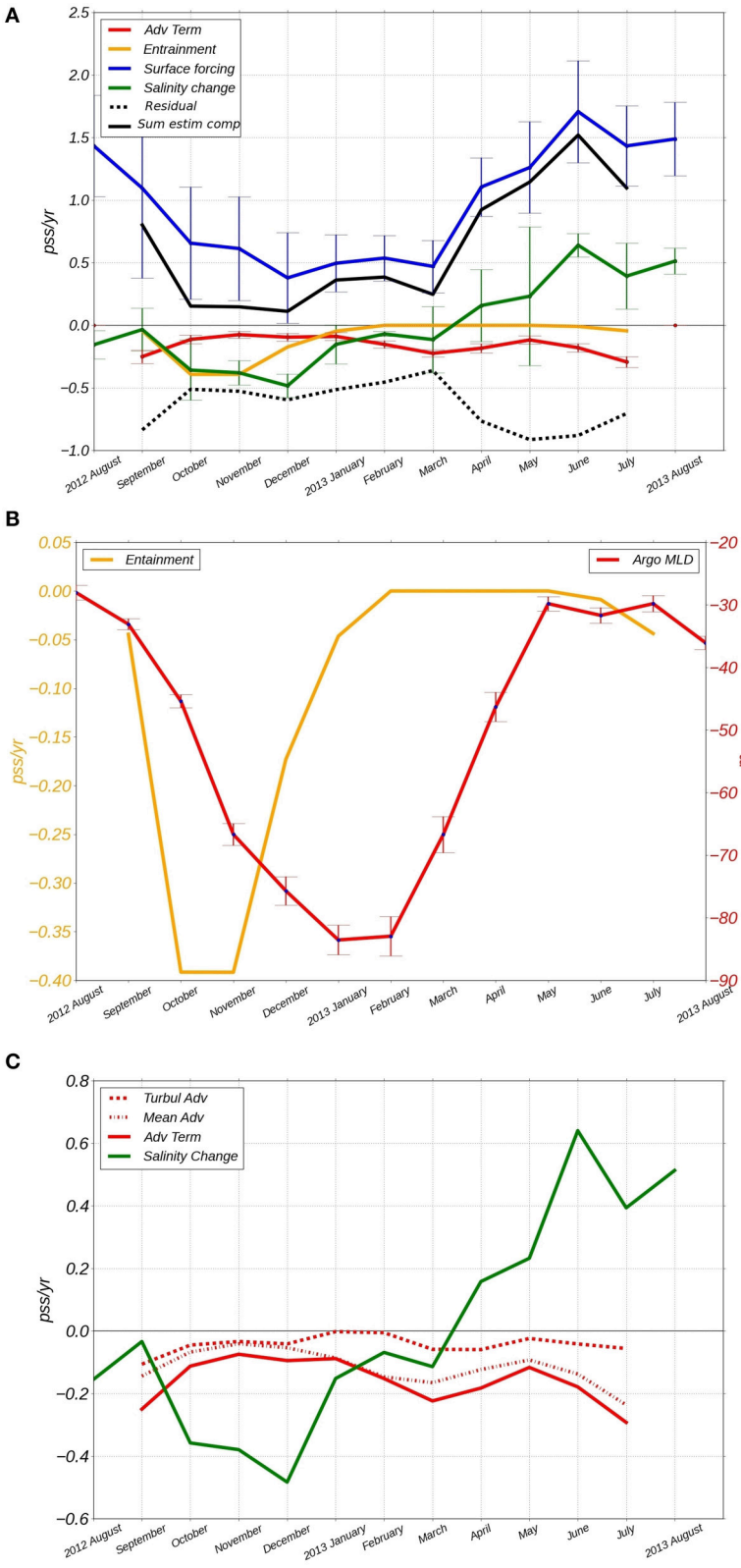

FIGURE 9 | (A) —components of salinity budget, residual (black dashed curve) and the sum of all estimated components of the right side of the Equation (1) (black curved); **(B)** —entrainment (orange curve) and Argo MLD (red); **(C)** —salinity change (green) and advection components (red).

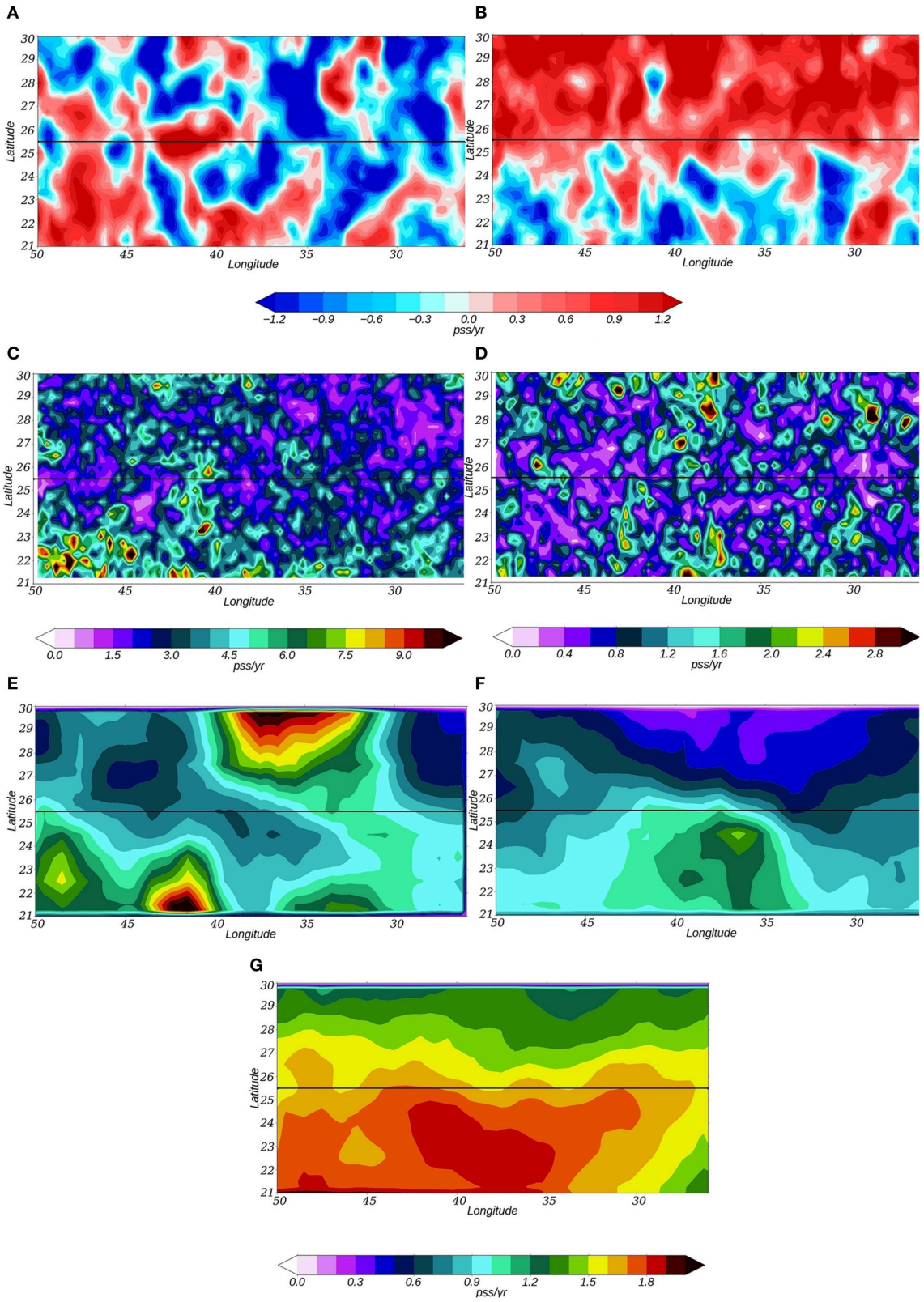

FIGURE 10 | Sea surface salinity change in winter (A) and summer (B). Turbulent advection standard deviation in autumn **(C)** and mean advection standard deviation in spring **(D)**. Surface forcing standard deviation in autumn **(E)** and spring **(F)** and surface forcing mean in summer **(G)**.

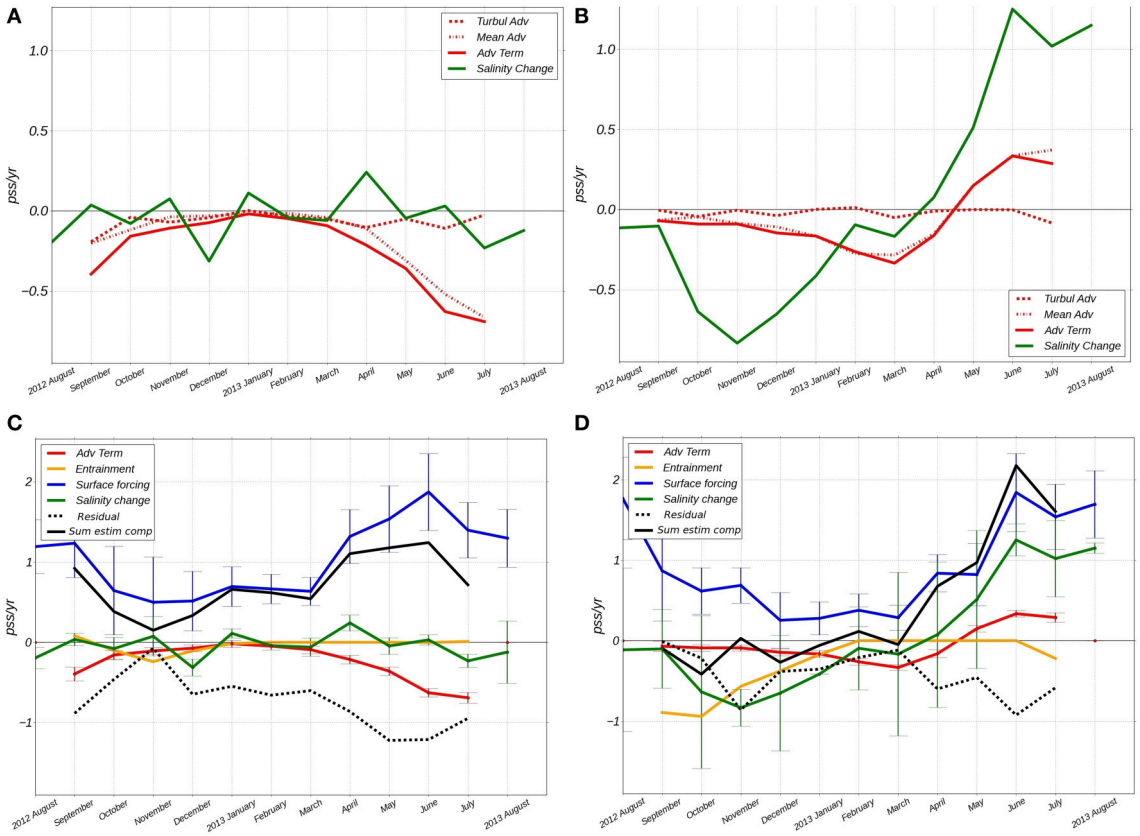

FIGURE 11 | Salinity change (green) and advection components (red) (A,B) and components of salinity budget, residuals (black dashed curves) and sums of right side's estimated equation components (C,D), Equation (1). (A,C) −21°−25°N, **(B,D)** −25°−30°N.

part (**Figure 11B**), advection does not show significant variability throughout the year except during summer when mean advection brings the salty water from the south and contributes to the salinity increase. In general, the domain-averaged salinity presents large month-to-month changes throughout the year (intraseasonal variability) in the southern part (**Figure 11C**) and seasonal cycle in salinity in the northern part (it decreases in winter and increases in summer). In the southern part, SSS decreases until October due to the small surface forcing, the effect of the advection and the entrainment terms. Afterwards there is a salinity increase in November. At this time the surface flux continues to decrease and the advection terms diminish in absolute value and reduces its freshening effect on the salinity. At that time even strong entrainment cannot significantly refresh the surface water. In December the salinity again decreases while freshwater flux increases, the entrainment starts to be smaller and there is only a small decrease in advection term that cannot match this strong change in salinity. Thus, in this month other processes contributing to the much larger residual term probably increase.

During the summer months, the salinity change is controlled by advection associated with transport of fresher water from the tropics that partially counterbalances the gain from evaporation. In the northern domain (**Figure 11D**) during winter the salinity change is strongly influenced by entrainment of deeper water and horizontal advection that contribute to a decrease of SSS. One of the two local minima of the residual component is found at this time.

In summer, the salinity increase strongly depends on advection which brings salty water from the E-P maxima region, and freshwater flux which concomitantly increases. The residual terms are large and in the range from 0 to −1.5 pss/yr in particular for the southern region.

Heat Budget

The estimation of the temperature budget based on Equation (2) in the subtropical gyre of the North Atlantic (**Figure 12**) indicates a near-balance between the terms retained, i.e., the error bar range of the two sides of the equation overlap [black solid (the sum of all elements in the right part of the Equation (2)] and green (temperature change) curves). The different components of the temperature budget have the same pattern irrespective of the domain [total region (**Figure 12A**), southern (B) and northern (C) parts]. SST (green curve) decreases in late autumn and winter and increases in spring and summer. The term of surface heat flux (blue curve) shows comparable variability in the two regions being largely responsible for the temperature change. The entrainment term (orange curve) is large during late autumn and winter and contributes to lower SST. Only the terms of horizontal advection are different for the southern (**Figure 12B**) and the northern (**Figure 12C**) parts. In the southern part, advection

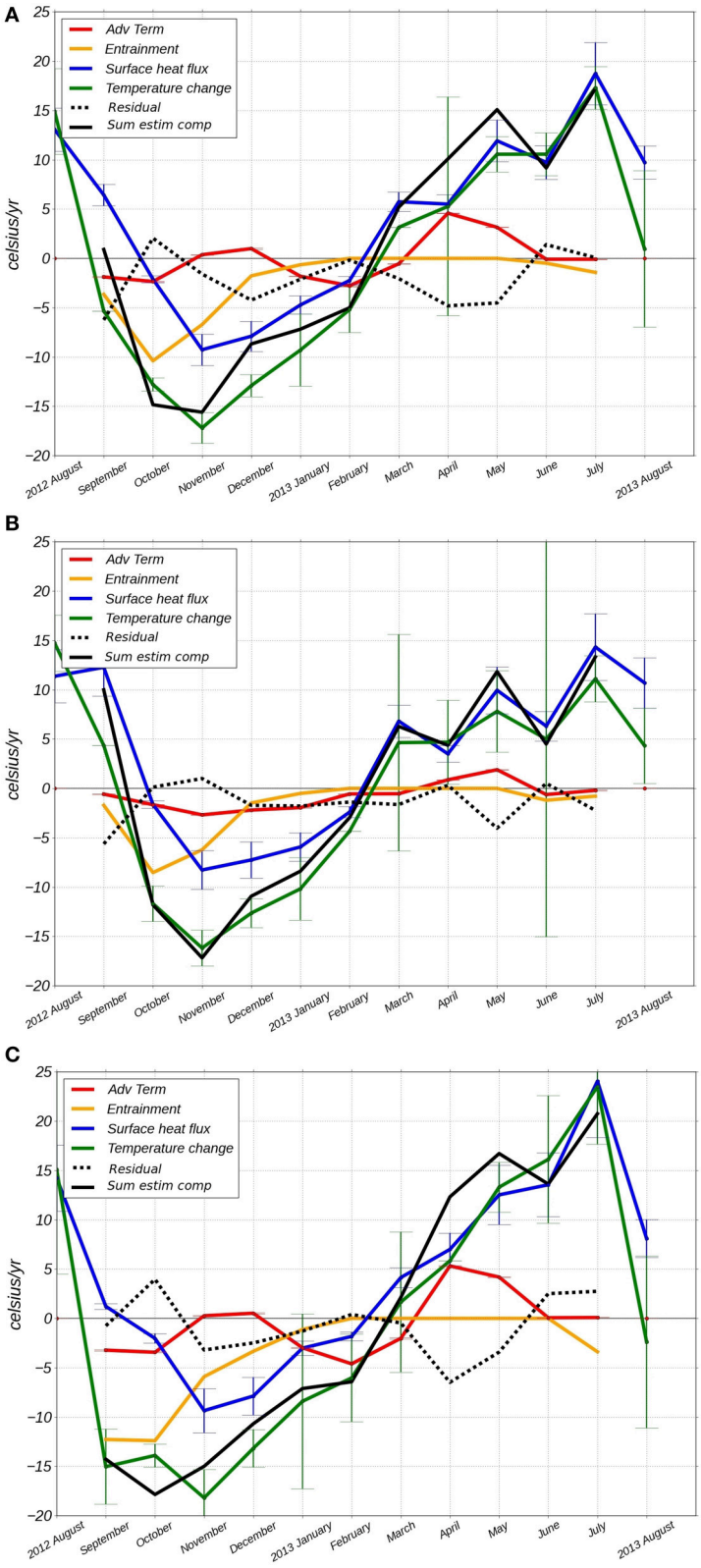

FIGURE 12 | Components of temperature budget for the period August 2012–2013, residual (black dashed curves) and the sum of all estimated components of the right side of the Equation (2). (A) —total considered region; **(B)** —southern part 21°–25°N; **(C)** —northern part 25°–30°N.

is negative throughout most of the year, bringing colder water mostly from the North, whereas it is positive during spring and late summer, the period of large warming. In the northern part the sign of advection is the same, except for November and December with a positive advection term. It implies that during these 2 months the horizontal gradient of SST was small over the region. After this period the colder water comes from the North and the East, resulting in negative advection terms. As commented the net residual terms are relatively small with an annual negative average.

DISCUSSION AND SUMMARY

We examined the salinity and temperature budgets in the subtropical gyre of the North Atlantic 21°-30°N/50°-26°W during the period August 2012–2013 based on the OSTIA data for SST and CATDS CEC LOCEAN SMOS corrected data (OI SMOS and OI SMOS SSH) for the SSS. The OI SMOS SSS gives promising results, as a comparison with drifter data shows RMS differences on the order of 0.15 even in winter; the introduction of a constraint coming from SSH marginally improves the results. The spatially-averaged SSS presents a realistic seasonal cycle with the minimum in winter and maximum in summer (**Figure 9A**), as is also found for SST (**Figure 12**). This region contains an Ekman convergence zone around 25.5°N which results in two different regimes within the box. The division of the region into two parts shows that in the southern part of the domain SSS does not present a seasonal cycle. In this region the freshwater flux is partially balanced by other terms of the salinity budget while in the northern region the effect of the freshwater flux is dominant. The SST budget presents a similar variability in the southern and northern parts. The gradient of SST changes sign on the diagonal (from South-West to North-East) of the box compared with the meridional gradient of the SSS. The effect of warm water from the equator is first felt in the southern part during early spring with an earlier and faster increase of SST than in the northern domain.

The freshwater flux is the dominant component in the salinity budget (0.88 ± 0.3 pss/yr, averaged over the period September 2012 – July 2013 and over 21°−30°N/50°−26°W region) while the heat flux (2.9 ± 1.34 C°/year; for the 13 month period it is 4.12 ± 1.43 C°/year) is the dominant component in the temperature budget. Both of them have a seasonal cycle with a minimum in winter and maximum in summer. The heat flux is responsible for the variability in SST throughout the year. SSS and SST do not show a strong tendency 0.014 ± 0.2 pss/yr and 1.5 C°/yr over these 11 months, similar to the results averaged over the 10-years (2004–2013) period and over the SPURS-1 region in Dong et al. (2015) (for salinity). Dong et al. (2015) have found a 1-month lag between the salinity change and the seasonal cycles of surface forcing term, which might be the result of a slightly different region retained in their analysis [notice that Dong et al. (2015) domain is 5° further south than the region in **Figure 1** (red box)].

The advection term depends on the scale, region and time period. Farrar et al. (2015) shows the strong influence of advection at the meso-scale, whereas in Dohan et al. (2015) the large-scale advection term is small compared with the amplitude of the sea surface forcing and is referred to as "residual term." Dong et al. (2015) have shown that the Ekman and geostrophic advection mean state component nearly compensate each other in the region 20°−30°N 45°−30°W. In the region that we retained we find that the advection term (**Figure 9A**, red curve) does not present a large seasonal variability and contributes to a negative (freshening) effect on the total budget (-0.16 ± 0.02 pss/yr in our work to be compared with Dong et al. (2015) -0.28 ± 0.01 pss/yr for the period 2004–2013 and over the larger region). The mean part of the advection term plays a dominant role in the salinity budget in the subtropical gyre of the North Atlantic (the mean part equals -0.11 ± 0.02 pss/yr whereas the turbulent part equals -0.04 ± 0.02 pss/yr). In the two sub-regions the role of the advection terms starts to be clearer: (1) the effect of the turbulent advection component is important in the southern part during the autumn when it contributes to a freshening; (2) in spring and summer Ekman advection brings fresher water from the equatorial zone to the southern part of the domain, whereas its salty water from the E-P maximum region is transferred further North where it contributes to the salinity increase; thus it explains the strong contribution of mean component in the southern region, -0.18 ± 0.04 pss/year and -0.06 ± 0.04 pss/year for the turbulent component. In the temperature budget the value of the averaged advection term over the period and domain plays a small negative (cooling) role (-0.04 ± 0.02 C°/yr) as the values of the mean and turbulent advections are -0.16 ± 0.02 C°/yr and 0.12 ± 0.02 C°/yr, respectively. This suggests that the turbulent advection has a strong positive effect (warming) than mean advection but the turbulent component is still small compared with the other terms while the mean term varies throughout the year which "compensate" when averaged over the year (not shown).

The entrainment component plays a role during autumn and winter when mixed layer deepens. In the salinity budget this term has a modest effect (−0.15 pss/yr) while in the temperature budget it is the major component that compensates the effect of the heat flux (−3.58 C°/yr).

Despite the physical consistency of the results, the salinity budget cannot be closed. The surface forcing term has a strong influence on the salinity and temperature budgets. Errors on this term induce errors in the salinity budget estimation as suggested by the fact that the residual terms (**Figures 9A**, **11C,D**, **12**) tend to mirror the freshwater flux terms. Furthermore, the error bar on freshwater flux (resulting from time-space variability) exceeds 0.6 pss/yr in autumn and spring/summer seasons, the periods where the residual term is large. In the autumn, there is also the possibility that the precipitation might not be correctly estimated, whereas in the summer months, the comparison with the mooring data suggested a possible overestimation of evaporation in the ERA-Interim reanalysis used here.

The error bars on advection terms are small but in some region the AVISO product underestimates the geostrophic velocity (comparison with surface drogued drifters, unpublished results). This later effect could change our results a little but probably not significantly as the results for the temperature

TABLE 1 | Annual averaged means of the components in Equations (1) and (2).

Salinity change $\frac{\partial\langle S\rangle}{\partial t}$	Turb. adv. of salinity $\langle u'\nabla S'\rangle$	Mean adv. of salinity $\left\langle \bar{u}\nabla\bar{S}\right\rangle$	Entrainment $\frac{(S_{10m}-S_{-entr})}{h}\left(\frac{\partial h}{\partial t}+\langle w_{-h}\rangle\right)$	Surface forcing $\left\langle\frac{(E-P)S}{h}\right\rangle$	Residual R
-0.014 ± 0.2 pss/yr	-0.04 ± 0.2 pss/yr	-0.11 ± 0.2 pss/yr	-0.15 pss/yr	0.88 ± 0.3 pss/yr	-0.36 ± 0.3 pss/yr
Temperature change $\frac{\partial\langle T\rangle}{\partial t}$	Turb. adv. of temperature $\langle u'\nabla T'\rangle$	Mean adv. of temperature $\langle\bar{u}\nabla\bar{T}\rangle$	Entrainment $\frac{(T_{10m}-T_{-entr})}{h}\left(\frac{\partial h}{\partial t}+\langle w_{-h}\rangle\right)$	Surface forcing $\left\langle\frac{\langle Q\rangle}{\rho Cph}\right\rangle$	Residual R
1.5 ± 0.25 C°/yr	0.12 ± 0.04 C°/yr	-0.16 ± 0.04 C°/yr	-3.58 C°/yr	2.9 ± 1.34 C°/yr	-0.77 ± 1.5 C°/yr

budget (**Figure 12**) with the same data sets show a much closer budget. There is however also for that term the possibility that the SMOS-product that we used presents too large errors or smooths out some of the scales responsible for the meso-scale advection (but see Appendix A in Supplementary Material, which suggests that at least at 0-order it produces a reasonable estimate).

The errors are also sensitive to the MLD chosen. In order to estimate entrainment we use the MLD averaged over the domain. This approach excludes the consideration of the horizontal gradient, and salinity change by induction which may be not negligible in the area (see for example Dohan et al., 2015; Dong et al., 2015). This contributes to uncertainties in our results, and obviously misses more local and smaller scale processes. At this point the data used do not allow to evaluate the effect of a spatial change in MLD at meso-scale. But the fact that this method gives good results for SST budget means that the SSS is more sensitive to the vertical processes such as restratification, mixing and etc.

Altogether we find large residuals from the salinity budget ~ -0.3 pss/yr (or 47% of the average modulus of $\frac{\partial\langle S\rangle}{\partial t}$ which varies in the range ±0.63 pss/yr), whereas they are much smaller for the temperature budget, also with a negative average, -0.77 C°/yr ($\sim$4% of the average magnitude of $\frac{\partial\langle T\rangle}{\partial t}$ which varies in the range ±18 C°/yr) (see **Table 1**). It is probably due to the strongest effect of the heat flux on the temperature change that simplifies the estimation of temperature budget, while the salinity variability strongly depends on the ocean dynamics (**Figure 8**). The advection is the most important component for the salinity budget in this region and can be the main source of errors due to the uncertainties in salinity field and underestimation of velocity field that was discussed above. Moreover it is thus difficult to blame a choice of a too shallow mixed layer in the summer months, as it would contribute to a negative residual in the SSS budget, but also in the SST budget. Small scale processes such as are found near filaments or fronts, could be a source of asymmetry between the SST and SSS budgets. Indeed, in the southern part of the domain, Kolodziejczyk et al. (2015c) showed that SSS spatial variability dominates the surface density gradients. This was also witnessed in summer during the Strasse cruise (Reverdin et al., 2015), and in early spring during the Midas cruise (Busecke et al., 2014). Dynamical processes that induce mixed layer restratification would thus contribute to an average SSS decrease, but with little notable effect on SST (Shcherbina et al., 2015). In addition, vertical mixing with salt fingering at the lower boundary of the mixed layer would also contribute to a larger SSS negative term compared with SST, but this would happen preferentially when there is a large salinity vertical stratification compared to temperature, and thus probably not in the summer months. In some studies the mismatch (residual) is parameterized by eddy horizontal diffusion terms, as in Dong et al. (2015) when such a term contributes to the MLS changes with the averaged magnitude of -0.28 ± 0.01 pss/yr thus comparable with our residual term (-0.3 pss/yr).

Using other data sets (for precipitation, evaporation, MLD, etc.) to estimate the salinity budget could help better understand the mechanism of formation of the salinity maximum of the subtropical North Atlantic and its seasonal variability. Further testing other ways to estimate entrainment or a relevant mixed layer depth would also improve the reliability of these results. In further work we will also estimate the SSS and SST budget based on Mercator PSY2V4R4 simulation data to improve the entrainment estimation method, to validate the model data on the meso-scale and to estimate subscale horizontal diffusion and impact of vertical processes.

AUTHOR CONTRIBUTIONS

AS has done the analysis of the budgets of surface temperature and salinity in the North Atlantic subtropical gyre during SPURS experiment. GR is the Thesis supervisor of AS. He tested the salinity drifters and contributed to their operation during SPURS. He is the French PI in SPURS experiment. NK has characterized meso-scale variability in surface salinity from SMOS band-L radiometer remote sensing data. JB is the specialist on band-L radiometry data and a SMOS-mission French PI. She also contributed to the supervision of AS.

ACKNOWLEDGMENTS

The authors thank the two reviewers for their helpful comments. The authors thank the CLS team who work on the regional AVISO altimetry product: R. Dussurget, S. Mulet, M.-I. Pujol, M.-H. Rio. The original altimeter products were produced by Ssalto/Duacs and distributed by AVISO, with support from CNES (http://www.aviso.altimetry.fr/duac). SVP drifters were provided by the Global Drifter Program, NOAA grant #NA10OAR432056. LC and VH were supported by NASA grant #NNX12AI67G and

NOAA grant #NA10OAR432056. This work was carried out in the frame of the SMOS-Ocean CNES/TOSCA project. The study was also supported in France by two grants of LEFE/IMAGO and LEFE/GMMC. A. Sommer is co-founded by CNES and UPMC PhD fellowships.

SUPPLEMENTARY MATERIAL

The Supplementary Material for this article can be found online at: http://journal.frontiersin.org/article/10.3389/fmars.2015.00107

REFERENCES

Adler, R. F., Gu, G., and Huffman, G. J. (2012). Estimating climatological bias errors for the global precipitation climatology project (GPCP). *J. Appl. Meteor. Climatol.* 51, 84–99. doi: 10.1175/JAMC-D-11-052.1

Boutin, J., Martin, N., Reverdin, G., Yin, X., and Gaillard, F. (2013). Seas surface freshening inferred from SMOS and Argo salinity: impact of rain. *Ocean Sci.* 9, 183–192. doi: 10.5194/os-9-183-2013

Busecke, J., Gordon, A. L., Li, Z., Bingham, F. M., and Font, J. (2014). Subtropical surface layer salinity budget and the role of mesoscale turbulence. *J. Geophys. Res. Oceans* 119, 4124–4140. doi: 10.1002/2013JC009715

Centurioni, L. R., Hormann, V., Chao, Y., Reverdin, G., Font, J., and Lee, D. K. (2015). Sea surface salinity observations with Lagrangian drifters in the tropical North Atlantic during SPURS: Circulation, fluxes, and comparisons with remotely sensed salinity from Aquarius. *Oceanography* 28, 96–105. doi: 10.5670/oceanog.2015.08

Colbo, K., and Weller, R. A. (2009). Accuracy of the IMET sensor package in the subtropics. *J. Atmos. Oceanic Technol.* 26, 1867–1890. doi: 10.1175/2009JTECHO667.1

Dai, A., Qian, T., Trenberth, K. E., and Milliman, J. D. (2009). Changes in continental freshwater discharge from 1948 to 2004. *J. Clim.* 22, 2773–2792. doi: 10.1175/2008JCLI2592.1

Delcroix, T., and Hénin, C. (1991). Seasonal and interannual variations of sea surface salinity in the tropical Pacific Ocean. *J. Geophys. Res*. 96, 22135–22150. doi: 10.1029/91JC02124

Dohan, K., Kao, H.-Y., and Lagerloef, G. S. E. (2015). The freshwater balance over the North Atlantic SPUS domain from aquarius satellite salinity, OSCAR satellite surface currents, and some simplified approaches. *Oceanography* 28, 86–95. doi: 10.5670/oceanog.2015.07

Dong, S., Goni, G., and Lumpkin, R. (2015). Mixed-layer salinity budget in the SPURS region on seasonal to interannual time scales. *Oceanography* 28, 78–85. doi: 10.5670/oceanog.2015.05

Donlon, C. J., Martin, M., Stark, J. D., Roberts-Jones, J., Fiedler, E., and Wimmer, W. (2012). The operational sea surface temperature and sea ice analysis (OSTIA). *Rem. Sens. Environ.* 116, 140–158. doi: 10.1016/j.rse.2010.10.017

Durack, P. J. (2015). Ocean salinity and the global water cycle. *Oceanography* 28, 20–31. doi: 10.5670/oceanog.2015.03

Durack, P. J., and Wijffels, S. E. (2010). Fifty-years in Global ocean salinities and their relationship to broad-scale warming. *J. Clim.* 23, 4342–4362. doi: 10.1175/2010JCLI3377.1

Dussurget, R., Mulet, S., Pujol, M.-J., Sommer, A., Kolodziejczyk, N., Reverdin, G., et al. (2015). Surface current field improvements – Regional altimetry for SPURS. *Coriolis Mercator Newslet.* 52, 39–44.

Farrar, J. T., Rainville, L., Plueddemann, A. J., Kessler, W. S., Lee, C., Hodges, B. A., et al. (2015). Salinity and temperature balances at the SPURS central mooring during fall and winter. *Oceanography* 28, 56–65. doi: 10.5670/oceanog.2015.06

Gaillard, F., Autret, E., Thierry, V., Galaup, P., Coatanoan, C., and Loubrieu, T. (2009). Quality control of large Argo data sets. *J. Atmos. Oceanic Technol.* 26, 337–351. doi: 10.1175/2008JTECHO552.1

Gordon, A. L., and Giulivi, C. F. (2014). Ocean eddy freshwater flux convergence into the North Atlantic subtropics. *J. Geophys. Res. Oceans* 119, 3327–3335. doi: 10.1002/2013JC009596

Gould, J., Roemmich, D., Wijffels, S., Freeland, H., Ignaszewsky, N., Jianping, X., et al. (2004). Argo profiling floats bring new era of *in situ* ocean observations. *Eos Trans. Am. Geophys. Union*. 85, 185–191. doi: 10.1029/2004EO190002

Hasson, A., Delcroix, T., and Boutin, J. (2013). Formation and variability of the South Pacific Surface Salinity maximum in recent decades. *J. Geophys. Res.* 118, 5109–5116. doi: 10.1002/jgrc.20367

Hernandez, O., Boutin, J., Kolodziejczyk, N., Reverdin, G., Martin, N., Gaillard, F., et al. (2014). SMOS salinity in the subtropical North Atlantic salinity maximum: Part 1. Comparison with Aquarius and in situ salinity. *J. Geophys. Res. Oceans* 119, 8878–8896. doi: 10.1002/2013JC009610

Huffman, G. J., Adler, R. F., Morrissey, M., Bolvin, D. T., Curtis, S., Joyce, R., et al. (2001). Global precipitation at one-degree daily resolution from multi-satellite observations. *J. Hydrometeor.* 2, 36–50. doi: 10.1175/1525-7541(2001)002<0036:GPAODD>2.0.CO;2

Kerr, Y. H., Waldteufel, P., Wigneron, J.-P., Delwart, S., Cabot, F., Boutin, J., et al. (2010). The SMOS mission: new tool for monitoring key elements of the global water cycle. *Proc. IEEE* 98, 666–687. doi: 10.1109/JPROC.2010.2043032

Kolodziejczyk, N., Boutin, J., Hernandez, O., Sommer, A., Reverdin, G., Marchand, S., et al. (2015a). Argo SSS and SMOS SSS combination helps monitoring SSS variability from basin scale to mesoscale. *Coriolis Mercator Newslett*. 52, 16–21.

Kolodziejczyk, N., and Gaillard, F. (2013). Variability of the heat and salt budget in the subtropical southeastern pacific mixed layer between 2004 and 2010: spice injection mechanism. *J. Phys. Oceanogr.* 43, 1880–1898. doi: 10.1175/JPO-D-13-04.1

Kolodziejczyk, N., Hernandez, O., Boutin, J., and Reverdin, G. (2015b). SMOS salinity in the subtropical North Atlantic salinity maximum: 2. Two-dimensional horizontal thermohaline variability. *J. Geophys. Res. Oceans* 120, 972–987. doi: 10.1002/2014JC010103

Kolodziejczyk, N., Reverdin, G., and Lazar, A. (2015c). Interannual variability of the mixed layer winter convection and spice injection in the eastern subtropical North Atlantic. *J. Phys. Oceanogr.* 45, 504–525. doi: 10.1175/JPO-D-14-0042.1

Lagerloef, G., Schmitt, R. W., Schanze, J., and Kao, H.-Y. (2010). The ocean and the global water cycle. *Oceanography* 23, 82–93. doi: 10.5670/oceanog.2010.07

Lumpkin, R., and Pazos, M. (2007). "Measuring surface currents with Surface Velocity Program drifters: the instrument, its data, and some recent results," in *Lagrangian Analysis and Prediction of Coastal and Ocean Dynamics*, eds A. Griffa, A. D. Kirwan Jr., A. J. Mariano, T. Özgökmen, and H. Thomas Rossby (New York, NY: Cambridge University Press), 39–67.

Madec, G., and the NEMO team (2014). *"NEMO Ocean Engine." Note du Pôle de Modélisation*. Paris: Institut Pierre-Simon Laplace.

Moisan, J. R., and Niiler, P. P. (1998). The seasonal heat budget of the North Pacific: net heat flux and heat storage rates (1950–1990). *J. Phys. Oceanogr.* 28, 401–421.

Morel, A., and Antoine, D. (1994). Heating rate within the upper ocean in relation to its bio-optical state. *J. Phys. Oceanogr.* 24, 1652–1665.

Qu, T., Gao, S., and Fukumori, I. (2011). What governs the North Atlantic salinity maximum in a global GCM? *Geophys. Res. Lett.* 38:7. doi: 10.1029/2011GL046757

Reverdin, G., Boutin, J., Lorenco, A., Blouch, P., Rolland, J., Niiler, P. P., et al. (2007). Surface salinity measurements – COSMOS 2005 experiment in the bay of biscay. *J. Atmos. Oceanic Technol.* 24, 1643–1654. doi: 10.1175/JTECH2079.1

Reverdin, G., Morisset, S., Marié, L., Bourras, D., Sutherland, G., Ward, B., et al. (2015). Surface salinity in the North Atlantic subtropical gyre during the STRASSE/SPURS summer 2012 cruise. *Oceanography* 28, 114–123. doi: 10.5670/oceanog.2015.09

Reynolds, R. W., and Chelton, D. B. (2010). Comparisons of daily sea surface temperature analyses for 2007–08. *J. Clim.* 23, 3545–3562. doi: 10.1175/2010JCLI3294.1

Schmitt, R. W. (1995). The ocean component of the global water cycle. *Rev. Geophys.* 33, 1395–1409. doi: 10.1029/95RG00184

Shcherbina, A. Y., D'Asaro, E. A., Riser, S. C., and Kessler, W. S. (2015). Variability and interleaving of upper-ocean water masses surrounding the North

Atlantic salinity maximum. *Oceanography* 28, 106–113. doi: 10.5670/oceanog.2015.12

Skliris, N., Marsh, R., Josey, S. A., Good, S. A., Liu, C., and Allan, R. P. (2014). Salinity change in the World Ocean since 1950 in relation to changing surface freshwater fluxes. *Clim. Dyn.* 43, 709–736. doi: 10.1007/s00382-014-2131-7

Sweeney, C., Gnanadesikan, A., Griffies, S. M., Harrison, M. J., Rosati, A. J., and Samuel, B. L. (2005). Impacts of shortwave penetration depth on large-scale ocean circulation and heat transport. *J. Phys. Oceanogr.* 35, 1103–1119. doi: 10.1175/JPO2740.1

Talley, L. D. (2002). *Salinity Patterns in the Ocean. Vol. 1. The Earth System: Physical and Chemical*. Chichester: John Wiley & Sons, Ltd.

Terray, L., Corre, L., Cravatte, S., Delcroix, T., Reverdin, G., and Ribes, A. (2012). Near-surface salinity as nature's rain gauge to detect human influence on the tropical water cycle. *J. Clim.* 25, 958–977. doi: 10.1175/JCLI-D-10-05025.1

Trenberth, K. E., Smith, L., Qian, T., Dai, A., and Fassullo, J. (2007). Estimates of the global water budget and its annual cycle using observational and model data. *J. Hydrometeor.* 8, 758–769. doi: 10.1175/JHM600.1

Yu, L. (2011). A global relationship between the ocean water cycle and near-surface salinity. *J. Geophys. Res. Oceans* 116:, C10025. doi: 10.1029/2010JC006937

Yu, L., Jin, X., and Weller, R. A. (2008). "Multidecade Global Flux Datasets from the Objectively Analyzed Air-sea Fluxes (OAFlux) Project: Latent and sensible heat fluxes, ocean evaporation, and related surface meteorological variables," in *Woods Hole Oceanographic Institution, OAFlux Project Technical Report. OA-2008-01* (Woods Hole, MA), 64.

Conflict of Interest Statement: The authors declare that the research was conducted in the absence of any commercial or financial relationships that could be construed as a potential conflict of interest.

List of Figures

List of Tables

Bibliography

Adler, R.F., Gu, G., Huffman, G. J. (2012). Estimating Climatological Bias Errors for the Global Precipitation Climatology Project (GPCP). *Journal of Applied Meteorology and Climatology*, 51 (1), 84–99. doi: http://dx.doi.org/10.1175/JAMC-D-11-052.1.

Amores, A., Melnichenko, O., Maximenko, N. (2015). Poster: *Mesoscale eddies in the North Atlantic subtropical gyre*: *3D composite structure from satellite and Argo profile data*. 2015 Ocean Surface Topography Science Team Meeting, Reston, VA, USA.

Baumgartner, A., and Reichel, E. (1975). *The World Water Balance: Mean Annual Global, Continental and Maritime Precipitation, Evaporation and Runoff.* Elsevier Science Ltd. Amsterdam, 179 pp.

Bosch, W., Dettmering, D., and Schwatke, C. (2014). Multi-Mission Cross-Calibration of Satellite Altimeters: Constructing a Long-Term Data Record for Global and Regional Sea Level Change Studies. *Remote Sensing*, 6 (3), 2255–2281. doi: 10.3390/rs6032255

Bosch, W., and Savcenko, R. (2007). *Satellite Altimetry*: *Multi-Mission Cross Calibration.* Chapter in Dynamic Planet, pp.51–56. doi: 10.1007/978-3-540-49350-1_8

Boutin, J., Martin, N., Kolodziejczyk, N., Reverdin, G. (2016). Interannual anomalies of SMOS sea surface salinity. *Remote Sensing of Environment*, 180, 128–136. doi: 10.1016/j.rse.2016.02.053

Boutin, J., Martin, N., Reverdin, G., Yin, X., and Gaillard, F. (2013). Seas surface freshening inferred from SMOS and Argo salinity: impact of rain. *Ocean Science*, 9, 183–192. doi: 10.5194/os-9-183-2013

Broecker, W. S. (1991). The great ocean conveyor. *Oceanography*, 4, 79–89.

Büsecke, J., Gordon, A. L., Li, Z., Bingham, F. M., and Font, J. (2014). Subtropical surface layer salinity budget and the role of mesoscale turbulence. *Journal of*

Geophysical Research: *Oceans*, 119, 4124–4140. doi: 10.1002/2013JC009715

Camps, A., Corbella, I., Torres, F., Vall-llossera, M., Duffo N. (2005). Polarimetric Formulation of the Visibility Function Equation Including Cross-Polar Antenna Patterns. *IEEE Geoscience and Remote Sensing Letters*, 2(3), 292–295. doi: 10.1109/LGRS.2005.846885

Camps, A. (2006). Tutorial on: *Microwave Aperture Synthesis Radiometers for Earth Observation*: *Application to the SMOS Mission.* IGARSS. Available: http://www.grss-ieee.org/wp-content/uploads/2010/06/camps-microwave-tutorial-06.pdf

Centurioni, L. R., Hormann, V., Chao, Y., Reverdin, G., Font, J., and Lee, D. K. (2015). Sea surface salinity observations with Lagrangian drifters in the tropical North Atlantic during SPURS: Circulation, fluxes, and comparisons with remotely sensed salinity from Aquarius. *Oceanography*, 28, 96–105. doi: 10.5670/oceanog.2015.08

Colbo, K., and Weller, R. A. (2009). Accuracy of the IMET sensor package in the subtropics. *Journal of Atmospheric and Oceanic Technology*, 26, 1867–1890. doi: 10.1175/2009JTECHO667.1

Conner, M. D., and Petty, G. W. (1998). Validation and Intercomparison of SSM/I Rain-Rate Retrieval Methods over the Continental United States. *Journal of Applied Meteorology*, 37, 679–700. doi: http://dx.doi.org/10.1175/1520-0450(1998)037<0679:VAIOSI>2.0.CO;2

Cox, R.A., Culkin, F., and Riley, J.P. (1967). The electrical conductivity/chlorinity relationship in natural sea water. *Deep-Sea Research and Oceanographic Abstracts*, 14 (2), 203–220. doi: 10.1016/0011-7471(67)90006-X

Cravatte, S., Delcroix, T., Zhang, D., McPhaden, M., Leloup, J. (2009). Observed freshening and warming of the western Pacific Warm Pool. *Climate Dynamics*, 33, 565–589. doi: 10.1007/s00382-009-0526-7

Dai, A., Qian, T., Trenberth, K. E., and Milliman, J. D. (2009). Changes in continental freshwater discharge from 1948 to 2004. *Journal of Climate*, 22, 2773–2792. doi: 10.1175/2008JCLI2592.1

Dee, D.P., and Coauthors, 2011. The ERA-Interim reanalysis: configuration and performance of the data assimilation system. *Quarterly Journal of the Royal Meteorological Society*, 137 (656), 553–597. doi: 10.1002/qj.828

de Boyer Montégut, C., Mignot, J., Lazar, A., and Cravatte, S. (2007). Control of salinity on the mixed layer depth in the world ocean: 1. General description.

Journal of Geophysical Research: *Oceans*, 112, C06011. doi: 10.1029/2006JC003953

de Boyer Montégut, C., Madec, G., Fischer, A. S., Lazar, A., and Iudicone, D. (2004). Mixed layer depth over the global ocean: an examination of profile data and a profile-based climatology. *Journal of Geophysical Research*, 109, C12003. doi:10.1029/2004JC002378

Dohan, K., Kao, H.-Y., and Lagerloef, G. S. E. (2015). The freshwater balance over the North Atlantic SPUS domain from aquarius satellite salinity, OSCAR satellite surface currents, and some simplified approaches. *Oceanography*, 28, 86–95. doi: 10.5670/oceanog.2015.07

Dong, S., Goni, G., and Lumpkin, R. (2015). Mixed-layer salinity budget in the SPURS region on seasonal to interannual time scales. *Oceanography*, 28, 78–85. doi: 10.5670/oceanog.2015.05

Donlon, C. J., Martin, M., Stark, J. D., Roberts-Jones, J., Fiedler, E., and Wimmer, W. (2012). The operational sea surface temperature and sea ice analysis (OSTIA). *Remote Sensing of Environment*, 116, 140–158. doi: 10.1016/j.rse.2010.10.017

Drévillon, M., Régnier, C., Levier, B., Desportes, C., Perruche, C. (2014). *QuO Va Dis? Quarterly Ocean Validation Display #13.* Validation bulletin for April-May-June (AMJ) 2013, Mercator Ocean. Available online: https://www.mercator-ocean.fr/wp-content/uploads/2015/05/QUOVADIS_num13_AMJ_2013.pdf

Durack, P. J. (2015). Ocean salinity and the global water cycle. *Oceanography*, 28, 20–31. doi: 10.5670/oceanog.2015.03

Durack, P. J., and Wijffels, S. E. (2010). Fifty-years in Global ocean salinities and their relationship to broad-scale warming. *Journal of Climate*, 23, 4342–4362. doi: 10.1175/2010JCLI3377.1

Durand, F., Alory, G., Dussin, R., Reul, N. (2013). SMOS reveals the signature of Indian Ocean Dipole events. *Ocean Dynamics*, 63, 1203–1212. doi: 10.1007/s10236-013-0660-y

Dussurget, R., Mulet, S., Pujol, M.-J., Sommer, A., Kolodziejczyk, N., Reverdin, G., et al. (2015). Surface current field improvements – Regional altimetry for SPURS. *Coriolis Mercator Newsletters*, 52, 39–44.

Fairall, C. W., Bradley, E. F., Rogers, D. P., Edson, J. B., Young, G. S. (1996). Bulk parameterization of air-sea fluxes for Tropical Ocean-Global Atmosphere Coupled-Ocean Atmosphere Response Experiment. *Journal of Geophysical Research*, 101 (C2), 3747–3764. doi: 10.1029/95JC03205

Farrar, J. T., Rainville, L., Plueddemann, A. J., Kessler, W. S., Lee, C., Hodges, B. A., et al. (2015). Salinity and temperature balances at the SPURS central mooring during fall and winter. *Oceanography*, 28, 56–65. doi: 10.5670/oceanog.2015.06

Font, J., Camps, A., Borges, A., Martin-Neira, M., Boutin, J., Reul, N., Kerr, Y.H., Hahne, A., and Mecklenburg, S. (2010). SMOS: The Challenging Sea Surface Salinity Measurement From Space. *Proceeding of the IEEE*, 98 (5), 649-665. doi: 10.1109/JPROC.2009.2033096

Gaillard, F., Autret, E., Thierry, V., Galaup, P., Coatanoan, C., and Loubrieu, T. (2009). Quality control of large Argo data sets. *Journal of Atmospheric and Oceanic Technology*, 26, 337–351. doi: 10.1175/2008JTECHO552.1

Gill, A. E. (1982). *Atmosphere – Ocean dynamics.* Academic Press, 662 pp.

Godfrey, J. S., and Beljaars, A. C. M. (1991). On the turbulent fluxes of buoyancy, heat and moisture at the air-sea interface at low wind speeds. *Journal of Geophysical Research*, 96, 22043–22048. doi: 10.1029/91JC02015

Gordon, A. L., and Giulivi, C. F. (2014). Ocean eddy freshwater flux convergence into the North Atlantic subtropics. *Journal of Geophysical Research: Oceans*, 119, 3327–3335. doi: 10.1002/2013JC009596

Gould, J., Roemmich, D., Wijffels, S., Freeland, H., Ignaszewsky, N., Jianping, X., et al. (2004). Argo profiling floats bring new era of in situ ocean observations. *Eos Trans. Am. Geophys. Union.*, 85, 185–191. doi: 10.1029/2004EO190002

Hasson, A., Delcroix, T., and Boutin, J. (2013). Formation and variability of the South Pacific Surface Salinity maximum in recent decades. *Journal of Geophysical Research*, 118, 5109–5116. doi: 10.1002/jgrc.20367

Hasson, A., Delcroix, T., Boutin, J., Dussin, R., and Ballabrera-Poy, J. (2014). Analyzing the 2010–2011 La Niña signature in the tropical Pacific sea surface salinity using in situ data, SMOS observations, and a numerical simulation. *Journal of Geophysical Research: Oceans*, 119, 3855–3867. doi:10.1002/2013JC009388

Hernandez, O., Boutin, J., Kolodziejczyk, N., Reverdin, G., Martin, N., Gaillard, F., et al. (2014). SMOS salinity in the subtropical North Atlantic salinity maximum: Part 1. Comparison with Aquarius and in situ salinity. *Journal of Geophysical Research: Oceans*, 119, 8878–8896. doi: 10.1002/2013JC009610

Huffman, G. J., R. F. Adler, D. T. Bolvin, and G. Gu, 2009. Improving the global precipitation record: GPCP Version 2.1. *Geophysical Research Letters*, 36 (17), L17808. doi: 10.1029/2009GL040000.

Kerr, Y. H., Waldteufel, P., Wigneron, J.-P., Delwart, S., Cabot, F., Boutin, J., et al. (2010). The SMOS mission: new tool for monitoring key elements of the global water cycle. *Proceeding of the IEEE*, 98, 666–687. doi: 10.1109/JPROC.2010.2043032

Knudsen, M. (1903). On the Standard-Water Used in the Hydrographical Research Until July 1903.

Kolodziejczyk, N., Boutin, J., Hernandez, O., Sommer, A., Reverdin, G., Marchand, S., et al. (2015a). Argo SSS and SMOS SSS combination helps monitoring SSS variability from basin scale to mesoscale. *Coriolis Mercator Newsletter*, 52, 16–21.

Kolodziejczyk, N., Boutin, J., Vergely, J.-L., Marchand, S., Martin, N., Reverdin, G. (2016). Mitigation of systematic errors in SMOS sea surface salinity. *Remote Sensing of Environment*, 180, 164–177, doi: 10.1016/j.rse.2016.02.061

Kolodziejczyk, N., and Gaillard, F. (2013). Variability of the heat and salt budget in the subtropical southeastern pacific mixed layer between 2004 and 2010: spice injection mechanism. *Journal Of Physical Oceanography*, 43, 1880–1898. doi: 10.1175/JPO-D-13-04.1

Kolodziejczyk, N., Hernandez, O., Boutin, J., and Reverdin, G. (2015b). SMOS salinity in the subtropical North Atlantic salinity maximum: 2. Two-dimensional horizontal thermohaline variability. *Journal of Geophysical Research: Oceans*, 120, 972–987. doi: 10.1002/2014JC010103

Kolodziejczyk, N., Reverdin, G., and Lazar, A. (2015c). Interannual variability of the mixed layer winter convection and spice injection in the eastern subtropical North Atlantic. *Journal Of Physical Oceanography*, 45, 504–525. doi: 10.1175/JPO-D-14-0042.1

Lagerloef, G., Schmitt, R. W., Schanze, J., and Kao, H.-Y. (2010). The ocean and the global water cycle. *Oceanography*, 23, 82–93. doi: 10.5670/oceanog.2010.07

Lellouche, J.-M., Le Galloudec, O., Drévillon, M., Régnier, C., Greiner, E., Garric, G. et al. (2013). Evaluation of global monitoring and forecasting systems at Mercator Océan. *Ocean Science*, 9, 57–81. doi: 10.5194/os-9-57-2013

Lumpkin R., and Johnson, G.C., (2013). Global ocean surface velocities from drifters: Mean, variance, El Nino-Southern Oscillation response, and seasonal cycle. *Journal of Geophysical Research Atmospheres*, 118, pp. 2992–3006.

Lumpkin, R., and Pazos, M. (2007). *Measuring surface currents with Sur-*

face Velocity Program drifters: *the instrument, its data, and some recent results* in Lagrangian Analysis and Prediction of Coastal and Ocean Dynamics, eds A. Griffa, A. D. Kirwan Jr., A. J. Mariano, T. Özgökmen, and H. Thomas Rossby (New York, NY: Cambridge University Press), 39–67.

Madec, G. the NEMO team (2014). *"NEMO Ocean Engine." Note du Pôle de Modélisation.* Paris: Institut Pierre-Simon Laplace.

Martin, A. (2013). *Analyse des measures radiométriques en bande-L au-dessus de l'océan*: *Campagne CAROLS.* PhD thesis, Université Pierre et Marie Curie, Paris 6.

Mecklenburg, S., Drusch, M., Kerr, Y., Font, J., Martin-Neira, M., and co-authors. (2012). ESA's Soil Moisture and Ocean Salinity Mission: Mission Performance and Operations. *IEEE Transactions Geoscience and Remote Sensing*, 50 (5), 1354–1366. doi:10.1109/TGRS.2012.2187666

Melnichenko, O., Hacker, P., Maximenko, N., Lagerloef, G., Pontemra, J. (2014). Spatial optimal interpolation of Aquarius sea surface salinity: Algorithms and implementation in the North Atlantic. *Journal of Atmospheric and Oceanic Technology*, 31, 1583–1600 http://dx.doi.org/10.1175/JTECH-D-13-00241.1

Mignot, J., de Boyer Montégut, C., Lazar, A., and Cravatte, S. (2007). Control of salinity on the mixed layer depth in the world ocean: 2. Tropical areas. *Journal of Geophysical Research*: *Oceans*, 112, C10010, doi:10.1029/2006JC003954

Millero, F.J., Feistel, R., Wright, D.G., and McDougall, T.J. (2008). The comparison of Standard Seawater and the definition of the Reference-Composition Salinity Scale. *Deep-Sea Research Part I – Oceanographic Research Papers*, 55(1), 50–72. doi: 10.1016/j.dsr.2007.10.001

Moisan, J. R., and Niiler, P. P. (1998). The seasonal heat budget of the North Pacific: net heat flux and heat storage rates (1950–1990). *Journal Of Physical Oceanography*, 28, 401–421.

Morel, A., and Antoine, D. (1994). Heating rate within the upper ocean in relation to its bio-optical state. *Journal Of Physical Oceanography*, 24, 1652–1665.

Oliva, R., Nieto, S., and Felix-Redondo, F. (2013). RFI Detection Algorithm: Accurate Geolocation of the Interfering Sources in SMOS Images. *IEEE Transactions on Geoscience and Remote Sensing*, 51(10), 4993–4998. doi: 10.1109/TGRS.2013.2262721

Portabella, M., Stoffelen, A., Lin, W., Turiel, A., Verhoef, A., Verspeek, J., and Ballabrera-Poy, J. (2012). Rain Effects on ASCATRetrieved Winds: Toward an Improved Quality Control. *IEEE Transactions Geoscience and Remote Sensing*,

50, 2495–2506. doi:10.1109/tgrs.2012.2185933

Qu, T., Gao, S., and Fukumori, I. (2011). What governs the North Atlantic salinity maximum in a global GCM? *Geophysical Research Letters*, 38 (7). doi: 10.1029/2011GL046757

Randa, J., Lahtinen, J., Camps, A., Gasiewski, A.J., Hallikainen, M., and co-authors (2008). *Recommended Terminology for Microwave Radiometry.* Gaithersburg, MD. Available: http://www.nist.gov/ctl/rf-technology/rf_electronics/upload/NIST-TN-1551.pdf

Reynolds, R. W., and Chelton, D. B. (2010). Comparisons of daily sea surface temperature analyses for 2007–08. *Journal of Climate*, 23, 3545–3562. doi: 10.1175/2010JCLI3294.1

Reverdin, G., Boutin, J., Lorenco, A., Blouch, P., Rolland, J., Niiler, P. P., et al. (2007). Surface salinity measurements – COSMOS 2005 experiment in the bay of biscay. *Journal of Atmospheric and Oceanic Technology*, 24, 1643–1654. doi: 10.1175/JTECH2079.1

Reverdin, G., Morisset, S., Marié, L., Bourras, D., Sutherland, G., Ward, B., et al. (2015). Surface salinity in the North Atlantic subtropical gyre during the STRASSE/SPURS summer 2012 cruise. *Oceanography*, 28, 114–123. doi: 10.5670/oceanog.2015.09

Rienecker, M.M., and Coauthors (2001). MERRA - NASA's Modern-Era Retrospective Analysis for Research and Application. *Journal of Climate*, 24, 3624–3648, doi: http://dx.doi.org/10.1175/JCLI-D-11-00015.1.

Rio, M.-H. (2012). Use of altimeter and wind data to detect the anomalous loss of SVP-type drifter's drogue. *Journal of Atmospheric and Oceanic Technology*, 29, 1663–1674. doi: 10.1175/JTECH-D-12-00008.1

Rio, M.-H., and Hernandez, F. (2003). High-frequency response of wind-driven currents measured by drifting buoys and altimetry over the world ocean. *Journal of Geophysical Research*, 108(C8), 3283. doi: 10.1029/2002JC001655

Rio M.-H , Mulet, S., and Picot, N. (2014). Beyond GOCE for the ocean circulation estimate: Synergetic use of altimetry, gravimetry and in-situ data provides new insight into geostrophic and Ekman currents. *Geophysical Research Letters*, 41, 8918–8925. doi: 10.1002/2014GL061773

Riser, S., Anderson, J., Shcherbina, A., and D'Asaro, E. (2015). Variability in near-surface salinity from hours to decades in the eastern North Atlantic: the SPURS region. *Oceanography*, 28(1), 66–77. doi: http://dx.doi.org/10.5670/oceanog.2015.11

Reul, N., Chapron, B., Lee, T., Donlon, C., Boutin, J., and Alory, G. (2014). Sea surface salinity structure of the meandering Gulf Stream revealed by SMOS sensor. *Geophysical Research Letters*, 41, 3141–3148. doi:10.1002/2014GL059215.

Reul, N., Tenerelli, J., Chapron, B., Vandemark, D., Quilfen, Y., Kerr, Y. H. (2012). SMOS satellite L-band radiometer: A new capability for ocean surface remote sensing in hurricanes. *Journal of Geophysical Research*: *Oceans*, 117. doi: 10.1029/2011JC007474

Schanze, J.J., Schmitt, R. W., and Yu, L. L. (2010). The global oceanic freshwater cycle: A state-of-the-art quantification. *Journal of Marine Research*, 68, 569–595. doi: http://dx.doi.org/10.1357/002224010794657164

Schmitt, R. W. (1995). The ocean component of the global water cycle. *Reviews of Geophysics*, 33, 1395–1409. doi: 10.1029/95RG00184

Schmitt, R.W., and Blair, A. (2015). A river of salt. *Oceanography*, 28(1), 40–45. doi: http://dx.doi.org/10.5670/oceanog.2015.04

Shcherbina, A. Y., D'Asaro, E. A., Riser, S. C., and Kessler, W. S. (2015). Variability and interleaving of upper-ocean water masses surrounding the North Atlantic salinity maximum. *Oceanography*, 28, 106–113. doi: 10.5670/oceanog.2015.12

Siedler, G., Griffies, S., Gould, J., and Church, J. (2013). *Ocean Circulation and Climate*: *a 21st Century perspective.* 2nd Ed., Oxford, GB, Academic Press, 904pp.

Simmons, A. J., S. Uppala, D. Dee, and S. Kobayashi, 2007. ERA-Interim: New ECMWF reanalysis products from 1989 onwards. *ECMWF Newsletter*, 110, 25–35.

Skliris, N., Marsh, R., Josey, S. A., Good, S. A., Liu, C., and Allan, R. P. (2014). Salinity change in the World Ocean since 1950 in relation to changing surface freshwater fluxes. *Climate Dynamics*, 43, 709–736. doi: 10.1007/s00382-014-2131-7

Skou, N., and Hoffman-Bang, D. (2005). L-band radiometers measuring salinity from space: atmospheric propagation effects. *IEEE Transactions on Geoscience and Remote Sensing*, 43 (10), 2210–2217. doi: 10.1109/TGRS.2005.856115

Soldo, Y., Khazaal, A., Cabot, F., Richaume, P., Anterrieu, E., Kerr, Y. H. (2014). Mitigation of RFIS for SMOS: A Distributed Approach. *IEEE Transactions on Geoscience and Remote Sensing*, 52 (11), 7470–7479. doi: 10.1109/TGRS.2014.2312988

Sommer, A., Barnier, B., Zolina, O., Gulev, S. K., Cosme, E., Dussin, R., and Albert, A. (2017). Assessment of global ocean daily precipitation produced by atmospheric reanalyses in regard to satellite estimates. *Journal of Climate*, in submission.

Sommer, A., Reverdin, G., Kolodziejczyk, N., and Boutin, J. (2015). Sea Surface Salinity and Temperature Budgets in the North Atlantic Subtropical Gyre during SPURS Experiment: August 2012-August 2013. *Frontiers in Marine Science*, 2:107. doi: 10.3389/fmars.2015.00107

Sprintall, J., and Tomczak, M. (1992). Evidence of the barrier layer in the surface layer of the tropics. *Journal of Geophysical Research*: *Oceans*, 97, 7305–7316. doi: 10.1029/92JC00407

SPURS Workshop Report Committee, 2010. *Salinity in the Upper-Ocean Regional Study.*

Steffen, K., Thomas, R. H., Rignot, E., Cogley, J. G., Dyurgerov, M. B., Raper, S. C. B., Huybrechts, P., and Hanna, E. (2010). *Cryospheric contributions to sea-level rise and variability.* Pp. 178–225 in Understanding Sea-Level Rise and Variability. J.A. Church, P.L. Woodworth, T. Aarup, and W.S. Wilson, eds, Wiley-Blackwell, Oxford, UK. doi: http://dx.doi.org/10.1002/9781444323276

Stull, R. B. (1994). A Convective Transport Theory for Surface Fluxes. *Journal of Atmospheric Sciences*, 51, 3–22. doi: http://dx.doi.org/10.1175/1520-0469(1994)051<0003:ACTTFS>2.0.CO;2

Sutherland, G., Marié, L., Reverdin, G., Christensen, K. H., Broström, G., and Ward, B. (2016). Enhanced turbulence associated with the diurnal jet in the ocean surface boundary Layer. *Journal Of Physical Oceanography*, in Press. doi: http://dx.doi.org/10.1175/JPO-D-15-0172.1

Sweeney, C., Gnanadesikan, A., Griffies, S. M., Harrison, M. J., Rosati, A. J., and Samuel, B. L. (2005). Impacts of shortwave penetration depth on large-scale ocean circulation and heat transport. *Journal Of Physical Oceanography*, 35, 1103–1119. doi: 10.1175/JPO2740.1

Swift, C. T., and McIntosh, R. E. (1983). Considerations for microwave remote sensing of ocean surface salinity. *IEEE Transactions on Geoscience and Remote Sensing*, GE-21 (4), 480–491.

Talley, L. D., Pickard, G. L., Emery, W. J., Swift, J. H. (2011). *Descriptive Physical Oceanography: An Introduction.* 6th Ed.. Academic Press, pp 560.

Terray, L., Corre, L., Cravatte, S., Delcroix, T., Reverdin, G., and Ribes, A. (2012). Near-surface salinity as nature's rain gauge to detect human influence on the tropical water cycle. *Journal of Climate*, 25, 958–977. doi: 10.1175/JCLI-D-10-05025.1

Tomczak, M., 1999. Some historical, theoretical and applied aspects of quantitative water mass analysis. *Journal of Marine Research*, 57, 275–303. doi: http://dx.doi.org/10.1357/002224099321618227

Treguier, A.-M., Deshayes, J., Lique, C., Dussin, R., and Molines, J.-M. (2012). Eddy contributions to the meridional transport of salt in the North Atlantic. *Journal of Geophysical Research*: *Oceans*, 117 (C5). doi:10.1029/2012JC007927

Treguier, A.-M., Deshayes, J., Le Sommer, J., Lique, C., Madec, G., Penduff, T., Molines, J.-M., Barnier, B., Bourdalle-Badie, B., and Talandier, C. (2014). Meridional transport of salt in the global ocean from an eddy-resolving model. *Ocean Science*, 10 (2), 243–255, doi:10.5194/os-10-243-2014.

Trenberth, K. E., Smith, L., Qian, T., Dai, A., and Fassullo, J. (2007). Estimates of the global water budget and its annual cycle using observational and model data. *Journal of Hydrometeorology*, 8, 758–769. doi: 10.1175/JHM600.1

Ueki, I. K., Ando, K., Kuroda, Y, and Kutsuwada, K. (2002). Salinity variation and its effect on dynamic height along the 156 degrees E in the Pacific warm pool. *Geophysical Research Letters*, 29 (14). doi: 10.1029/2001GL013993

Unesco, C. i. D. é. européenes, I. C. o. S. U. S. C. o. O. Research, I. A. f. t. P. S. o. t. Ocean, and J. P. o. O. T. a. Standards (1981). *Background papers and supporting data on the International equation of state of seawater 1980.* Unesco. Available: http://unesdoc.unesco.org/images/0004/000479/047932eb.pdf

Van Meurs, P., and Niiler, P. P. (1997). Temporal variability of the large scale geostrophic surface velocity in the Northeast Pacific. *Journal of Physical Oceanography*, 27, 2288–2297.

Venables, H. J., and Meredith, M. P. (2009).Theory and observations of Ekman flux in the chlorophyll distribution downstream of South Georgia. *Geophysical Research Letters*, 36, L23610. doi: 10.1029/2009GL041371

Vialard, J., and Delecluse, P. (1998). An OGCM study for the TOGA decade. Part I: Role of salinity in the physics of the western Pacific fresh pool. *Journal of Physical Oceanography*, 28, 1071–1088. doi: http://dx.doi.org/10.1175/1520-0485(1998)028<1071:AOSFTT>2.0.CO;2

Warren, B. A. (2009). Note on the vertical velocity and diffusive salt flux

induced by evaporation and precipitation. *Journal of Physical Oceanography*, 39(2), 680–682, doi: http://dx.doi.org/10.1175/2009JPO4069.1

Wüst, G. (1936). Oberflächensalzgehalt, Verdunstung und Niederschlag auf dem Weltmeere. Länderkundliche Forschung, Festschrift Norbert Krebs, 347–359.

Yin, X., Boutin, J., Dinnat, E., Song, Q., and Martin, A. (2016). Roughness and foam signature on SMOS-MIRAS brightness temperatures: A semi-theoretical approach. *Remote Sensing of Environment*, 180. doi: http://dx.doi.org/10.1016/j.rse.2016.02.005

Yueh, S.H., West, R., Wilson, W.J., Li, F.K., Njoku, E.G., Rahmat-Samii, Y. (2001). Error sources and feasibility for microwave remote sensing of ocean surface salinity. *IEEE Transactions on Geoscience and Remote Sensing*, 39 (5), 1049-1060. doi: 10.1109/36.921423

Yu, L. (2011). A global relationship between the ocean water cycle and near-surface salinity. *Journal of Geophysical Research*: *Oceans*, 116, C10025. doi: 10.1029/2010JC006937

Yu, L., Jin, X., and Weller, R. A. (2008). *Multidecade Global Flux Datasets from the Objectively Analyzed Air-sea Fluxes (OAFlux) Project*: *Latent and sensible heat fluxes, ocean evaporation, and related surface meteorological variables* in Woods Hole Oceanographic Institution, OAFlux Project Technical Report. OA-2008-01 (Woods Hole, MA), 64 pp.

Zilberman, N. V., Roemmich, D. H., and Gille, S. T. (2013). The Mean and the Time Variability of the Shallow Meridional Overturning Circulation in the Tropical South Pacific Ocean. *Journal of Climate*, 26, 4069–4087. doi: http://dx.doi.org/10.1175/JCLI-D-12-00120.1

Zine, S., Boutin, J., Font, J., Reul, N., Waldteufel P., Gabarro, C., Tenerelli, J., Petitcolin F., Vergely J.-L., Talone, M., and Delwart S. (2008). Overview of the SMOS sea surface salinity prototype processor. *IEEE Transactions on Geoscience and Remote Sensing*, 46 (3), 621–645. doi: 10.1109/TGRS.2008.915543